

3098

2342149

TR 3099

**THE DYNAMIC RESPONSE OF TYRES  
TO BRAKE TORQUE VARIATIONS  
AND ROAD UNEVENNESSES**



# **THE DYNAMIC RESPONSE OF TYRES TO BRAKE TORQUE VARIATIONS AND ROAD UNEVENNESSES**

PROEFSCHRIFT

ter verkrijging van de graad van doctor  
aan de Technische Universiteit Delft,  
op gezag van de Rector Magnificus Prof. ir. K.F. Wakker  
in het openbaar te verdedigen  
ten overstaan van een commissie,  
door het College voor Promoties aangewezen  
op maandag 16 maart 1998 te 13:30 uur

door

**Peter Willem Anton ZEGELAAR**

werktuigkundig ingenieur  
geboren te Sliedrecht

**Dit proefschrift is goedgekeurd door de promotor:**

Prof. dr. ir. H.B. Pacejka

**Samenstelling promotiecommissie:**

Rector Magnificus,	Technische Universiteit Delft, voorzitter
Prof. dr. ir. H.B. Pacejka,	Technische Universiteit Delft, promotor
Prof. dr. ir. E. van der Giessen,	Technische Universiteit Delft
Prof. dr. ir. A.A.A. Molenaar,	Technische Universiteit Delft
Prof. dr. ir. J.A. Mulder,	Technische Universiteit Delft
Prof. dr. R.S. Sharp,	Cranfield University, Engeland
Dr. ir. A.Th. van Zanten,	Robert Bosch GmbH, Duitsland
Prof. ir. C.P. Keizer,	Technische Universiteit Delft, reserve

Delft University of Technology  
Mekelweg 2  
2628 CD Delft  
The Netherlands

ISBN 90-370-0166-1

Copyright © by Peter W.A. Zegelaar, 1998.

All rights reserved. No part of the material protected by this copyright may be reproduced or utilised in any form by any means, electronic or mechanical, including photocopying, recording or by any information storage and retrieval system, without the prior written permission of the author.

The author makes no warranty that the methods, calculations and data in this book are free from error. The application of the methods and results are at the user's risk and the author disclaims all liability for damages, whether direct, incidental or consequential, arising from such application or from any other use of this book.

Printed in Delft, the Netherlands



## **Stellingen**

behorende bij het proefschrift

### **“The Dynamic Response of Tyres to Brake Torque Variations and Road Unevennesses”**

1. De aanstoting van een band door korte wegdekoneffenheden kan worden weergegeven met behulp van drie effectieve inputs welke gemeten worden bij zeer lage snelheid: de effectieve wegdekhoogte, de effectieve wegdekhelling en de variaties van de effectieve rolstraal (*dit proefschrift*).
2. Het flexibele-ring-model kan gebruikt worden om de quasi-statische responsies van de band rollend over korte wegdekoneffenheden te bepalen indien de niet-lineariteiten van de zijwangstijfheden ingevoerd worden in dit model (*dit proefschrift*).
3. Het starre-ring-model waarin de gordel van de band gemodelleerd wordt als een starre ring afgesteund op de zijwangstijfheden geeft een realistische beschrijving van het dynamisch gedrag van de band in het frequentiegebied 0-80 Hz (*dit proefschrift*).
4. De eerste orde differentiaalvergelijking met de relaxatielengte als parameter kan ook worden gebruikt voor zeer lage rijnsnelheden indien de bandvervorming of de slip als toestandsvariabele wordt gebruikt en de slipsnelheid als ingangsvariabele (*dit proefschrift*).
5. De invloed van een relaxatielengte-systeem op het gedrag van de band wordt sterk bepaald door de gekozen randvoorwaarden van het wiel: de stuurhoek als ingangsvariabele voor het dwarsgedrag en het remmoment als ingangsvariabele voor het langsgedrag (*dit proefschrift*).
6. De uitdrukking voor de relaxatielengte voor het langsgedrag van de band (langsslipstijfheid gedeeld door langsstijfheid) is overeenkomstig aan de uitdrukking voor de relaxatielengte voor het dwarsgedrag (dwarsslipstijfheid gedeeld door dwarsstijfheid) (*dit proefschrift*).

7. Experimenteel onderzoek is essentieel voor de ontwikkeling van een realistisch bandmodel. Tevens moeten de experimentele condities zo gekozen worden dat ze zo goed mogelijk overeenkomen met de condities waarvoor het model ontwikkeld wordt.
8. Het onderzoek naar comfort (trillingen en geluid) van voertuigen op een slechte weg en het ontwerp van regelsystemen zoals ABS en VDC met behulp van computersimulaties vergen een geschikt dynamisch bandmodel.
9. Gezien het feit dat op de Nederlandse wegen nauwelijks loslopend vee voorkomt, moeten voertuigaccessoires zoals 'bull-bars' verboden worden omdat deze in geval van een aanrijding de overige verkeersdeelnemers onnodig schade en letsel kunnen toebrengen.
10. Het gebruik van verkeersdrempels om de gemiddelde snelheid van voertuigen te verlagen is vanuit het milieu-oogpunt een verkeerde methode.
11. Om te kunnen promoveren op een voertuigdynamisch onderzoek is het bezit van een motorvoertuig geen noodzakelijke voorwaarde.
12. Bij de discussie over het gebruik van de randen van de nacht voor het vliegverkeer, wordt vaak ten onrechte voorbijgegaan aan het ongemak voor reizigers die of midden in de nacht thuiskomen of midden in de nacht thuis moeten vertrekken.
13. Geavanceerde computeranimaties vergroten de betrouwbaarheid van een weersvoorspelling niet.
14. Het proefschrift van een AIO mag geen levenswerk zijn.  
(*Prof.dr W.A. Wagenaar, Mare, 29 januari 1998*)

Delft, 16 maart 1998

Peter W.A. Zegelaar

# Acknowledgments

---

This thesis presents the results of my work performed at the Delft University of Technology for a period of seven years. I would like to express my gratitude to Professor H.B. Pacejka for the trust he had in me and for the freedom to I got to do this research project. His guidance and stimulations were indispensable for the completion of this thesis.

I would like to extend my gratitude to all of my colleagues at the Vehicle Research Laboratory of the Delft University of Technology for the pleasant working environment, the stimulating discussions and their friendship. I had a very good feedback from my fellow PhD student Jan Pieter Maurice who developed the model for the out-of-plane tyre dynamics and from Sven Jansen of TNO Road-Vehicles Research Institute who implemented the rigid ring model in a multi-body simulation code. I would like to thank the SWIFT partners, not only for their financial contribution to this project, but also for the stimulating and fruitful discussions we had during the progress meetings.

The key factor in this research were the experimental facilities in the Vehicle Research Laboratory of the Delft University of Technology. I would to express my gratitude to Peter Roest for his excellent design of the mechanical brake system. Furthermore, I would like to thank Xu Zhixin of the Tongji University in Shanghai, P.R. of China, who worked as a guest researcher in the Vehicle

## Acknowledgements

---

Research Laboratory. He designed and constructed the hydraulic system to control the brake pressure. His system allowed us to control the brake pressure conveniently.

The research presented in this thesis was not possible without the contributions of students to either theoretical work or, sometimes tedious, experimental work. I would like to thank Anton Slagboom, Paul van der Hek, René Heusdens, Richard de Jager, Pieter Aalberts, Martin Heijkamp, Arjan Spaargaren, Adriaan Westland, Ivo Wahlen, Marcello Berzeri, Daniele Casanova, Govert de With, Jeroen Pleizier, Marc de Graaf and Christiaan Langelaar for their contribution to this research project.

Finally, I would like to thank Korien for her help and support during the preparation of this thesis.

Delft, February 2, 1998

Peter Zegelaar

# C

## ontents

---

<b>Notation</b>	<b>9</b>
<b>Chapter 1 General Introduction</b>	
1.1 The pneumatic tyre.....	13
1.2 Tyre modelling for vehicle dynamic analysis.....	15
1.3 Objectives and scope .....	17
1.4 Outline of the thesis .....	21
<b>Chapter 2 Static Tyre Properties</b>	
2.1 Introduction .....	25
2.2 Contact patch dimensions .....	26
2.3 Vertical tyre stiffnesses .....	28
2.4 Longitudinal tyre stiffnesses .....	34
2.5 Inertia properties of the tyre .....	37

<b>Chapter 3</b>	<b>Stationary Slip Characteristics</b>	
3.1	Introduction .....	39
3.2	Definition of slip variables .....	41
3.3	The brush model .....	42
3.4	The Magic Formula model.....	46
3.5	Measured slip characteristics.....	48
3.6	Rolling resistance.....	50
3.7	Tyre radii.....	51
<b>Chapter 4</b>	<b>The Rolling Tyre as a Geometric Filter over Short Wavelength Road Unevennesses</b>	
4.1	Introduction .....	57
4.2	The flexible ring model .....	63
4.3	The simulation model .....	71
4.4	Validation of the static behaviour of the flexible ring model.....	74
4.5	The tyre rolling over short wavelength obstacles.....	77
4.6	Effective inputs from short wavelength obstacles.....	81
4.7	Effective rolling radius variations on an effective road surface ..	87
4.8	Definition of a geometric filter .....	96
<b>Chapter 5</b>	<b>Physical Transient Tyre Model</b>	
5.1	Introduction .....	101
5.2	Analytical response to small variations of slip .....	102
5.3	Analytical response to small variations of vertical load .....	110
5.4	Discretisation of the tread .....	116
<b>Chapter 6</b>	<b>Pragmatic Transient Tyre Models</b>	
6.1	Introduction .....	127
6.2	Pragmatic tyre models based on the relaxation length concept.....	129
6.3	Discussion of the simulation results of the pragmatic models ..	142
6.4	Basic influence of a relaxation system on tyre dynamics .....	149
<b>Chapter 7</b>	<b>Development of the Rigid Ring Tyre Model</b>	
7.1	Introduction .....	153
7.2	The dynamics of a rotating free tyre-wheel system .....	156
7.3	The dynamics of the tyre touching the road surface .....	163
7.4	The rotation wheel and the application of a brake torque .....	171
7.5	The linearised equations of motion for constraint axle motion ..	172
7.6	Validation of the model and parameter assessment .....	175

**Chapter 8 Modal Analysis of Tyre In-Plane Vibrations**

8.1	Introduction .....	181
8.2	Experimental modal analysis.....	185
8.3	Theoretical modal analysis using the flexible ring model.....	189
8.4	Comparison of the experimental findings with the theoretical results using the flexible ring model.....	194
8.5	Theoretical modal analysis using the rigid ring model.....	199

**Chapter 9 Dynamic Tyre Responses to Brake Torque Variations**

9.1	Introduction .....	205
9.2	Frequency Response Functions.....	208
9.3	Braking with successive steps in brake pressure.....	216
9.4	Braking with wheel lock .....	221
9.5	Braking to stand-still.....	225
9.6	Conclusions .....	226

**Chapter 10 Dynamic Tyre Responses to Short Wavelength Road Unevennesses**

10.1	Introduction .....	231
10.2	Experimental setup .....	234
10.3	Natural frequencies obtained directly from the measurements ..	235
10.4	Excitation of the tyre by the effective road surface.....	240
10.5	Vertical tyre responses to a trapezoid cleat.....	247
10.6	Longitudinal tyre responses to a trapezoid cleat .....	251
10.7	Tyre responses to other obstacle shapes.....	257
10.8	Tyre responses during braking .....	259
10.9	Simulations with non-constraint axle height .....	263

**Chapter 11 Dynamic Tyre Responses to Axle Height Oscillations While Braking**

11.1	Introduction .....	267
11.2	Comparison of the results.....	269

**Chapter 12 Conclusions and Recommendations**

12.1	The rigid ring model .....	277
12.2	Tyre enveloping properties.....	279
12.3	Recommendations for further research .....	280

**Appendix A Experimental Setup**

A.1 Cleat and brake test stand.....	283
A.2 Tyre measurement tower.....	286
A.3 Data acquisition and processing.....	287

**Appendix B The Magic Formula and the Rigid Ring Model 289**

**References 293**

**Summary 303**

**Samenvatting 307**

**Curriculum Vitae 313**

**List of Publications 315**



# Notation

---

Symbol	Unit	Description
$a$	[m]	half the contact length
$A$	[m <sup>2</sup> ]	area of the cross-section of the ring
$A$	[rad]	height of the basic functions for effective plane angle
$A_c$	[m <sup>2</sup> ]	total area of the contact patch
$a_n$	[m]	modal displacements of tyre ring
$b$	[m]	half the contact width
$\beta$	[rad]	effective plane angle
$b_n$	[m]	modal displacements of tyre ring
$b_R$	[m]	width of the tyre ring
$\mathbf{C}$		damping matrix
$C_\kappa$	[N]	longitudinal slip stiffness
$C_x$	[N/m]	longitudinal tyre stiffness
$C_z$	[N/m]	vertical tyre stiffness
$c$	[-]	coefficient of the contact ellipsoid
$c_b$	[N/m]	translational sidewall stiffness
$c_{b\theta}$	[Nm/rad]	rotational sidewall stiffness
$c_{bv}$	[N/m <sup>2</sup> ]	tangential sidewall stiffness per unit of length

## Notation

---

$c_{bw}$	[N/m <sup>2</sup> ]	radial sidewall stiffness per unit of length
$c_{ep}$	[N/m <sup>2</sup> ]	longitudinal tread element stiffness per unit of length
$c_{cx}$	[N/m]	longitudinal stiffness of tread in the contact patch
$c_n$	[m]	modal displacements of tyre ring
$d_n$	[m]	modal displacements of tyre ring
$E$	[-]	error
$E$	[N/m <sup>2</sup> ]	modules of elasticity
$EA$	[N]	extensional stiffness tyre ring
$EI$	[Nm <sup>2</sup> ]	bending stiffness tyre ring
$f$	[Hz]	frequency
$f_r$	[-]	rolling resistance coefficient
$F_s$	[N]	pre-tension of tyre ring
$G$	[N/m <sup>2</sup> ]	shear modules of elasticity
$H$		frequency response function
$H$	[m]	height of the basic functions for effective plane height
$h_s$	[m]	height of the tyre sidewall
$I_a$	[kg m <sup>2</sup> ]	moment of inertia of part of tyre that moves with rim
$I_b$	[kg m <sup>2</sup> ]	moment of inertia of part of tyre that moves with tyre ring
$j$	[-]	complex variable
<b>K</b>		stiffness matrix
$k_b$	[Ns/m]	translational sidewall damping coefficient
$k_{b\theta}$	[Nsm/rad]	rotational sidewall damping coefficient
$k_{bv}$	[Ns/m <sup>2</sup> ]	tangential sidewall damping per unit of length
$k_{bw}$	[Ns/m <sup>2</sup> ]	radial sidewall damping per unit of length
$l_s$	[m]	arc length of the tyre sidewall
<b>M</b>		mass matrix
$m_b$	[kg]	mass of part of tyre that moves with tyre ring
$m$	[-]	number of modes
$n$	[-]	number of points
$p$	[N/m <sup>2</sup> ]	tyre inflation pressure
$p_c$	[N/m <sup>2</sup> ]	average vertical pressure in the contact patch
<b>Q</b>		transformation matrix from fixed to rotating coordinate system
$q_a$		coefficients polynomial half the contact length as function of vertical load
$q_{bV}$	$[\sqrt{s}/\sqrt{m}]$	coefficients decrease in sidewall stiffness with velocity
$q_{Fcx}$	[1/m]	coefficients decrease in radial deflection with longitudinal deflection

$q_{fr}$		coefficients polynomial rolling resistance coefficient as function of velocity
$q_{Fz}$		coefficients vertical force as function of vertical deflection
$q_{kc}$		coefficients tread element damping as function of velocity
$q_{re}$		coefficients polynomial effective rolling radius as function of vertical load
$q_{tot}$	[N/m <sup>2</sup> ]	total external pressure distribution per unit of length
$q_v$		coefficients velocity dependency vertical tyre stiffness
$q_v$	[N/m <sup>2</sup> ]	tangential pressure distribution (force per unit of length)
$q_w$	[N/m <sup>2</sup> ]	radial pressure distribution (force per unit of length)
$q_x$	[N/m <sup>2</sup> ]	longitudinal pressure distribution (force per unit of length)
$q_z$	[N]	vertical pressure distribution (force per unit of length)
$R$	[m]	radius of the test drum
$\Delta r$	[m]	increase tyre radius with velocity
$r_0$	[m]	radius of the free tyre
$r_e$	[m]	effective rolling radius
$r_l$	[m]	loaded tyre radius
$r_s$	[m]	radius of the tyre sidewall
$s$	[m]	position in the contact patch relative to the centre of the contact patch
$S_{xx}$		auto spectral density function
$S_{xy}$		cross spectral density function
$t$	[m]	thickness of the tyre sidewall
$t$	[s]	time
$u$	[m]	longitudinal deformation
$v$	[m]	tangential displacement
$V_r$	[m/s]	rolling velocity
$V_{sx}$	[m/s]	longitudinal slip velocity
$V_x$	[m/s]	longitudinal velocity
$w$	[m]	effective plane height
$w$	[m]	radial displacement
$x$	[m]	displacement in the longitudinal direction
$y$	[m]	displacement in the lateral direction
$z$	[m]	displacement in the vertical direction

## Notation

Symbol	Unit	Description
$\varepsilon_z$	[m]	horizontal shift vertical force in contact zone
$\varepsilon_z$	[m]	vertical shift horizontal force in contact zone
$\Gamma$	[-]	coherence function
$\eta$	[m/N]	load dependency of the effective rolling radius
$\eta$	[N/m]	modal force acting on the tyre ring
$\varphi$	[rad]	angle of rotation about the wheel axis
$\kappa$	[-]	practical slip
$\kappa$	[-]	relative damping
$\lambda$	[-]	transition point sliding region of the brush model
$\lambda_{bf}$	[m]	width of the basic functions
$\lambda_{imp}$	[m]	shift of the basic functions
$\lambda_{os}$	[m]	offset of the basic functions
$\mu$		mean value
$\mu$	[-]	friction coefficient
$\theta$	[-]	tyre parameter of the brush model
$\theta$	[rad]	angle of rotation about the wheel axis
$\rho_A$	[kg/m]	mass density of tyre ring
$\rho_x$	[m]	longitudinal tyre deformation
$\rho_z$	[m]	vertical tyre deformation
$\sigma$		standard deviation
$\sigma$	[m]	relaxation length
$\tau$	[s]	time interval, time constant
$\omega$	[rad/s]	frequency
$\Omega$	[rad/s]	rotational velocity
$\xi$	[N/m]	modal force acting on the tyre ring
$\zeta_x$	[-]	theoretical longitudinal slip

## Indices:

$a$	axle, rim or suspension	$n$	mode number
$b$	tyre belt or tyre sidewall	$\theta$	rotation about y-axis
$c$	contact patch	$r$	rolling
$e$	effective	$r$	residual
$e$	external	$s$	slip
$i$	internal	$T$	tangential direction
$i$	at point $i$	$x$	in $x$ direction
$l$	loaded	$z$	in $z$ direction
$N$	normal direction	$0$	undeformed, static value

# 1

## General Introduction

---

### 1.1 The pneumatic tyre

The pneumatic tyre forms a vital component of a road vehicle as it interacts with the road in order to produce the forces necessary for support and movement of the vehicle. A thorough understanding of the behaviour of the pneumatic tyre is an essential aspect of analysing the dynamics of vehicles.

The forces and moments generated in the tyre are the result of tyre deflections due to the interaction between wheel and road. Tyre vibrations arise through road irregularities, wheel axle motions, and tyre non-uniformities. The complex tyre structure with its compliance and inertia may give rise to isolation from these irregularities in certain frequency ranges but also to magnification at other frequencies.

In the longitudinal direction the force variations arise through road irregularities, which are transmitted to the wheel axle and through the wheel suspension to the car body and steering wheel. Fluctuations in the wheel angular speed due to braking and driving will also generate longitudinal force variations. The cornering force acts in the lateral direction; road irregularities and wheel vertical and steering oscillations have a large influence on the force generated. The vertical oscillations induced by road and tyre irregularities are transmitted

to the axle and further to the vehicle. The variations in normal load of the tyre have an important, often adverse, effect on the generation of horizontal shear forces.

The behaviour of the pneumatic tyre is related to its complex construction, it can be seen as a visco-elastic torus composed of high-tensile-strength cords and rubber. Figure 1.1 shows the construction of a radial-ply tyre which is the typical construction of modern automobile tyres. The radial-ply tyre (in short radial tyre) is characterised by parallel cords running directly across the tyre from one bead to the other. These cords are referred to as the carcass plies. Directional stability of the tyre is supplied by the enclosed pressurised air acting on the sidewalls of the carcass and by a stiff belt of fabric or steel that runs around the circumference of the tyre. The direction of the parallel plies of the belt is relatively close to the circumferential: typically  $20^\circ$ .

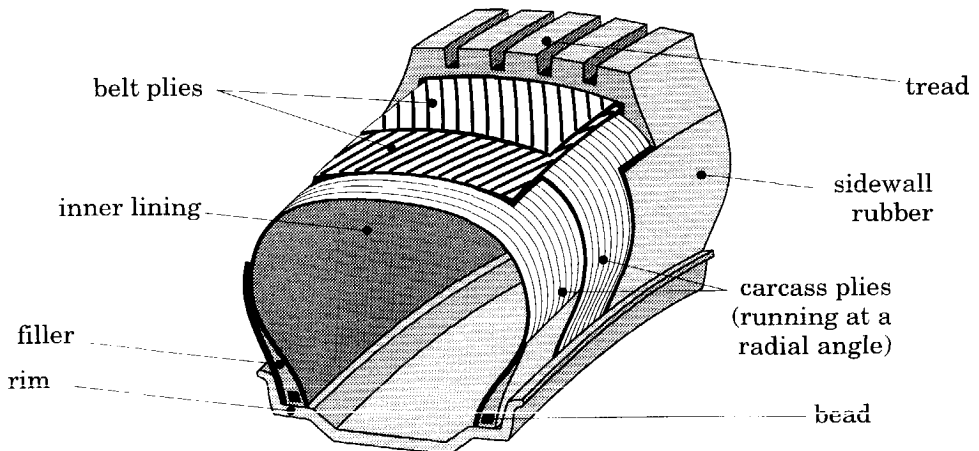


**Figure 1.1:** *Construction of a radial-ply tyre.*

The relatively soft carcass provides the radial tyre with a soft ride and the stiff belt provides the radial tyre with good cornering properties by keeping the tread flat on the road despite horizontal deflections of the tyre. The function of the tread is to establish and maintain contact between the tyre and the road. The key factor for the generation of horizontal forces in the contact zone is the adhesion between tread and road. The remaining components of the tyre are the steel-cable beads which firmly anchor the assembly to the rim.

## 1.2 Tyre modelling for vehicle dynamic analysis

Understanding of tyre properties is essential to the proper design of vehicle components such as wheel suspensions, steering and braking systems. For this purpose, different kinds of mathematical models of the behaviour of the pneumatic tyre are used in vehicle dynamic simulations. We may distinguish theoretical models based on the physics of the tyre construction, and empirical models which are based on experimental data. Combinations of both approaches are also used in the development of the tyre models.

To understand the force generation of the tyre, it is useful to introduce the concept of *slip* of a rolling tyre, which is connected with the difference between the actual wheel velocity and the wheel velocity at free rolling. Free rolling is the situation in which the tyre is neither braked nor driven. The relationship that depicts the generated horizontal force as function of the slip in steady-state conditions is called the *steady-state slip characteristic* or the *stationary slip characteristic*. At small values of slip, the horizontal forces depend mainly on the elastic deformation of tyre. At very small values of slip the generated horizontal force is proportional to the slip, and the ratio is called the *slip stiffness*. At higher levels of slip the horizontal forces are limited by the friction between tyre and road. The strongly non-linear slip characteristics determine to a great extent the behaviour of vehicles manoeuvring at high levels of lateral acceleration [2,41,45,92,99].

Physical tyre models based on detailed modelling of the tyre can provide accurate results only by excessive consumption of computer resources and calculation time. Hence, at present, these kinds of models are not suitable for vehicle dynamic studies [22,84,99]. The empirical models, on the other hand, are much faster in calculation as these models represent measured tyre data in a rather compact form [87,88].

Steady-state tyre models will lose their validity when the motion of the wheel shows variations in time as the horizontal tyre deformation does not instantaneously follow slip variations. To build up a horizontal deflection the tyre has to travel a certain distance. The distance travelled needed to reach 63% of the steady-state deflection after a step change is generally designated *relaxation length* and is approximately independent of the running speed of the tyre.

Figure 1.2a shows the typical response of the horizontal force  $F$  to a step change in the slip as function of the travelled distance  $x$ . Figure 1.2b shows the step response of the tyre as function of the time  $t$ . The time constant  $\tau$  of this

transient response is defined as the relaxation length  $\sigma$  divided by the velocity  $V$  and decreases with the velocity:

$$\tau = \frac{\sigma}{V} \quad (1.1)$$

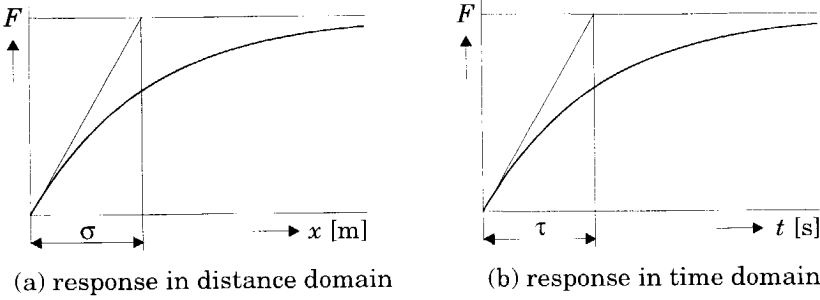


**Figure 1.2:** *A first order response in both the distance and the time domains.*

It is important to include the relaxation length when studying vehicle manoeuvres with a relatively fast steering input such as lane changes [100]. Furthermore, the relaxation length plays an important role in the ‘shimmy’ phenomenon. Shimmy is a self-excited vibration of the steerable wheels about the steering axis, which may occur in the front wheels of a road vehicle [80] or in the landing gear of a taxiing aircraft [14,18]. To accurately represent the weave and wobble modes of single track vehicles (*i.e.* motorcycles) it is essential to include the relaxation length [73,102]. The relaxation length increases with increasing vertical load and decreases with increasing slip. This non-constant relaxation length has an adverse effect on the generation of horizontal forces during variations in vertical load while cornering [86,106,107].

The relaxation length approach, however, is satisfactory only for low frequencies, as the inertia properties of the tyre cannot be neglected at higher frequencies. Furthermore, the influences of the inertia forces become more important at higher velocities [67]. The dynamic properties of tyres play an important role in the design of control algorithms like Anti-lock Brake Systems (ABS) or Vehicle Dynamics Control systems (VDC). For instance, the rapid brake pressure variations during ABS operation cause oscillations of the tyre-wheel system. Adequate dynamic tyre models are needed to design and evaluate the control systems [121,122], or to analyse the operation of ABS on uneven roads [44].



A fairly new area of interest is the development of tyre models for driving simulators. In these simulators the human-vehicle interaction is investigated rather than the behaviour of the vehicle itself. The requirements for a driving simulator are that it should have realistic behaviour and the 'real time' simulations. One aspect of the realistic behaviour is that the driving simulator needs to be able to stop and to start again. This requirement puts additional stress on the tyre model, as most simulations encounter numerical problems at low speeds because the speed appears in the denominator of the expressions of slip [11,117].

To study ride and comfort of vehicles in the low and intermediate frequency range (0-50 Hz) the tyre may be represented by its vertical compliance only, while the damping is usually neglected. Such simple tyre models are used for the development of passive and actively controlled vehicle suspensions [48].

The investigation of noise, vibration and harshness (NVH) requires a more detailed tyre model. An overview is given in the state-of-the-art paper of Willumeit and Böhm [118]. An elegant model to study the in-plane vibrational properties of tyres is the flexible ring model introduced by Tielking [109]. Gong used such a model to study the vibration transmission properties of tyres in the frequency range 0-250 Hz [33]. At higher frequencies (200-1000 Hz) the tread pattern produces airborne noise [89].

The last category of tyre models is represented by models that give a detailed description of the tyre structure. The tyre structure is very complex as the tyre is a multi-layered, non-uniform, anisotropic, cord-rubber composite [22]. These physical models are based on powerful finite element computer codes. Ridha and Theves give an overview [94] of the mechanics of tyres, in which they focus on durability, wear, noise, rolling resistance, vibrations and adhesion of a rolling and slipping tyre. These kinds of models, which suit the tyre engineer rather than the vehicle engineer, are beyond the scope of the research presented.

### **1.3 Objectives and scope**

The research presented in this thesis forms part of a project carried out at the Vehicle Research Laboratory of the Delft University of Technology and the TNO Road-Vehicles Research Institute. The project is called SWIFT, which stands for Short Wavelength Intermediate Frequency Tyre model. This project is supported by an international industrial consortium: Audi AG, BMW AG, Continental AG, Ford GmbH, Goodyear Technical Center Luxembourg, ITT Automotive Europe

GmbH, Mercedes-Benz AG, PSA Peugeot-Citroën, Robert Bosch GmbH. The objectives of this research project are the development and implementation of a mathematical model of a pneumatic tyre that is well suited for vehicle simulations even under extreme manoeuvring conditions. The requirements for the model development are:

- A compact relatively fast tyre model, as it has to be used for vehicle dynamic simulations.
- Accurate representation of measured stationary slip characteristics.
- High and low velocities, including starting to roll from stand-still.
- Medium frequency range ( $f < 50$  Hz).
- Short wavelengths ( $\lambda > 0.2$  m).
- Uneven roads with relatively short and sharp unevennesses.

In this thesis the development of the tyre model for in-plane dynamics will be discussed, the model for the out-of-plane tyre dynamics is being developed by Maurice [65] while TNO is responsible for the professional software development of the model. The tyre in-plane dynamics refer to tyre vibrations in the wheel plane. The wheel plane is the central plane of the tyre normal to the axis of rotation, see Figure 1.3. The tyre stands on the road plane and the contact patch is defined as the interface between tyre and road.

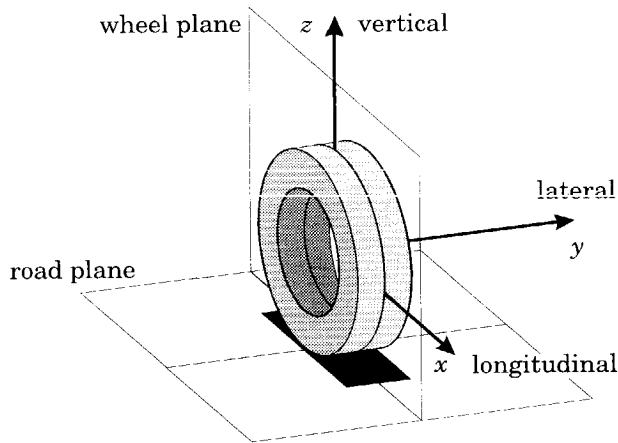


**Figure 1.3:** *The coordinate system used.*

A right-handed Cartesian coordinate system  $(x,y,z)$  oriented according to ISO 8855 is used. The  $x$ -axis is oriented along the intersection line of the wheel plane and the road plane with the positive direction forwards. The  $z$ -axis is perpendicular to the road plane with the positive direction upwards. The  $y$ -axis is perpendicular to

the wheel plane, its direction is chosen to make the axis system orthogonal and right-handed. This convention produces a positive vertical force for a loaded tyre. In addition, if the tyre rolls in positive  $x$  direction, the rotational velocity about the  $y$ -axis is positive as well, traction forces are oriented in the positive  $x$  direction and braking forces are negative.

Tyre in-plane dynamics are referred to as vibrations in the longitudinal and the vertical directions and rotational vibrations about the wheel-axis. From the geometrical point of view, the tyre is assumed to be symmetrical with respect to the wheel plane. Tyre in-plane dynamics may also be referred to as *symmetrical* tyre behaviour, while tyre out-of-plane dynamics may be referred to as *anti-symmetrical* behaviour [83].

### Domains used for the analysis of tyre behaviour

The responses of the tyre will be analysed in both the time domain and the frequency domain. The frequency domain is most suitable for estimating frequency response functions and natural frequencies of the tyre. The time domain will be used for analysing the non-linear tyre responses. The Fourier transformation is used to transform the signals between the time domain and the frequency domain.

The transient tyre response is characterised by the relaxation length which is approximately independent of the velocity. Therefore, the tyre transient responses will be studied in the travelled distance domain. Analogously, the responses in the frequency domain can be transformed into responses in the road-frequency domain. Figure 1.4 presents the transformations between the various domains.

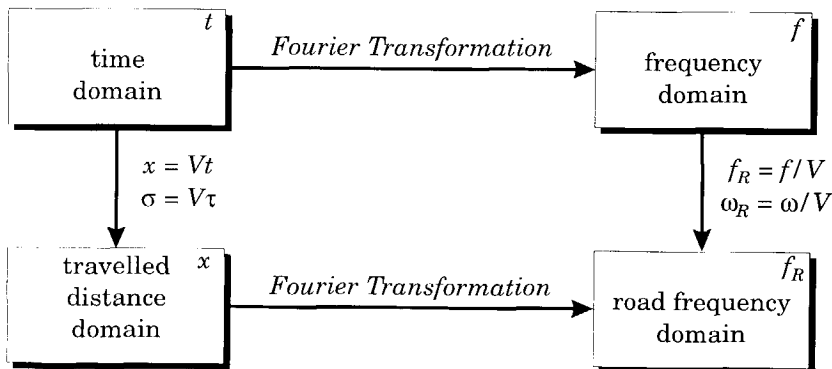


Figure 1.4: The domains used in the analysis.

The road frequency  $f_R$  can be expressed in terms of the time frequency  $f$ :

$$f_R = \frac{f}{V} \quad (1.2)$$

The road irregularities can be expressed in terms of wavelength. The wavelength  $\lambda$  of the excitation is defined as:

$$\lambda = \frac{1}{f_R} = \frac{V}{f} \quad (1.3)$$

### The tyre used as reference for the model development

In this thesis *many* aspects of one tyre are investigated rather than *one* aspect of many tyres because we focus on the model development rather than on comparing the performance of several tyres. The model developed in this thesis is considered to be a general model for the in-plane tyre behaviour even though this model has been validated for one tyre only. It is expected that the basic structure of the model will not have to be changed to represent different types of tyres.

The tyre used in this research is a standard passenger car tyre with the dimensions 205/60R15 91V, where (cf. [93] and Figure 1.5):

205 = section width of the tyre in millimetres.

60 = aspect ratio: the ratio between the section height and section width in %.

R = construction of the tyre: radial tyre.

15 = diameter of the rim in inches.

91 = load index: the maximum nominal wheel load is 6030 N.

V = speed rating: the maximum velocity is 240 km/h.

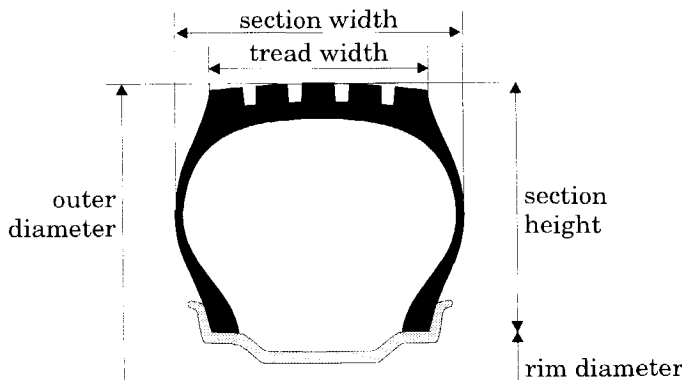


**Figure 1.5:** *The tyre cross-section.*

## Experimental setup

The experiments were carried out on the rotating drum test stand in the Vehicle Research Laboratory of the Delft University of Technology. The wheel with the tyre is mounted in a rig on top of the rotating drum that represents the road surface. The experimental conditions are:

- Constant inflation pressure of 2.2 bar for a cold tyre.
- Three constant axle heights corresponding to 2000, 4000, 6000 N vertical load for a non-rotating tyre. Due to the constant axle height the vertical force grows with increasing velocity.
- Five constant drum velocities: 25, 39, 59, 92 and 143 km/h.
- Relative new tyre with little or no wear.

Appendix A presents the experimental configurations.

## 1.4 Outline of the thesis

Rather than modelling the complex tyre structure in all its details, the most important dynamic properties of the tyre will be taken into account in a mathematical model of the tyre. Such an approach will lead to a relatively compact tyre model. The typical structure of the radial tyre is a stiff belt mounted on a relatively soft carcass. The development of the model is based on the assumption that the belt remains rigid in the frequency range considered. Accordingly, the tyre belt is modelled as a rigid ring suspended on the rim by means of springs and dampers representing the carcass which contains pressurised air. A contact model is added to the ring dynamics to generate the forces between tyre and road. The complete model will be called the *rigid ring model*.

Figure 1.6 presents a schematic outline of this thesis. The central chapter of this thesis is Chapter 7: the development of the rigid ring tyre model. To be able to develop this model some detailed theoretical and experimental studies of the tyre behaviour are presented in Chapters 2 through 6. The goal of these preliminary chapters is to gain insight into certain aspects of the behaviour of the tyre and the results of these chapters are used as building blocks for the rigid ring model. The rigid ring model is validated for various situations in the Chapters 8 through 11.

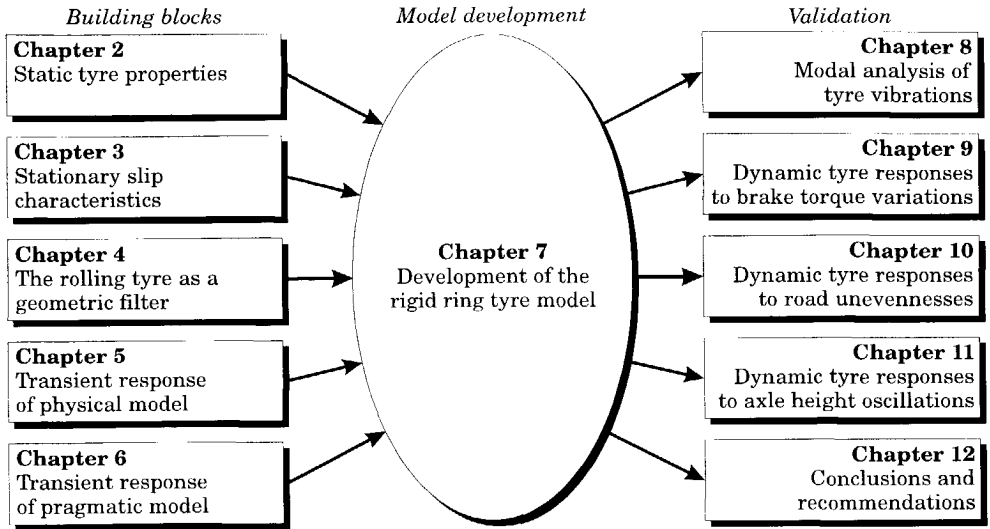


**Figure 1.6:** *Structure of the development and the validation of the rigid ring tyre model.*

Chapter 2 presents the basic tyre properties which are needed for the model development like the vertical and longitudinal tyre stiffnesses, the inertia properties of the tyre and the dimensions of the contact patch. The force generation of a rolling tyre under steady-state conditions is presented in Chapter 3.

The excitation of tyres by short wavelength unevennesses is discussed in Chapter 4. The rolling tyre acts as a geometric filter and smoothenes the sharp edges of these short wavelength unevennesses. The rigid ring model cannot be used directly on such irregularities because the interface of this model with the road is represented by a single point only. This problem is approached in an empirical way: the tyre is rolled over the obstacle at very low velocity and these quasi-static tyre responses are transformed into an effective road surface. The effective road surface is used as input to the rigid ring model rather than the actual shape of the obstacle concerned.

Chapters 5 and 6 present the transient response of the tyre. Chapter 5 approaches this problem from a physical point of view where the tread is modelled as individual elements. Chapter 6 approaches the problem pragmatically: the tyre transient response is represented by a first order differential equation based on the relaxation length concept.

After all sub-models and building blocks have been developed, the rigid ring model is developed in Chapter 7. The modes of vibration of a non-rotating tyre are validated in Chapter 8. Unfortunately, the experimental modal analysis technique used did not allow the validation of the modes of a rotating tyre. Instead, the natural frequencies of the rolling tyre were validated in Chapter 9, 10 and 11.

The tyre in-plane dynamics are generally excited by road unevennesses, longitudinal and vertical axle motions, brake torque fluctuations and tyre non-uniformities. The tyre model will be validated for three of the five possible excitations: Chapter 9 presents the tyre responses to brake torque variations; Chapter 10 presents the tyre responses to uneven roads; and Chapter 11 presents the tyre responses to axle height oscillations.

In the experimental investigations, tyre non-uniformities were not considered. We may refer to an earlier study on this type of tyre responses [82]. The longitudinal axle motions are also not used as excitation of the tyre because no facilities were available. The responses to such an excitation do not provide information additional to that provided by brake torque variations because the longitudinal and rotational tyre dynamics are coupled.

The mechanical properties of a pneumatic tyre are rather complex and non-linear: the stiffness and damping depend on the amplitude and frequency of excitation and on the tyre temperature. Therefore, it is very important that excitation of the tyre for the validation of the model and parameter estimation is realistic. Thus, the excitations of the tyre during the experiments have to be comparable to the excitations of the tyre operating on a vehicle. Most of the dynamic parameters will be obtained from measured frequency response functions of the tyre responses to brake torque variations presented in Chapter 9. The parameters related to the vertical tyre dynamics will be obtained from cleat excitations in Chapter 10.

The rigid ring model has been validated for a number of severe conditions. Chapter 9 presents the tyre responses to large brake torque variations like successive steps in brake torque, braking to stand-still and braking with wheel lock. In Chapter 10 the tyre model is validated for short wavelength road unevennesses. The effective road surface assessed in Chapter 4, is used as excitation of the model rather than the actual road surface. Chapter 10 shows that the effective inputs can also be used at higher velocities and during braking.

It is well known that axle height oscillations during cornering have an adverse effect on the generation of lateral forces [86,106,107]. Chapter 11 presents responses of a tyre subjected to a constant brake torque during axle

height oscillations. The tyre model is validated for large and small variations of the axle height. Very severe conditions were also considered including axle height oscillations where the vertical force decreases to such an extent that wheel lock occurs and the case in which the tyre loses contact with the road.

Finally, the most important conclusions of this study are presented in Chapter 12. The parameters of the tyre and how these values were determined will also be discussed. Recommendations for further development of the model are mentioned. In the Appendices detailed information on the experimental configurations is given.



# 2

## Static Tyre Properties

---

### 2.1 Introduction

This chapter presents basic tyre properties which are needed for the development of the dynamic tyre models in the subsequent chapters. Section 2.2 presents the dimensions of the contact patch which are important for the generation of shear forces in the tyre-road interface.

Sections 2.3 and 2.4 present the total vertical and longitudinal tyre stiffnesses. These stiffnesses are related to overall tyre deflection due to axle and rim displacements. In the subsequent chapters more elaborate tyre models are used in which the total tyre stiffness is represented by a number of stiffnesses in series. The tyre stiffnesses play an important role in the tyre dynamics. First, the tyre natural frequencies are related to the tyre stiffnesses, and second, the tyre transient responses are related to the tyre stiffnesses as the tyre needs some distance travelled to build up the horizontal deflections.

Section 2.5 presents the masses and moments of inertia of the tyre. Although, the moment of inertia is not a *static* tyre propriety as it is related to tyre dynamics it is nevertheless presented in this chapter. This is because of the fact that this property was obtained from static measurements of the tyre dimensions and mass density of the tyre.

## 2.2 Contact patch dimensions

If the tyre is loaded on the road the tyre is flattened near the tyre contact zone and a finite contact length arises. The size of the contact patch increases with increasing load. The dimensions of the contact patch are important for the generation of shear forces in the contact zone. See for instance the brush model which is introduced in Section 3.3.

The dimensions of the contact patch were measured by pressing the tyre on carbon paper. These measurements showed that the shape of the contact patch changes from an oval shape at very low values of vertical load to a more rectangular shape at higher values of vertical load. To represent the measured shape of the contact area, an ellipsoid shape is proposed:

$$\left(\frac{x}{a_c}\right)^c + \left(\frac{y}{b_c}\right)^c = 1 \quad (2.1)$$

in which  $a_c$  denotes half the contact length,  $b_c$  half the contact width,  $x$  and  $y$  the envelope of the contact area and  $c$  the power of the ellipsoid. The shape factor  $c$  provides a smooth transition between the oval and the rectangular shape as shown schematically in Figure 2.1.

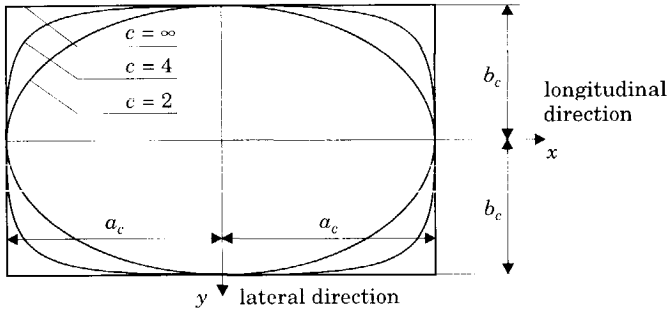


**Figure 2.1:** *The general shape of the contact area.*

The expression for the total area  $A_c$ , which cannot be calculated analytically for  $c \neq 2$ , reads:

$$A_c = \int_{x=-a_c}^{x=a_c} 2b_c \cdot \sqrt[c]{1 - (x/a_c)^c} dx \quad (2.2)$$

The effective contact area ( $a_e, b_e$ ) is defined as a rectangle with the same area and the same length/width proportion:

$$4a_e b_e = A_c, \quad \frac{a_e}{b_e} = \frac{a_c}{b_c} \quad (2.3)$$

The dimensions of the contact area have been measured both on a flat road surface as on the 2.5 meter diameter drum for four vertical loads and the results are presented in Tables 2.1a and 2.1b. The contact patch on the drum is relatively shorter and wider and more rectangular than the contact patch on the flat road.

**Table 2.1a:** *Dimensions of the contact area on a flat road.*

vertical load $F_z$ [N]	actual contact patch			eff. contact patch		total area $A_c$ [cm <sup>2</sup> ]	contact pressure $p_c$ [bar]
	length $a_c$ [mm]	width $b_c$ [mm]	power $c$ [-]	length $a_e$ [mm]	width $b_e$ [mm]		
2000	43.0	59.5	2.18	38.7	53.5	82.8	2.41
4000	67.0	72.1	2.19	60.3	65.0	156.7	2.55
6000	84.0	74.8	2.85	78.5	69.9	219.2	2.74
8000	100.5	76.9	3.48	95.7	73.2	280.3	2.85

**Table 2.1b:** *Dimensions of the contact area on a 2.5 meter diameter drum.*

vertical load $F_z$ [N]	actual contact patch			eff. contact patch		total area $A_c$ [cm <sup>2</sup> ]	contact pressure $p_c$ [bar]
	length $a_c$ [mm]	width $b_c$ [mm]	power $c$ [-]	length $a_e$ [mm]	width $b_e$ [mm]		
1157	30.8	54.7	2.22	27.8	49.3	54.8	2.11
2000	37.2	62.4	2.42	34.0	57.1	77.7	2.57
4000	57.2	74.6	2.62	53.0	69.0	146.1	2.74
6000	73.2	79.3	3.13	69.0	74.9	206.7	2.90

The  $x$  and  $y$  coordinates of the carbon contact prints were measured directly. The coefficients of the analytical shape (Eq. 2.1) were fitted using a least square error method. The total contact area and the effective contact length and width were calculated from the coefficients of the analytical shape. The contact pressure  $p_c$  is defined as the vertical load divided by the total area of the contact patch, including the gaps due to the tread pattern:

$$p_c = \frac{F_z}{A_c} \quad (2.4)$$

The width of the contact area will not be used as parameter in this thesis. The contact length measured for four vertical loads is represented by a polynomial as function of the square root of the vertical load  $F_z$ :

$$a = q_{a2}\sqrt{F_z^2} + q_{a1}\sqrt{F_z} \quad (2.5)$$

where  $q_{a1}$  and  $q_{a2}$  denote the coefficients of the polynomial.

Figure 2.2 shows the measured contact lengths (Table 2.1) and the fitted contact lengths (Eq. 2.5) for the tyre standing on the flat road and the tyre standing on the drum. In the subsequent chapters the effective contact length will be used. Therefore the *effective* contact length will be referred to as *the* contact length.

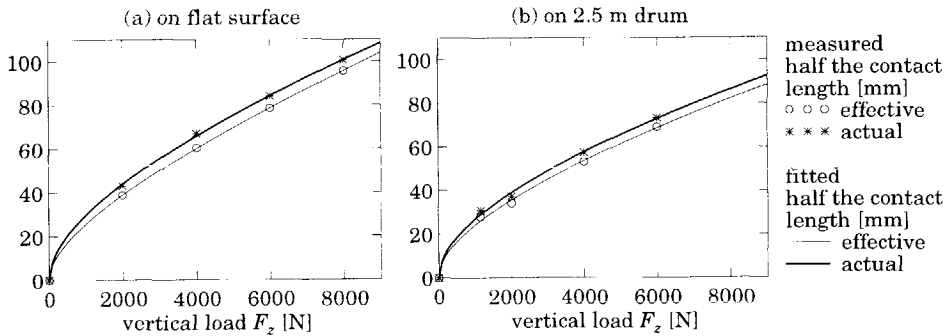


**Figure 2.2:** The measured and fitted half contact length as function of the vertical load.

## 2.3 Vertical tyre stiffnesses

The vertical tyre force vs. vertical deflection is an important tyre characteristic:

- The vertical tyre stiffness influences the natural frequencies of the vertical vibrations of the tyre.
- The tyre is excited by road unevennesses through the vertical tyre stiffness.
- The dynamic experiments, presented in Chapters 9 and 10, were performed at constant axle heights. The sensors used for these experiments cannot measure the static components of the forces accurately. Thus, to evaluate the results of

the dynamic experiments the vertical load at constant axle height has to be derived from separate alternative measurements.

Four methods were used to measure the vertical tyre stiffness:

- Static stiffness of a non-rotating tyre on both the 2.5 m drum and the flat road surface: by measuring the settling value of the vertical force after very slowly increasing the deflection.
- Dynamic stiffness of both a non-rotating and a rotating tyre obtained from small amplitudes of random axle height vibrations around four average vertical loads (2000, 4000, 6000, 8000 N) and at six velocities (0, 25, 39, 59, 92, 143 km/h).
- Dynamic stiffness of both a non-rotating and a rotating tyre obtained from large sinusoidal axle height motions ( $F_z = 500 - 9000$  N) at three low frequencies ( $\frac{1}{16}$ ,  $\frac{1}{4}$ , 1 Hz) and six velocities (0, 25, 39, 59, 92, 143 km/h).
- Force vs. deflection characteristics of a rotating tyre: the vertical force obtained from stationary rolling at four constant axle heights and five velocities (25, 39, 59, 92, 143 km/h).

The static experiments of a non-rotating tyre were performed on a flat surface and on the 2.5 meter drum. The vertical deflection was increased very slowly to several selected levels and the vertical force was measured at these deflections after the tyre had settled. To eliminate the effect of hysteresis forces, the tyre deflection was slowly decreased to the previous levels, and the force was measured again. The measured vertical force was fitted with a second order polynomial as function of the vertical deflection. Table 2.2 presents the vertical tyre stiffness  $C_z$ , which was obtained from differentiating the polynomials with respect to the vertical tyre deflection  $p_{z0}$  at different levels of the vertical load. Figure 2.3 presents the resulting load vs. deflection characteristic.

**Table 2.2:** *The static vertical tyre stiffnesses obtained from the static deformation of a non-rolling tyre.*

vertical load $F_z$ [N]	measured on flat road		measured on 2.5 m drum	
	deflection $p_{z0}$ [mm]	stiffness $C_z$ [N/m]	deflection $p_{z0}$ [mm]	stiffness $C_z$ [N/m]
0	0.00	163400	0.00	158000
2000	11.23	192700	11.90	178300
4000	20.96	218200	22.57	196500
6000	29.68	240900	32.33	213200
8000	37.64	261700	41.38	228700

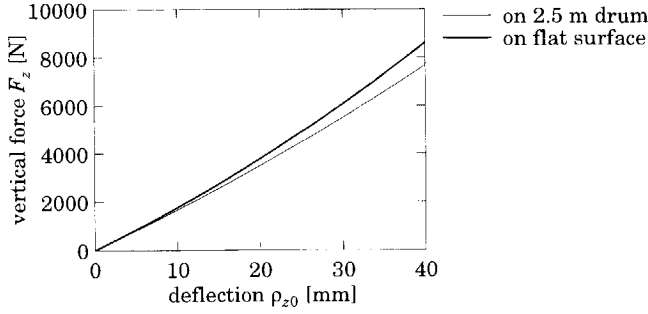


**Figure 2.3:** The measured static vertical force of a standing tyre as function of the static deflection.

The measured static stiffness on the drum at low values of vertical load is only 4% smaller than the measured stiffness on the flat road. This difference increases to 14% at 8000 N. The influence of the drum radius can be approximated by [83]:

$$\frac{C_{z,curved}}{C_{z,flat}} = \left( \frac{R}{R + r_0} \right)^{1/3} \quad (2.6)$$

where  $C_{z,curved}$  and  $C_{z,flat}$  denote the vertical tyre stiffness on the curved road and the flat road, respectively,  $R$  denotes the drum radius (1.25 m) and  $r_0$  denotes the tyre free radius (0.31 m). According to expression (2.6) the vertical stiffness on the drum should be 7% lower than the stiffness on the road.

The results of the dynamic stiffness experiments are presented in Tables 2.3a, b and c. The experiments were carried out using the *measurement tower* equipped with a strain gauged measuring hub. In this test stand the tyre rotates on a 2.5 m drum and the vertical axle motion is controlled by a hydraulic cylinder. For more details see Appendix A.2.

Table 2.3a presents the vertical tyre stiffness obtained from small random axle height oscillations with a standard deviation of 0.15 mm which is equivalent to 40 N vertical load variations. These experiments were carried out at four average vertical loads (2000, 4000, 6000, 8000 N) and at six velocities (0, 25, 39, 59, 92, 143 km/h). The vertical tyre stiffness was estimated from the measured Frequency Response Function (FRF) of vertical force measured in the hub with respect to the axle height variation in the frequency range 0-30 Hz. In this relatively low frequency range the FRF is mainly determined by the vertical tyre stiffness and the mass of the relevant moving part of the tyre test stand including the wheel with the tyre.

**Table 2.3a:** *The measured dynamic vertical tyre stiffnesses on the 2.5 m drum obtained from small random axle height oscillations.*

velocity V [km/h]	vertical tyre stiffness [N/m] at vertical load			
	$F_z = 2000 \text{ N}$	$F_z = 4000 \text{ N}$	$F_z = 6000 \text{ N}$	$F_z = 8000 \text{ N}$
0	289000	318000	324000	338000
25	205000	215000	229000	235000
39	207000	217000	230000	243000
59	197000	207000	221000	231000
92	199000	207000	221000	238000
143	204000	210000	225000	231000

Table 2.3a shows that the vertical stiffness of a non-rotating tyre is much higher than the stiffness of a rotating tyre. To emphasise this difference the row representing zero velocity is shaded. The measured vertical stiffness increases with the vertical load.

Table 2.3b presents the measured vertical tyre stiffness obtained from large sinusoidal variations in axle height. The sinusoidal variation in axle height corresponds to a variation of vertical load from 500 to 9000 N. The experiments were carried out at three low frequencies ( $\frac{1}{16}$ ,  $\frac{1}{4}$ , 1 Hz) and six velocities (0, 25, 39, 59, 92, 143 km/h). The stiffnesses at each velocity were obtained by differentiating the fitted load vs. deflection characteristics at the load indicated.

**Table 2.3b:** *The measured dynamic vertical tyre stiffnesses on the 2.5 m drum obtained from large sinusoidal axle height oscillations.*

velocity V [km/h]	vertical tyre stiffness [N/m] at vertical load			
	$F_z = 2000 \text{ N}$	$F_z = 4000 \text{ N}$	$F_z = 6000 \text{ N}$	$F_z = 8000 \text{ N}$
0	196000	211000	224000	237000
25	194000	202000	211000	219000
39	198000	207000	215000	223000
59	200000	208000	216000	224000
92	203000	212000	220000	228000
143	207000	216000	225000	233000

The difference between the vertical stiffness obtained from the random experiments (Table 2.3a) and sinusoidal experiments (Table 2.3b) for a non-rotating tyre is very large: up to 50%. The differences in stiffness for a rotating tyre is much smaller: 5-8% at low velocity, 2-3% at high velocity.

The dynamic experiments to validate the rigid ring model are presented in Chapters 9 and 10. These dynamic experiments were carried out at constant axle heights corresponding to 2000, 4000, 6000 N vertical load for a non-rotating tyre. The dynamic experiments were carried out on the *cleat and brake* test stand (see Appendix A.1). The piezo electric force transducers used in this test stand could only measure variations in the forces accurately and not the static components. Therefore, the stationary vertical force at constant axle height was measured separately with the *tyre measurement tower*. Table 2.3c presents the measured vertical force at stationary rolling conditions at four axle heights and six velocities. The four constant axle heights correspond to 0, 11.90, 22.57 and 32.33 mm vertical tyre deflections  $\rho_{z0}$  for a non-rotating tyre. These values correspond to 0, 2000, 4000 and 6000 N vertical load for a non-rotating tyre as shown in Table 2.2.

**Table 2.3c:** *The measured vertical force obtained from stationary rolling on 2.5 m drum.*

velocity V [km/h]	vertical force [N] at constant axle height			
	$\rho_{z0} = 0.00$ mm	$\rho_{z0} = 11.90$ mm	$\rho_{z0} = 22.57$ mm	$\rho_{z0} = 32.33$ mm
0	0	2000	4000	6000
25	20	2211	4235	6240
39	63	2246	4312	6374
59	58	2273	4361	6520
92	94	2342	4518	6753
143	329	2593	4871	7243

The dynamic stiffness measurements presented in Tables 2.3a, b and c show that the vertical tyre stiffness is not constant:

- The vertical load vs. deflection characteristic is progressive [26]. It may be represented by a second order polynomial. Then the vertical stiffness increases linearly with vertical load.
- The vertical stiffness increases approximately linearly with the velocity [22,26].
- The offset in the vertical load vs. deflection curve increases proportionally with the square of the velocity: the tyre radius grows due to the centrifugal force acting on it [26].



The following expressions are used to represent the vertical force as function of the deflection at given rotational wheel velocity  $\Omega$ :

$$F_z = (1 + q_{V2}|\Omega|)\{q_{Fz2}(\rho_{z0} + \Delta r)^2 + q_{Fz1}(\rho_{z0} + \Delta r)\} \quad (2.7a)$$

$$\Delta r = q_{V1}\Omega^2 \quad (2.7b)$$

where  $q_{Fz1}$  and  $q_{Fz2}$  denote the coefficients of the second order polynomial of the vertical force as function of the vertical deflection,  $q_{V1}$  controls the increase of the radius  $\Delta r$  and  $q_{V2}$  controls the increase of the tyre stiffness with the wheel velocity. The total vertical deflection of the tyre  $\rho_z$  equals the deflection  $\rho_{z0}$  at zero velocity plus the growth of the tyre radius  $\Delta r$  due to the rotational wheel velocity  $\Omega$ . The values of the parameters are presented in According to Dixon [22] the increase of the vertical tyre stiffness with speed is approximately 0.4% per m/s. Our measurements showed a lower value.

Figure 2.4 shows the resulting characteristics according to expression (2.7). Figure 2.4a shows the tyre load as function of the total tyre deflection  $\rho_z$ . Figure 2.4b shows the increase of the tyre radius with the velocity.

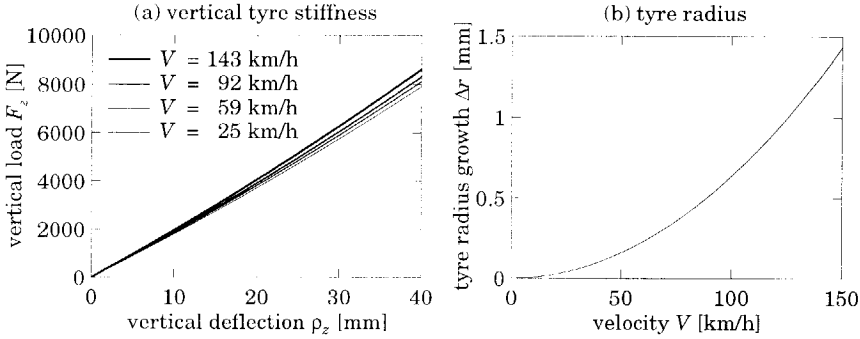


**Figure 2.4:** (a) The variation in vertical load with total deflection during rolling at various velocities, (b) the tyre growth with the velocity.

Table 2.4a presents the vertical tyre stiffnesses obtained from expression (2.7b), and Table 2.4b presents the vertical load as function of the velocity at constant axle heights. The values presented in Table 2.4b are used in Chapters 9 and 10 as vertical load at constant axle height. The parameters were obtained from the measured vertical force at stationary rolling (*cf.* Tables 2.3c). The fitted stiffnesses (Table 2.4a) of a rolling tyre correspond well to the stiffnesses obtained from the large axle height oscillations (Table 2.3b) and reasonably well to stiffnesses obtained from the small random axle height oscillations (Table 2.3a).

The fitted parameters were obtained from the experiments with a rolling tyre only. Consequently, there is a considerable difference between the fitted and measured stiffnesses and vertical loads for a non-rotating tyre.

**Table 2.4a:** *The fitted vertical tyre stiffness on the 2.5 m drum.*

velocity V [km/h]	vertical tyre stiffness [N/m] at constant vertical load			
	$F_z = 2000 \text{ N}$	$F_z = 4000 \text{ N}$	$F_z = 6000 \text{ N}$	$F_z = 8000 \text{ N}$
0	184000	196000	208000	219000
25	187000	200000	211000	222000
39	189000	202000	213000	224000
59	192000	205000	216000	227000
92	197000	209000	221000	232000
143	204000	216000	228000	239000

**Table 2.4b:** *The fitted vertical force on 2.5 m drum.*

velocity V [km/h]	vertical force [N] at constant axle height			
	$\rho_{z0} = 0.00 \text{ mm}$	$\rho_{z0} = 11.90 \text{ mm}$	$\rho_{z0} = 22.57 \text{ mm}$	$\rho_{z0} = 32.33 \text{ mm}$
0	0	2115	4153	6133
25	7	2166	4246	6268
39	17	2202	4307	6352
59	40	2264	4404	6483
92	100	2388	4588	6726
143	249	2642	4939	7169

## 2.4 Longitudinal tyre stiffnesses

The longitudinal tyre stiffness is an important parameter for the longitudinal dynamic behaviour of the tyre. It is well known that the lateral relaxation length can be obtained by dividing the cornering stiffness by the lateral tyre stiffness [63,115]. In this thesis we will see that a similar relationship holds for the longitudinal direction. The longitudinal stiffness may be used to obtain the longitudinal relaxation length.

In contrast to vertical tyre stiffness, the longitudinal tyre stiffness can only be measured directly for a non-rotating tyre. The longitudinal tyre stiffness can be obtained by either applying a longitudinal displacement of the rim, or by

applying a rotation of the rim while the tyre is loaded on the road. In total four different tangential stiffnesses may be identified:

- Longitudinal force due to longitudinal rim displacement:  $C_{F,x}$ .
- Longitudinal force due to rim rotation:  $C_{F,\theta}$ .
- Torque about the wheel axis due to longitudinal rim displacement:  $C_{M,x}$ .
- Torque about the wheel axis due to rim rotation:  $C_{M,\theta}$ .

The displacement or rotation of the rim was increased very slowly and the force and moment were measured after the tyre had settled. To eliminate the effect of tyre hysteresis the displacement and rotation were increased to a maximum value, decreased to a negative value and increased to zero. The stiffnesses were approximated by dividing the force and moment by the displacement or rotation of the rim. Only the small values of displacements and rotations were used, so linearity is assumed to hold. The measured stiffnesses are presented in Tables 2.5a and 2.5b. Figure 2.5 presents the stiffnesses as function of the vertical load.

**Table 2.5a:** *The measured tangential stiffnesses on a flat surface obtained from the static deformation of a non-rolling tyre.*

vertical load $F_z$ [N]	stiffness from displacement rim $C_{F,x}$ [N/m]	$C_{M,x}$ [Nm/m]	stiffness from rotation rim $C_{F,\theta}$ [N/rad]	$C_{M,\theta}$ [Nm/rad]
2000	195127 <sup>1</sup>	$\times^2$	69537	21216
4000	198200 <sup>1</sup>	$\times^2$	78090	21735
6000	206844 <sup>1</sup>	$\times^2$	78595	21862
8000	188788 <sup>1</sup>	$\times^2$	77955	21547

<sup>(1)</sup> was not measured accurately, <sup>(2)</sup> could not be measured.

**Table 2.5b:** *The measured tangential stiffnesses on the 2.5 m drum obtained from the static deformation of a non-rolling tyre.*

vertical load $F_z$ [N]	stiffness from displacement rim $C_{F,x}$ [N/m]	$C_{M,x}$ [Nm/m]	stiffness from rotation rim $C_{F,\theta}$ [N/rad]	$C_{M,\theta}$ [Nm/rad]
2000	231077	72297	72986	22405
4000	244567	74689	77062	23277
6000	237211	71343	79278	23818
8000	271796	80821	83017	24681

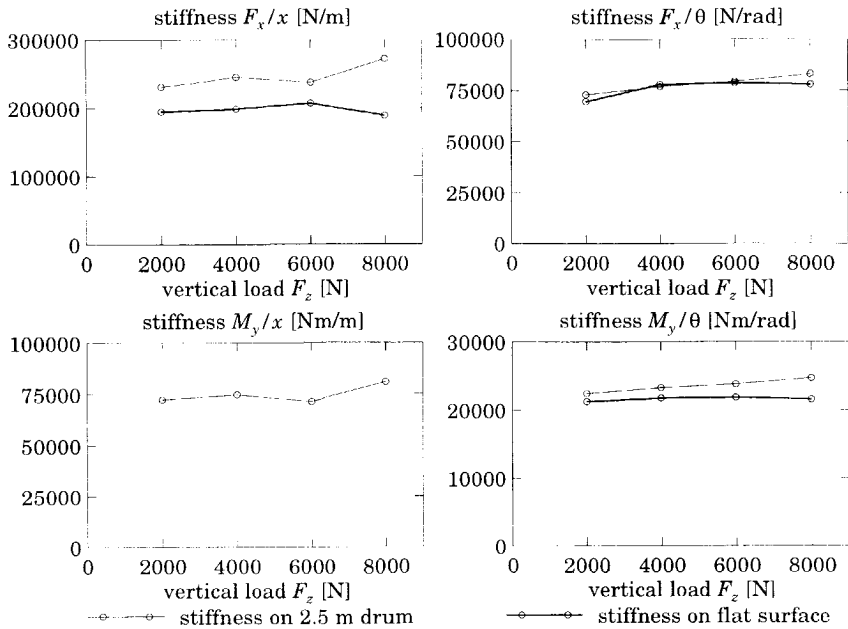


**Figure 2.5:** *The measured tangential stiffnesses obtained from the static deformation of a non-rolling tyre.*

The measured stiffness ( $C_{F,\theta}$ ) representing the force due to rim rotation, appeared to be approximately equal to the stiffness ( $C_{M,x}$ ) representing the torque due to rim displacement. Furthermore, the ratio between measured torques and measured forces appeared to be close to the tyre radius. Figure 2.6 presents a model for representing the tangential tyre stiffnesses: a longitudinal spring in the contact zone. Section 3.6 goes further into this matter.

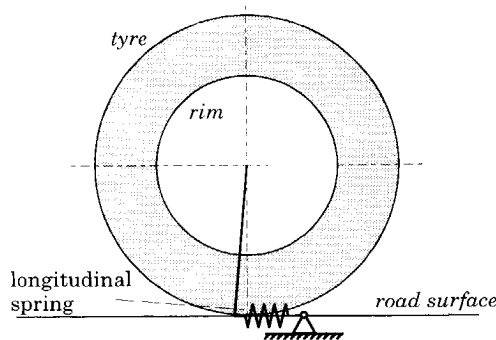


**Figure 2.6:** *Model to represent the tyre tangential stiffness.*

Chapter 9 presents the dynamic tyre responses to brake torque variations. The value of the longitudinal tyre stiffness estimated from the corresponding experiments lies between 350000 and 400000 N/m. This value is much larger than the values presented in Table 2.5. As in the case of the vertical tyre stiffnesses, the measured longitudinal stiffnesses of a non-rotating tyre cannot be used for a rolling tyre.

## 2.5 Inertia properties of the tyre

The dynamic properties of the tyre are largely determined by the inertia and stiffness properties of the tyre. The mass of both the tyre and rim were measured directly. The moments of inertia about the wheel axis ( $y$ -axis) were measured indirectly by measuring the natural frequency of the wheel rotating about the wheel axis, constrained by a known additional rotational spring. This method was used to assess the moment of inertia of the wheel (*i.e.* tyre plus rim) and of the rim. The moment of inertia of the tyre was obtained from the difference between these two values. The results of these measurements are presented in the first three rows of Table 2.6.

The objective of the research presented in this thesis is the development of the rigid ring tyre model. In this model, which will be introduced in Chapter 7, the tyre tread-band is represented by a rigid ring suspended on springs representing the tyre sidewalls and pressurised air. Consequently, the mass and moment of inertia of the tyre has to be subdivided into a part that moves together with the rigid ring and a part that moves together with the rim.

To enable this, the tyre is divided into five components: two beads, two sidewalls and one tread-band, see Figure 2.7. Obviously, the two beads move together with the rim, and the tread-band moves together with the rigid ring. The sidewall connects the tread-band with the beads. The mass of the sidewall is divided into two pieces: the inner half of the sidewall is assumed to move together with the rim while the outer half of the sidewall is assumed to move together with the rigid ring.

To estimate the masses and moments of inertia of the five tyre components, the tyre was cut into five pieces. The mass and dimensions of each piece were measured carefully. The moment of inertia about the wheel axis of each piece was calculated by assuming that each piece could be represented by a homogeneous cylinder. The measured mass and calculated moment of inertia of each component are given in the middle rows of Table 2.6. The difference between the

measured and calculated moment of inertia of the total tyre is 8%. The last rows present the mass and moment of inertia of the part of the tyre that moves together with the rim and the part that moves together with the rigid ring. These values will be used in the tyre models.

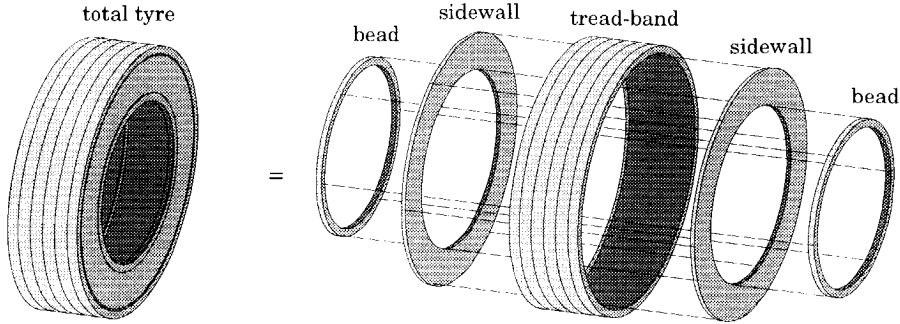


**Figure 2.7:** *Decomposition of the tyre into five components.*

**Table 2.6:** *The masses and moments of inertia about the y-axis of the tyre.*

component	measured moment of inertia	measured mass
tyre and rim	1.048 kgm <sup>2</sup>	17.7 kg
rim	0.367 kgm <sup>2</sup>	8.4 kg
tyre	0.681 kgm <sup>2</sup>	9.3 kg
component of tyre	calculated moment of inertia	measured mass
one tread-band	0.532 kgm <sup>2</sup>	5.7 kg
two sidewalls (outer half)	0.104 kgm <sup>2</sup>	1.4 kg
two sidewalls (inner half)	0.061 kgm <sup>2</sup>	1.2 kg
two beads	0.039 kgm <sup>2</sup>	1.0 kg
component of tyre	calculated moment of inertia	calculated mass
part that moves with rim	0.100 kgm <sup>2</sup>	2.2 kg
part that moves with belt	0.636 kgm <sup>2</sup>	7.1 kg

# 3

## Stationary Slip Characteristics

---

### 3.1 Introduction

The objective of the research presented in this thesis is the development of a mathematical model of the tyre that can be used in vehicle simulations. In this chapter the shear force generated by tyres under steady-state conditions is discussed as this is one of the most important aspects affecting the low frequency vehicle responses [2,41,45,92,99].

A driving or braking torque applied to a wheel will accelerate or decelerate the wheel. Longitudinal forces are developed in the tyre-road contact zone due to the difference in circumferential and forward velocity of the wheel. The difference between these velocities is defined as the *slip velocity* of the wheel. The *slip* of the wheel is defined as the ratio of the slip velocity and the forward speed of the wheel centre. The relationship which depicts the horizontal force generated as function of the slip in steady-state conditions is called the steady-state or stationary *slip characteristic* of the tyre.

Figure 3.1 presents a typical slip characteristic: the longitudinal force as function of the longitudinal slip. With the sign convention used, the slip and the force are negative for braking and positive for traction. The slip stiffness  $C_k$  is defined as the slope of the slip characteristics. At very small values of slip the

horizontal force generated is proportional to the slip and the ratio is defined as the slip stiffness at free rolling denoted by  $C_{\kappa 0}$ . At larger levels of slip the horizontal force smoothly transits from the linear range to saturation at the peak. The peak value of the longitudinal force is limited by the coefficient of friction  $\mu$  between tyre and road. Beyond the peak the friction force diminishes until the wheel locks. On dry road, the resulting force at wheel lock (sliding value) is approximately 70-80% of the peak value [119]. On wet and icy roads this ratio may become smaller.

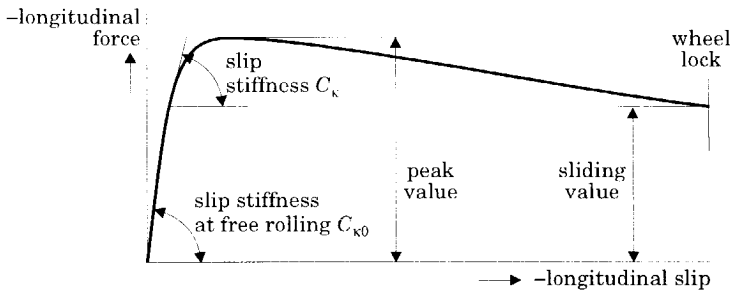


**Figure 3.1:** A typical stationary longitudinal slip characteristic.

There is a wide range of models that describe the steady-state shear force generation of tyres [84]. The approaches used for the model development can be theoretical (based on physics of the tyre construction) or empirical (based on experimentally obtained data). The physical models may contain a detailed representation of the tyre structure and the interaction between tyre and road. Detailed physical models are not suitable for studies of vehicle dynamics because accurate results can only be provided at excessive consumption of computer resources and calculation time [22,84,99].

In Section 3.3 the brush model is introduced. Although, this model is physically based, it is sufficiently simple that an analytical solution can be given. This solution has a qualitatively reasonable correspondence with experimentally found tyre characteristics. In Chapters 4 and 5 a discrete brush model will also be used for the analysis of the tyre transient response. In the discrete model the tread elements are handled as individual elements which may adhere to the road surface or slide. This type of model is appropriate for time simulations as these elements can be followed during a passage through the contact patch.

Section 3.4 presents the Magic Formula [87,88] which is an empirical tyre model. The Magic Formula represents the measured tyre data in a rather compact form by fitting the measured data with basic mathematical expressions.



The last two sections of this chapter present the rolling resistance of a rolling tyre and the effective and loaded radii of a rolling tyre.

### 3.2 Definition of slip variables

Figure 3.2 shows a side view of a tyre during braking. The slip point  $S$  is introduced. This imaginary point is attached to the wheel rim. In a free rolling condition, the point  $S$  is the centre of the rotation of the wheel body. The slip point  $S$  is normally located slightly below the road surface. The distance of point  $S$  to the wheel centre is defined as the effective rolling radius  $r_e$ . By definition, the speed of rolling  $V_r$  is equal to the product of the angular wheel velocity  $\Omega$  and the effective rolling radius:

$$V_r = r_e \Omega \quad (3.1)$$

The longitudinal slip velocity  $V_{sx}$  of point  $S$  is defined as the difference between the forward velocity of the wheel centre  $V_x$  and the rolling velocity of the wheel  $V_r$ :

$$V_{sx} = V_x - V_r = V_x - \Omega r_e \quad (3.2)$$

As the lateral dynamics of the tyre are not considered in this thesis, we do not have to discriminate between the longitudinal and the lateral directions. Therefore, the adverb longitudinal is superfluous and the longitudinal slip velocity will be called *the* slip velocity.

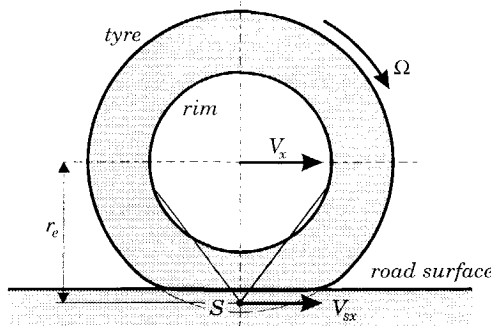


**Figure 3.2:** Kinematics of rolling.

During free rolling (no driving or braking torque), the longitudinal slip velocity equals zero. During braking, the rotational velocity is smaller than the forward velocity and point  $S$  moves forward with the slip velocity  $V_{sx}$ . The practical

longitudinal slip  $\kappa$  is obtained by dividing the slip velocity by the forward velocity of the wheel centre:

$$\kappa = -\frac{V_{sx}}{V_x} \quad (3.3)$$

A minus sign is added to make the slip stiffness a positive quantity. The theoretical slip  $\zeta_x$ , which is a more convenient definition for theoretical analysis, is defined by:

$$\zeta_x = -\frac{V_{sx}}{V_r} \quad (3.4)$$

The relation between the theoretical and practical slip quantities is:

$$\zeta_x = \frac{\kappa}{1 + \kappa}, \quad \kappa = \frac{\zeta_x}{1 - \zeta_x} \quad (3.5)$$

For small values of slip, linear tyre characteristics may suffice and the difference between the two slip definitions vanishes:

$$\zeta_x \approx \kappa \quad (3.6)$$

At low levels of longitudinal slip also the force vs. slip relationship may be represented by a linear function containing a coefficient  $C_\kappa$ , known as the slip stiffness:

$$F_x = C_\kappa \cdot \kappa \quad (3.7)$$

For the chosen sign convention the slip velocity is positive during braking and the force and the slip are negative. At large levels of slip, the relationship (3.7) no longer holds as the increase longitudinal force is not proportional to the increasing slip, and the maximum level of the force is limited by the friction between tyre and road. The subsequent two sections will introduce two models representing the non-linear relationship between force and slip: the brush model and the Magic Formula model.

### 3.3 The brush model

The brush model belongs to the group of physical tyre models. This category of models is based on a description, possibly detailed, of the tyre structure and of the interaction of the tread with the ground. Usually, these models can only be solved by using computers. The brush model, however, is a simple physical model which has an analytical solution.

The brush model, depicted in Figure 3.3, is an idealised representation of the tyre in the region of contact. The model consists of a row of elastic cylinders radially attached to a circular belt. The belt is assumed to be deformed only through the action of the vertical wheel load in the direction normal to the road. The contact length is finite and in the case of a frictionless contact surface (undeformed cylinders) the cylinders are assumed to be oriented normal to both the road and the flat portion of the belt. In the presence of friction the cylinders will deform longitudinally when the wheel deviates from the free rolling state. The deformation of the cylinders (tread elements) in the adhesion range is easily established by considering the displacements of both ends of the cylinder. That is the base point where the element is attached to the belt and the tip which contacts the road surface. The base points move (relative to the wheel axis) starting at the front edge of the contact patch and leaving the contact zone at the rear edge of the contact patch.

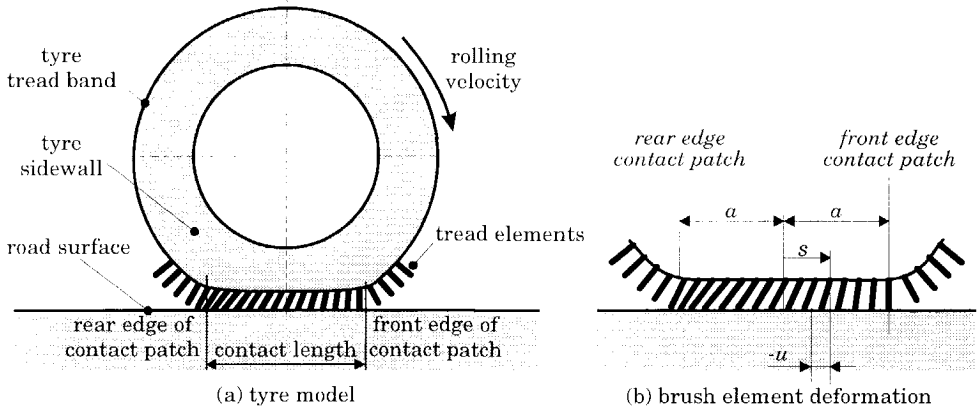


**Figure 3.3:** *Tread elements attached to the tyre tread-band.*

In the adhesion region the longitudinal deformation  $u$  at the position  $s$  in the contact patch is directly related to the longitudinal slip:

$$u = (a - s) \cdot \frac{\kappa}{1 + \kappa} = (a - s) \zeta_x = -(a - s) \frac{V_{sx}}{V_r} \quad (3.8)$$

where  $a$  denotes half the contact length. In the case of vanishing sliding, which will occur for infinitely small slip, expression (3.8) holds for the entire region of contact and the practical and theoretical slips are equal to each other. After the introduction of the stiffnesses  $c_{cp}$  of the tread elements per unit of length the following expression for the longitudinal force  $F_x$  is obtained:

$$F_x = c_{cp} \int_{-a}^a u(x) dx = 2c_{cp} a^2 \zeta_x \approx 2c_{cp} a^2 \kappa \quad (3.9)$$

The slip stiffness  $C_{\kappa 0}$  at free rolling reads:

$$C_{\kappa 0} = 2c_{cp} a^2 \quad (3.10)$$

To investigate the tyre at high values of slip, sliding of the tread elements is introduced. Sliding will occur as soon as the deformation exceeds the frictional force. To determine the frictional force the vertical pressure distribution must be known. For the sake of simplification, a parabolic pressure distribution is assumed. This yields the following expression for the vertical force per unit of length  $q_z$ :

$$q_z = \frac{3F_z}{4a} \left\{ 1 - \left( \frac{s}{a} \right)^2 \right\} = \frac{3}{4} F_z \left\{ \frac{a^2 - s^2}{a^3} \right\} \quad (3.11)$$

By assuming dry friction and introducing the coefficient of friction  $\mu$ , the maximum longitudinal force per unit of length reads:

$$|q_{x,max}| = \mu q_z \quad (3.12)$$

For the sake of abbreviation the tyre parameter  $\theta$  is introduced:

$$\theta = \frac{2}{3} \frac{c_{cp} a^2}{\mu F_z} \quad (3.13)$$

The distance from the leading edge to the point where the transition from adhesion to sliding region occurs equals  $2a\lambda$  and is determined by the non-dimensional quantity  $\lambda$ :

$$\lambda = 1 - \theta \cdot \left| \frac{\kappa}{1 + \kappa} \right| = 1 - \theta \cdot |\zeta_x| \quad (3.14)$$

From these equations the slip  $\zeta_{x,sl}$  can be calculated at which total sliding starts ( $\lambda = 0$ ):

$$\zeta_{x,sl} = \pm \frac{1}{\theta} \quad (3.15)$$

Now the force function can easily be derived:

$$\begin{aligned} F_x &= \mu F_z \left\{ 3|\theta \zeta_x| - 3|\theta \zeta_x|^2 + |\theta \zeta_x|^3 \right\} \text{sgn}(\zeta_x) & \text{if } |\zeta_x| \leq \zeta_{x,sl} \\ F_x &= \mu F_z \cdot \text{sgn}(\zeta_x) & \text{if } |\zeta_x| > \zeta_{x,sl} \end{aligned} \quad (3.16)$$

Figure 3.4 illustrates the influences of the parameters  $F_z$ ,  $\mu$  and  $c_{cp}$  on the shape of the characteristics. Half the contact length  $a$  is not considered to be an independent parameter (cf. Eq. 2.5). The vertical load influences the peak level of the friction force. It also influences the slip stiffness through the contact length  $a$ . The vertical load has a small influence on the value of slip at which sliding starts (cf. Eq. 3.13 and 3.15) since the ratio  $F_z/a^2$  changes only slightly with the vertical load.

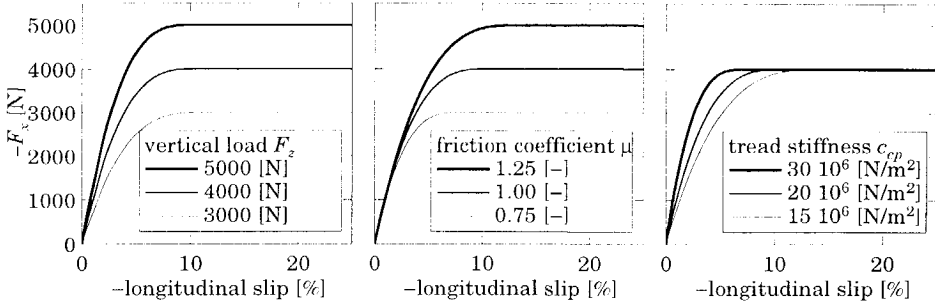


**Figure 3.4:** The influence of the parameters on the shape of the brush model characteristic. Nominal values  $F_z=4000$  N,  $c_{cx}=20 \cdot 10^6$  N/m<sup>2</sup>,  $\mu=1$ .

In the case of a non-rotating tyre, the tyre acts like a spring instead of a damper, as the force generated by the tyre is proportional to the displacement instead of the velocity. For this situation, the deformation of the tread elements is uniform. The total stiffness in the  $x$  direction of all the tread elements present in the contact patch is indicated with  $c_{cx}$ :

$$F_x = c_{cx}x, \quad c_{cx} = 2ac_{cp} \quad (3.17)$$

The slip characteristics of the brush model (Eq. 3.16) are used for the development of the pragmatic transient tyre model (Chapter 6), for the development of the rigid ring model (Chapter 7) and for the validation of the rigid ring model (Chapters 9, 10 and 11). The main advantage of the use of brush model characteristics is that a few parameters are needed (tread elements stiffness, contact length and friction coefficient). The disadvantage is that the brush model characteristics do not give very accurate representations of measured slip characteristics. The simple brush model, in particular, does not have a decreasing characteristic at high levels of slip.

The discrete version of the brush model is used as a possible tyre-road interface slip model of the flexible ring tyre model (Chapters 4 and 8) and is used to study the tyre transient responses (Chapter 5).

### 3.4 The Magic Formula model

The Magic Formula forms the heart of an empirical tyre model. Such models are based on the mathematical representation of measured tyre data, rather than modelling the tyre structure itself. Empirical tyre models are usually used in full vehicle simulations. The tyre forms only a part of the entire simulation model and the computational load of that part in the model should be fairly low.

The development of the Magic Formula started in the mid-eighties and since then several versions have been developed [6,7,85]. In these models the combined slip situation was modelled from a physical view point. Bayle *et al.* changed the combined slip calculation technique into a simpler empirical method [10] which is now adopted in the most recent version of the Magic Formula tyre model [87,88]. All versions show the same basic form for the pure slip characteristics: a sine of an arctangent. The Magic Formula for longitudinal slip reads:

$$F_x = D \sin \left[ C \arctan \left\{ B(\kappa + S_H) + E \left( \arctan(B(\kappa + S_H)) - B(\kappa + S_H) \right) \right\} \right] + S_V \quad (3.18)$$

where  $F_x$  stands for the longitudinal force and  $\kappa$  denotes the longitudinal slip. The coefficients  $B$ ,  $C$ ,  $D$  and  $E$  together with the offsets  $S_H$  and  $S_V$  characterise the shape of the slip characteristics. Each coefficient represents a specific aspect of the slip characteristic: the shape factor  $C$  influences the overall shape of the characteristic, the peak factor  $D$  influences the maximum value of the characteristic, the curvature factor  $E$  influences the characteristic around the peak value, and the slip stiffness  $K (=BCD)$  influences the slip stiffness at low values of slip. Figure 3.5 illustrates the influences of the coefficients on the shape of the characteristic.

The coefficients of the Magic Formula depend on the vertical load. Dimensionless parameters  $p$  are introduced to describe this influence:

- shape factor  $C = p_{C1} \cdot \lambda_C$  (3.19a)

- peak factor  $D = \mu \cdot F_z$  (3.19b)

- friction coefficient  $\mu = (p_{D1} + p_{D2} df_z) \cdot \lambda_\mu$  (3.19c)

- curvature factor  $E = (p_{E1} + p_{E2} df_z + p_{E3} df_z^2) \cdot \{1 - p_{E4} \operatorname{sgn}(\kappa + S_H)\} \cdot \lambda_E$  (3.19d)

- slip stiffness  $K = F_z \cdot (p_{K1} + p_{K2} df_z) \cdot \exp(-p_{K3} df_z) \cdot \lambda_K$  (3.19e)

- stiffness factor  $B = \frac{K}{C \cdot D}$  (3.19f)

- horizontal shift  $S_H = (p_{H1} + p_{H2} df_z) \cdot \lambda_H$  (3.19g)

- vertical shift  $S_V = F_z \cdot (p_{V1} + p_{V2} df_z) \cdot \lambda_V \cdot \lambda_\mu$  (3.19h)

The relative offset  $df_z$  of the vertical load is introduced in Equations (3.19):

$$df_z = (F_z - F_{z0}) / F_{z0} \quad (3.20)$$

Furthermore, this equation introduces six scaling factors  $\lambda_C$ ,  $\lambda_\mu$ ,  $\lambda_E$ ,  $\lambda_K$ ,  $\lambda_H$ ,  $\lambda_V$  to scale the formula without changing the parameter values. In this way the influence of several important factors can be investigated easily.

In the most recent version of Magic Formula [87,88] all coefficients and parameters have subscripts to discriminate between the characteristics of longitudinal force, lateral force or self aligning torque. In this thesis only the longitudinal tyre behaviour is considered and the subscripts to discriminate between the characteristics have been omitted.

The main advantage and disadvantage of the Magic Formula are opposite to the advantage and disadvantage of the brush model: The Magic Formula gives an accurate representation of measured data but needs more parameters.

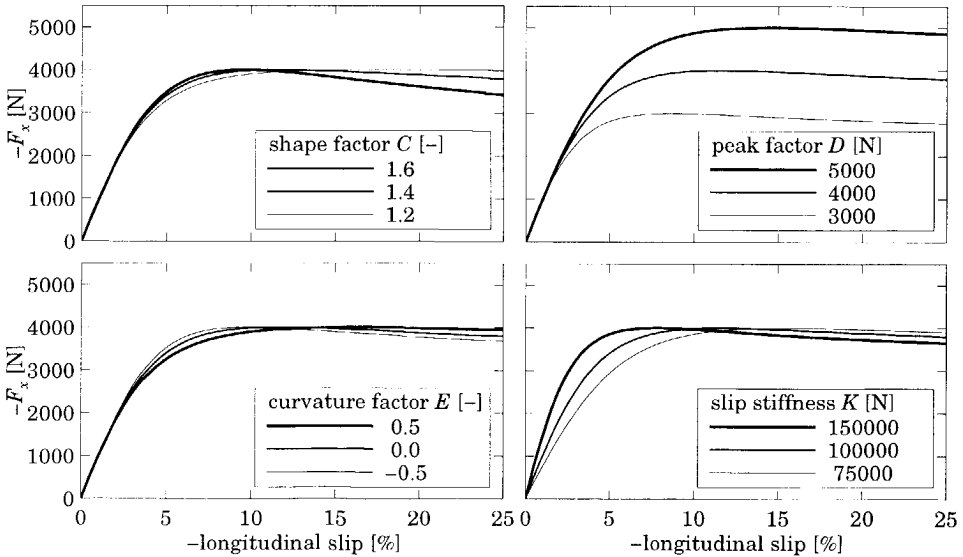


**Figure 3.5:** The influence of the coefficients on the shape of the Magic Formula characteristic. Nominal values:  $C = 1.4$ ,  $D = 4000$ ,  $E = 0$ ,  $K = 100000$ ,  $S_H = 0$ ,  $S_V = 0$ .

### 3.5 Measured slip characteristics

Figures 3.6 and 3.7 present a comparison of the measured stationary slip characteristics with both the brush model and the Magic Formula. The measurements were performed on the rotating drum test stand (*cf.* Appendix A) at three constant axle heights at a drum velocity of 92 km/h.

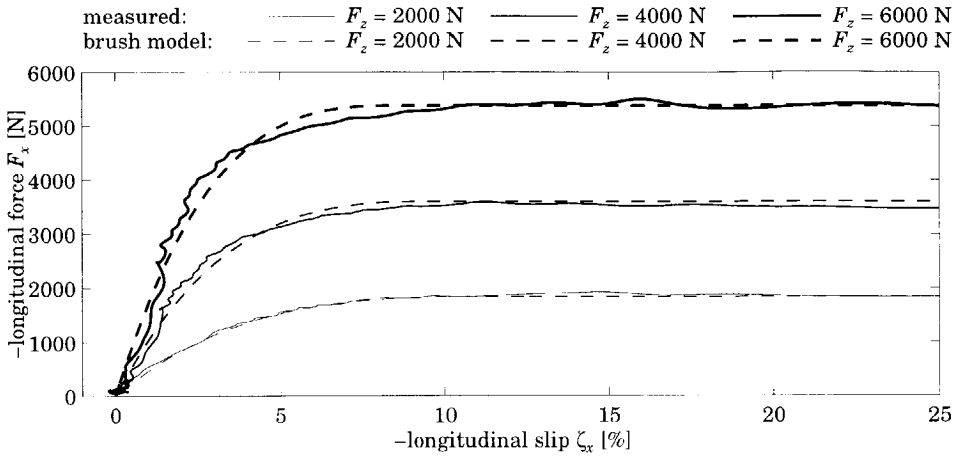


**Figure 3.6:** The measured slip characteristics on the 2.5 m drum and the brush model representation ( $V=92$  km/h).

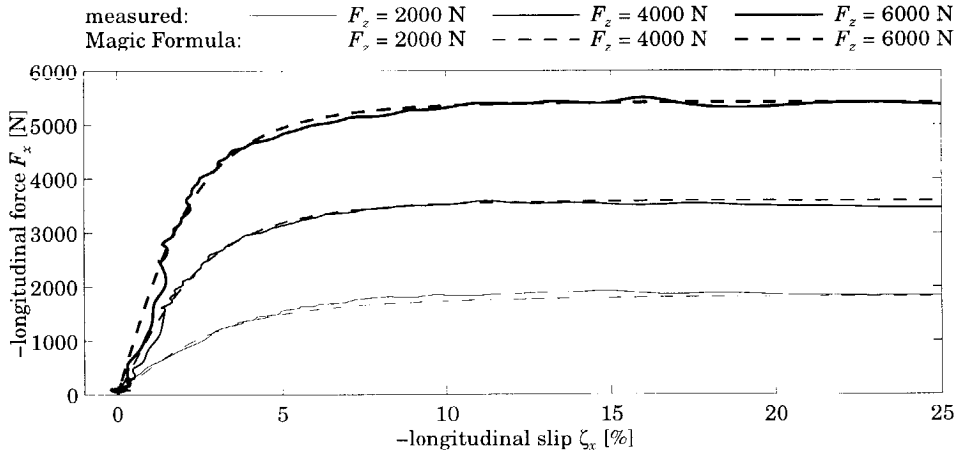


**Figure 3.7:** The measured slip characteristics on the 2.5 m drum and the Magic Formula representation ( $V=92$  km/h).



The measurements do not show a clear peak in the characteristics, as the longitudinal force generated at wheel lock is only slightly smaller than the maximum value of longitudinal force. The relatively flat slip characteristic makes it possible that the brush model can be used in the entire slip region. Nevertheless, the quality of the fit of the Magic Formula is better than that of the brush model.

The slip characteristics have also been measured on the road with the Tyre Test Trailer of the Vehicle Research Laboratory of the Delft University of Technology. The measurements were performed at a velocity of 60 km/h on two different road surfaces: an asphalt road and a concrete road. The slip stiffnesses and friction coefficients obtained by fitting the measured data with the brush model are presented in Table 3.1, and the values obtained from fitting the Magic Formula are presented in Table 3.2.

**Table 3.1:** *Slip stiffnesses  $C_k$  and peak friction coefficients  $\mu$  obtained from fitting the measured slip characteristics with the brush model.*

Vertical load	On steel drum $V = 92 \text{ km/h}$		On asphalt road $V = 60 \text{ km/h}$		On concrete road $V = 60 \text{ km/h}$	
$F_z \text{ [N]}$	$C_{k0} \text{ [N]}$	$\mu \text{ [-]}$	$C_{k0} \text{ [N]}$	$\mu \text{ [-]}$	$C_{k0} \text{ [N]}$	$\mu \text{ [-]}$
2000	53000	1.013	43000	1.209	35000	1.158
4000	119000	0.972	98000	1.184	79000	1.167
6000	196000	0.931	171000	1.165	135000	1.160

**Table 3.2:** *Slip stiffnesses  $C_k$  and peak friction coefficients  $\mu$  obtained from fitting the measured slip characteristics with the Magic Formula.*

Vertical load	On steel drum $V = 92 \text{ km/h}$		On asphalt road $V = 60 \text{ km/h}$		On concrete road $V = 60 \text{ km/h}$	
$F_z \text{ [N]}$	$C_{k0} \text{ [N]}$	$\mu \text{ [-]}$	$C_{k0} \text{ [N]}$	$\mu \text{ [-]}$	$C_{k0} \text{ [N]}$	$\mu \text{ [-]}$
2000	54000	1.006	38000	1.228	34000	1.146
4000	124000	0.973	86000	1.210	76000	1.149
6000	208000	0.939	145000	1.191	128000	1.152

The difference between the slip stiffness on the three road surfaces (steel drum, asphalt road and concrete road) is rather big: the slip stiffness on the drum is much bigger than the slip stiffness on the road. The tyre-road friction on the road is slightly bigger than the friction on the steel drum. The shape of the characteristics measured on the road differs from those derived from the drum

measurements: the peak in the road measurements is much more pronounced as the friction coefficient at wheel lock is only 70% of the friction coefficient at the peak. Accordingly, the shape factor  $C$  of the Magic Formula increases from 1.1 for the drum measurements to 1.65 for the road measurements. The fast decaying characteristic after the peak means that the brush model cannot represent the road measurements accurately.

### 3.6 Rolling resistance

The rolling resistance of tyres results in dissipation of energy in the tyre due to the continuous deformations near the contact zone [19]. At low and medium velocities, the rolling resistance is approximately constant and is a direct result of the damping in the tyre, especially the damping of the tread compound. Tread compounds with little damping will decrease the rolling resistance. But the rolling resistance is directly related to the brake performance on wet roads: a 10% decrease of rolling resistance results in a 10% increase of the brake distance on wet roads [93].

Experiments show that the rolling resistance force  $F_r$  is proportional to the vertical force  $F_z$  [19,71]:

$$F_r = f_r F_z \quad (3.21)$$

The rolling resistance coefficient  $f_r$  is introduced. This coefficient can be expressed as a polynomial in the forward velocity  $V$  [71]:

$$f_r = q_{fr0} + q_{fr1}V + q_{fr4}V^4 \quad (3.22)$$

where the coefficients  $q_{fr0}$  and  $q_{fr1}$  control the slight increase in the rolling resistance force with the velocity, and the coefficient  $q_{fr4}$  controls the fast increase of the rolling resistance at high velocities that is caused by the phenomenon known as standing waves. For a given tyre in a particular operating condition, a threshold speed exists (approximately 150-200 km/h) above which the standing waves in the tyre can be observed. Standing waves are formed because the tyre tread does not recover immediately from distortion originating from tyre deflection after it leaves the contact patch, and the residual deformation initiates a wave. The formation of the standing wave greatly increases energy loss, resulting in a high rolling resistance and considerable heat generation that could lead to tyre failure. This places an upper limit on the safe operating speed of tyres.

### 3.7 Tyre radii

#### Tyre radii of a non-rotating tyre

Besides the loaded tyre radius  $r_l$ , which can be obtained from the vertical tyre deflection, and the effective rolling radius  $r_e$ , introduced in Section 3.2, a third tyre radius plays an important role in the tyre dynamics: the brake lever arm  $r_b$ . The brake lever arm is defined as the ratio of the applied constant brake torque  $M_y$  and the longitudinal force  $F_x$ . Consequently, the point of application of  $F_x$  lies a distance  $r_b$  below the wheel centre. This section will show that this radius can be approximated by the effective rolling radius. When the wheel load approaches zero, all these radii will reduce to the free unloaded radius  $r_0$ .

Figure 3.8 presents three methods for representing the forces acting in the contact zone on the tyre. The figure shows the forces during braking and the additional subscript  $c$  is used to designate the forces in the contact zone. Figure 3.8a depicts the pressure distributions in the contact patch from which the reaction forces at the rim can be calculated directly: the longitudinal pressure distribution  $q_{cx}$ , acts on the loaded radius  $r_l$ , and the non-symmetrical vertical pressure distribution  $q_{cz}$  will give an additional torque about the wheel axis. This approach, however, can only be used if the pressure distributions are known, thus with a detailed physical tyre model.

If the pressure distributions are not known, the torque at the rim has to be calculated from the positions of the resulting forces in the contact zone. In many studies the positions of the line of action of these forces are chosen such that the vertical force acts in the centre of the contact zone below the wheel centre and the longitudinal force acts in the ground plane at the loaded radius. In these studies the influence of the non-symmetrical pressure distribution is neglected. To complete the description, the total rolling resistance moment  $-M_{cy}$  acting about the transverse axis through the contact centre, should be added (*cf. e.g. [44]*). Its magnitude changes with  $F_x$ .

Figures 3.8b and c show two alternative solutions. In Figure 3.8b the non-symmetrical vertical pressure distribution is represented by a longitudinal shift  $\epsilon_x$  of the vertical force. Then the torque  $M_y$  at the rim becomes:

$$M_y = -r_l F_{cx} - \epsilon_x F_{cz} \quad (3.23)$$

The additional torque may also be represented by a vertical shift  $\epsilon_z$  of the longitudinal force (Figure 3.8c), then:

$$M_y = -r_l F_{cx} - \varepsilon_z F_{cx} = -(r_l + \varepsilon_z) F_{cx} \quad (3.24)$$

From the equation above the brake lever arm  $r_b$  is defined as:

$$r_b = r_l + \varepsilon_z \quad (3.25)$$

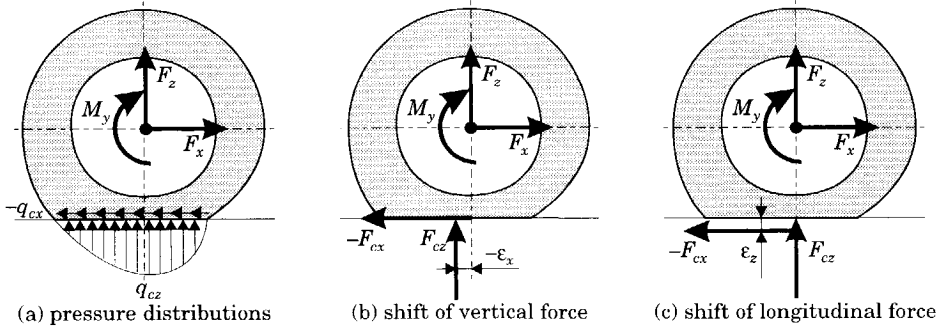


**Figure 3.8:** Three models for representing the forces between tyre and road.

Another way to calculate the force at the rim is to use the power balance of the tyre. The torque at the rim  $M_y$  propels the wheel which rotates at a velocity  $\Omega$ . The slip velocity of the wheel in the contact zone is  $V_{sx}$ . Thus, the point of application of the longitudinal force  $F_{cx}$  which acts in the contact zone moves forward with the same speed  $V_{sx}$ . At free rolling, this speed (according to its definition) becomes zero. However, at free rolling power is still dissipated through rolling resistance:  $F_{cz} f_r \Omega$ . From the power balance considerations (depicted in Figure 3.9) the following relationship appears to hold ( $M_y$  is drive torque at the rim and  $F_x$  is traction force):

$$M_y = -r_e F_{cx} - F_{cz} f_r \quad (3.26)$$

The force  $F_{cx}$  acts effectively at an arm  $r_e$  on the wheel rim (*i.e.* in point  $S$  of Figure 3.2). The remaining rolling resistance moment  $F_{cz} f_r$  acts about this point  $S$  on the wheel rim body in a negative direction.

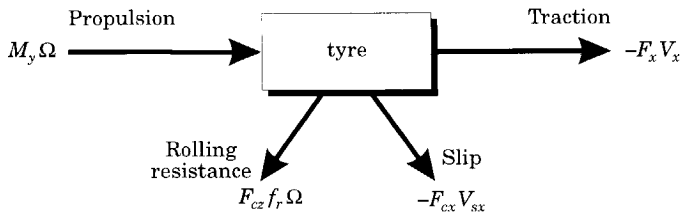


**Figure 3.9:** The power balance of the tyre.

Summing up, according to the power balance considerations: if the effective rolling radius is used to transform rotational velocity of the wheel  $\Omega$  to a slip velocity in the contact patch (cf. Eq. 3.2) then the same radius has to be used to transform the force in the contact patch to a torque acting on the rim (cf. Eq. 3.26).

The idea is substantiated with measurements. Figure 3.10 shows the effective rolling radius  $r_e$ , the loaded tyre radius  $r_l$ , and the brake lever arm  $r_b$  as functions of the vertical load for a non-rotating tyre. The effective rolling radius and the load radius are represented by the polynomials. This figure shows that the brake lever arm can be approximated by the effective rolling radius.

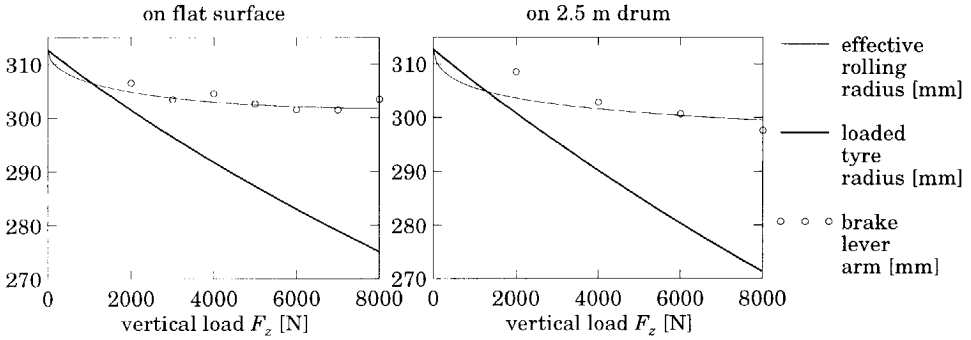


**Figure 3.10:** The tyre radii as function of the vertical load at zero velocity.

The loaded tyre radius was obtained from the experiments set up to assess the vertical stiffness of a non-rotating tyre, see Section 2.3. The brake lever arm was obtained from the experiments also meant to measure the tangential stiffnesses of a non-rotating tyre, see Section 2.4. The effective rolling radius was obtained from tests in which the tyre is rolled at a very low velocity. The result is found by dividing the total distance travelled by the total angle of rotation covered. The measured effective rolling radius was fitted with a third order polynomial in the square root of the vertical force in the contact zone:

$$r_e = q_{re3}\sqrt{F_{cz}^3} + q_{re2}\sqrt{F_{cz}^2} + q_{re1}\sqrt{F_{cz}} + q_{re0} + \Delta r \quad (3.27)$$

where  $\Delta r$  represents the velocity influence on the effective rolling radius, which is zero for a non-rotating tyre. The velocity influence of the effective rolling radius is assumed to be equal to the velocity influence of the loaded tyre radius (cf. Eq. 2.7b).

### Tyre radii of a rotating tyre

The effective rolling radius is defined as the ratio of the forward velocity of the wheel and the rotational velocity of the wheel (*cf.* Eq. 3.1). The influence of the vertical load on the effective rolling radius is rather small as indicated in Figure 3.10: approximately 1% in the vertical load range 2000-8000 N. To measure these variations accurately, it is necessary to use very accurate and linear sensors. Unfortunately, the available sensors were not sufficiently accurate, so another method was used. The variations in forces at free rolling are related to tyre non-uniformities. In other words, the frequencies of these force variations are multiples of the rotational velocities of the tyre. Hence, we can estimate the rotational velocity of the wheel from these force variations. Furthermore, if the measurement time is long enough, the frequencies related to the tyre non-uniformities can be estimated accurately.

Figure 3.11a shows the measured effective rolling radius and the fitted radius according to Equation (3.27) at constant axle height, as a function of the velocity. The fitted radius is a rather good representation of the directly measured radius. The velocity has two influences on the effective rolling radius: First, the free tyre radius  $r_0$  increases owing to the centrifugal force (*cf.* expression 2.7b). It is assumed that the increase of the effective rolling radius is equal to the increase of the tyre free radius. Second, the vertical load increases owing to the increasing vertical tyre stiffness (*cf.* expression 2.7a).

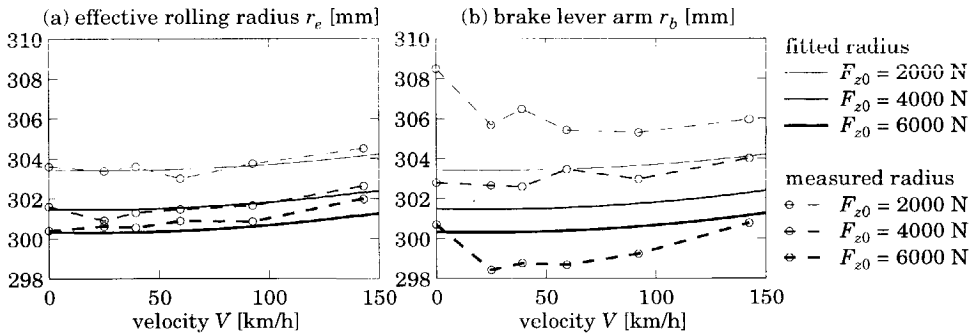


**Figure 3.11:** The tyre radii as function of the velocity at three constant axle heights on the 2.5 m drum. Note:  $F_{z0}$  holds at zero velocity.

The brake lever arm of a rolling tyre was obtained from dynamic brake experiments: the frequency response functions of the longitudinal reaction force

on the wheel with respect to the applied brake torque which are presented in Section 9.2. The brake lever arm is equal to the estimated amplitude at frequency zero. In Figure 3.11b the estimated brake lever arm is compared with the fitted effective rolling radius. This figure shows that the brake lever arm can be approximated by the effective rolling radius. It should be noted that the results presented in Figure 3.11b were obtained at small levels and variations of brake torque: the average brake torque was 120 Nm, and the standard deviation was 22 Nm.

Figure 3.12 presents the brake lever arm as function of average brake force  $F_x$ . These results were also obtained from the frequency response functions presented in Section 9.2. Figure 3.12 shows that the variations in the estimated brake lever arm are relatively big. But it should be noted that the experimental conditions were severe: small variations in brake torque around an average value. The average value could be nearly as large as the torque needed for wheel lock. Even for these conditions the brake lever arm may be approximated by the effective rolling radius. It should be noted that at low values of vertical load and large levels of brake torque the brake lever arm approaches the tyre free radius (312 mm).

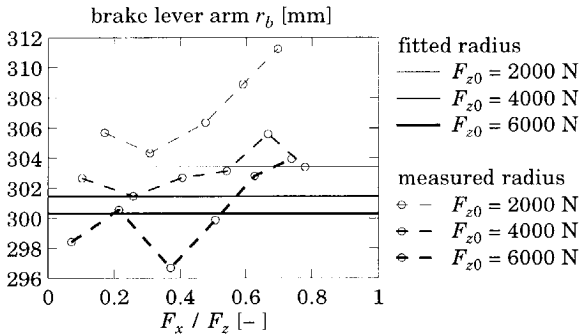


**Figure 3.12:** The brake lever arm as function of the average brake force at three constant axle heights and a velocity of 25 km/h on the 2.5 m drum.

In conclusion, the above considerations show that the point of application of the longitudinal force may be approximated by the effective rolling radius. In this way, together with the remaining rolling resistance moment  $F_{cz}f_r$ , the earlier mentioned total rolling resistance  $-M_{cy}$  can be very well accommodated. The measurements show that the brake lever arm is approximately equal to the effective rolling radius, and that the differences between the brake lever arm and

the loaded tyre radius are much larger (*cf.* Figure 3.10). Therefore, in this research point  $S$  located at a distance equal to the effective rolling radius below the wheel centre will be used as point of application of the longitudinal force.



# 4

## The Rolling Tyre as a Geometric Filter over Short Wavelength Road Unevennesses

---

### 4.1 Introduction

The excitation of the tyre by short wavelength road unevennesses (*e.g.* cleats) is very complex. The tyre, which acts as a geometric filter due to its finite dimensions, smoothens the sharp edges of the unevennesses. If we would like to simulate the tyre dynamics on uneven roads we should take into account this effect. In other words, before we develop and validate the *rigid ring* tyre model in Chapters 7 through 11 we will study the excitation of the tyre by short wavelength road unevennesses in this Chapter.

Figure 4.1 presents the phenomena of the tyre rolling over short wavelength road unevennesses. The length of short wavelength irregularities is small in comparison to the length of the contact patch. Discrete irregularities such as steps also fit into this definition. If the tyre rolls over a discrete obstacle, the tyre will always hit the obstacle before the centre of the axle is above the obstacle as indicated in Figure 4.1a. This makes the influence of the discrete obstacle longer than the length of the obstacle. Furthermore, the tyre partially or wholly envelopes (or swallows) small irregularities [49], see Figure 4.1b. Both effects result in a filtering of the irregularities: the response at the axle is much smoother than the shape of the actual road surface, see Figure 4.1c.

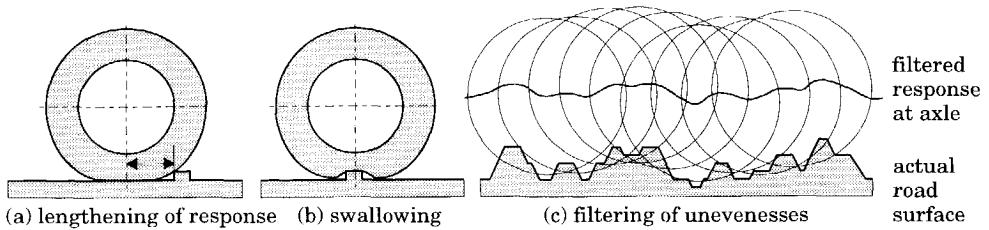


**Figure 4.1:** *The phenomena of the tyre rolling on discrete road unevennesses.*

There are several models which can simulate the enveloping properties of tyres on uneven roads. Figure 4.2 presents an overview of tyre models for rolling over obstacles. This overview is partially based on the overview given by Badalamenti and Doyle [5]. Both Captain [16] and Kisilowski [52] used several models to study the enveloping properties of these models.

- **Single-point contact model.** The most extensively used model is the single-point contact model [5]. This model is generally represented by a spring and damper in parallel. This approximation is valid for long wavelengths (longer than 3 meter) and gradual slope (smaller than 5%) surface irregularities [49]. This model can be used on surfaces with random unevennesses generated by filtered white noise. Rolling over discrete obstacles (*e.g.* cleats) gives too high accelerations of the tyre with a point contact model.
- **Roller contact model.** The roller contact model consists of a rigid wheel rolling over the obstacles and one spring and damper. There is only one contact point, neglecting the special cases of road geometry where the rigid wheel has more than one contact point with the road. The contact point is not restricted to lie directly beneath the wheel axle. Small wavelength bumps are filtered out by this model and its representation is much better than the single-point contact model [5,36]. Misun used the roller contact model to study the stresses in driving systems in a vehicle operating on an uneven road surface [69,70].
- **Fixed footprint model.** This model uses an linearly distributed stiffness and damping in the contact area. In this model the road irregularities in the footprint area are averaged, giving a smoother and more realistic excitation of the tyre than the point contact model.
- **Radial spring model.** The radial spring model is an improvement on the rigid wheel model. The tyre is not modelled as a rolling rigid body, but as a radially deformable body. The radial spring model uses circumferentially distributed independent linear spring elements. A model with linear stiffnesses has a limited range through which it is able to predict forces. A model with non-linear degressive radial springs is able to show the typical dip in vertical

force while rolling over cleats. Badalamenti *et al.* [5] enhanced the radial spring model. They made the force generated in the radial springs depend on the deformation of adjacent springs as well.

- **Flexible ring model.** The flexible ring model involves the tread-band, which is modelled as a deformable beam, and radially and tangentially distributed sidewall stiffnesses. Owing to the bending of the tread-band the vertical stiffness in the centre of the contact patch is lower than the stiffness at the edges of the contact patch. Even without the non-linear sidewall stiffnesses this model is able to show the typical dip in the vertical force while rolling over cleats. The toroidal membrane tyre model [49] is also classified as a flexible ring model. Captain [16] and Kisilowski [52] named the flexible ring model the *adaptive footprint model* as the deflection of the flexible carcass provides the model with an adaptive footprint.
- **Finite elements models (FEM).** These models are based on detailed description of the tyre structure. The FEM models are very powerful and they can be used directly to calculate the dynamic forces of the tyre rolling over obstacles at high velocities [24,25,46,75,78]. Apart from the study presented by Mousseau [74], elaborate investigations of the quasi-static tyre enveloping properties of FEM models are often omitted.

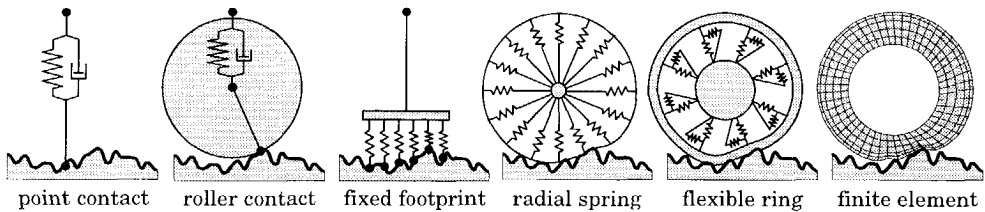


**Figure 4.2:** Tyre models used for rolling over obstacles. Tyre-road interface models.

The research on tyre excitation caused by road irregularities was started in the 60s by Hey [38], Gough [34], and Lippmann *et al.* [61,62]. At that time Hey stated that little was known about the forces generated between tyre and road during the rolling over obstacles [38]. In his PhD Thesis he used a smooth obstacle shape of 55 cm length and 1 or 2 cm height to ensure uninterrupted contact between tyre and road. He simulated the tyre response by using a rigid wheel model.

Gough [34] investigated the tyre rolling over short wavelength obstacles experimentally. He indicated that a tyre rolling over obstacles shows three responses: (1) variations in the vertical force, (2) variations in the longitudinal

force and (3) variations in the rotational velocity. The variations in the rotational velocity generate additional longitudinal forces which develop quite considerable magnitude at high speeds [34].

Lippmann *et al.* [61,62] studied the responses of truck and passenger car tyres to sharp obstacles like cleats and steps. They showed experimentally that an almost linear relationship exists between tyre force variation and obstacle height. Therefore, the superposition principle which is based on (a series of) step responses could be used to calculate the responses of any obstacle. More than 20 years later Bandel and Monguzzi disputed the linearity of the tyre rolling over different obstacles [8]. On the other hand, they showed that the response due to a single obstacle could be decomposed into two separate identical responses. These separate identical responses will be referred as *basic functions* in this Chapter.

Table 4.1 presents a chronological survey of the literature on the enveloping properties of tyres. A survey of the dynamic tyre responses on short wavelength obstacles will be presented in Table 10.1. The following items of interest are considered in Table 4.1:

- **Tyre type.** Most researchers used passenger car or truck tyres. In the 60s the research was focused on the differences between radial ply and bias ply tyres [34]. Kilner studied the dynamic responses of an aircraft tyre for simulations to predict aircraft dynamics in response to runway roughness [49].
- **Velocity.** The velocity is an important factor. At low velocity the tyre response involves only its enveloping and elastic properties. At high velocity the response is a result of a combination of these properties and tyre dynamics.
- **Direction response.** Usually only the responses of the longitudinal and vertical reaction forces on the axle are measured. Only Gough measured the variations in rotational velocity [34]. He stated that these variations are very important at high velocity.
- **Basic curves.** The measurements of the enveloping properties of tyres is time consuming. The concept of basic functions is used to estimate the enveloping properties for situations which have not been measured: a different shape of the obstacle, or a different velocity. Lippmann *et al.* calculated the enveloping response of an arbitrary road geometry by superposing the responses of a series of positive and negative step changes [61,62]. Bandel *et al.* [8] used the measured response at low velocity as a basic function for the excitation of the tyre at high velocity. Oldenettel *et al.* measured the vertical response at low velocity (2 km/h) and determined the response function between the high and the low velocity excitation [79].

- **Enveloping models.** Several models were used to simulate the enveloping properties of tyres. These models are depicted in Figure 4.2.
- **Measurement.** The tyre responses were measured with obstacles either attached to a test drum or to a flat road surface.

**Table 4.1:** Literature survey on the enveloping properties of tyres.

reference	tyre type			velocity		direction response			basic curves		enveloping model					experiments		
	car	truck	aircraft	low	high	longitudinal	vertical	rotational	shape	velocity	single-point	roller contact	footprint	radial spring	flexible ring	FEM	on drum	on road
Hey [38]	●			●	●	●	●					●						●
Gough [34]		●		●		●	●	●									●	
Lippmann [61]		●		●		●	●		●								●	
Lippmann [62]	●			●		●	●		●								●	
Davis [20]	●			●		●	●							●				
Captain [16]		●			●	●	●				●	●	●		●			●
Pacejka [83]	●			●		●	●							●			●	
Kilner [49]			●	●		●	●								●			●
Kisilowski [52]	●			●	●		●				●	●	●	●	●			
Lozia [64]	●				●	●	●								●			
Bandel [8]	●			●	●	●	●			●							●	
Ushijima [111]	●			●	●		●			●							●	
Badalamenti [5]	●					●	●							●				
Misun [69,70]		●		●	●	●	●					●						●
Guo [36]	●			●	●		●			●		●						
Mousseau [74]		●		●		●	●									●	●	
Turpin [110]	●			●		●	●			●								●
Oldenettel [79]	●			●	●	●	●			●							●	

The main goal of the research presented in this thesis is the development of the *rigid ring* tyre model described in Chapter 7. This is a compact model to ensure relatively fast vehicle simulations. The tyre-road interface of the *rigid ring* model is governed by a single-point only. This means that this model does not directly show the enveloping properties of the tyre on short wavelength irregularities as presented in Figure 4.1. In other words, the short wavelength irregularities cannot serve directly as inputs for simulations with the *rigid ring* tyre model. So, for this model the quasi-static responses of the real tyre on the actual road surface should be used as inputs. These quasi-static responses are transferred into an effective road surface: the effective plane height, the effective road plane angle and the effective rolling radius variation. This approach results in quasi-static responses of the model on the effective road surface that are identical to quasi-static responses of the real tyre on the real road surface.

This chapter presents the transformation of the actual road surface into the effective road surface. The transformation is called the geometric filtering effect of the rolling tyre. First the quasi-static responses of the tyre are investigated using the flexible ring model. Section 4.2 presents the equations of motion of this model, and Section 4.3 presents the simulation model. To balance the internal and external forces acting on the flexible ring the deformation of the tyre sidewalls is solved iteratively.

The static properties of the *flexible ring* model (deformations and stiffnesses) are validated in Section 4.4. The enveloping properties are validated in the subsequent section. In this section the simulated responses are compared to the measured low velocity responses. During the measurements, the horizontal and vertical axle motions were constrained to preclude unwanted suspension resonances. The *flexible ring* model is validated for three obstacle shapes: a trapezoid cleat, a positive step, and a negative step.

Section 4.6 derives the effective road surface from the quasi-static simulations or measurements. Finally, Section 4.7 discusses the general properties of a geometric filter. With this filter any road surface can be transformed into an effective road surface.

The dynamic tyre responses of the *rigid ring* model using the effective road surface as input are presented in Chapter 10.

## 4.2 The flexible ring model

This section presents the equations of motion of the *flexible ring* tyre model. This *flexible ring* model is used to calculate the quasi-static excitation of the tyre by short wavelength obstacles. The model and equations are based on the research presented in the PhD Thesis of S. Gong [32]. Although the flexible ring model is most suitable for investigations into high frequency dynamics it may also be used statically to calculate the tyre deflections.

This flexible ring model consists of a deformable circular beam representing the tread-band, and radially and tangentially distributed stiffnesses representing the tyre sidewalls and pressurised air. The equations of motion of the rotating ring on an elastic foundation were derived from Hamilton's principle [32]. For that, the expressions of the energy components (strain, kinetic and elastic energy) and the expressions of the virtual work of the external forces were used. The governing equations were found by integrating over the entire circumference of the ring.

The flexible ring model is also used in Chapter 8 for the modal analysis of tyre in-plane vibrations.

### Equations of motion of the free tyre

For the quasi-static analysis of the enveloping properties of tyres only the static equations of the flexible ring model are necessary. To obtain a model describing only the static deformations of the tyre belt and sidewalls, all derivatives in the equations have to be set to zero.

The flexible ring model, shown in Figure 4.3, involves a circular ring representing the tyre tread-band; a rigid body representing the rim; circumferentially distributed radial and tangential springs representing the tyre sidewall and pressurised air in the tyre. The rim has three degrees of freedom in the plane of the wheel: the vertical and horizontal displacements and the rotation about the axis perpendicular to the wheel plane. Two coordinate systems will be used: a fixed Cartesian coordinate system  $(x, z)$  and a rotating coordinate system  $(x^*, z^*)$ .

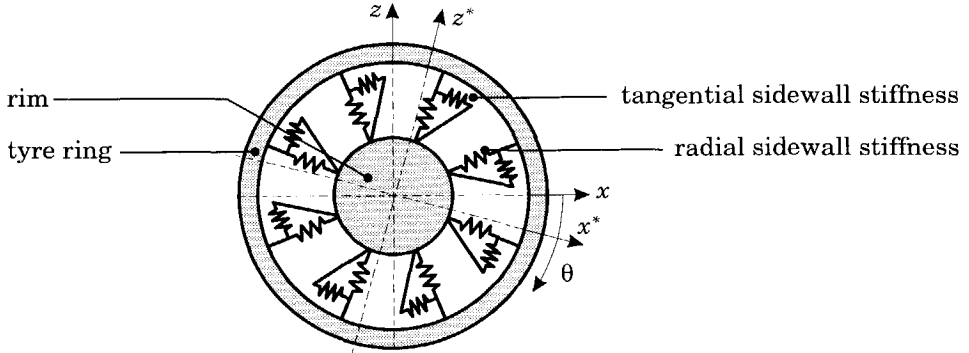


**Figure 4.3:** *The flexible ring tyre model.*

The equations of motion of the flexible ring tyre model are based on the PhD Thesis of S. Gong [32]. However, the coordinate systems used in the present thesis are slightly different: the definitions of the orientation of the rotational velocity  $\Omega$ , the tangential displacement  $v_b$  and the rotation about the  $y$ -axis are opposite to those given in [32]. Figure 4.4 shows the coordinate system used here.

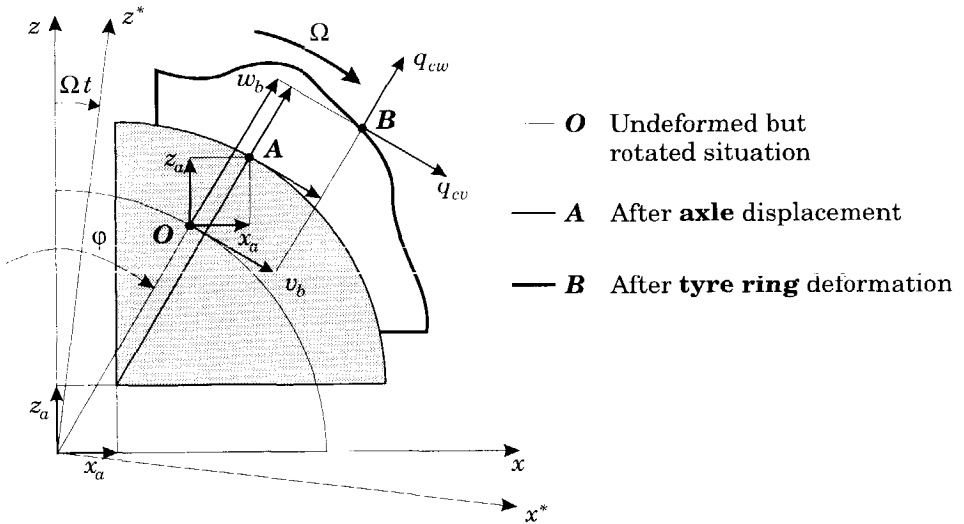


**Figure 4.4:** *The tyre ring and the deformation and the coordinate system used.*

The equation of motion of the flexible tyre ring model, according to the coordinate system introduced in Figure 4.4 read [32]:



$$\frac{EI}{r^4} \left( \frac{\partial^3 w_b}{\partial \theta^3} - \frac{\partial^2 v_b}{\partial \theta^2} \right) - \frac{EA}{r^2} \left( \frac{\partial w_b}{\partial \theta} + \frac{\partial^2 v_b}{\partial \theta^2} \right) + \frac{F_s}{r^2} \left( v_b - \frac{\partial w_b}{\partial \theta} \right) + \frac{p_0 b_R}{r} \left( \frac{\partial w_b}{\partial \theta} - v_b \right) + c_{bw} (v_b + x_a \sin \theta + z_a \cos \theta - r \theta_a) + \rho A (\dot{v}_b + 2\Omega \dot{w}_b - \Omega^2 v_b) = q_{cv} \quad (4.1a)$$

$$\frac{EI}{r^4} \left( \frac{\partial^4 w_b}{\partial \theta^4} - \frac{\partial^3 v_b}{\partial \theta^3} \right) + \frac{EA}{r^2} \left( w_b + \frac{\partial v_b}{\partial \theta} \right) + \frac{F_s}{r^2} \left( \frac{\partial v_b}{\partial \theta} - \frac{\partial^2 w_b}{\partial \theta^2} \right) - \frac{p_0 b_R}{r} \left( \frac{\partial v_b}{\partial \theta} + w_b \right) + c_{bw} (w_b - x_a \cos \theta + z_a \sin \theta) + \rho A (\ddot{w}_b - 2\Omega \dot{v}_b - \Omega^2 w_b) = q_{cw} \quad (4.1b)$$

$$m_a \ddot{x}_a + \pi r (c_{bv} + c_{bw}) x_a - r \int_0^{2\pi} (c_{bw} w_b \cos \theta - c_{bv} v_b \sin \theta) d\theta = F_{ax} \quad (4.1c)$$

$$m_a \ddot{z}_a + \pi r (c_{bv} + c_{bw}) z_a + r \int_0^{2\pi} (c_{bw} w_b \sin \theta + c_{bv} v_b \cos \theta) d\theta = F_{az} \quad (4.1d)$$

$$I_{ay} \ddot{\theta}_a + 2\pi c_{bw} r^3 \theta_a - r^2 \int_0^{2\pi} c_{bv} v_b d\theta = M_{ay} \quad (4.1e)$$

where  $q_{cv}$  and  $q_{cw}$  are the external distributed forces acting on the ring in the tangential and radial directions;  $F_{ax}$  and  $F_{az}$  are the external forces acting on the rim;  $M_{ay}$  is the external torque acting on the rim;  $v_b$  and  $w_b$  are the tangential and radial displacements of the ring element;  $x_a$  and  $z_a$  are the horizontal and vertical rim displacements and  $\theta_a$  is the small deviation of the angular displacement of the rim on top of the displacement due to steady speed of rotation  $\Omega$ . The parameters of the flexible ring model are:

- bending stiffness of the ring:  $EI$
- pre-tension of the ring:  $F_s$
- tangential sidewall stiffness:  $c_{bv}$
- radial sidewall stiffness:  $c_{bw}$
- radius of the ring:  $r$
- width of the ring:  $b_R$
- tyre inflation pressure:  $p_0$
- mass of the rim:  $m_a$
- moment of inertia of the rim:  $I_{ay}$

The pre-tension force  $F_s$  depends on the inflation pressure and the centrifugal force acting on the ring:

$$F_s = p_0 b_R r + \rho A r^2 \Omega^2 \quad (4.2)$$

The equations of the tyre ring model can be simplified with the introduction of the *in-extensibility assumption*, which means that the circumferential length of the middle surface of the ring is constant during the deformation [32]. This

assumption is usually valid for rings with high extensional stiffness, which is the case for radial tyres. If it is assumed that the tyre tread-band is in-extensible in the circumferential direction, the following relation between the radial and tangential displacements applies:

$$w_b = -\frac{\partial v_b}{\partial \theta} \quad (4.3)$$

The flexible ring model will be used to simulate the quasi-static response of the tyre rolling over road unevennesses, so, the rotational velocity in Equations (4.1) and (4.2) is set to zero as are the derivatives of all variables. The resulting equations that describe the static deformation of the flexible ring model read:

$$-\frac{EI}{r^4} \left( \frac{\partial^2 v_b}{\partial \theta^2} + 2 \frac{\partial^4 v_b}{\partial \theta^4} + \frac{\partial^6 v_b}{\partial \theta^6} \right) + \frac{p_0 b_R}{r} \left( \frac{\partial^2 v_b}{\partial \theta^2} + \frac{\partial^4 v_b}{\partial \theta^4} \right) + \quad (4.4a)$$

$$c_{bv}(v_b - r\theta_a) - c_{bw} \frac{\partial^2 v_b}{\partial \theta^2} + (c_{bv} + c_{bw})(x_a \sin \theta + z_a \cos \theta) = q_{cv} + \frac{\partial q_{cw}}{\partial \theta}$$

$$\pi r(c_{bv} + c_{bw})x_a + r \int_0^{2\pi} \left( c_{bw} \frac{\partial v_b}{\partial \theta} \cos \theta + c_{bv} v_b \sin \theta \right) d\theta = F_{ax} \quad (4.4b)$$

$$\pi r(c_{bv} + c_{bw})z_a + r \int_0^{2\pi} \left( -c_{bw} \frac{\partial v_b}{\partial \theta} \sin \theta + c_{bv} v_b \cos \theta \right) d\theta = F_{az} \quad (4.4c)$$

$$2\pi c_{bv} r^3 \theta_a - r^2 \int_0^{2\pi} c_{bv} v_b d\theta = M_{ay} \quad (4.4d)$$

The *Modal Expansion Method* is used to simplify the analysis [32]. The basic idea behind the modal expansion method is that the response of a linear system to any external excitation force can be expressed as a weighted summation of the natural mode shapes of the system. The mode shapes of a system are usually time independent while the weight factors are space independent. According to the modal expansion method, the tangential and radial displacements of the ring can be expressed as follows:

$$v_b(\theta, t) = \sum_{n=0}^{+\infty} a_n(t) \cos n\theta + b_n(t) \sin n\theta \quad (4.5a)$$

$$w_b(\theta, t) = -\frac{\partial v_b}{\partial \theta} = \sum_{n=0}^{+\infty} n a_n(t) \sin n\theta - n b_n(t) \cos n\theta \quad (4.5b)$$

where  $a_n(t)$ , and  $b_n(t)$  are the generalised modal displacements. Substituting Equations (4.5) into (4.4); multiplying the resulting equations by  $\cos(n\theta)$  and

$\sin(n\theta)$ ; and integrating these equations over  $2\pi$  yields the equations for the generalised modal displacements:

$$a_n(t) = \frac{\xi_{cn}(t)}{C_{bn}} \quad (n = 0, 1, 2, 3, \dots) \quad (4.6a)$$

$$b_n(t) = \frac{\eta_{cn}(t)}{C_{bn}} \quad (n = 0, 1, 2, 3, \dots) \quad (4.6b)$$

where  $n$  denotes the mode number. The generalised modal forces  $\xi_{cn}(t)$  and  $\eta_{cn}(t)$  read:

$$\xi_{c0} = \frac{1}{2\pi} \int_0^{2\pi} \left( q_{cv} + \frac{dq_{cw}}{d\theta} \right) d\theta, \quad \xi_{cn} = \frac{1}{\pi} \int_0^{2\pi} \left( q_{cv} + \frac{dq_{cw}}{d\theta} \right) \cos n\theta d\theta \quad (n = 1, 2, 3, \dots) \quad (4.7a)$$

$$\eta_{c0} = 0, \quad \eta_{cn} = \frac{1}{\pi} \int_0^{2\pi} \left( q_{cv} + \frac{dq_{cw}}{d\theta} \right) \sin n\theta d\theta \quad (n = 1, 2, 3, \dots) \quad (4.7b)$$

the modal stiffnesses  $C_n$  are:

$$C_{bn} = \left( \frac{EI}{r^4} (n^2 - 1) + \frac{p_0 b_R}{r} \right) n^2 (n^2 - 1) + c_{bv} + n^2 c_{bw} \quad (4.8)$$

and the reaction forces at the axle and reaction torque at the rim read:

$$F_{ax} = \pi r (c_{bv} + c_{bw}) x_a + \pi r (c_{bv} + c_{bw}) b_1 \quad (4.9a)$$

$$F_{az} = \pi r (c_{bv} + c_{bw}) z_a + \pi r (c_{bv} + c_{bw}) a_1 \quad (4.9b)$$

$$M_{ay} = 2\pi r^3 c_{bv} \theta_a - 2\pi r^2 c_{bv} a_0 \quad (4.9c)$$

## Tyre-road interface

If the tyre is loaded on the road surface, deformations of the tyre occur and a finite contact length arises. In the contact patch the deformations of the tyre ring are prescribed by the (first assumedly) flat road surface. The relations between the tyre sidewall deformation (radial and tangential displacements of the tread-band) and the contact forces (radial and tangential pressures) are governed by the equations of motion. If the contact forces are known, the tyre tread-band displacements can be obtained by solving the equations of motion.

In reality, the contact forces are not known because they depend on the tread-band displacements. In a typical tyre-road contact problem, the tyre deflections are the ones that need to be determined. Therefore, an additional set of relations between the tyre tread-band displacements and the contact forces is needed to solve the tyre-road contact problem. To serve this purpose, a small modification

to the physical model of the tyre is made to take into account the flexibility of the tyre tread rubber, *i.e.* an extra component is added to the model: radial and tangential springs distributed along the outer surface of the ring circumference. [32, 120]. The height of these new tread elements in the model is assumed to be zero. The modified ring model is shown in Figure 4.5.

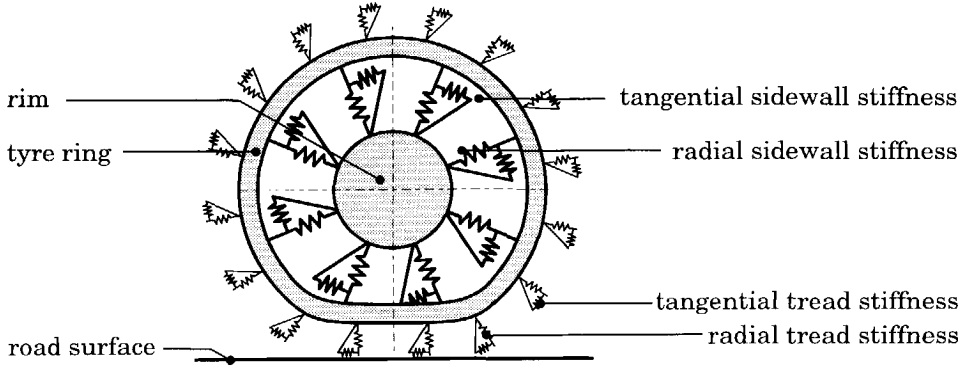


**Figure 4.5:** *The modified flexible tyre ring model.*

Tangential and radial contact pressure distributions  $q_{cw}$  and  $q_{cv}$  arise only if the radial tread element deformation is positive:

$$q_{cv} = c_{cv}(v_r - v_b), \quad q_{cw} = c_{cw}(w_r - w_b) \quad \text{if } (w_r - w_b) > 0 \quad (4.10a)$$

$$q_{cv} = 0, \quad q_{cw} = 0 \quad \text{if } (w_r - w_b) \leq 0 \quad (4.10b)$$

where  $c_{cv}$  and  $c_{cw}$  denote the tangential and radial distributed tread element stiffness per unit length, and  $v_r$  and  $w_r$  denote the position of the point contacting the road surface.

### Non-linear tyre sidewall spring characteristics

It is well known, that the forces in the tyre sidewalls depend non-linearly on the tyre deflection. This effect should be taken into account for accurate predictions of the enveloping properties of radial tyres [1]. Figure 4.5 shows the tyre cross section. The tyre sidewall is assumed to behave as an in-extensible membrane. Furthermore, the internal air pressure  $p_0$  is assumed to be constant during the tyre deflection. This is an acceptable assumption for automobile tyres [83].

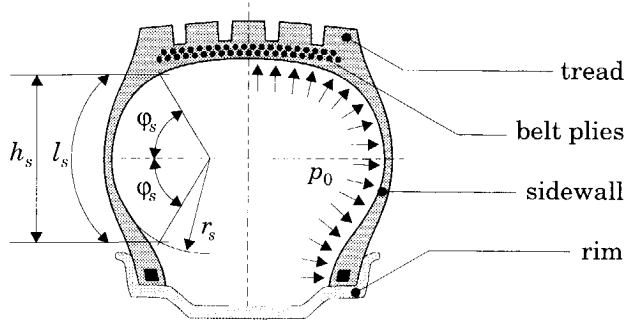


**Figure 4.6:** *The carcass cross section.*

The arc length  $l_s$  of the tyre sidewall is assumed to be constant:

$$l_s = 2r_s \varphi_s \quad (4.11)$$

where  $r_s$  is the radius of the tyre sidewall and  $\varphi_s$  half the angle which covers the tyre sidewall arc. The relationship between this angle and the height  $h_s$  reads:

$$\sin \varphi_s = \frac{h_s}{2r_s} = \frac{h_s}{l_s} \varphi_s \quad (4.12)$$

According to Rotta the radial stiffness  $c_{bw}$  and tangential stiffness  $c_{bv}$  read as function of the parameter  $\varphi_s$  [12]:

$$c_{bw} = p_0 \frac{\cos \varphi_s + \varphi_s \sin \varphi_s}{\sin \varphi_s - \varphi_s \cos \varphi_s}, \quad c_{bv} = \frac{Gt}{l_s} + p_0 \frac{1}{\tan \varphi_s} \quad (4.13)$$

The following sidewall geometry parameters have been measured: the radius of the tyre, the radius of the tyre sidewall arc and the thickness  $t$  of the sidewall. The total length of the sidewall arc was estimated as it is difficult to determine where the arc begins and ends, and also it was impossible to measure the shear modulus of the sidewall rubber  $G$ . The values of the estimated parameters were used to optimise the static behaviour of the model with respect to measurements. The sidewall geometry parameters are given in Table 4.2.

The stiffness characteristics based on the sidewall geometry have been compared with the directly measured sidewall stiffnesses. For this experiment the tyre was placed inside a drum with a radius slightly larger than the free radius of the tyre. The gap between the tyre and the inside of the drum was filled with an epoxy resin forcing the tyre tread-band to retain its circular shape. Forces and torques were applied to the drum and the deformation of the tyre was measured. The experiments were carried out at the nominal inflation pressure (2.2 bar) and at zero inflation pressure. Two in-plane stiffnesses were measured:

the overall translational sidewall stiffness  $c_b$  and the overall rotational sidewall stiffness  $c_{b\theta}$ .

**Table 4.2:** *Parameters for the undeformed tyre sidewall at an inflation pressure of 2.2 bar.*

measured Parameters:			
symbol	value	unit	description
$r$	0.300	m	tread-band radius
$r_s$	0.054	m	radius tyre sidewall arc
$t$	0.010	m	sidewall thickness
Estimated Parameters:			
$l_s$	0.121	m	length of sidewall arc
$G$	$1.6 \cdot 10^6$	N/m <sup>2</sup>	shear modules of tyre sidewall
Calculated Parameters:			
$\varphi_s$	62.3	deg	half the angle of tyre sidewall
$h_s$	0.0867	m	height of the tyre sidewalls

The overall sidewall stiffnesses  $c_b$  and  $c_{b\theta}$  can be calculated easily from the distributed sidewall stiffnesses  $c_{bv}$  and  $c_{bw}$  (cf. Eq. 7.15). Small variations in the deflection were used. Therefore, the sidewall stiffnesses  $c_{bv}$  and  $c_{bw}$  of the undeflected tyre were employed. Table 4.3 presents the comparison of the calculated overall sidewall stiffnesses based on the sidewall geometry to the directly measured sidewall stiffnesses.

In the original version of the *flexible ring* model the sidewall stiffness characteristics are described linearly. Therefore, the differences between the forces showing by the non-linear and linear sidewall representations are added as forces acting between rim and tyre ring.

**Table 4.3:** *Comparison of the overall measured sidewall stiffnesses and the calculated sidewall stiffnesses according to the membrane theory.*

inflation pressure $p_0$ [bar]	symbol	measured sidewall stiffness	calculated sidewall stiffness	unit
2.2	$c_{b\theta}$	$4.26 \cdot 10^4$	$4.04 \cdot 10^4$	Nm/rad
2.2	$c_b$	$1.02 \cdot 10^6$	$0.95 \cdot 10^6$	N/m
0.0	$c_{b\theta}$	$2.08 \cdot 10^4$	$1.11 \cdot 10^4$	Nm/rad
0.0	$c_b$	$0.25 \cdot 10^6$	$0.13 \cdot 10^6$	N/m

### 4.3 The simulation model

The flexible ring model is used to simulate the responses of the tyre rolling over obstacles at very low velocity. The forces generated between the road surface (with obstacle) and the flexible ring depend on the deformation of the tread elements. These distributed forces per unit of length of the circumference acting on the tyre are referred to as the *external pressure distribution*. During each step in the enveloping process the deformation of the flexible ring due to the external pressure distribution is calculated. The distributed forces per unit of length acting in the tyre sidewalls are referred to as the *internal pressure distribution*.

To solve the tyre-road contact problem an iteration procedure is used. The deformation of the tyre ring which balances the internal and the external pressure distributions has to be determined. Figure 4.7 shows the basic iteration procedure and the domains used. The radial and tangential deformations of the flexible ring are calculated from the modal coordinates. The radial and tangential ring deformations are used to calculate the horizontal and vertical tread element deformations. The external pressure distributions in the contact patch depend on the tread element deformations. Now, the horizontal and vertical external pressure distributions are transformed into radial and tangential pressure distributions acting on the flexible ring. Finally, the modal forces are calculated from the radial and tangential pressure distributions.

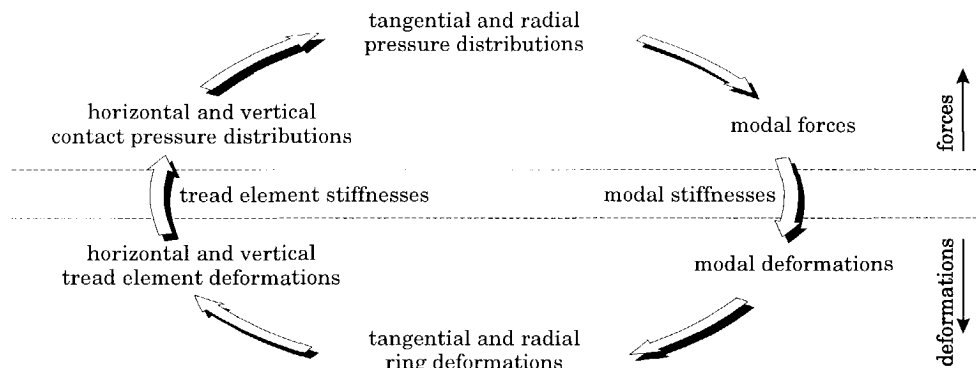


**Figure 4.7:** The basic iteration scheme and the transformations of the forces and displacements between the various domains.

The iteration procedure is a basically unstable process because the tread element stiffnesses are much larger than the modal stiffnesses of the flexible ring model. To obtain a stable iteration the procedure has to be altered: the pressure

distributions in the tread elements in the current iteration step depend on both the pressure distributions in the previous iteration step and the tread element deformations in the current iteration step. Balancing the ratio between these pressure distributions guarantees the stability of the procedure. The iteration procedure is terminated if the internal and external pressure distributions have approached each other sufficiently closely.

We might possibly have employed a continuous description for the forces generated in the contact patch, but the derivation of analytical results is cumbersome. Therefore, the displacements in the contact patch will be calculated for a finite number of contact points  $n_e$  using a finite number of modes  $m$ . The radial and tangential displacements of the ring at these points read:

$$v_{b,i} = \sum_{n=0}^m a_n \cos n\theta_i + b_n \sin n\theta_i, \quad w_{b,i} = -\frac{\partial v_{b,i}}{\partial \theta} = \sum_{n=0}^m n a_n \sin n\theta_i - n b_n \cos n\theta_i \quad (4.14)$$

where the subscript  $i$  denotes the situation at the discrete point at an angular position  $\theta_i$ . The discrete points are equally spaced along the ring circumference:

$$\theta_i = \frac{i}{n_e} 2\pi \quad i = 0, 1, 2, \dots, n_e \quad (4.15)$$

The vertical and horizontal displacements of the flexible ring read:

$$x_{b,i} = -\sin \theta_i \cdot v_{b,i} + \cos \theta_i \cdot w_{b,i} \quad (4.16a)$$

$$z_{b,i} = -\cos \theta_i \cdot v_{b,i} - \sin \theta_i \cdot w_{b,i} \quad (4.16b)$$

The vertical and horizontal forces per unit of length equal the displacements multiplied by the tread stiffnesses:

$$q_{cv,i} = c_{cv}(x_{r,i} - x_{b,i}), \quad q_{cw,i} = c_{cw}(z_{r,i} - z_{b,i}) \quad \text{if } (z_{r,i} - z_{b,i}) > 0 \quad (4.17a)$$

$$q_{cv,i} = 0, \quad q_{cw,i} = 0 \quad \text{if } (z_{r,i} - z_{b,i}) \leq 0 \quad (4.17b)$$

where  $c_{cx}$  and  $c_{cz}$  are the horizontal and vertical tread stiffnesses per unit of length, respectively. Since the tread element stiffnesses only play a role in the contact patch, the names chosen for the stiffnesses are *horizontal* and *vertical* rather than *tangential* and *radial*. The radial and tangential forces acting on the tyre ring read:

$$q_{cv,i} = -\sin \theta_i \cdot q_{cx,i} - \cos \theta_i \cdot q_{cz,i} \quad (4.18a)$$

$$q_{cw,i} = \cos \theta_i \cdot q_{cx,i} - \sin \theta_i \cdot q_{cz,i} \quad (4.18b)$$



As we consider only a finite number of points in the contact patch, rather than a continuous description, the integrals for the generalised modal forces (Equation 4.7) change into summations of the forces in the discrete points considered:

$$\xi_{c0} = \Delta\theta \frac{1}{2\pi} \sum_{i=1}^{n_e} (q_{cv,i} + \frac{\partial q_{cw,i}}{\partial \theta}), \quad \xi_{cn} = \Delta\theta \frac{1}{\pi} \sum_{i=1}^{n_e} (q_{cv,i} + \frac{\partial q_{cw,i}}{\partial \theta}) \cos n\theta_i \quad (n = 1, 2, 3, \dots) \quad (4.19a)$$

$$\eta_{c0} = 0, \quad \eta_{cn} = \Delta\theta \frac{1}{\pi} \sum_{i=1}^{n_e} (q_{cv,i} + \frac{\partial q_{cw,i}}{\partial \theta}) \sin n\theta_i \quad (n = 1, 2, 3, \dots) \quad (4.19b)$$

And the modal deformations read:

$$a_n = \frac{\xi_{cn}}{C_{bn}}, \quad b_n = \frac{\eta_{cn}}{C_{bn}} \quad (4.20)$$

For optimal results the simulation model has several advanced features. First, sliding of the tread elements is introduced. This means that the horizontal force generated in the tread elements depends on the vertical pressure distribution. Furthermore, the simulations can be performed on a flat road surface or on a drum. In the latter situation, the vertical coordinate of the drum surface depends on the longitudinal coordinate owing to the curvature of the drum.

Another aspect of the tyre rolling over road irregularities is free rolling of the tyre. Free rolling is defined as the situation where no traction or braking torques are acting on the rim. Unfortunately, the torque at the rim is a reaction resulting from the motions of the wheel which are used as input to the model. In order to perform simulations of free rolling, the rim should be rotated over an additional angle in order to make the resulting torque zero.

Simulations may be performed at constant axle height or constant vertical load. The first situation is similar to conditions during the measurements. The second situation is preferable for simulations over large step changes in road surface height. In that case, the stationary value of the contact length will not change due to the step change and the responses of the tyre will be due only to the step change and not to the change in vertical load.

Tread elements are modelled along the entire ring circumference. Each tread element can get into contact with the road. It is possible to have more than one contact patch, or in other words the model is able to represent gaps between two or more individual contact patches. This forms a further extension to the model application as suggested by Gong [32,51]. He used the front and rear contact angle only and he solved the tyre road contact problem analytically rather than the numerically as in this chapter.

## 4.4 Validation of the static behaviour of the flexible ring model

The accuracy of the flexible ring model improves if the number of modes and/or the number of tread elements increases, but conversely, the simulation time needed is influenced adversely if the number of modes and number of tread elements increases. Hence, it is important to balance between the accuracy of the model and the simulation time needed.

The tread-band displacements converge very quickly with the increase in the mode number  $n$ . To obtain reliable results for the tread-band displacements on a flat road surface fifteen or more modes should be included. The convergence of the contact pressure is somewhat slower than that of the tread-band displacements: at least twenty modes should be included. These results correspond to the results found by Gong [32]. For simulating the enveloping properties of the tyre thirty modes are used.

The tread elements are not only modelled in the contact patch, but are also equally spaced along the entire tread-band circumference, see also Figure 4.5, otherwise tread elements entering or leaving the contact patch have to be monitored. It is difficult to assess the number of tread elements needed. We have chosen 800 elements. This means that the number of elements in contact with an even road surface varies between 27 and 55 in the vertical load range from 2000 to 6000 N. The smallest obstacle used for studying the enveloping properties is 30 mm long, which covers 12 tread elements.

The extensional stiffness of the tyre tread-band is very high ( $EA = 5.0 \cdot 10^6$  N). The *in-extensibility* assumption was validated by comparing simulations with an extensible tread-band with simulations with an in-extensible tread-band. There is no significant difference between the results of the two models. The calculation time, on the other hand, was much longer for the model with the extensible tread-band.

The sidewall non-linearity plays an important role in the force generation in the tyre. The linear model with constant sidewall stiffnesses generates forces which are 40% too high compared to the measurements.

Figure 4.8 presents a validation of the *flexible ring* model for a non-rotating tyre. This figure presents the measured and simulated properties as function of the vertical tyre deflection for two situations: the tyre standing on a flat road surface, and the tyre standing on the curved drum surface.

The size of the contact patch is an important factor for the generation of horizontal forces. With the flexible ring model a simulation was performed at increasing tyre deflection. Owing to the discrete number of tread elements the

simulated contact length increases by steps of 2.5 mm. The flexible ring model represents the measured contact length well. Given the same vertical load, the measured contact length on the flat road is 14% longer than the measured contact length on the drum. This difference for the flexible ring model is 10% only.

Figure 4.8 presents a comparison between the measured vertical load and vertical stiffness and their simulated values. The vertical reaction force on the wheel was measured as a function of the vertical tyre deflection. The relationship between measured deflection and force was fitted with a second order polynomial as the vertical load increases slightly more than proportionally with the deflection. The vertical stiffness was found by differentiating this second order polynomial. The vertical stiffness of the flexible ring model deviates only at high values of tyre deflection. Both the measured and calculated vertical stiffnesses on the drum are about 5% smaller than the vertical stiffnesses on a flat road.

The longitudinal stiffnesses of the model has also been validated, see Figure 4.8. Two longitudinal stiffnesses were investigated: the longitudinal force as function of the longitudinal displacement of the wheel at constant rim angle; and the longitudinal force as function of the rotational angle of the rim at constant longitudinal position of the axle. The measurements were carried out at 4 axle heights. The simulations were conducted at 25 axle heights. If the tyre deflection approaches zero, the longitudinal tyre stiffnesses will approach zero as well due to the vanishing contact patch.

Finally, Figure 4.8 presents the effective rolling radius. The measured rolling radius decreases with vertical load. The simulated rolling radius is almost constant and about equal to the radius of the ring. The flexible ring model is not capable of showing the effective rolling radius variations accurately. For that one needs to model not only the tread element deformation, but the height and the orientation of the tread elements as well [51]. The influence of tread element orientation on the effective rolling radius is illustrated in Figure 4.23 in Section 4.7.

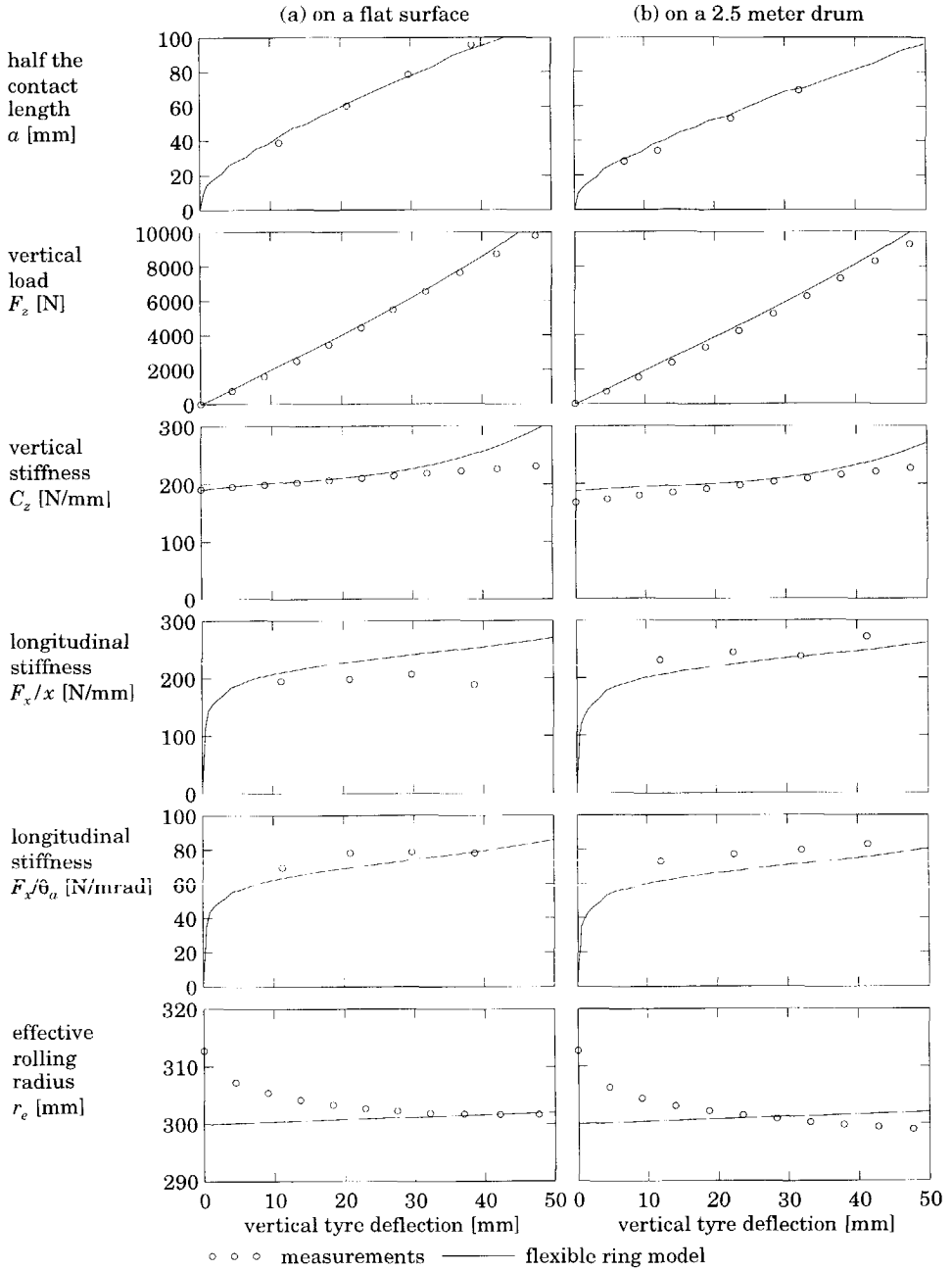


**Figure 4.8:** *The deformations and stiffnesses of the tyre as function of the vertical tyre deflection.*

## 4.5 The tyre rolling over short wavelength obstacles

The enveloping properties of the tyre rolling over obstacles were studied experimentally on the rotating drum test stand and theoretically with the flexible ring model. Figure 4.9 depicts the three obstacle shapes used as road unevennesses: a trapezoid cleat of 10 mm height and a base length of 50 mm and a top length of 30 mm, a positive step of 15 mm, and a negative step of 15 mm. Three constant axle heights were used corresponding to 2000, 4000 and 6000 N vertical load for an undisturbed road surface.

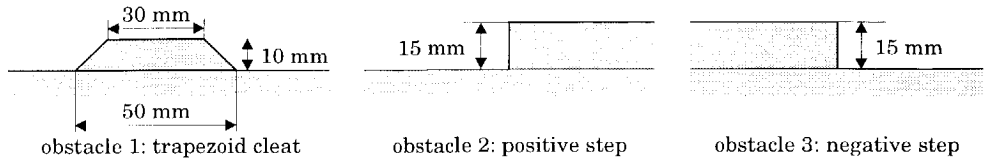


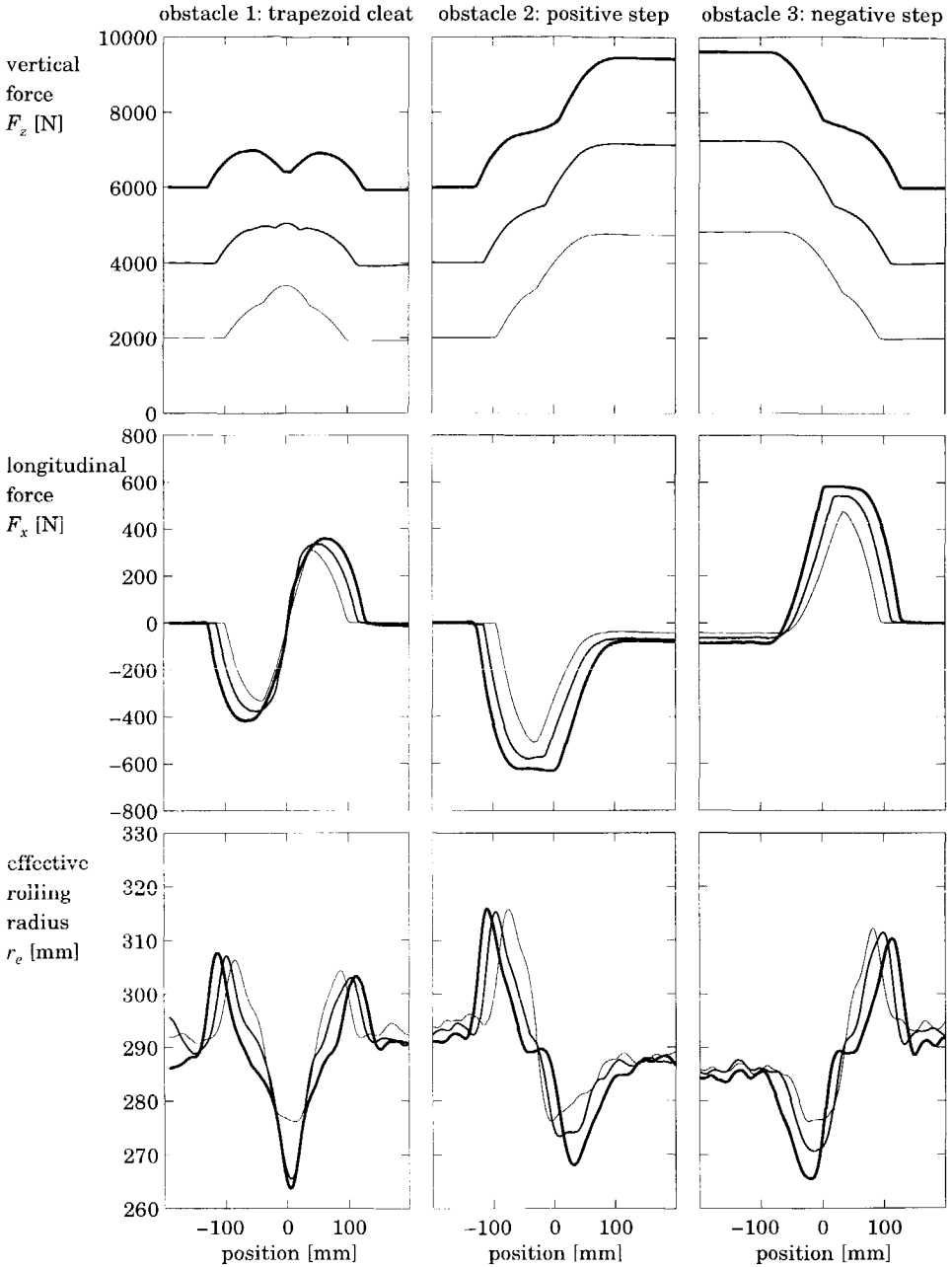
**Figure 4.9:** The three obstacles used: a trapezoid cleat, a positive step, and a negative step.

During the experiments the wheel axle is fixed in a frame constraining both the vertical and horizontal motions of the axle. The wheel is able to rotate freely as no braking or traction torque is applied to the rim. The horizontal and vertical reaction forces of the tyre are measured at the bearings of the wheel axle. The rotational velocities of the drum and the wheel are also measured. The rotating drum test stand is described in detail in Appendix A.

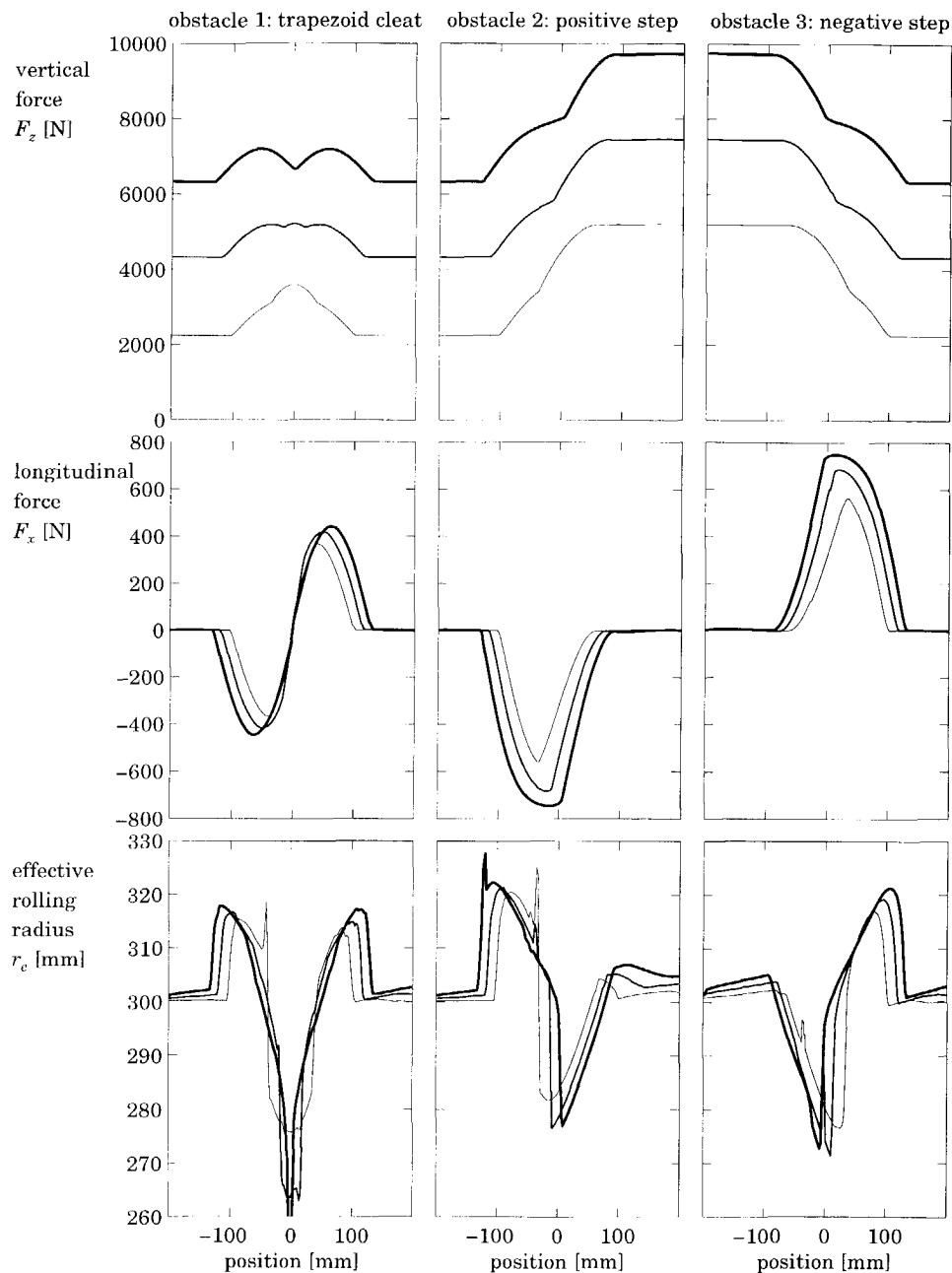
To suppress the influence of the tyre dynamics, the experiments had to be carried out at very low velocity. Initial experiments showed that even at a velocity of 3 km/h the influence of tyre dynamics could not be neglected. A special drum propulsion system was used to carry out the final experiments at 0.2 km/h. The measured responses were averaged 20 times to reduce the influence of tyre non-uniformities.

Figure 4.10 presents the measured enveloping responses of the tyre rolling over the three obstacles at three constant axle heights. This figure presents the measured vertical force, the measured longitudinal force and the measured (slightly varying) rotational velocity. The latter variation is represented by the varying effective rolling radius, which is defined as the ratio between the forward velocity of the drum  $V_x$  and the rotational velocity of the wheel  $\Omega$ :

$$r_e = \frac{V_x}{\Omega} \quad (4.21)$$



**Figure 4.10:** The measured enveloping response of the tyre at three constant axle heights.



**Figure 4.11:** The simulated enveloping properties of the tyre at three constant axle heights.

During the quasi-static experiments at 0.2 km/h the travelled distances of the wheel and the drum were measured rather than the velocities. The displacement signals were differentiated and filtered to obtain the velocities. The cut-off frequency of the filtering characteristic used was too low, *cf.* the very smooth measured rolling radius variations in Figure 4.10. Unfortunately, the raw data of the measurements were deleted, and the filtering effect could not be undone unless the experiments were carried out once more. New quasi-static experiments were not carried out because they are very time consuming and would not provide any significant new data. The only advantage of new data would be a reduction in the filtering effect of effective rolling radius. In that case, the measured rolling radius variations will probably correspond better to the simulated ones.

Figure 4.11 presents the simulated responses of the tyre rolling over the three obstacles: the variations in vertical force, the variations in longitudinal force, and the rolling radius variations. The response was simulated statically: for each longitudinal position in the enveloping process the static equilibrium forces in the tyre were calculated iteratively. The correspondence between the measurements and the simulations indicate that we may use the flexible ring model also for simulating conditions other than the measured conditions (*e.g.* another axle height or another obstacle shape).

The measured and simulated step responses (*cf.* Figures 4.10 and 4.11) correspond well with quasi-static experimental studies of the vertical and longitudinal forces presented in the literature [61,62,74,110]. Also the force responses of the tyre rolling over the cleat obstacle correspond well with the experimental studies presented in the literature [5,8,34,49,61,62,110]. The measured and simulated effective rolling radius corresponds qualitatively with the measured cleat response of the wheel rotation with respect to distance travelled by road presented by Gough [34].

The results presented also correspond well with the simulation results of the forces presented in the literature: Mousseau *et al.* [74] used a Finite Element Model to simulate the tyre rolling over a positive step, and Badalamenti *et al.* [5] used a radial spring model to roll the tyre over a cleat obstacle.

It is well known that the vertical stiffness at the edges of the contact patch is much higher than the stiffness in the centre of the contact patch. This effect influences the response of the vertical force, especially at high values of vertical load when the response of the vertical force shows two successive responses: the front edge of the contact patch rolling over the obstacle and the rear edge rolling over the obstacle.



The longitudinal force is negative when the tyre rolls over a positive step, and this force becomes positive when the tyre rolls over a negative step. The longitudinal force response also appears to vary asymmetrical when the tyre rolls over a symmetrical obstacle (e.g. the trapezoid cleat).

The mechanism of the variation in effective rolling radius is harder to understand. The first influence is the well known dependency of the effective rolling radius on the vertical load. This influence is rather small: the measured step responses show that the stationary value of the effective rolling radius before and after the step changes by 3 to 7 mm. Figure 4.10 shows that the total variations in effective rolling radius are much larger than the variations due to the load dependency only. The flexible ring model is not able to represent the variation of the stationary value of the effective rolling radius accurately (cf. Figure 4.8).

The spikes in the simulated rolling radius variation are probably due to the discretisation of the tread elements in the model. The number of elements in contact with either the road or the obstacle has to be an integer value. This means that the number of elements may vary by one between two simulation steps. This influences the forces generated in the tread elements.

## 4.6 Effective inputs from short wavelength obstacles

The geometry of a road surface with short wavelength irregularities cannot serve directly as input for a model with a single-point tyre-road interface (like the rigid ring model of Chapter 7). Davis introduced an *equivalent ground plane*, which reflects both the elevation and slope characteristics of the original road geometry [20]. He obtained this equivalent ground plane from simulations with a radial spring tyre model.

If we monitor the reaction forces at the axle of an enveloping tyre we may imagine the tyre rolling piece wise over a flat road surface at a given height and inclination, as depicted in Figure 4.12. Besides the two inputs introduced by Davis [20]: the effective height  $w$  and the effective angle  $\beta$  of the effective road surface, a third input is used: the effective rolling radius variation  $\tilde{r}_e$ .

The idea behind the introduced *effective road surface* is that the quasi-static responses of a tyre model with a single-point tyre-road interface on an effective road surface are similar to the quasi-static responses of the real tyre on the real road. Accordingly, the effective excitation of the tyre will be assessed from the quasi-static enveloping properties of the tyre. This section shows how the

effective plane height can be assessed from the measured or simulated response of the quasi-static vertical force and also how the effective plane angle can be assessed from the response of the quasi-static longitudinal force. The next section will show how the third input (the effective rolling radius variation) can be derived approximately from the other two effective inputs.

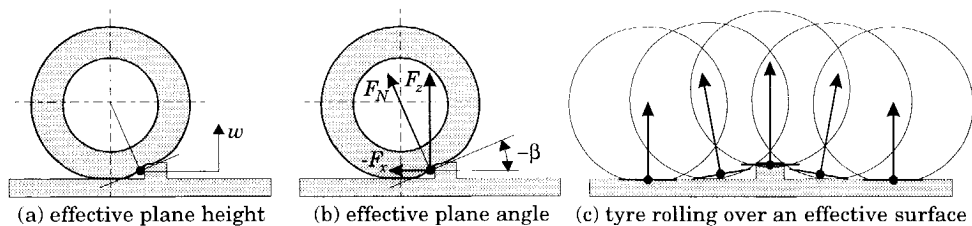


**Figure 4.12:** The definition of the effective road surface.

Figure 4.12a shows the definition of the effective plane height  $w$ , which is defined as the variation in vertical force divided by the vertical tyre stiffness  $C_z$  (note: axle vertical position is fixed):

$$w = \frac{F_z - F_{z0}}{C_z} \quad (4.22a)$$

According to the definition of the effective plane height, the vertical force should be divided by the current vertical stiffness  $C_z$ , which is generally non-constant. However, if we would like to use this input in a linear tyre model, the vertical force must be divided by a constant vertical stiffness  $C_{z0}$ :

$$w = \frac{F_z - F_{z0}}{C_{z0}} \quad (4.22b)$$

Figure 4.12b shows the forces of the tyre rolling over the obstacle. It is assumed that the effective plane is perpendicular to the normal force  $F_N$ . The angle  $\beta$  of the effective slope of the road is defined as:

$$\beta = -\arctan\left(\frac{dw}{ds}\right) = \arctan\left(\frac{(F_x - F_{x0})}{F_z} + \frac{f_r(F_z - F_{z0})}{F_z}\right) \quad (4.23a)$$

A correction is made for the influence of the change in rolling resistance force  $f_r F_z$  because that is the only tangential force that remains at very low speed of rolling. As in to the previous effective input, the equations of the effective plane angle can be linearised: the constant vertical force  $F_{z0}$  is used in the division rather than the varying vertical force  $F_z$ .

$$\beta = -\arctan\left(\frac{dw}{ds}\right) = \arctan\left(\frac{(F_x - F_{x0})}{F_{z0}} + \frac{f_r(F_z - F_{z0})}{F_{z0}}\right) \quad (4.23b)$$

Figures 4.13 and 4.14 present the two effective inputs obtained from experiments and the simulation of the tyre rolling at three axle heights over the three obstacles. These figures indicate that the flexible ring model describes the enveloping properties of the tyre rather well. Figures 4.13a and 4.14a show the 'non-linear' effective inputs according to the definitions of (4.22a) and (4.23a). These inputs can be used in a non-linear model. Figures 4.13b and 4.14b show the 'linear' effective inputs according to the definitions of (4.22b) and (4.23b). These inputs can be used in a linearised model.

The differences between the linear and non-linear effective plane heights are small because the vertical tyre stiffness  $C_z$  varies only slightly as function of the vertical load. The differences between the linear and non-linear effective plane angle are much larger. This is because the vertical load in expression (4.23a) varies considerably.

One difference between the measurements and the simulation is the asymmetry in the variation of the plane height  $w$  obtained from measurements for rolling over the trapezoid cleat. This asymmetry is probably caused by hysteresis of the tyre. Another difference with the measurements is the effective plane angle  $\beta$  at high levels of vertical load: the measured amplitudes are somewhat lower than the simulated amplitudes.

The effective excitations of the tyre caused by obstacles depend highly on the obstacle shape and axle height. Bandel and Monguzzi decomposed the response of the tyre into basic curves [8]. Accordingly, the effective plane height variation for a short symmetrical cleat may be obtained by summing two equal but shifted half sine waves, see Figure 4.15. The height of the half sine wave is denoted by  $\frac{1}{2}H$ , the width with  $\lambda_{bf}$  and the shift of the second sine wave by  $\lambda_{imp}$ . A similar basic function may be used to represent the effective plane angle. The height is now denoted with  $A$  and the first half sine is different in sign. The basic functions of the tyre rolling over the positive or negative step are quarters of sine waves as shown in Figure 4.16.

The summation of the basic functions is identical to a convolution of one basic function with two impulse functions. The properties of the convolution integral will be used in Section 10.4 for the study of the frequency content of the excitation of the tyre by short wavelength obstacles.

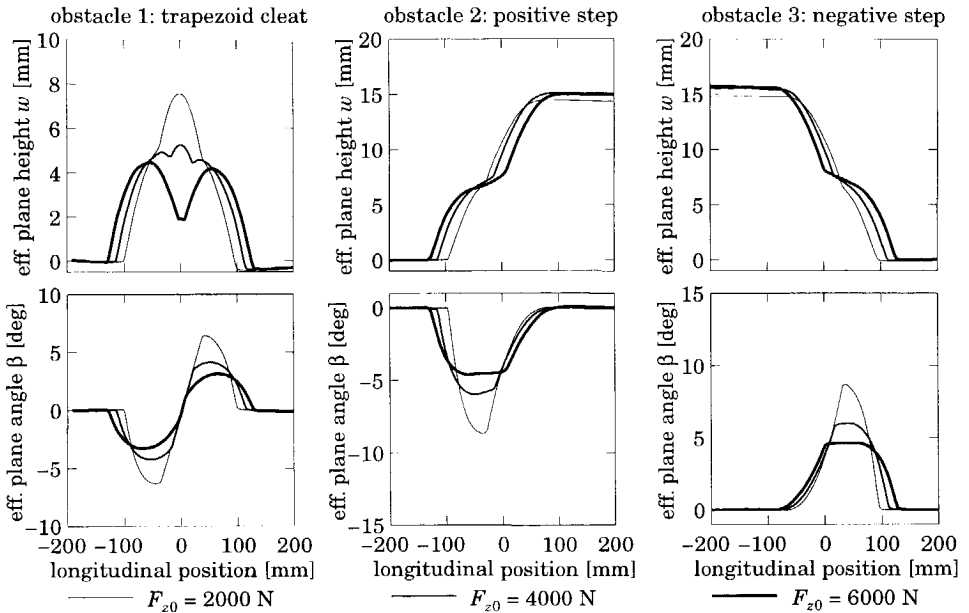


**Figure 4.13a:** The non-linear effective road surface obtained from measurements.

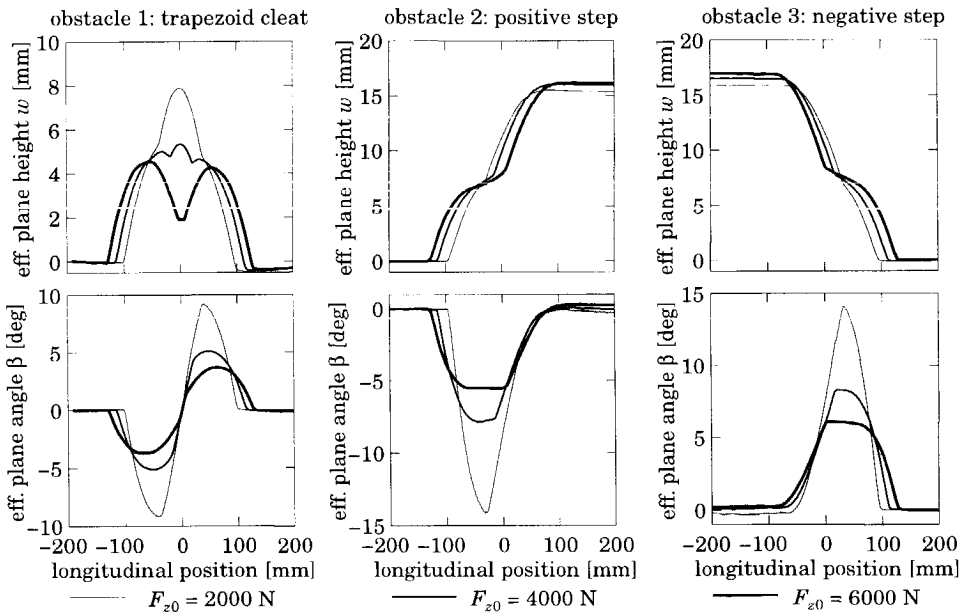


**Figure 4.13b:** The linear effective road surface obtained from measurements.

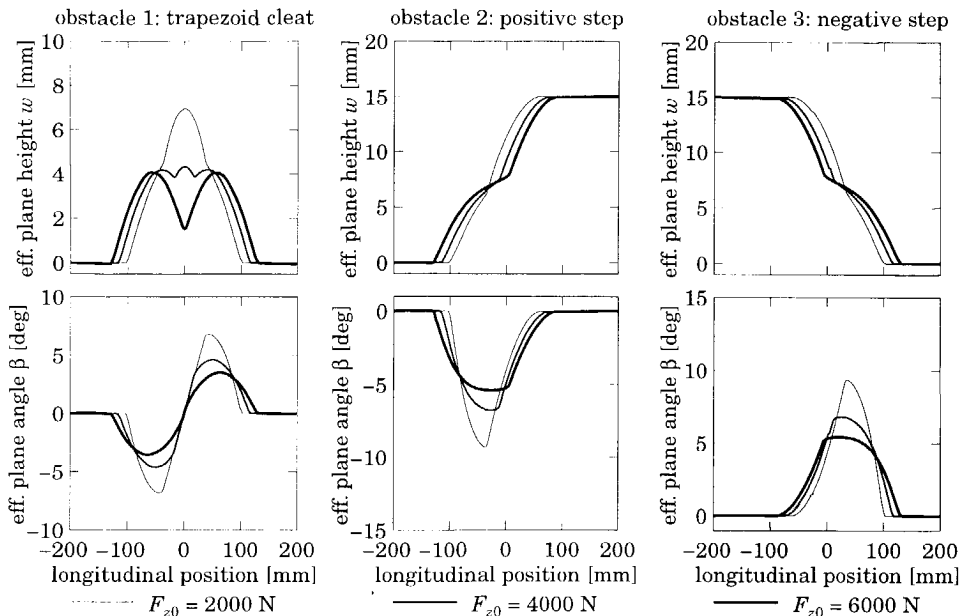


**Figure 4.14a:** The non-linear effective road surface obtained from simulations.

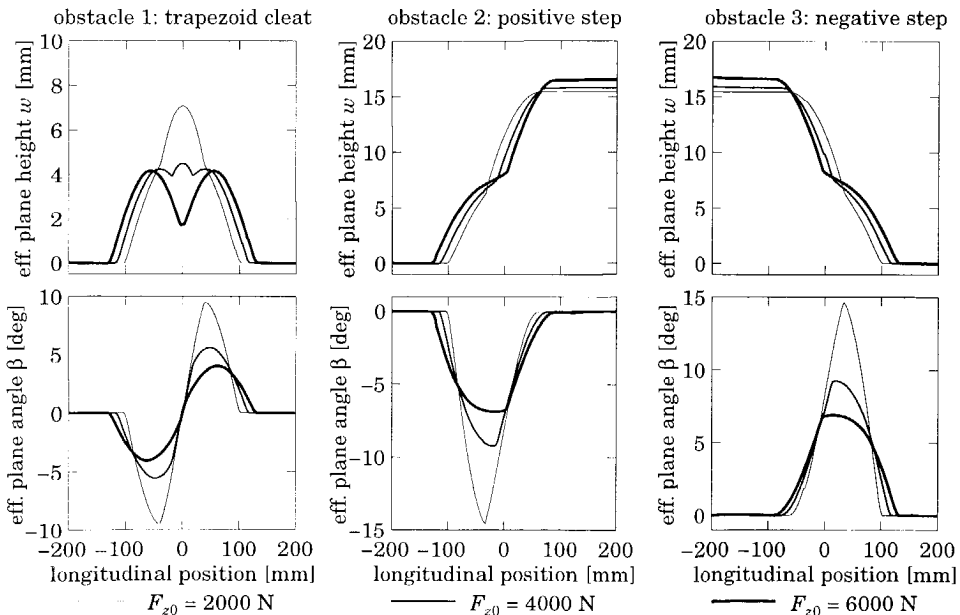


**Figure 4.14b:** The linear effective road surface obtained from simulations.

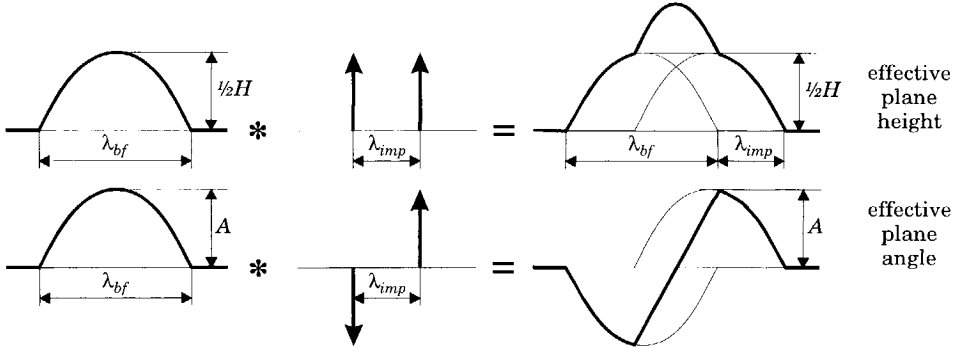


**Figure 4.15:** The composition of the effective road surface from basic functions for obstacle 1 (trapezoid cleat).

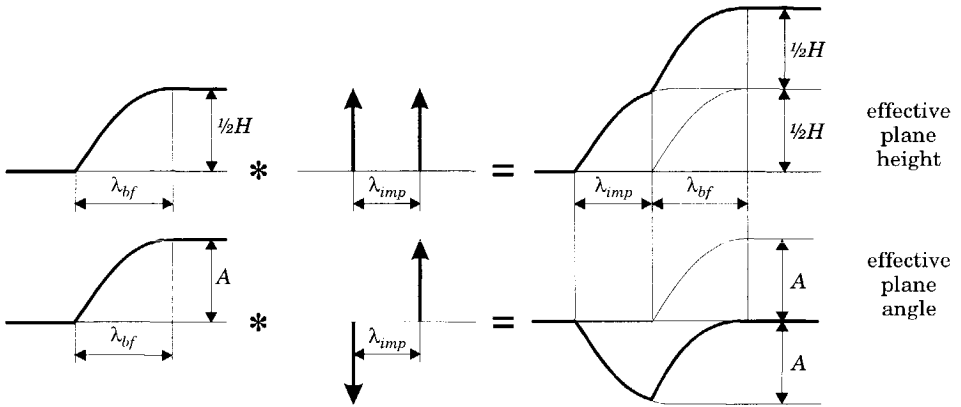


**Figure 4.16:** The composition of the effective road surface from basic functions for obstacle 2 (positive step).

The parameters of the basic functions (shown in Figures 4.15 and 4.16) are obtained by fitting the effective plan height and the effective plan angle obtained from either the experiments or the simulations with the flexible ring model. The width of the basic functions  $\lambda_{bf}$  and the heights  $H$  and  $A$  are approximately independent of the vertical load. The shift of the basic functions  $\lambda_{imp}$  varies with the vertical load: this shift is slightly smaller than the contact length  $2a$ . With a vertical load (and thus the contact length) approaching zero, the two basic functions coincide. At higher levels of vertical load these basic functions are mutually shifted over approximately the contact length. If the vertical load is very large, we get the typical response of the tyre on a short symmetrical obstacle: a response with two maxima rather than a response with one

maximum. Figure 4.17 presents the influence of the shift of the basic function on the effective road surface. The bold lines in this figure represent the effective surface at 2000, 4000 and 6000 N vertical load.

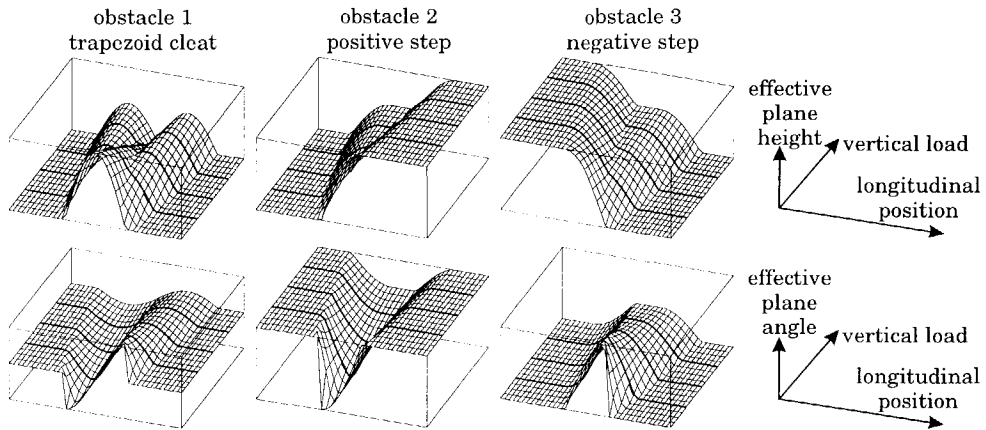


**Figure 4.17:** *The effective plane height and the effective plane angle as function of the vertical load and longitudinal position (obstacle 1, 2, and 3).*

#### 4.7 Effective rolling radius variations on an effective road surface

The effective road surface is used as input for high velocity simulations with the rigid ring model in Chapter 10. For these simulations the effective plane height  $w$  is used as vertical excitation of the tyre, and the effective plane angle  $\beta$  is used as longitudinal excitation of the tyre. Unfortunately, these two excitations do not suffice. The variations in the rotational velocity of the tyre during cleat passage are essential. These variations generate slip velocity variations in the contact patch, and thus additional longitudinal forces in the contact patch. Hence, it is very important that these variations of the rotational velocity are modelled correctly.

The measured and simulated effective rolling radius variations are related to the responses of the longitudinal force (*cf.* Figures 4.10 and 4.11): when the longitudinal force is decreasing the effective rolling radius is larger than the average rolling radius, and when the longitudinal force is increasing, the effective rolling radius is smaller than the average value. Numerical analysis of the data showed that the effective rolling radius variation is approximately equal to the

vertical tyre deformation multiplied by the derivative of the effective plane angle with respect to wheel angle of revolution (first term of the following equation):

$$\tilde{r}_e = \underbrace{\frac{r_t - r_0}{\Omega_0} \frac{d\beta}{dt}}_1 + \underbrace{r_e(1 - \cos \beta)}_2 + \underbrace{\eta(F_z - F_{z0})}_3 \quad (4.24)$$

The second and third contributions in the formula above are relatively small (less than 5% of the first contribution): the second contribution is due to the slope itself, the third contribution is the influence of the load dependency on the effective rolling radius.

In Figure 4.18 the measured effective rolling radius is compared to the rolling radius variations according to expression (4.24). The major difference is that the directly measured effective rolling radius was filtered too much. In Figure 4.19 the simulated radius using the flexible ring model is compared to the result of expression (4.24) with the effective road geometry resulting from flexible ring model calculations. This expression represents the measured and simulated effective rolling radius variations rather well.

A disadvantage of Equation (4.24) is that the derivative of the road plane angle is used for the calculation of the rolling radius variations. For that we need to differentiate the road plane angle during numerical simulations. This problem is solved in Section 7.3 by replacing the differentiator by a high-pass filter.

### A possible model for representing the effective rolling radius variations

Expression (4.24) showed that the effective rolling radius variations can be deduced from the other two effective inputs. In this section we will discuss the background of the contributions represented in expression (4.24). If the tyre rolls over an uneven road surface we may monitor variations in actual road geometry: road plane height, road plane angle and road surface curvature. All these variations will generate rolling radius variations.

It is assumed that the effect of the tyre rolling over a road geometry may be decomposed into the effect of the road plane height, the effect of the road plane angle and the effect of the road surface curvature. The latter effect is again decomposed and thought to be the result of the sum of two mechanisms: rolling over a rotating curved surface (e.g. drum) and rolling over a flat surface that is rotated about a transverse axis through the contact centre with equal and opposite speed of rotation. In that way the total speed of rotation of the road cancels out as it should be.



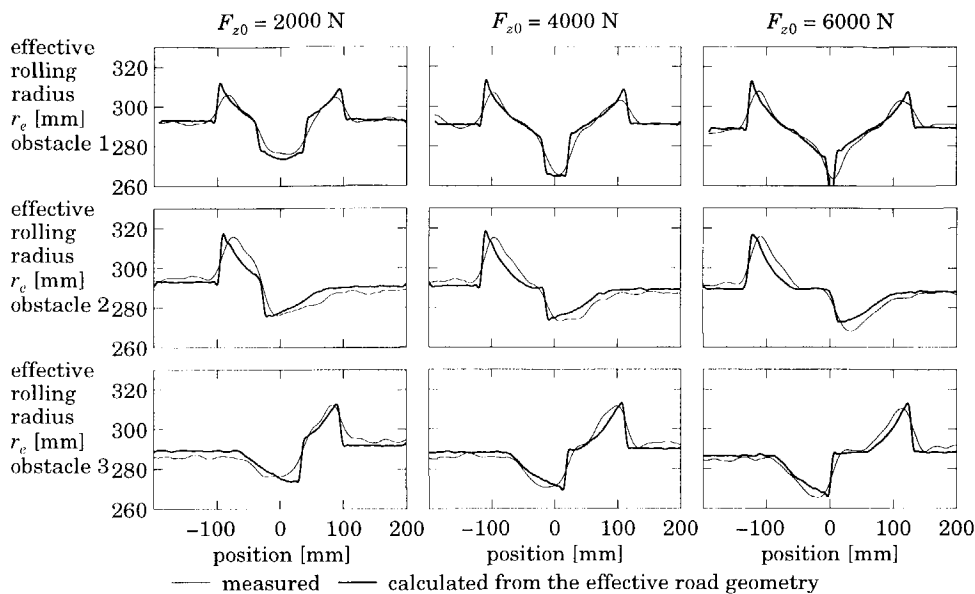


**Figure 4.18:** Comparison of directly measured effective rolling radius and the calculated effective rolling radius from effective road geometry.

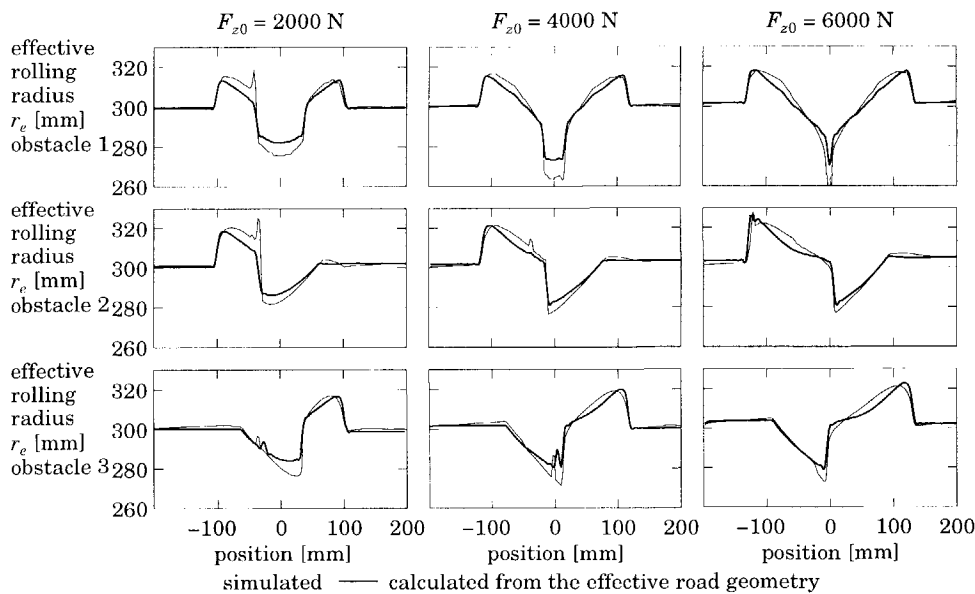


**Figure 4.19:** Comparison of simulated effective rolling radius and the calculated effective rolling radius from effective road geometry.

Figure 4.20 presents three of the four mechanisms of effective rolling radius variations due to the road geometry. The most important mechanism is the variation of the plane angle at zero road curvature. The second mechanism is the tyre rolling over a curved road at constant road plane angle. The third mechanism is the difference in orientation between the horizontal velocity  $V_x$  and the velocity tangential to the road surface  $V_T$ . The fourth mechanism, not shown in Figure 4.20, is the well-known vertical load dependency of the effective rolling radius. This influence is rather small compared to the other three mechanisms.

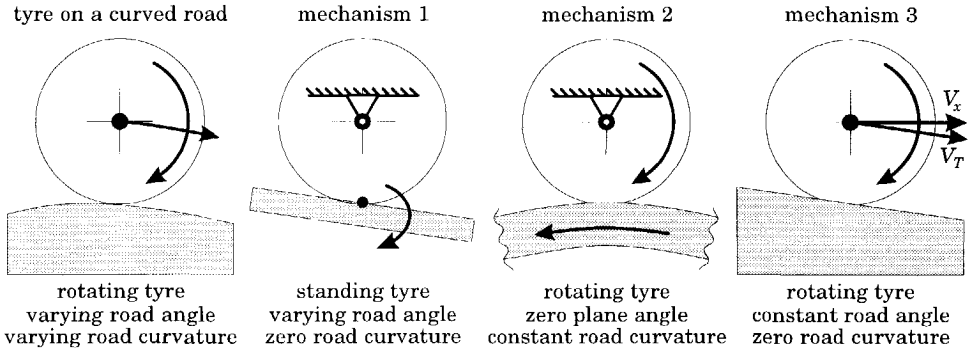


**Figure 4.20:** *The mechanisms of the effective rolling radius variations of the tyre due to the road geometry.*

### The influence of the varying road plane angle

The following theoretical considerations are based on the assumption that the influence of the varying road plane angle of the rolling tyre over a curved road may be studied with a standing tyre on a varying road plane angle. The variation of the plane angle is the major contribution to the variations of the effective rolling radius. Figure 4.21a presents the transformation of the forces from the road plane frame into a horizontal frame. The road plane angle  $\beta$  is used to transform the tangential force  $F_{cT}$  and normal force  $F_{cN}$  in the contact patch to a horizontal force  $F_{cx}$  and a vertical force  $F_{cz}$ :

$$\begin{bmatrix} F_{cx} \\ F_{cz} \end{bmatrix} = \begin{bmatrix} \cos \beta & \sin \beta \\ -\sin \beta & \cos \beta \end{bmatrix} \begin{bmatrix} F_{cT} \\ F_{cN} \end{bmatrix} \quad (4.25)$$

The transpose of the transformation matrix is used to transform the positions in the contact patch from the horizontal frame to the road plane frame (Fig. 4.21b):

$$\begin{bmatrix} x_{cT} \\ z_{cN} \end{bmatrix} = \begin{bmatrix} \cos \beta & -\sin \beta \\ \sin \beta & \cos \beta \end{bmatrix} \begin{bmatrix} x_c \\ z_c \end{bmatrix} \quad (4.26)$$

where  $x_c$  and  $z_c$  denote the horizontal and vertical displacements of the wheel at point  $C$ , and  $x_{cT}$  and  $z_{cN}$  the tangential and normal displacements of the wheel at point  $C$ .

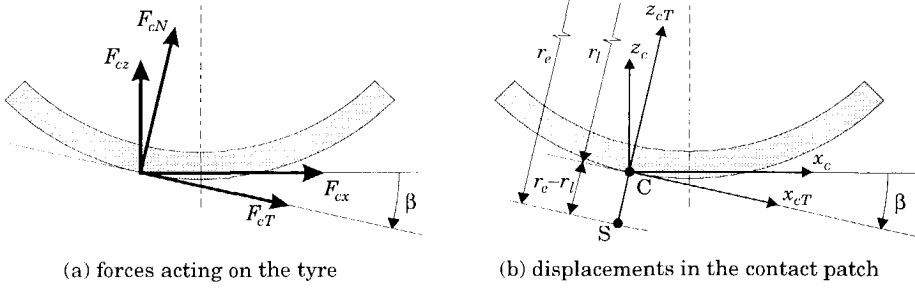


**Figure 4.21:** The influence of the road plane angle on the displacements and forces in the contact patch.

Figure 4.21b shows that a rotation of the road plane about the contact point  $C$  will generate additional tangential velocity variations in point  $S$ . If point  $S$  lies beneath the road surface, the road moves backwards relative to point  $S$  when the rotation of the road plane is positive ( $\dot{\beta} > 0$ ). Or, the other way around, the additional velocity of point  $S$  due to a positive rotation of the road is positive. Thus the tangential slip velocity  $V_{c,sx}$  in the contact patch (which is defined as the velocity of point  $S$ ) becomes:

$$V_{c,sx} = V_x - \Omega r_e + \frac{d\beta}{dt}(r_e - r_l) \quad (4.27)$$

where  $r_e$ , and  $r_l$  denote the effective rolling radius and the loaded tyre radius, respectively. The difference in these radii is the difference between the location of the contact point  $C$  and the centre of wheel rotation  $S$ . In our model considerations we would like to write the contribution of the varying road plane angle on the slip velocity as an additional rolling radius variation  $\tilde{r}_{e,rot}$ :

$$V_{c,sx} = V_x - \Omega(r_e + \tilde{r}_{e,rot}) \quad (4.28)$$

Combining the Equations (4.27) and (4.28) gives:

$$\tilde{r}_{e,rot} = -\frac{r_e - r_l}{\Omega_0} \frac{d\beta}{dt} \quad (4.29)$$

The influence of the road plane angle variations at zero velocity on the rotational wheel angle variations is substantiated through measurements. The experiment was carried out at a fixed axle position ( $V_x=0$ ,  $V_z=0$ ), resulting in increasing vertical load at increasing (absolute) road plane angle. The rim could rotate freely about its spindle axis as no traction or braking force was applied to the rim. Thus, the tangential slip velocity ( $V_{c,tx}$ ) in the contact patch has to be zero. Rewriting Equation (4.27) gives the following relationship between the variation of wheel angle  $\theta_w$  as function of the variation of road plane angle ( $\dot{\theta}_w = d\beta/dt$ ):

$$\frac{\partial \theta_w}{\partial \theta_a} = \frac{r_e - r_l}{r_e} \quad (4.30)$$

Figure 4.22 presents the measured variation of wheel angle as function of the road angle, and the variation according to Equation 4.30. Indeed this equation is able to predict the variation in wheel velocity due to road plane angle variations. The relationship between road plane angle and wheel angle at constant axle height is non-linear because the vertical load varies with the road angle as well influencing both the loaded radius and the effective rolling radius.

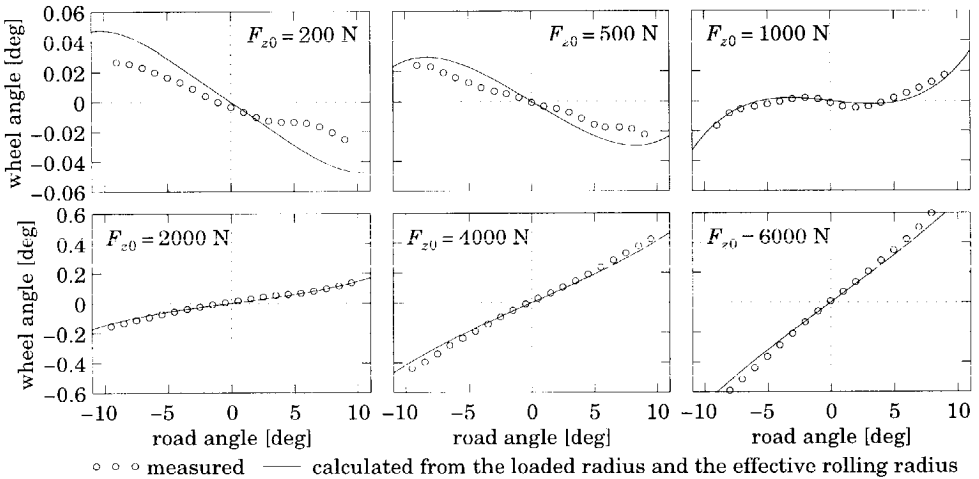


**Figure 4.22:** The measured and calculated wheel angle as function of the road angle, at six constant axle heights.

At low values of vertical load the difference between the loaded radius and the effective rolling radius is rather small and the variations in the wheel angle are very small and difficult to measure accurately. At approximately 1000 N vertical

load point  $S$  and point  $C$  appear to coincide and the variations of wheel angle are about zero. It is most striking to see that at smaller values of vertical load, the tyre rotation is opposite to the road plane rotation. At these values of vertical load the effective rolling radius is smaller than the loaded radius. In other words, point  $S$  lies above the contact point  $C$  at low values of vertical load, see also Figure 4.23b.

The results presented in Figure 4.22 are not surprising. It is basically an effective rolling radius experiment. The effective rolling radius  $r_e$  defines the radius of pure rolling of the tyre rolling with respect to the surface irrespective of whether the tyre is rotated or the drum is rotated.

Note: the theoretical considerations above explain the variation of the wheel angle as function of the variation of the angle of the road plane. The theoretical result was validated by experiments in which the road rotated as rigid body. In reality, however, the road does not rotate as the tyre moves over a fixed road. To compensate for this rotation of the road the effect of the curved surface rotating in opposite direction is added in the subsequent sub-section.

### The influence of road curvature

The second contribution to the rolling radius variation depicted in Figure 4.20 is due to the rotating curved road at constant road plane angle. This situation can be compared with a tyre rotating on a rotating drum. The curvature of the drum influences the effective rolling radius. To be able to understand the influence of the drum curvature we will first discuss the mechanism of the variation of the effective rolling radius on a flat road.

Figures 4.23a through 4.23c depict a rotating radial tyre on a flat road surface in three loading conditions. The possible locations of the centre of rotation are denoted by  $S$ . At zero wheel load point  $S$  lies at road level and the effective rolling radius  $r_e$  of the tyre assumes the free radius of the tyre  $r_0$ . At low values of wheel load the effective rolling radius decreases: point  $S$  may even lie above the road surface [82]. At large values of wheel load the effective rolling radius approaches the radius  $r_r$  of the nearly in-extensible tread-band.

The variations of effective rolling radius are caused by the orientations of the tread elements entering the contact patch. At low values of vertical load the tread elements entering the contact patch are oriented approximately radially. This means that an additional slip velocity of the belt is needed to rotate the tread elements in the contact patch. At very large levels of vertical load the tread elements enter the contact patch almost vertically: only little rotation of the tread

elements is needed and the effective rolling radius is approximately equal to the radius of the tread-band.

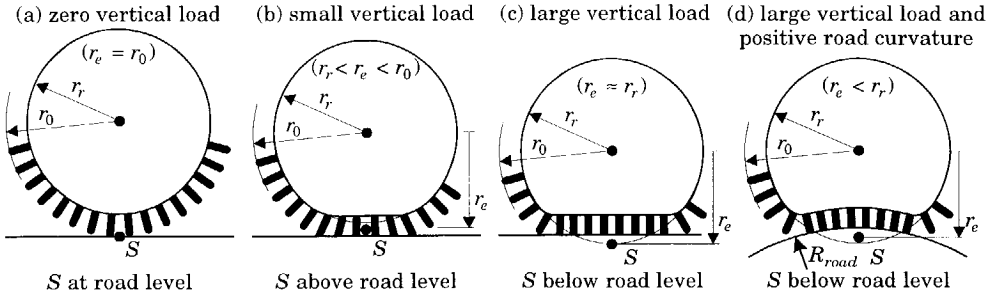


**Figure 4.23:** The position of the centre of rotation.

If the tyre rotates on a drum at high values of vertical load (see Figure 4.23d), the tread elements entering the contact patch are oriented approximately perpendicularly to the drum surface. This means that again an additional slip velocity of the belt (but now negative) is needed to change the orientation of the tread elements. In conclusion, a positive road curvature will decrease the effective rolling radius while a negative curvature will increase this radius. The limit situation is a negative road curvature with a radius equal to the free radius of the tyre. In that case, the effective rolling radius is equal to the tyre free radius. Hence, we may derive the following formula for the effective rolling radius  $r_{e,curved}$  on a curved drum surface as function of the effective rolling radius on a flat road  $r_{e,flat}$ , the free radius of the tyre  $r_0$  and the curvature radius  $R_{road}$ :

$$r_{e,curved} = r_{e,flat} + (r_{e,flat} - r_0) \frac{r_0}{R_{road}} \quad (4.31)$$

where the radius of the road curvature  $R_{road}$  follows from:

$$1/R_{road} = d\beta/ds \quad (4.32)$$

This results in the change in effective rolling radius ( $r_{e,flat} = r_{e0}$ ):

$$\tilde{r}_{e,curved} = (r_{e0} - r_0) r_0 \frac{d\beta}{ds} \approx \frac{r_{e0} - r_0}{\Omega_0} \frac{d\beta}{dt} \quad (4.33)$$

We only have one experiment to validate expression (4.31): the difference between effective rolling radius of the tyre rotating on a flat road and on a drum with a positive curvature radius of 1.25 meter. Figure 4.24 shows the difference between the measured effective rolling radius on the drum and the flat road, and the difference according to expression (4.31). The difference between the

theoretical calculated radius and the measured radius is rather large, but we should realise that a 1 mm accuracy requires 0.3 % accuracy in the measurements.

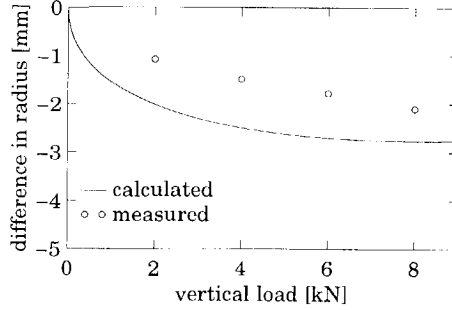


**Figure 4.24:** *The decrease in effective rolling radius of the tyre on a 2.5 meter drum with respect to the case on a flat road.*

### The influence of road plane angle

The third contribution to the effective rolling radius variation is the road plane angle itself. During the experiment we monitored the horizontal velocity  $V_x$  rather than the velocity  $V_T$  tangential to the effective road plane. The effective rolling radius  $r'_e$  is equal to the ratio between the tangential velocity  $V_T$  and rotational velocity  $\Omega$ :

$$r'_e = \frac{V_T}{\Omega} \quad (4.34)$$

During the cleat passage we monitored the horizontal velocity  $V_x$ . So, the ratio  $V_x$  and  $\Omega$  that we still define as the effective rolling radius now becomes slightly smaller than the value expected from (4.34):

$$r_{e,slope} = \frac{V_x}{\Omega} = \frac{V_T \cos \beta}{\Omega} = r'_e \cos \beta \quad (4.35)$$

So that we may write:

$$\tilde{r}_{e,slope} = r_{e0}(1 - \cos \beta) \quad (4.36)$$

### The influence of road plane height

The road plane height (and thus the vertical load) is the last contribution to the effective rolling radius variations considered. As depicted in Figure 4.23 the effective rolling radius decreases with the vertical load. This influence is represented by the coefficient  $\eta$  ( $<0$ ). The variation in the effective rolling radius  $\tilde{r}_{e,\eta}$  is equal to the coefficient  $\eta$  multiplied by the variation in normal force  $\tilde{F}_{cN}$ . If the axle position is fixed, the variation in the normal force is equal to the effective road plane height  $w$  with respect to the original condition multiplied by the vertical stiffness  $C_z$ :

$$\tilde{r}_{e,\eta} = \eta \tilde{F}_{cN} = \eta C_z \tilde{w} \quad (4.37)$$

### The total variation of effective rolling radius

Expression (4.24) is now formed by adding the different effects (*cf.* Eqs 4.29, 4.33, 4.36 and 4.37):

$$\tilde{r}_e = \tilde{r}_{e,rot} + \tilde{r}_{e,curved} + \tilde{r}_{e,slope} + \tilde{r}_{e,\eta} \quad (4.38a)$$

The variation of the effective rolling radius due to the vertical load variations ( $\tilde{r}_{e,\eta}$ ) will be included in the rigid ring tyre model (*cf.* Section 7.3). Consequently, the effective rolling radius variations without this contribution will be used as input to the rigid ring model. The effective rolling radius variations  $\tilde{r}_{ec}$  resulting only from the contact between tyre and road on uneven roads reads:

$$\tilde{r}_{ec} = \tilde{r}_{e,rot} + \tilde{r}_{e,curved} + \tilde{r}_{e,slope} \quad (4.38b)$$

## 4.8 Definition of a geometric filter

The key factors for establishing the effective inputs are the basic functions. To obtain these basic functions for a general road geometry a more general approach is introduced in this section.

Section 4.6 presented the effective inputs representing the enveloping properties of the tyre rolling over short wavelength obstacles. These effective inputs depend on the average vertical load and obstacle shape and could be decomposed into two shifted basic functions (*cf.* Figures 4.15 and 4.16). Figure 4.25 presents a model of the tyre-road interface showing the two mechanisms which contribute to the enveloping properties of tyres. First, the obstacle shape is



rounded and broadened owing to the finite radius of the tyre. The resulting characteristic is called the basic curve or basic function. Second, the front edge and the rear edge of the contact patch moves over this smoothed surface.

The effective plane height is obtained from the average height of the basic function at the edges of the contact patch. The effective plane angle is obtained from the difference between the basic functions at both edges. This approach can only produce the ‘non-linear’ effective plane angle (cf. Eq 4.22a and 4.23a). The effective rolling radius variations can be obtained from the other two effective inputs (cf. expression 4.24).

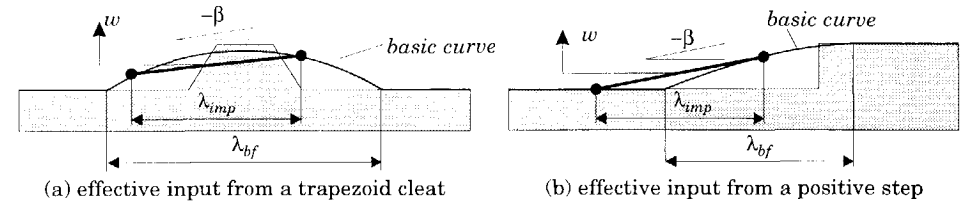


**Figure 4.25:** The tyre-road interface model of a tyre rolling over obstacles.

Figure 4.26 shows that the shapes of the basic functions are very similar to the response of the motion of the centre of a rigid wheel rolling over the obstacle. Obviously, the height of the basic functions and the rigid wheel responses when rolling over the step changes are equal to the height of the step. An obvious difference is the offset of the basic function with respect to the rigid wheel response.

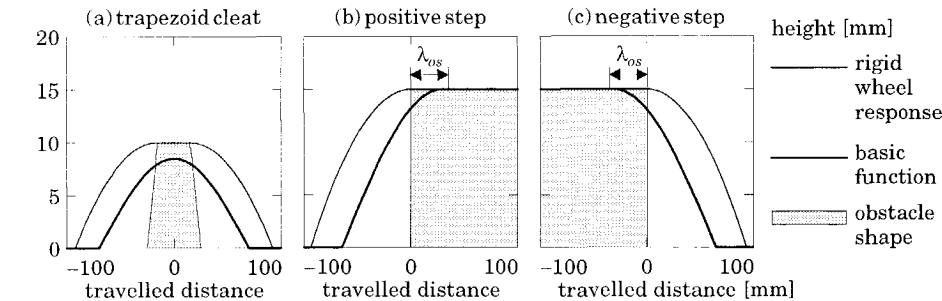


**Figure 4.26:** Comparison of the basic functions with the responses of a rigid wheel rolling over the obstacles.

Lippmann [61,62] showed that the geometry of any road surface may be decomposed into a series of step changes. The total quasi-static response to such

a road surface can be obtained from the quasi-static responses to a step input. Figure 4.26a shows that this idea also holds for establishing the basic functions: the basic function of the trapezoid cleat can be composed of the basic functions of the step changes. The offsets of the basic functions of the positive and negative step is so large that the height of the basic function of the trapezoid cleat is lower than height of the cleat itself. If the trapezoid obstacle is longer (probably longer than 50 mm) the basic function will be as high as the height of the cleat.

Sections 4.5 and 4.6 showed that the flexible ring model gives an accurate representation of the enveloping properties of the tyre rolling over obstacles at constant axle height. Accordingly, we will use the flexible ring model to study the influence of the obstacle shape. If the tyre rolls at constant axle height over a step change in road elevation the vertical load increase depends on the height of the step. Unfortunately, this change in vertical load will influence the contact length, and thus the enveloping properties, since the contact length plays a key role in the shift of the basic functions. Therefore, the simulations will be performed at constant vertical load rather than constant axle height and the effective plane height (for constant  $F_z$ ) is defined as the vertical motion of the wheel needed to keep the vertical load constant.

Figures 4.27, 4.28 and 4.29 show the properties of the basic functions of the tyre rolling at three constant vertical loads as a function of the height of the step change in road elevation. These basic functions were obtained from the simulated quasi-static responses using the flexible ring model. Figure 4.27 shows the width  $\lambda_{bf}$  of the basic functions. The values of the width are compared with the width of the response of a rigid wheel. This width can be easily calculated from the tyre radius and the height of the obstacle. The figure shows a reasonable match between the width of the basic functions and the width of the rigid wheel response. Figure 4.28 shows the shift  $\lambda_{imp}$  of the basic functions. This figure shows that the shift is approximately independent of the height of the obstacle and approximately equal to 80% of the contact length  $2a$ .

The Figures 4.27 and 4.28 show that the shift  $\lambda_{imp}$  of the basic functions is dependent on the vertical load but is independent of the step height. Conversely, the width  $\lambda_{bf}$  of the basic functions is less dependent on the vertical load but is obviously dependent on the step height. Figure 4.29 shows the offset  $\lambda_{os}$  of the basic functions. The influence of the vertical load on the offset turns out to be relatively small.

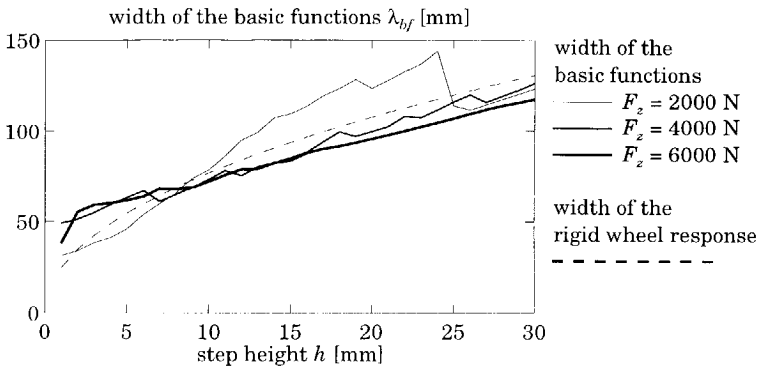


Figure 4.27: The width of the basic functions.

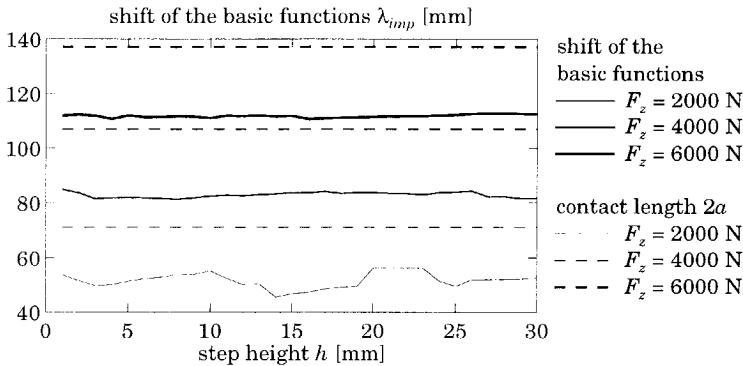


Figure 4.28: The shift of the basic functions.

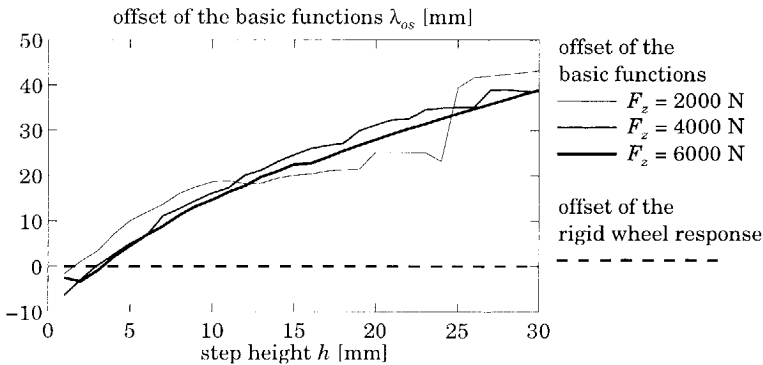


Figure 4.29: The offset of the basic functions.

The analysis presented in this section shows that roughly the basic functions depend only on the road geometry. The basic functions are very similar to the motion response of a rigid wheel (= tyre at  $F_z=0$ ). Special attention must be paid to the representation of the offset of the basic functions with respect to the response of the rigid wheel. Furthermore, the superposition of the response to a series of step changes should be studied in more detail as well.

The obtained basic functions of the given road geometry may be applied in a dynamic simulation model. The effective excitation of this model can be obtained by rolling a two-point contact model over the basic functions. The distance between the two points is approximately 80% of the contact length and varies with the vertical load.

# 5

## Physical Transient Tyre Model

---

### 5.1 Introduction

In Chapter 4 a brush model was used as the tyre-road interface of the flexible ring model. In this chapter a brush model is considered again, but now for the study of the transient tyre behaviour. This model will be called *physical* tyre model as it is based on the modelling of the tread in the contact patch as a number of individual elements. The results of the research presented in this chapter are applied in the next chapter where the *pragmatic* tyre model, which is based on the relaxation length concept, will be developed. The research presented in this chapter and the following chapter can be regarded as the first steps in the development of the dynamic tyre model. In this phase the dynamic (inertial) forces are considered small and will be neglected. However, the slip behaviour at low velocity and short wavelength variations of slip and vertical load are still included.

It is well known that the force response of the tyre to various external inputs is delayed. This phenomenon is typically characterised by the relaxation length of the tyre. But, short wavelength wheel oscillations and road irregularities require more detailed contact line considerations [58,87]. This short wavelength condition implies the consideration of varying slip within a single passage through the

contact length. One way to model the variation of slip is to consider the tread as a finite number of elements. However, for linear modelling where no sliding occurs and where the variations in the input quantities are small, an analytical approach is preferable.

Sections 5.2 and 5.3 present the analytically obtained Frequency Response Functions (FRFs) of the brush model: the FRFs to small variations of slip are presented in Section 5.2; and the FRFs to small variations of vertical load at constant slip are presented in Section 5.3. It should be noted that the brush model governs the transient behaviour due to the finite contact length only. Therefore, the longitudinal compliance of the carcass to which the tread elements are attached will be introduced. This model with carcass compliance will show an adequate transient response of the complete tyre.

Section 5.4 presents a simulation model for large variations of slip. In this model the tread elements are modelled as individual elements which may slide or adhere to the road surface. This type of model is appropriate for time simulations as each element can be followed during a passage through the contact patch. In Chapter 6 the non-linear simulation model will be used as basis for the evaluation of the non-linear responses of the pragmatic tyre models.

## 5.2 Analytical response to small variations of slip

This section presents the analytical derivation of the frequency response function of a brush model to small variations of slip. This approach uses the deformation of a single tread element as a function of time and position in the contact patch. The FRF is obtained by integrating the deformation over the entire contact patch and transforming the results into the Laplace domain. The assumptions in the model development are:

- constant coefficient of friction.
- rectangular contact patch.
- small variations of slip allowing linearisation of the resulting equations.

### The response of the contact model only

Figure 5.1 shows the side view of a tyre during varying braking. The situation depicted in Figure 5.1 is rather similar to the situation depicted in Figure 3.3. The difference between these figures is that in this chapter the tyre response to varying slip is considered while in Chapter 3 the tyre forces at constant slip are

considered. The longitudinal slip velocity  $V_{c,sx}$  in the contact patch is defined as the difference in the forward velocity in the contact patch  $V_{cx}$  and the rolling velocity in the contact patch  $V_{cr}$ :

$$V_{c,sx} = V_{cx} - V_{cr} \quad (5.1)$$

This definition is similar to the definition of the slip velocity  $V_{sx}$  based on the velocity of the wheel rim (Eq. 3.2), the additional subscript  $c$  in Equation (5.1) is used to denote that this slip velocity is based on the velocities in the contact zone. The longitudinal slip  $\kappa_c$  and theoretical slip  $\zeta_{cx}$  based on the velocities in the contact zone are defined:

$$\kappa_c = -\frac{V_{c,sx}}{V_{cx}} \quad , \quad \zeta_{cx} = -\frac{V_{c,sx}}{V_{cr}} \quad (5.2)$$

For steady-state conditions, the longitudinal deformation of the tread elements  $u$  is proportional to the position  $s$  of the element in the contact patch:

$$u(s) = -(a-s) \frac{V_{c,sx}}{V_{cr}} \quad (5.3)$$

In the case of vanishing sliding, which will occur at infinitely small slip, expression (5.3) holds for the entire region of contact.

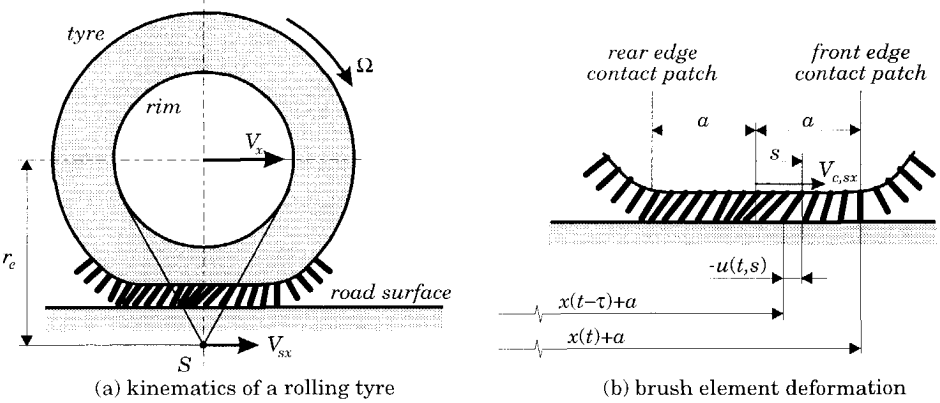


**Figure 5.1:** Side view of a tyre during braking, (a) the kinematics of the rolling tyre and (b) the deformation of the tread elements.

In the case of time varying braking, the deformation  $u$  of the tread elements depends on both the time  $t$  and the position  $s$  of the element in the contact area. The position of an element in the contact patch reads:

$$a - s = \int_{t-\tau}^t V_{cr} dt' \quad (5.4)$$

During the interval  $\tau$  the tread element under consideration has been deformed. This deformation  $u$  equals the integral of the slip velocity over the time interval  $\tau$ :

$$u(t, \tau) = - \int_{t-\tau}^t V_{c,sx} dt' \quad (5.5)$$

Integrating the deformation along the entire contact length and multiplying the result by the tread stiffness per unit of length  $c_{cp}$  gives the longitudinal force in the contact patch  $F_{cx}(t)$ :

$$F_{cx}(t) = c_{cp} \int_{s=-a}^{+a} u(t, s) ds \quad (5.6)$$

To solve the integral above, we have to express the tread element deformation  $u$  (Eq. 5.5) as a function of time  $t$  and position  $s$ . For this the time  $\tau$  has to be solved from Equation (5.4). To simplify the analysis a linearisation is applied: the variables are written as small variations (denoted by a tilde) on top of constant values (denoted by an additional subscript 0)

$$\text{longitudinal force } F_{cx} = F_{cx0} + \tilde{F}_{cx} \quad (5.7a)$$

$$\text{forward velocity } V_{cx} = V_{cx0} + \tilde{V}_{cx} \quad (5.7b)$$

$$\text{rolling velocity } V_{cr} = V_{cr0} + \tilde{V}_{cr} \quad (5.7c)$$

$$\text{slip velocity } V_{c,sx} = V_{c,sx0} + \tilde{V}_{c,sx} \quad (5.7d)$$

$$\text{time interval } \tau = \tau_0 + \tilde{\tau} \quad (5.7e)$$

We furthermore assume that the average slip is zero:

$$V_{c,sx0} = 0, \quad V_{cx0} = V_{cr0}, \quad F_{cx0} = 0 \quad (5.8)$$

Now, the linearised expression of the time interval reads:

$$\tau_0 = \frac{a - s}{V_{cr0}} \quad (5.9)$$

And the variations in the longitudinal force can be expressed as:



$$\tilde{F}_{cx}(t) = c_{cp} \int_{s=-a}^{+a} u(t,s) ds = -c_{cp} \int_{s=-a}^{+a} \int_{t-(a-s)/V_{cr0}}^t \tilde{V}_{c,sx}(t') dt' ds \quad (5.10)$$

This equation may be solved by transforming it to the *Laplace* domain:

$$\tilde{F}_{cx}(p) = -c_{cp} \int_{s=-a}^{+a} \frac{1}{p} \left(1 - e^{-p(a-s)/V_{cr0}}\right) \tilde{V}_{c,sx}(p) ds \quad (5.11)$$

where  $p$  is the *Laplace* variable. The following basic *Laplace* transformations have been used in the transformation of Equation (5.10):

$$\mathcal{L}\{y(t-\tau) - y(t)\} = (e^{-p\tau} - 1)Y(p), \quad \mathcal{L}\left\{\int y(t)\right\} = \frac{1}{p}Y(p) \quad (5.12)$$

Solving the integral of equation (5.11) leads to:

$$\tilde{F}_{cx}(p) = 2c_{cp}a \left( -\frac{1}{p} + \frac{V_{cr0}}{2a p^2} \left(1 - e^{-p2a/V_{cr0}}\right) \right) \tilde{V}_{c,sx}(p) \quad (5.13)$$

The frequency response function is obtained by dividing the left and right members by the slip velocity and replacing the *Laplace* variable  $p$  by  $j\omega$ :

$$H_{F_{cx}, V_{c,sx}}(\omega) = 2c_{cp}a \left\{ \frac{-1}{j\omega} + \frac{e^{-j\omega 2a/V_{cr0}} - 1}{\omega^2 2a/V_{cr0}} \right\} \quad (5.14)$$

The transient behaviour of the tyre depends on the travelled distance rather than on the time. Therefore, the road frequency  $\omega_s$  is introduced:

$$\omega_s = \frac{\omega}{V_{cx0}} \quad (5.15)$$

Note that the average forward velocity is assumed to be equal to the average rolling velocity (Eq. 5.8). The frequency response function reads as a function of road or spatial frequency  $\omega_s$ :

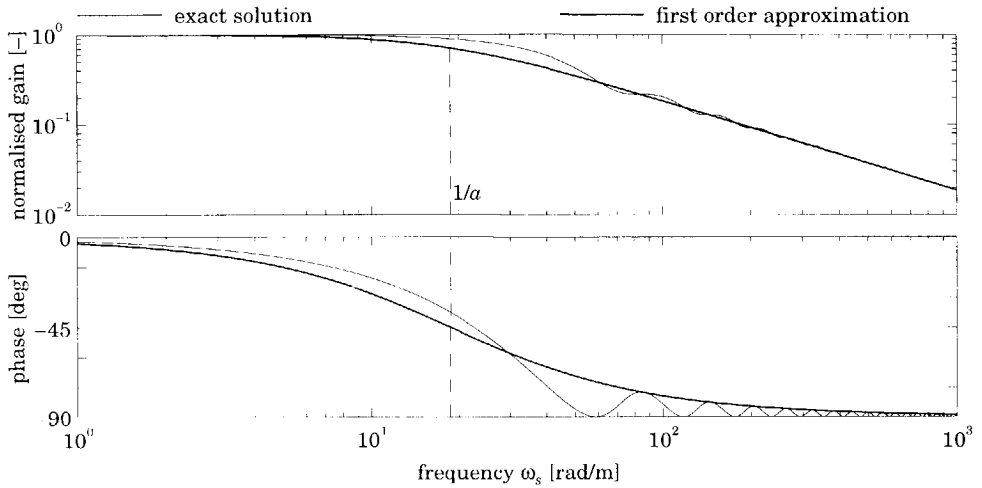
$$H_{F_{cx}, V_{c,sx}}(\omega_s) = \frac{2c_{cp}a^2}{V_{r0}} \left\{ \frac{-1}{j\omega_s a} + \frac{e^{-j2\omega_s a} - 1}{2\omega_s^2 a^2} \right\} \quad (5.16)$$

Figure 5.2 shows the exact Frequency Response Function (FRF) of the contact model to slip variations. This FRF is normalised by dividing the expression (5.16) by  $-V_{r0}/c_{cp}a^2$ . The parameters used are presented in Table 5.1 at the end of the present chapter. Owing to the time delay, the analytically obtained FRF is not suitable for some of the standard linear analysis techniques. The standard approach for approximating a time delay is by a finite number of first order systems in series. In this case it was found that the frequency response function

of the contact model (5.14) could be approximated by a single first order system, with a time constant  $a/V_{r0}$  and a gain of  $2c_c a^2/V_{r0}$ . The approximated frequency response function reads as function of the road frequency:

$$H_{F_{cx}, V_{c,xy}}(\omega_s) \approx \frac{2c_{cp}a^2}{V_{r0}} \cdot \frac{-1}{1 + j\omega_s a} \quad (5.17)$$

Apparently, the contact patch relaxation length (= space constant) takes the value  $a$  denoting half the contact length. The approximation approaches the exact values at both  $\omega \rightarrow 0$  and  $\omega \rightarrow \infty$ . The normalised frequency response function of the approximation of the contact model is presented in Figure 5.2 as well.



**Figure 5.2:** *The normalised longitudinal force frequency response function of the contact model to slip variations.*

Figure 5.3a shows the impulse response of both contact models in the travelled distance domain. The impulse responses were obtained by inverse *Fourier* transformation of Equations (5.16) and (5.17) and normalised by dividing by the factor  $-V_{r0}/c_{cp}a^2$ . Immediately after a slip impulse, all tread elements are deformed equally. During rolling of the tyre new undeformed elements enter the contact patch and deformed elements leave the contact patch. Finally at a travelled distance of  $2a$  after the impulse, all deformed tread elements are replaced by undeformed ones. The slip impulse response of the approximation is exponentially decaying. Figure 5.3b presents the step responses which were obtained by integrating the impulse responses.

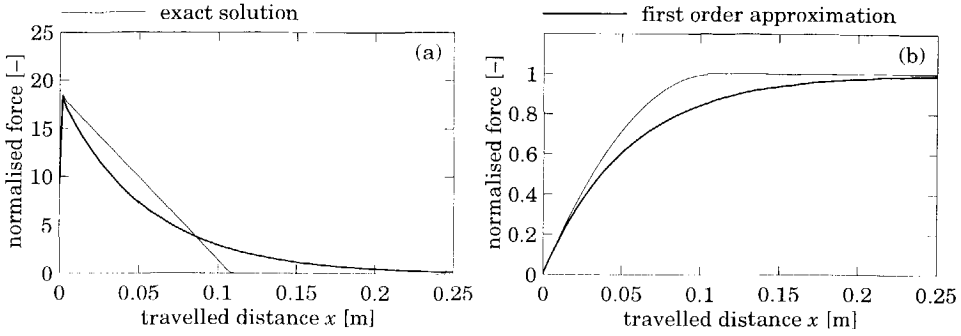


**Figure 5.3:** The normalised response to a change in slip velocity of the longitudinal force of the contact model in the distance domain: (a) impulse response and (b) step response.

### The response of the contact models with carcass flexibility

The carcass flexibility is modelled as a longitudinal spring with stiffness  $C_x$  in series with either of the two contact models as shown in Figure 5.4. The slip velocity in the contact patch  $V_{c,sx}$  equals the wheel slip velocity  $V_{sx}$  plus the rate of change of the carcass deformation:

$$V_{c,sx} = V_{sx} + \frac{1}{C_x} \frac{dF_x}{dt} \quad (5.18)$$

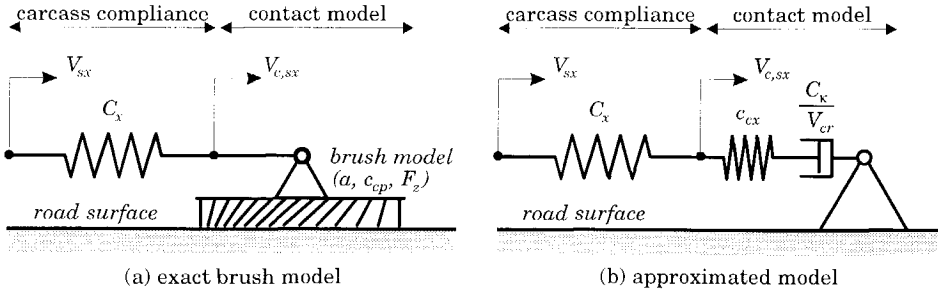


**Figure 5.4:** The carcass compliance in series with both contact models.

Although the models of Figure 5.4 can be used to calculate the frequency response function directly, we will use the calculated frequency response functions of the contact models (Eq. 5.16 and 5.17) to eliminate the slip velocity in the contact patch  $V_{c,sx}$ . Figure 5.5 presents the resulting block diagram. This approach is advantageous also for more complex systems.

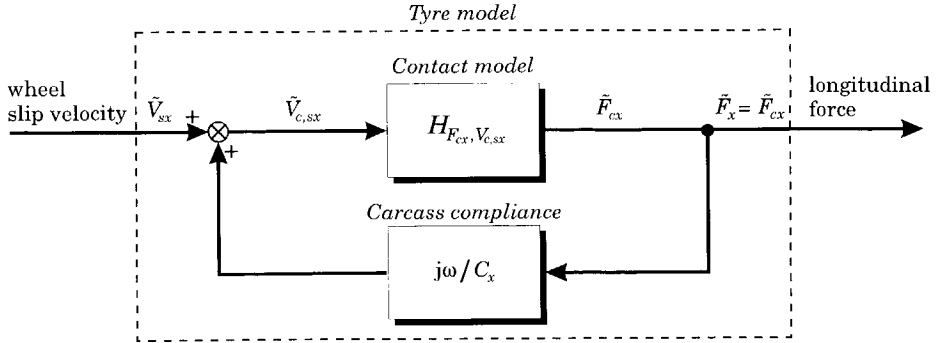


**Figure 5.5:** Block diagram of the tyre response to wheel slip variations including the effect of carcass compliance.

Figure 5.6 shows the frequency response function of both the exact and the approximate slip models in series with the longitudinal carcass spring. Clearly, the first order system in combination with the soft carcass approximates the exact response much better. It can be seen that the contact model in series with the carcass spring shows a smaller cut-off frequency, indicated by  $1/\sigma$ . Obviously, the relatively large oscillations of the exact FRF of the contact model (Figure 5.2) are filtered by the carcass flexibility.

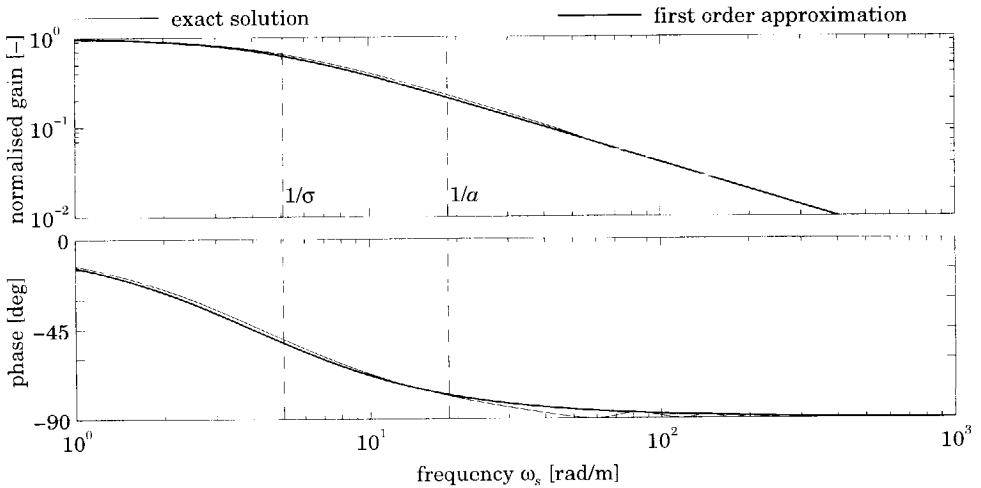


**Figure 5.6:** The normalised longitudinal force frequency response function of the overall transient tyre model to wheel slip variations.

Figure 5.4b shows the carcass spring in series with the approximated model. As indicated in the figure, the frequency response function of this approximation (Eq. 5.17) may be accomplished by a spring and damper in series: the value of the damper coefficient equals the slip stiffness divided by the velocity; and the value of the stiffness equals the total tread element stiffness  $c_{cx}=2ac_{cp}$ . In the subsequent chapters the approximated model will be called the *relaxation length* model, as its primary property is the relaxation length. The relaxation length  $\sigma_{c0}$  of the contact model at full adhesion equals half the contact length  $a$ .

The carcass spring in series with the relaxation length contact model will decrease the total longitudinal stiffness  $C_{x,tot}$  of the model:

$$\frac{1}{C_{x,tot}} = \frac{1}{C_x} + \frac{1}{c_{cx}} \quad (5.19)$$

Accordingly, the relaxation length of the relaxation length contact model plus the soft carcass will become much larger:

$$\sigma_0 = \frac{C_{k0}}{C_{x,tot}} = \frac{C_{k0}}{C_x} + a \quad (5.20)$$

where  $\sigma_0$  denotes the relaxation length of the tyre (carcass + contact model), and  $C_{k0}$  denotes the slip stiffness at free rolling.

Figure 5.7 presents the impulse and step responses of the contact models with carcass compliance. The soft carcass increases the response length, and decreases the differences between the exact solution according to the brush model and the approximation with the first order model.

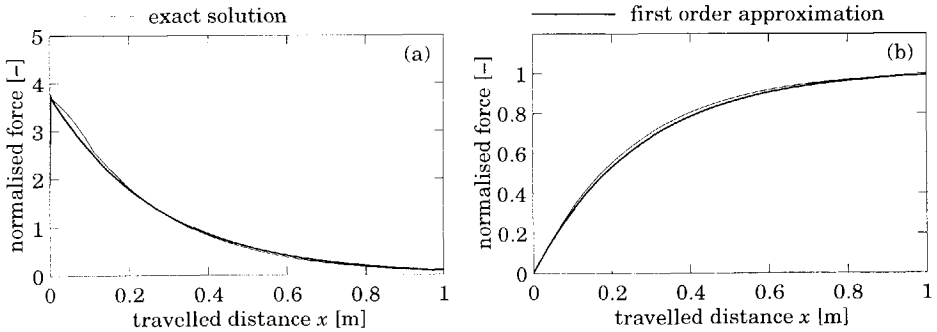


**Figure 5.7:** The normalised response to a change in slip velocity of the longitudinal force of the overall transient model in the distance domain: (a) impulse response and (b) step response.

### 5.3 Analytical response to small variations of vertical load

#### The response of the contact model only

The brush model is used again to study the non-stationary response of a tyre at a constant brake slip velocity to a varying vertical force. For the sake of simplicity, only small values of longitudinal slip are considered. Consequently, all brush elements in the contact zone adhere to the road surface.

The varying vertical force directly affects the contact length (cf. Eq 2.5). Only small variations in vertical load are assumed. Thus we may write half the contact  $a$  as a small variation  $\tilde{a}(x)$  on top of the stationary value  $a_0$ :

$$a = a_0 + \tilde{a}(x) \quad (5.21)$$

The contact length  $a$  may be written as a function of the travelled distance  $x(t)$  rather than as a function of the time  $t$ , because in this analysis the forward velocity  $V_{cx0}$  is assumed to be constant. The deformation  $u$  of a tread element is then proportional to the time it has spent in the contact patch.

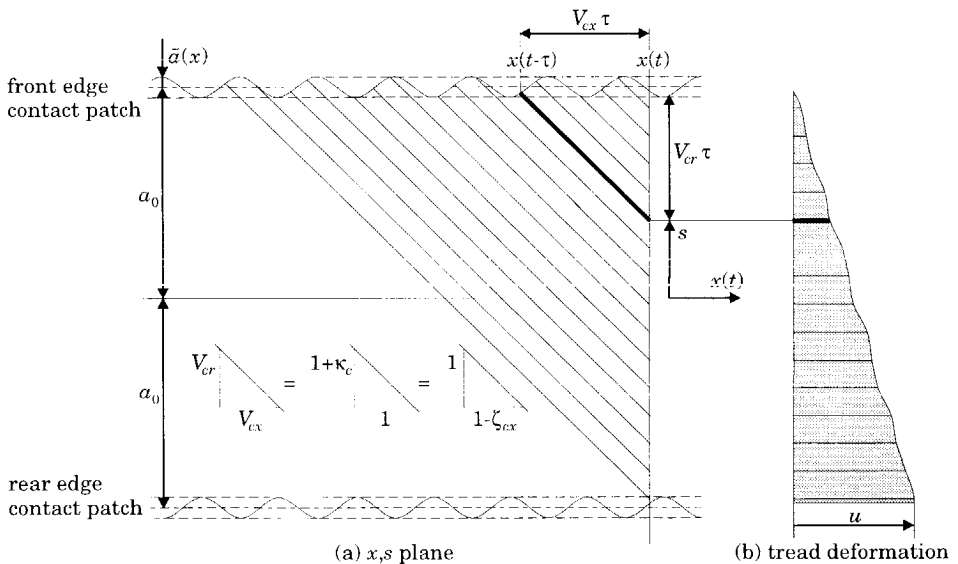


**Figure 5.8:** *The brush element deformation as function of travelled distance and position in contact patch.*

A travelled distance ( $x$ ) versus brush position ( $s$ ) diagram is most suitable to study the influence of varying contact length on the longitudinal force. For a

certain distance travelled  $x(t)$  the longitudinal deformation  $u$  has been depicted as a function of the position coordinate  $s$  in Figure 5.8.

The brush element at time  $t$  and position  $s$ , started at the front edge of the contact patch at time  $t-\tau$ . The positions of this element during the interval  $\tau$  have been indicated by the bold line. The longitudinal deformation  $u$  can be expressed as a function of the travelled distance  $x(t)$  or as a function of the position  $s$  in the contact patch:

$$u(x, \tau) = (x(t) - x(t - \tau)) \frac{\zeta_{cx}}{1 - \zeta_{cx}} \quad (5.22a)$$

$$u(x, \tau) = (a(x(t - \tau)) - s) \zeta_{cx} \quad (5.22b)$$

To calculate the tread deformation it is necessary to solve the time interval  $\tau$  from Equations (5.22). This time interval will be linearised (*cf.* Eq. 5.7e). The interval  $\tau_0$  due to constant slip and constant contact length  $a_0$  is equal to:

$$\tau_0 = \frac{(a_0 - s)}{V_{cr0}} \quad (5.23)$$

The small variations  $\tilde{\tau}$  in the time interval due to the contact length variations cannot be neglected. A new small variable  $\xi$  is introduced which is equal to the travelled distance in the interval  $\tilde{\tau}$ :

$$\xi = V_x \tilde{\tau} \quad (5.24)$$

Furthermore, we rewrite the displacement  $x$  at time  $t-\tau_0$  as function of the displacement at  $t$  and the position in the contact patch  $s$ :

$$x(t - \tau_0) = x(t) - \tau_0 V_{cx} = x(t) - \frac{(a_0 - s)}{V_{cr0}} V_{cx} = x(t) - (a_0 - s)(1 - \zeta_{cx}) \quad (5.25)$$

Now, the tread deformations can be expressed as:

$$u(x, \tau) = (V_{cx} \tau_0 + \xi) \frac{\zeta_{cx}}{1 - \zeta_{cx}} \quad (5.26a)$$

$$u(x, \tau) = (a(x(t - \tau_0) - \xi) - s) \zeta_{cx} \quad (5.26b)$$

Rather than solving  $\tau$  from Equations (5.22), the distance  $\xi$  will be solved from Equations (5.26). If  $\tilde{a}(x)$  is small, the distance  $\xi$  is also small. Hence, we may expand Equation (5.26b) into a Taylor series. Furthermore, Equation (5.25) is substituted, and the contact length is linearised in  $\xi$ :

$$a(x(t - \tau_0) - \xi) \approx a_0 + \tilde{a}(x(t) - (a_0 - s)(1 - \zeta_{cx})) - \xi \tilde{a}'(x(t) - (a_0 - s)(1 - \zeta_{cx})) \quad (5.27)$$

Where  $\tilde{a}'(x)$  is the derivative of the contact length variation  $\tilde{a}(x)$  with respect to the travelled distance  $x$ . The distance  $\xi$  can be solved by substituting Expression (5.27) into (5.26):

$$(V_{cx}\tau_0 + \xi) \frac{1}{1 - \zeta_{cx}} = a_0 + \tilde{a}(x(t) - (a_0 - s)(1 - \zeta_{cx})) - \xi \tilde{a}'(x(t) - (a_0 - s)(1 - \zeta_{cx})) - s \quad (5.28)$$

Rewriting and linearising gives:

$$\xi \approx (1 - \zeta_{cx}) \tilde{a}(x(t) - (a_0 - s)(1 - \zeta_{cx})) \quad (5.29)$$

Integrating the tread deformation, obtained by substituting Expression (5.29) into (5.26b), over the contact length and multiplying by the tread element stiffness per unit of length  $c_{cp}$  gives the longitudinal force  $F_{cx}$ :

$$F_{cx} = \int_{s=-a-\tilde{a}(x)}^{a+\tilde{a}(x)} c_{cp} u(t, s) ds = c_{cp} \zeta_{cx} \int_{s=-a-\tilde{a}(x)}^{a+\tilde{a}(x)} (a_0 - s + \tilde{a}(x(t) + (s - a_0)(1 - \zeta_{cx}))) ds \quad (5.30)$$

Solving the integral gives:

$$F_{cx} = c_{cp} \zeta_{cx} \left[ a_0 s - s^2 + \frac{1}{(1 - \zeta_{cx})} \tilde{A}(x(t) + (s - a_0)(1 - \zeta_{cx})) \right]_{s=-a_0-\tilde{a}(x)}^{s=a_0+\tilde{a}(x)} \quad (5.31)$$

Introduced is  $\tilde{A}(x)$ , which is integral of  $\tilde{a}(x)$  with respect to the travelled distance:

$$\tilde{A}(x) = \int \tilde{a}(x) dx \quad (5.32)$$

We furthermore simplify:

$$\tilde{A}(x + \tilde{a}(x)) \approx \tilde{A}(x) + \tilde{a}(x) \cdot \tilde{a}(x) \approx \tilde{A}(x) \quad (5.33a)$$

$$\tilde{A}(x - 2\tilde{a}_0 - \tilde{a}(x)) \approx \tilde{A}(x - 2\tilde{a}_0) - \tilde{a}(x) \quad \tilde{a}(x) \approx \tilde{A}(x - 2\tilde{a}_0) \quad (5.33b)$$

Substituting the integration limits in (5.31) yields the force  $F_x$  which includes both the stationary part:

$$F_{cx0} = 2c_{cp} a_0^2 \zeta_{cx} \quad (5.34)$$

and the variations due to contact length variations:

$$\tilde{F}_{cx} = 2a_0 c_{cp} \tilde{a}(x) \zeta_{cx} + \frac{1}{(1 - \zeta_{cx})} c_{cp} \zeta_{cx} (\tilde{A}(x) - \tilde{A}(x - (1 - \zeta_{cx}) 2a_0)) \quad (5.35)$$

Transforming the equation above into the *Laplace* domain gives the response function. This function can be expressed as function of the path frequency  $\omega_s$  or as function of the (time) frequency  $\omega$ :



$$H_{F_{cx},a} = \frac{\tilde{F}_x}{\tilde{a}} = 2a_0 c_{px} \zeta_{cx} \left( 1 + \frac{1 - e^{-j\omega_s 2a_0(1-\zeta_{cx})}}{2j\omega_s a_0(1-\zeta_{cx})} \right) = 2a_0 c_{px} \zeta_{cx} \left( 1 + \frac{1 - e^{-2j\omega a_0/V_{cr0}}}{2j\omega a_0/V_{cr0}} \right) \quad (5.36)$$

Or,

$$H_{F_{cx},a} = \frac{\tilde{F}_x}{\tilde{a}} = \frac{F_{x0}}{a_0} \left( 1 + \frac{1 - e^{-2j\omega a_0/V_{cr0}}}{2j\omega a_0/V_{cr0}} \right) \quad (5.37)$$

Figure 5.9 presents the exact FRF according to Equation (5.36). In contrast to the FRF to slip variations, the exact FRF to contact length variations approaches 0.5 at infinitely high frequencies rather than zero. The exact solution may be approximated again by a first order system with a relaxation length  $a$ . This approximated model which is similar to Equation (5.17) represents the exact solution reasonably well until the cut-off frequency. At higher frequencies, the first order approximation deviates strongly from the exact solution. Although a more accurate approximation can be achieved, the first order system will be used because it is thought to be advantageous to use an approximation for the vertical force variations that is similar to that used for slip variations.

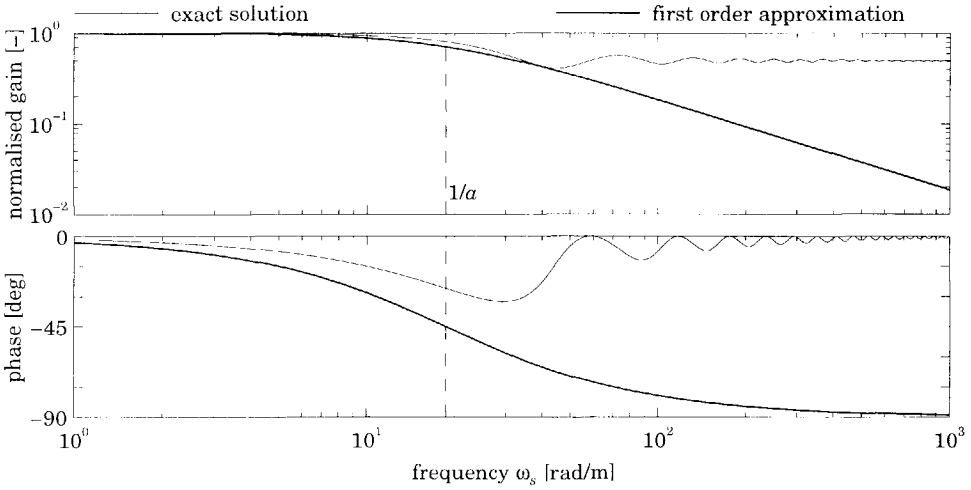


**Figure 5.9:** *The normalised longitudinal force frequency response of the brush model to vertical force variations.*

The step and impulse responses to contact length variations are presented in Figure 5.10. The responses of the approximation follow an exponential function. The response derived from the exact solution is rather different. After a very

small step-increase in contact length (Figure 5.10b), the tread element at the rear edge will remain slightly longer in the contact patch, resulting in a step increase in the longitudinal force with a normalised magnitude of 0.5. This result is in agreement with the FRF in which the normalised gain equals 0.5 at  $(\omega \rightarrow \infty)$ . New elements will enter the contact patch slightly earlier, due to the step increase in contact length. Therefore, these new elements will also have a slightly larger deformation. After the tyre has rolled over a distance of  $2a$  a new stationary situation is reached as the deformations of all tread elements are based on the new contact length.

The impulse response is similar to the step response. During the impulse (we assume full adhesion) the contact length is slightly larger and the force will be larger as well. After the impulse only the tread element which was at the front edge during the impulse has obtained a slightly larger deformation, because it entered the contact patch slightly earlier. This tread element will leave the contact patch when the tyre has travelled a distance of  $2a$ .

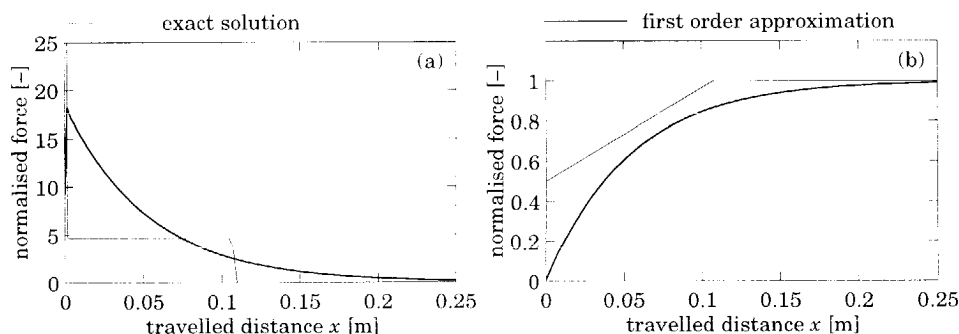


**Figure 5.10:** *The normalised response to a change in vertical load of the longitudinal force of the contact model in the distance domain: (a) impulse response and (b) step response.*

### The response of the contact models with carcass flexibility

As already introduced in Figure 5.4, the carcass flexibility is modelled as a longitudinal spring with stiffness  $C_x$  in series with a contact model. The variations in the longitudinal force will give additional carcass deformations, and thus additional slip velocity variations in the contact zone. In the analysis only small variations of the variables are assumed, allowing the contributions of both contact length variations and contact patch slip variations to be superposed:

$$\tilde{F}_{cx} = H_{F_{cx}, V_{c,sx}} \tilde{V}_{c,sx} + H_{F_{cx}, a} \frac{\partial a}{\partial F_z} \tilde{F}_{cz} \quad (5.38)$$

The equation of the carcass deflection (5.18) also holds if the wheel slip velocity  $\tilde{V}_{sx}$  is set equal to zero. Figure 5.11 presents the resulting block diagram. The variations in vertical load will generate contact length variations and thus longitudinal force variations. Additional slip velocities in the contact patch are generated through the feedback.

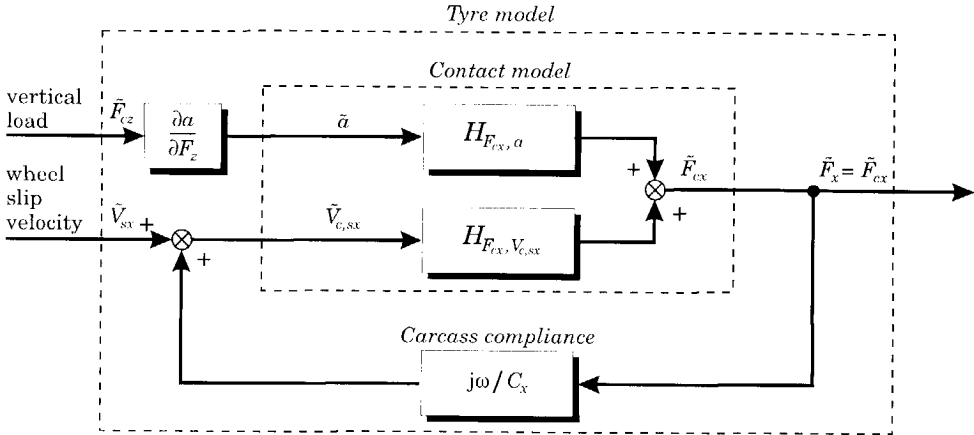


**Figure 5.11:** Block diagram of the tyre response to wheel slip variations and vertical load variations including the effect of carcass compliance.

The FRFs, impulse responses and step responses of the contact models with carcass compliance with respect to contact length variations are presented in Figures 5.12 and 5.13. Even though the differences in the frequency domain are rather large, the time response of the first order model approximates the time response of the exact solution rather well.

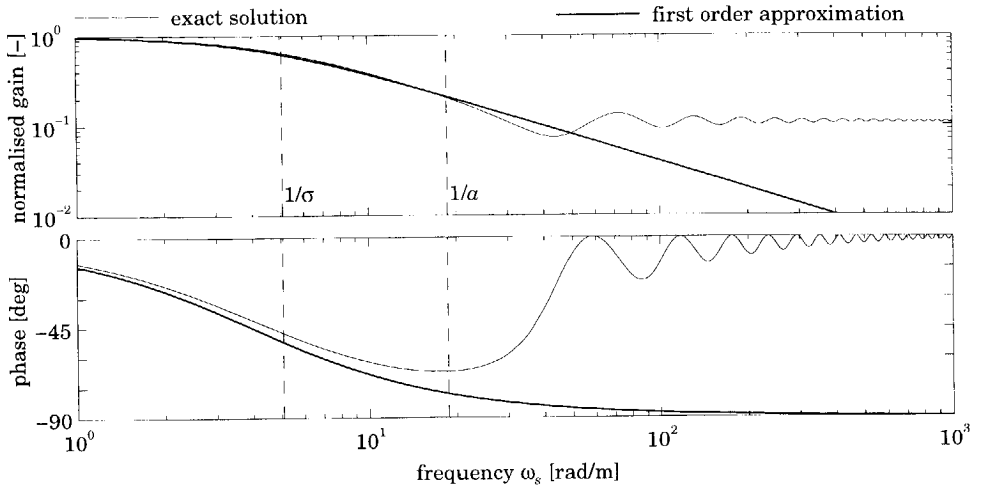


**Figure 5.12:** *The normalised longitudinal force frequency response functions of the brush model with carcass flexibility to vertical force variations.*

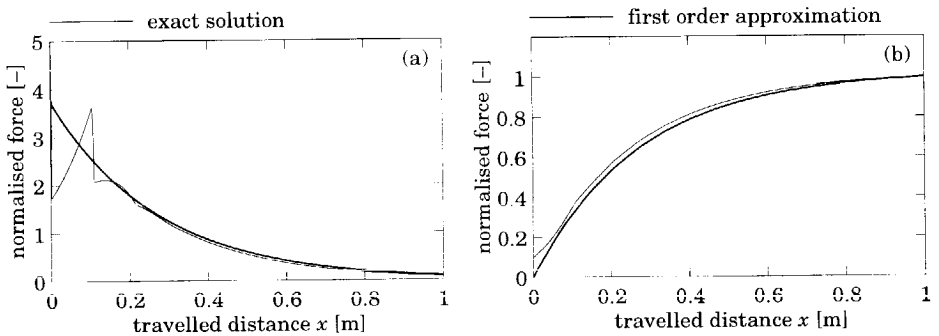


**Figure 5.13:** *The normalised response to a change in slip velocity of the longitudinal force of the overall transient model in the distance domain: (a) impulse response and (b) step response.*

## 5.4 Discretisation of the tread

The analytical response functions, derived in the previous sections, cannot be used to study the tyre response to large variations in the input quantities. Therefore, a simulation model will be developed to study these non-linear responses. The main reason why this discrete brush model was developed is that transient measurements were not available: it is very difficult not to excite tyre

dynamics during the measurements of longitudinal transient tyre responses. In Chapter 6, the responses of the discrete brush model are used for the development and validation of a pragmatic transient tyre model.

In the discrete brush model the tread elements are modelled as individual elastic elements radially attached to the tyre belt (*cf.* Figure 5.1). The tread elements are modelled as (massless) springs that can only deform in tangential direction. This deformation results from the slip velocity of the tyre in the contact zone. The maximum deformation of the tread elements is limited by the friction between the tyre and the road.

Oertel [77] discusses two approaches to develop such a simulation model: the continuum approach (Euler method), and the modelling of individual contact elements (Lagrange method). In the Euler description [13,77,121,122] the tread elements are considered to be fixed to the contact area. The deformation of the tread elements travels through the contact patch rather than the tread elements themselves. For this, the deformation is written as partial derivatives with respect to position and time. With this method the increase in the computation time is close to the square of the number of tread elements [121].

In the Lagrange description, the tread elements are modelled as a finite number of elements and they are followed during their passage through the contact patch. One approach is to model the tread elements on the entire tyre circumference. During rolling only those elements in contact with the road will generate forces. The disadvantage of this approach is that a large overhead is needed as nearly all elements are not in contact with the road. Nevertheless, this approach is rather popular in the application of finite element models [24,25,46,74,75,78] as the additional overhead needed to model the tread elements is relatively small. In Chapter 4 this approach was used to model the tyre-road interface of the flexible ring model.

In this section the Lagrange description is employed, but the tread elements are modelled in the contact patch only, thereby reducing the size of the model considerably. An element that leaves the contact patch at one side is redefined in the model so that it will enter the contact patch at the opposite side. After a new element has entered the contact patch, the elements are also renumbered so that element number one is always the first element in the contact patch.

### The discrete contact model for slip variations

In the discrete simulation model, the deformation of the tyre is considered only at discrete time intervals and discrete tread element positions in the contact patch. The number of tread elements is denoted by  $n$  and the pitch of the elements is denoted by  $\Delta e (= 2a/n)$ . During rolling over the time interval  $\Delta t$ , the position of the tread elements in the contact patch increases by  $\Delta s$ , and the deformation by  $\Delta u$ :

$$\Delta s = -V_r \Delta t \quad (5.39a)$$

$$\Delta u = -(V_x - V_r) \Delta t = -V_{sx} \Delta t \quad (5.39b)$$

During rolling, both the position  $s_i$  and the deformation  $u_i$  of the tread changes:

$$s_i(t + \Delta t) = s_i(t) + \Delta s \quad (5.40a)$$

$$u_i(t + \Delta t) = u_i(t) + \Delta u \quad (5.40b)$$

where the index  $i$  denotes the number of a specific tread element in the contact patch. During forward rolling the tread elements in the contact patch move to the rear edge and Equations (5.40) hold as long as all tread elements remain in the contact patch. When tread elements leave the contact patch will depend on the simulation time step, the number of tread elements and the rotational velocity.

Figure 5.14 shows the position of the elements in the contact patch schematically. For the sake of simplicity, a model with only 12 elements during stationary forward rolling and at a very small slip level has been depicted. In this case the tread deformation increases linearly from the front edge to the rear edge of the contact patch, resulting in the largest deformation for the last element.

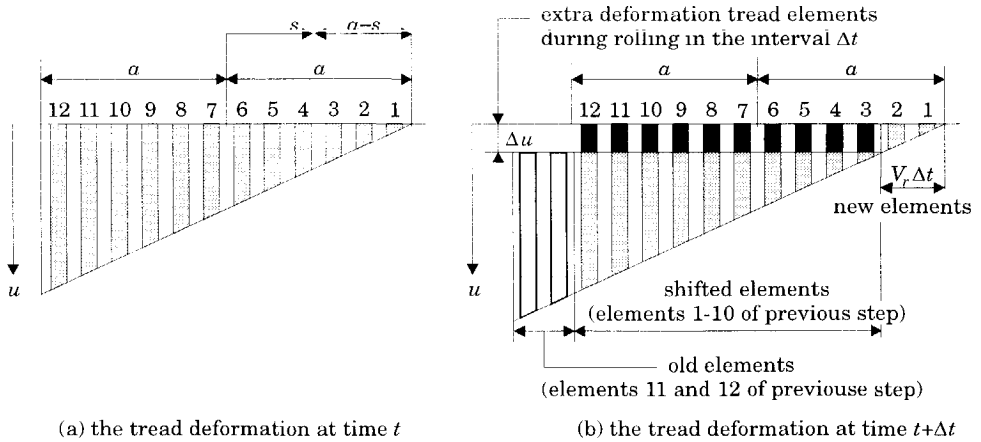


**Figure 5.14:** The tread element deformation during rolling over an interval  $\Delta t$ .

Figure 5.14b gives the situation after rolling a little further. In this case the tyre has rolled over a length of exactly two tread elements resulting in the elements 11 and 12 leaving the contact patch. At the front edge two new elements have entered the contact patch and elements 1-10 have travelled partially through the contact patch. Simultaneously, the deformation  $u$  of these elements increases with  $\Delta u$ .

In the simulation model the element numbering is defined to start at the front edge of the contact patch. This means that the elements have to be renumbered. Or, in other words, the index  $i$  of the elements has to shift. For example element 1 at  $t$  (Figure 5.14a) becomes element 3 at  $t+\Delta t$  (Figure 5.14b). If the shift in index is  $n_s$  then Equation (5.40) takes the form:

$$s_{i+n_s}(t+\Delta t) = s_i(t) + \Delta s \quad i = 1, 2, \dots, (n - n_s) \quad \wedge \quad (n_s \geq 0) \quad (5.41a)$$

$$u_{i+n_s}(t+\Delta t) = u_i(t) + \Delta u \quad i = 1, 2, \dots, (n - n_s) \quad \wedge \quad (n_s \geq 0) \quad (5.41b)$$

where  $n$  denotes the total number of tread elements in the contact patch. This equation gives the position and deformation of the elements which remain in the contact patch. If the tyre rolls forward,  $n_s$  new elements have entered the contact patch at the front edge. The position of these new elements  $s_i$  results from the fact that the tread elements are equally spaced. If constant velocities are assumed in the time interval  $\Delta t$  the deformation  $u_i$  of the new elements increases linearly with the positions  $s_i$ :

$$s_i(t+\Delta t) = s_1(t) + \Delta s - \Delta e(n_s + 1 - i) \quad i = 1, 2, \dots, n_s \quad \wedge \quad (n_s > 0) \quad (5.42a)$$

$$u_i(t+\Delta t) = \frac{\Delta u}{\Delta s}(s_i(t+\Delta t) - a) \quad i = 1, 2, \dots, n_s \quad \wedge \quad (n_s > 0) \quad (5.42b)$$

When the tyre rolls backwards ( $n_s$  is negative) the expressions for the position and the deformation (Eq. 5.41) hold but the index  $i$  of the elements which are involved in the shift change:

$$s_{i+n_s}(t+\Delta t) = s_i(t) + \Delta s \quad i = (1 - n_s), \dots, n \quad \wedge \quad (n_s < 0) \quad (5.43a)$$

$$u_{i+n_s}(t+\Delta t) = u_i(t) + \Delta u \quad i = (1 - n_s), \dots, n \quad \wedge \quad (n_s < 0) \quad (5.43b)$$

The deformation of the new elements which have entered the contact patch at the rear edge is given by:

$$s_i(t+\Delta t) = s_n(t) + \Delta s + \Delta e(n + n_s - i) \quad i = (n + n_s + 1), \dots, n \quad \wedge \quad (n_s < 0) \quad (5.44a)$$

$$u_i(t+\Delta t) = \frac{\Delta u}{\Delta s}(s_i(t+\Delta t) + a) \quad i = (n + n_s + 1), \dots, n \quad \wedge \quad (n_s < 0) \quad (5.44b)$$

Note that Equations (5.41) and (5.43) give the deformation of the elements which remain in the contact patch. The deformation of the new elements which enter the contact patch at either the front edge or the rear edge are represented by Equations (5.42) and (5.44).

### The discrete contact model for vertical load variations

To simulate the tyre response to vertical load variations, the contact pressure distribution changes. But even more important are the variations in the contact length. During a fast increase in vertical load we may have new elements entering both at the front and rear edges of the contact patch. Three possible solutions may be employed to vary the contact length of the simulation model:

- The pitch of the elements is kept constant and the number of tread elements depends on the contact length. This means that the size of the model has to vary during simulation.
- The number of tread elements in contact with the road is kept constant and the pitch of these elements varies with the contact length. Interpolation will be needed as the length and stiffness of the tread elements will vary during simulation.
- Both the number of elements and the pitch are kept constant. The length of the contact model is kept constant and set equal to the maximum expected contact length. Only a part of the elements of this model are in contact with the road. The deformation of the elements of the model outside the actual contact length is set to zero.

The last option is most feasible, even though this approach requires extra elements. Figure 5.15 shows a model which is longer than the actual contact length. The length of the simulation model is equal to the maximum expected contact length ( $2a_{max}$ ). During rolling in the time interval  $\Delta t$ , the tyre rolls over a distance  $V_r \Delta t$ . The increase in half the contact length  $\Delta a$  reads:

$$\Delta a = a(t + \Delta t) - a(t) \quad (5.45)$$

Again the situation presented in Figure 5.14a is used as initial state but the element numbering of this figure is not used. Now element 1 denotes the first element of the model rather than the first element in contact with the road. The total length of the new simulation model is longer than the contact length, see Figure 5.14a.

Figure 5.15 shows the situation after rolling over the interval  $\Delta t$ . During the interval, the contact length increases by  $2 \times 3$  elements and the tyre rolls over 2



elements. These two effects result in five new elements at the front edge and one new element at the rear edge of the contact patch.

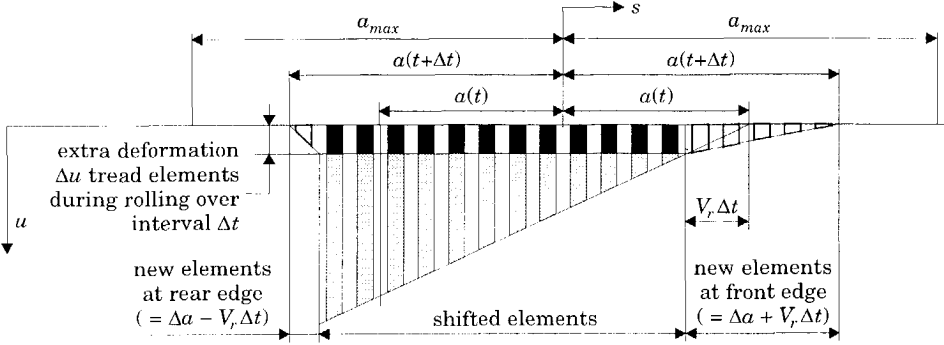


**Figure 5.15:** The tread element deformation during rolling with contact length variations.

Equations (5.41) and (5.43) hold for the elements which remain in the contact patch. The deformation of the elements entered at the front edge of the contact patch reads:

$$u_i(t+\Delta t) = \frac{\Delta u}{\Delta s - \Delta a} (s_i(t+\Delta t) - a(t+\Delta t)) \quad (5.46)$$

and the deformation of the elements entered at the rear edge reads:

$$u_i(t+\Delta t) = \frac{\Delta u}{\Delta s + \Delta a} (s_i(t+\Delta t) + a(t+\Delta t)) \quad (5.47)$$

The last step in the calculation process is the check for sliding and adhesion. For the analytical contact pressure distribution, a parabolic pressure distribution is assumed. To match the stationary characteristics with the analytically calculated ones also a parabolic distribution is assumed:

$$q_{z,i} = \begin{cases} \frac{3F_z}{4a^3} (a^2 - s_i^2) & \text{if } (-a \leq s_i \leq a) \\ q_{z,i} = 0 & \text{if } (s_i < -a) \vee (s_i > +a) \end{cases} \quad (5.48)$$

Obviously, the vertical pressure distribution is equal to zero outside the contact zone. The longitudinal deformation  $u_i$  is now limited by the maximum frictional force:

$$u_i = \begin{cases} u_i & \text{if } |u_i| \leq \mu q_{z,i}/c_{cp} \\ \mu q_{z,i}/c_{cp} & \text{if } u_i > \mu q_{z,i}/c_{cp} \\ -\mu q_{z,i}/c_{cp} & \text{if } u_i < -\mu q_{z,i}/c_{cp} \end{cases} \quad (5.49)$$

The integration of the longitudinal force (Eq. 5.6) becomes a summation:

$$F_{cx} = \frac{2ac_{cp}}{n} \sum_{i=1}^n u_i \quad (5.50)$$

### The influence of carcass flexibility

The analytically calculated frequency response functions showed that a soft carcass increases the time lag of the transient response. The block diagram of Figure 5.11 was used to calculate the transient tyre response including the carcass compliance in the frequency domain. This block diagram cannot be used for time simulations because of a causality conflict: both the carcass stiffness and the contact model need a velocity (or displacement) as input and give a longitudinal force as output. Therefore, an iteration procedure, based on the model introduced in Figure 5.4a, is applied to balance the forces in the carcass and contact model.

The wheel slip velocity  $V_{sx}$  is defined as input to the tyre model. Equation (5.18) can be reformulated such that the increase of the carcass force depends on the difference of the wheel slip velocity and contact slip velocity multiplied by the time step  $\Delta t$ :

$$F_{sx}(t+\Delta t) = F_{sx}(t) + C_{sx}(V_{c,sx} - V_{sx})\Delta t \quad (5.51)$$

The key factor in the iteration procedure is to balance the slip velocity in the contact patch  $V_{c,sx}$  such that the longitudinal force in the carcass equals the longitudinal force in the discrete contact model. A small increase in the slip velocity in the contact patch generates an increase in the force in the carcass and a decrease of the force in the contact patch. Equations (5.49) and (5.50) show that the additional contact forces can only be generated by contact elements in the adhesion zone. Multiplying this adhesion length (which does not have to be uninterrupted) by the tread element stiffness per unit length  $c_{cp}$  gives the equivalent longitudinal stiffness of the contact model in the given operating condition. With this equivalent stiffness and the carcass stiffness the slip velocity needed to balance the forces can be calculated easily.

## The responses of the discrete brush model

The discrete brush model cannot be validated by comparison with experimental results as appropriate measurements are not available. Instead, the analytical model behaviour is used to check the discrete model. For this, the responses of the discrete brush model are compared to the analytically calculated FRFs and to the stationary slip characteristics of the brush model. As a result, it has been ascertained that:

- The discrete simulation model has the same stationary slip characteristics as the analytically calculated characteristic (*cf.* Eq. 3.16).
- The estimated frequency response function of the discrete brush model, obtained by small variations of either wheel slip or contact length is identical with the analytically calculated FRFs of Figures 5.6 and 5.12.
- The simulated response to a step change in wheel slip velocity and the simulated response to a step change in contact length are identical with the analytically calculated responses of Figures 5.7a and 5.13a.

The analytically calculated FRFs showed that the transient tyre responses at small levels of slip may be approximated by a first order system with a relaxation length  $\sigma$  (Eq. 5.20). It is well known that with increasing slip the relaxation length decreases [86,106,107]. The discrete simulation model is used to estimate the relaxation length at high levels of slip. For this the response due to a small increase in the slip or a small increase in the vertical load is simulated. These simulated step responses showed that these responses are rather similar to an exponential function (see also the analytically calculated step responses in Figures 5.7a and 5.13a). The relaxation length  $\sigma$  of such a response can be estimated by fitting the response with an exponential function:

$$\Delta F_x(x) = \Delta F_{x0} (1 - e^{-x/\sigma}) \quad (5.52)$$

where  $\Delta F_x$  denotes the transient increase in longitudinal force and  $\Delta F_{x0}$  the steady-state value of the increase of the force. These fitted relaxation lengths of the responses of the discrete brush model are presented in Figures 5.16 and 5.17 as function of the average longitudinal force, or as function of the average slip. Figure 5.16 presents the relaxation length of the longitudinal force response to slip variations and Figure 5.17 presents the relaxation length of the longitudinal force response to vertical load variations. The fitted relaxation length of the simulation model in response to slip variations appears to be equal to the

relaxation length in response to vertical load variations even though the analytically calculated responses are rather different.

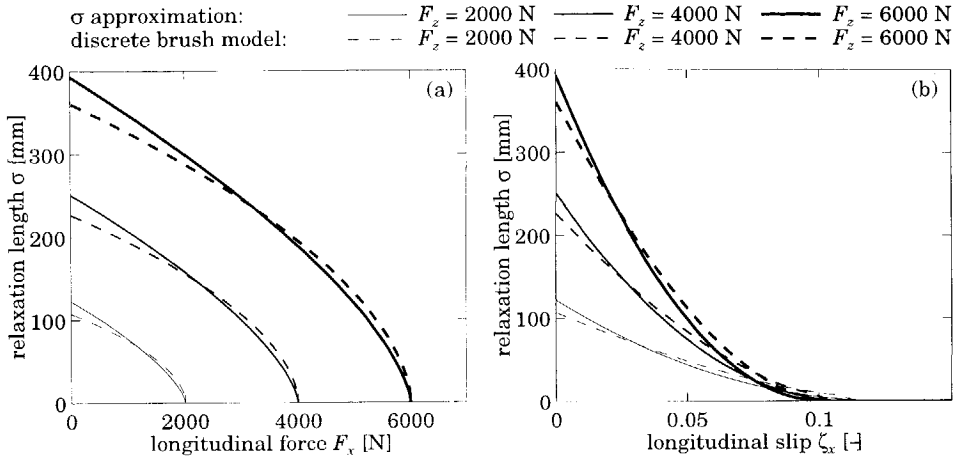


**Figure 5.16:** The relaxation length of the longitudinal force response due to slip variations.

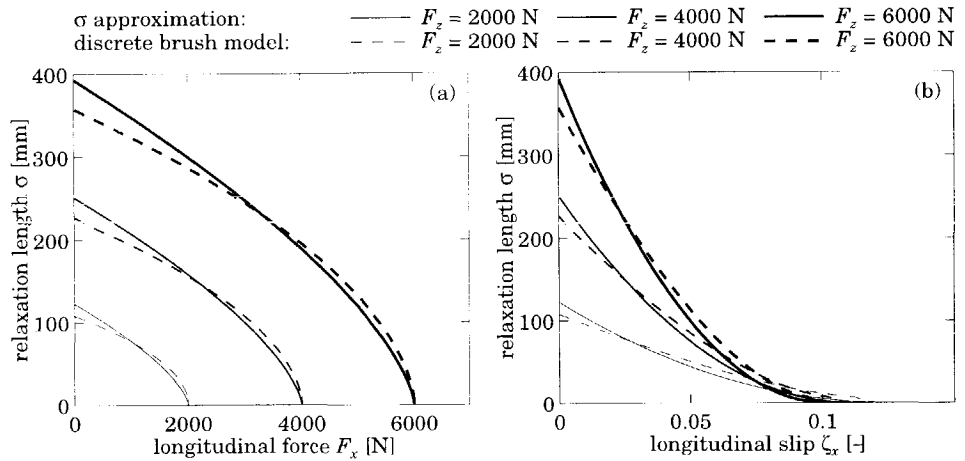


**Figure 5.17:** The relaxation length of the longitudinal force response to vertical load variations.

The parameters used are presented in Table 5.1. The longitudinal carcass stiffness  $C_x$ , the tread element stiffness per unit length  $c_p$ , half the contact length  $a$ , and the friction coefficient  $\mu$  are independent parameters. The values are based

on the identified parameter values of the rigid ring model. The relaxation lengths at zero slip and slip stiffness at zero slip are calculated values. To simulate the response to a small increase in contact length the number of tread elements of the model was chosen large (1000).

**Table 5.1:** *The parameter values used.*

description	symbol	value at	value at	value at	unit
		$F_z = 2000 \text{ N}$	$F_z = 4000 \text{ N}$	$F_z = 6000 \text{ N}$	
longitudinal carcass stiffness	$C_x$	550000	550000	550000	N/m
tread element stiffness	$c_{cp}$	$19 \cdot 10^6$	$19 \cdot 10^6$	$19 \cdot 10^6$	N/m <sup>2</sup>
half the contact length	$a$	0.0355	0.0534	0.0685	m
friction coefficient	$\mu$	1.0	1.0	1.0	–
relaxation length tyre	$\sigma_0$	0.1230	0.2515	0.3944	m
relaxation length contact model	$\sigma_{c0}$	0.0355	0.0534	0.0685	m
slip stiffness	$C_{\kappa 0}$	48000	109000	179000	N

The transient response of the discrete brush model can also be directly represented by a relaxation length system. For this the Equation (5.20) for the relaxation length at full adhesion  $\sigma_0$  is extended for higher slip levels. This relaxation length  $\sigma$  can be approximated by the actual local slip stiffness  $C_\kappa (= \partial F_x / \partial \zeta_x)$  divided by the total longitudinal tyre stiffness  $C_x$ , or as the ratio between the actual slip stiffness  $C_\kappa$  and the slip stiffness at free rolling  $C_{\kappa 0}$  multiplied by the relaxation length at free rolling  $\sigma_0$ :

$$\sigma = \frac{C_\kappa}{C_{x,tot}} = \frac{\sigma_0}{C_{\kappa 0}} \frac{\partial F_x}{\partial \zeta_x} = \sigma_0 \frac{C_\kappa}{C_{\kappa 0}} \quad (5.53)$$

Note: the relaxation length at free rolling  $\sigma_0$  is defined in Equation (5.20). The relaxation length according to the approximation is presented in Figures 5.16 and 5.17 as well. These figures show that the approximated model (Eq. 5.53) represents the transient response of the discrete brush model reasonably well: at small values of slip the approximated relaxation length (*cf.* Eq. 5.53) is longer than calculated according to time constant of the discrete brush model. The previously calculated FRFs of the contact models (Figures 5.2 and 5.9) showed a similar effect: a first order system with a shorter relaxation length would represent the exact solution better. The quality of fit between the approximation and the exact solution increases by adding the carcass compliance (Figures 5.6

and 5.12), but nevertheless, a slightly shorter relaxation length of the approximation would give a better result.

At high value of slip the approximated relaxation length becomes too small. This relaxation length decreases at increasing slip because the slip stiffness  $C_x$  decreases, and the total longitudinal tyre stiffness  $C_{x,tot}$  is assumed to be constant. In reality, it may be assumed that the longitudinal carcass stiffness  $C_x$  is constant, but the equivalent longitudinal tread stiffness decreases at increasing slip, see Equations (5.49) and (5.50).

### Conclusions

The frequency response functions (Figures 5.6 and 5.12) showed that the first order approximation is an adequate representation of the force generation in the contact patch. The largest deviation between the exact solution and the approximation is around the cut-off frequency. The frequency range of the approximation for slip variations is not limited. This means that this approximation can be used to simulate the tyre transient response at very high frequencies and very short wavelengths. The approximation of the FRF to vertical load variations is valid until the cut-off frequency.

Although the analytically calculated frequency response to slip variations is very different from the frequency response to vertical load variations, the step responses are rather similar. Although this is true, the simulations with the discrete brush showed that the relaxation length for slip variations and the relaxation length for vertical load variations are identical. Furthermore, the simulation model showed that the relaxation length decreases with increasing slip.

Expression (5.53) gives a reasonable approximation of the relaxation length that was obtained. This expression will be used in Chapter 6, where four pragmatic tyre models based on the first order approximation will be developed. The responses of these pragmatic models to linear input conditions (small variations of slip and vertical load) are identical to the responses presented in this chapter. The non-linear responses, on the other hand, differ considerably: these differences are the main subject of the study presented in Chapter 6. The pragmatic tyre models are evaluated by comparing the non-linear responses with the response of the discrete brush model which was developed in this chapter. The pragmatic tyre model which gives the best results will be used as contact model of the rigid ring model in Chapter 7.

# 6

## Pragmatic Transient Tyre Models

---

### 6.1 Introduction

It is well known that the force and moment responses of the tyre to various external inputs show a lag in time. The fact that tyre deflections have to be built up to create a force calls for a model that contains carcass compliance [87]. This phenomenon is typically characterised by the relaxation lengths of the tyre. The goal of the research presented in this chapter is the development of pragmatic transient tyre models based on the relaxation length concept. These models are named *pragmatic* models as they are based on matching transient tyre responses with a small set of differential equations rather than extensively modelling of physical tyre properties.

The pragmatic tyre models are evaluated by comparing the dynamic responses to the responses of the *physical* model that was developed in the previous chapter. The advantages of the *pragmatic* models over *physical* models are that the computations are much easier and faster, and that measured slip characteristics can easily be incorporated.

Four pragmatic tyre models, which are based on the relaxation length concept, are introduced in Section 6.2. These models differ in the position in the model where the filtering effect of the relaxation length system is applied: model

1 filters the longitudinal force  $F_x$ ; model 2 filters the longitudinal slip  $\zeta_x$ ; model 3 filters the longitudinal deformation  $u$ ; and model 4, uses a mass-spring system to represent the transient tyre deformation and a contact patch relaxation length.

The responses of these models in linear conditions (small variations of slip) are identical with each other. The non-linear responses, on the other hand, differ considerably: these differences are the subject of the study presented in Section 6.3. The pragmatic model with the optimal properties will be added to the rigid ring model in Chapter 7. The last section of this chapter discusses the influence of relaxation length on the in-plane tyre dynamics.

Table 6.1 presents a chronological survey of the literature on pragmatic tyre modelling, based on the relaxation length concept. These models are used in vehicle simulations [7,44,98,101], or to study shimmy phenomena [80]. They are valid for simulations with relatively large wavelengths ( $> 1.5$  m) [88]. The following items of interest are considered in Table 6.1:

- **Pragmatic tyre model.** For convenience, these models are classified into four categories according to the pragmatic models 1-4 of Section 6.2. The tyre models of the first category (filtering of the forces) is most commonly used for vehicle simulations. The advantage of model 2, filtering of the slip, is that it can also be used at zero velocity. The third model: filtering of the deformation, is based on the stretched string theory [80]. Even though this theory was developed specifically for the lateral tyre responses it also holds for the longitudinal tyre responses. The disadvantage of the string theory is that the numerical stability of this method is not guaranteed for decreasing relaxation length at large slip levels [88,106,107]. The basis of the fourth model is rather similar to that of the deflection theory: an additional mass is added in the contact patch to avoid iterations and to ensure a numerically stable solution of the tyre deformation.
- **Slip conditions.** There is a body of published literature which deals with transients in tyre lateral force build up. Both the transient response of the lateral force and the transient response of the longitudinal force may be represented by a relaxation length system. Therefore, we may use the experience gained in theoretical and experimental work on the transient lateral force response in this study.
- **Investigated responses.** The tyre transient models are used to study the responses of vehicles, for example, to external inputs like road unevennesses or fluctuating braking. The case of fast vertical load variations at a specific value of slip challenges the tyre models as the delayed longitudinal or lateral forces should never become larger than the maximum frictional force ( $\mu F_z$ ) [100].



There used to be little interest in the low speed behaviour of tyre models as there is almost no dynamic response of vehicles at low speeds. The recent interest in driving simulators, on the other hand, has led into interest in low speed simulation: a driving simulator needs to be able to start and stop again, even on a slope [11].

**Table 6.1:** *Literature survey on pragmatic tyre modelling.*

reference	pragmatic tyre model				slip conditions			investigated responses			
	(1) force filtering	(2) slip filtering	(3) deformation filtering	(4) mass in contact patch	pure longitudinal	pure lateral	combined	vehicle simulations	slip variations	load variations	very low velocity
Pacejka [80]			•			•			•		
Shapley [101]		•				•		•			
Pacejka [82]			•		•				•	•	
Takahashi [106,107]			•			•				•	
Bakker [7]	•				•	•	•	•			
van der Jagt [44]			•		•			•	•		
Schieschke [98]	•					•		•	•	•	
Loeb [63]			•			•			•		
Wang [114]	•					•			•		
Bernard [11]		•			•	•	•		•		•
Gim [31]				•	•	•	•				
Pacejka [88]				•	•	•	•				
Higuchi [39,40]			•			•			•		•

## 6.2 Pragmatic tyre models based on the relaxation length concept.

The basic scheme of the pragmatic tyre models used in this chapter is depicted in Figure 6.1. These models involve a slip definition, a first order filter, and a stationary slip characteristic. The behaviour of vehicles subjected to low

frequency inputs is largely determined by the stationary slip characteristics [2,41,45,92,99]. Consequently, it is important to incorporate the entire slip characteristic in the pragmatic model and not only the slip stiffness at a given value of average slip. The input to these models is the slip velocity  $V_{sx}$  which is defined as the difference in forward and rolling velocity of the wheel (Eq. 3.2). The output of the pragmatic models is the longitudinal force  $F_x$  generated by the tyre.

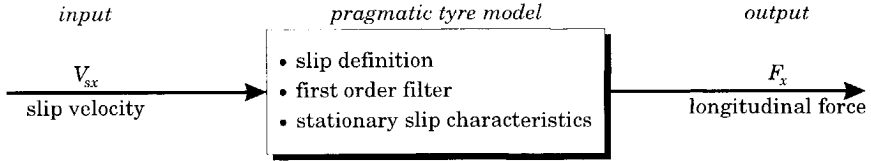


**Figure 6.1:** Basic scheme of the pragmatic tyre models.

To match the responses of the pragmatic tyre models with the responses of the discrete brush model, the stationary slip characteristic of the brush model, depicted in Figure 6.2, is used in this analysis. The parameters used in this chapter are identical with the parameters used in the previous chapter (see Table 5.1). To study the transient response of the tyre on the road, the brush tyre characteristics may be replaced by experimentally obtained characteristics.

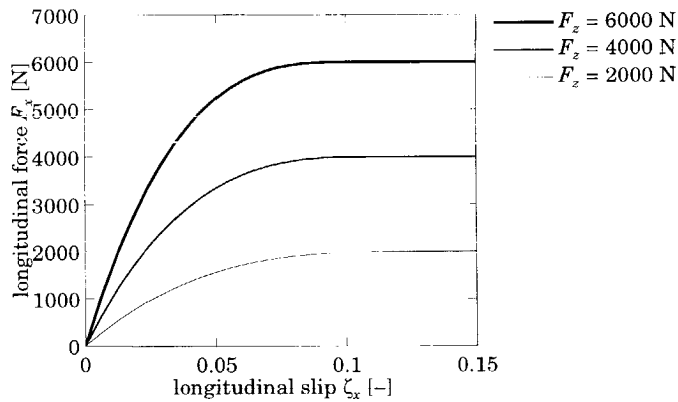


**Figure 6.2:** Stationary slip characteristics according to the brush model.

Chapter 5 showed that the transient response of the tyre to small variations of slip and vertical load can be approximated by a first order differential equation:

$$\dot{X} = \frac{|V_r|}{\sigma} (X_0 - X) \quad (6.1)$$

where  $X_0$  denotes the input, and  $X$  the filtered response. This equation will give the appropriate filter characteristic with a cut-off frequency  $f_c (= |V_r|/(\sigma 2\pi))$ . The relaxation length  $\sigma$  decreases with increasing slip. In Section 5.4 the relaxation length was defined as the ratio between the actual local slip stiffness  $C_\kappa (= \partial F_x / \partial \zeta_x)$  and the slip stiffness at free rolling  $C_{\kappa 0}$  multiplied by the relaxation length at free rolling  $\sigma_0$ :

$$\sigma = \frac{\sigma_0}{C_{\kappa 0}} \frac{\partial F_x}{\partial \zeta_x} = \sigma_0 \frac{C_\kappa}{C_{\kappa 0}} \quad (5.53)$$

Figure 6.3 presents the tyre relaxation length according to the expression above as function of the longitudinal force and the longitudinal slip.

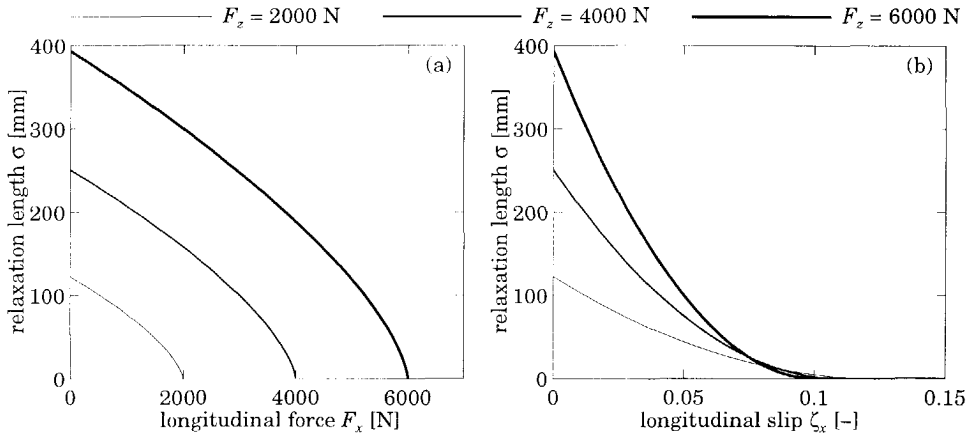


**Figure 6.3:** *The relaxation length as function of the longitudinal force, and as function of the longitudinal slip.*

In this chapter the tyre transient response will be discussed on the basis of the theoretical slip because this slip is used as input to the stationary slip characteristics used (*i.e.* according to the brush model). Accordingly, the rotational velocity  $V_r$  is used in the first order differential equation (6.1) because the theoretical slip  $\zeta_x$  is used for the computation of the local slip stiffness  $C_\kappa$  and thus for the computation of the relaxation length  $\sigma$ .

Appendix B discusses the tyre transient response in combination with the stationary slip characteristics of the Magic Formula in which the practical slip  $\kappa$

serves as input. In that case, the same slip ( $\kappa$ ) will be used for the computations of the slip stiffness and the relaxation length. To obtain a differential equation with the same time lag, the rolling velocity  $V_r$  in the differential equation (6.1) has to be replaced by the forward velocity  $V_x$ .

### Model 1: Filtering the longitudinal force

In the first pragmatic tyre model the horizontal force is filtered. This approach is most commonly used in vehicle simulations. The calculation scheme reads:

$$\zeta_x = -\frac{V_{sx}}{V_r} \quad (6.2a)$$

$$\sigma_1 = f_1(\zeta_x, F_z), \sigma_2 = f_2(F_x, F_z), \sigma = \min(\sigma_1, \sigma_2) \quad (6.2b)$$

$$F_{x,ss} = brush(\zeta_x, F_z, \mu) \quad (6.2c)$$

$$\sigma \frac{dF_x}{dt} + |V_r|F_x = |V_r|F_{x,ss} \quad (6.2d)$$

Figure 6.4 depicts the calculation scheme schematically. First, the longitudinal slip  $\zeta_x$  is obtained by normalising the slip velocity  $V_{sx}$  by the rolling velocity  $V_r$ . The stationary slip characteristic is used to obtain the steady-state force  $F_{x,ss}$ , filtering this force gives the transient response of the longitudinal force  $F_x$ .

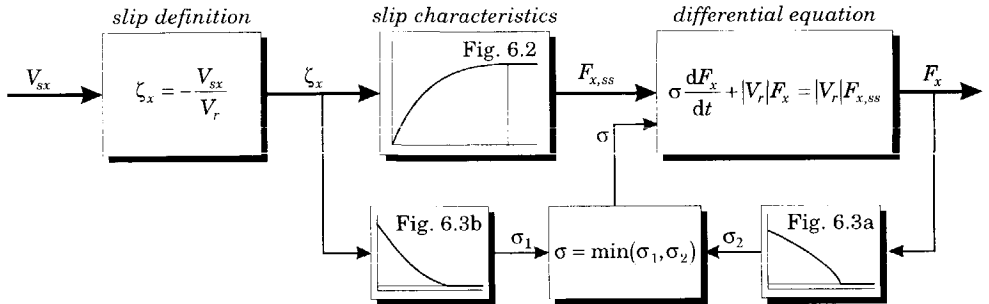


**Figure 6.4:** The calculation scheme of pragmatic tyre model 1.

The relaxation length depending on the longitudinal slip ( $\sigma_1$ ) results in a sufficiently fast response to variations of slip. But, this method leads to large errors to fast decreasing vertical load and relatively large average slip values: The delayed longitudinal force might become larger than the maximum friction force (vertical load multiplied by the friction coefficient). In order to make the model react faster to decreasing vertical load, a second relaxation length  $\sigma_2$ ,

which depends on  $F_x$ , is introduced. If the longitudinal force approaches the maximum friction force, the relaxation length  $\sigma_2$  will approach zero, resulting in a fast response of the longitudinal force.

The best simulation results were obtained by using the smallest value of the two relaxation lengths  $\sigma_1$  and  $\sigma_2$ . This will give good response to both slip variations and vertical load variations when compared with discrete model.

The minimum value of the relaxation length used in the differential equation (6.2d) is limited to 1 cm, to prevent the time constant  $\tau (= \sigma/|V_r|)$  of the differential equation to become too small. Otherwise, the time step in the numerical integration routine must also be very small. In the limit case ( $\sigma=\tau=0$ ) the differential equation cannot be integrated with an explicit numerical integration method.

## Model 2: Filtering the longitudinal slip

In the second model the longitudinal slip rather than the longitudinal force is filtered. This method was probably first introduced by Shapley [101]. The advantage of model 2 over model 1 is that the slip definition (Eq. 6.2a), which excludes zero velocity simulations, is not used. The second calculation scheme reads:

$$\sigma = f(\zeta_x, F_z) \quad (6.3a)$$

$$\sigma \frac{d\zeta_x}{dt} + |V_r|\zeta_x = -V_{sx} \quad (6.3b)$$

$$\zeta_{x,min} \leq \zeta_x \leq \zeta_{x,max} \quad (6.3c)$$

$$F_x = brush(\zeta_x, F_z, \mu) \quad (6.3d)$$

where  $\zeta_x$  now denotes the transient slip instead of the original definition of Equation (3.4). Figure 6.5 shows the calculation schematically.

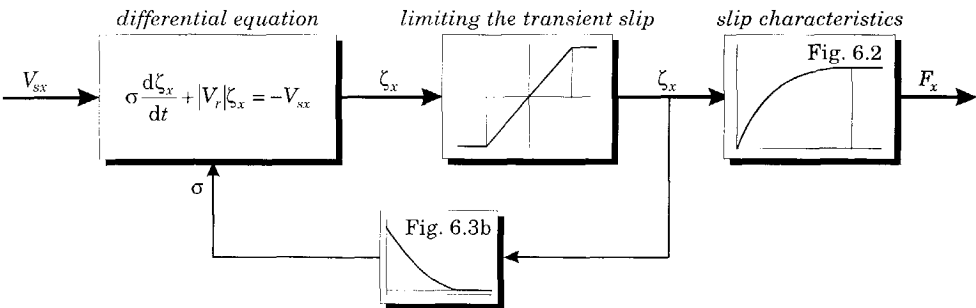


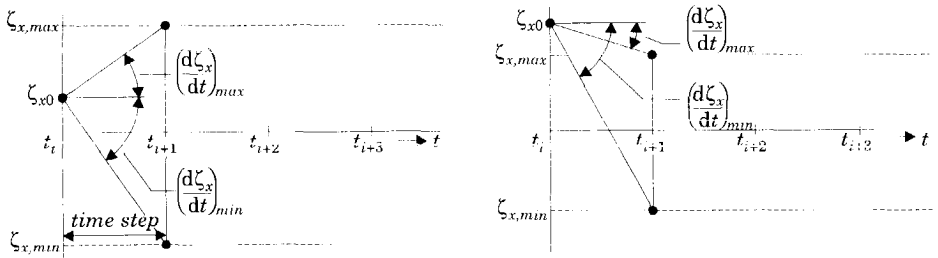
**Figure 6.5:** The calculation scheme of pragmatic tyre model 2.

A variation of slip velocity  $V_{sx}$  will generate through differential equation (6.3b) a transient slip  $\zeta_x$  which is used as input to the stationary slip characteristics (Eq. 6.3d). The vertical force only influences the stationary slip characteristics (Eq. 6.3d). This means that a variation of vertical force at constant slip will generate a direct (non-delayed) response of the longitudinal force. Therefore, this model cannot be used for varying vertical load.

The longitudinal slip velocity  $V_{sx}$  is used directly as input to the differential equation (Eq. 6.3b). The advantage of this formulation is that this differential equation is able to handle a zero velocity ( $V_r = 0$ ) condition. In that case the derivative of the slip is proportional to the slip velocity. Or, if we integrate this equation, the slip (and thus the force) in the contact patch is proportional to the deformation in the contact patch:

$$\frac{d\zeta_x}{dt} = -\frac{V_{sx}}{\sigma} \Rightarrow \zeta_x = -\int \frac{V_{sx}}{\sigma} dt \quad (6.4)$$

To prevent the transient slip from being integrated to plus or minus infinity, its value has to be limited. The best value to limit the slip is its value at the start of full sliding, that is at the  $F_x$  peak. The limitation of the transient slip is rather difficult as it is a state variable and state variables should not be altered during a numerical integration process. Therefore, the *derivative* of the transient slip is limited instead. The method used is depicted in Figure 6.6.



(a) slip  $\zeta_{x0}$  is between the two limit values

(b) slip  $\zeta_{x0}$  is outside the two limit values

**Figure 6.6:** Limiting the derivative of the transient slip  $\zeta_x$ .

At the beginning of an integration step (from time  $t_i$  to  $t_{i+1}$ ), the value of the longitudinal slip is denoted by  $\zeta_{x0}$ . At the end of this integration step, the slip  $\zeta_x$  should not become larger than the maximum allowed slip ( $\zeta_{x,max}$ ), or smaller than the minimum allowed slip ( $\zeta_{x,min}$ ). If a first order numerical integration method (method of EULER) is used, the maximum and minimum derivatives of the slip can be calculated easily. Now, the calculated derivative of the slip (from Eq. 6.3b),

is limited by these two values. Using this method the slip at the end of this integration step will never become larger than  $\zeta_{x,max}$  or become smaller than  $\zeta_{x,min}$ .

During the simulation process the maximum and minimum allowed slip may vary. The maximum allowed slip may decrease so quickly that the slip  $\zeta_x$  is outside the allowed slip range, as depicted in Figure 6.6b. Nevertheless, this method forces the slip to return to the allowed range.

Figure 6.6 presents the limitation of the slip when a first order numerical integration method is used. Generally higher order simulation methods which use more than one function evaluation per time step are used. Then the expressions for the maximum and minimum allowed slip read:

$$\dot{\zeta}_{x,max} = \frac{\zeta_{x,max} - \zeta_x}{q \cdot h}, \quad \dot{\zeta}_{x,min} = \frac{\zeta_{x,min} - \zeta_x}{q \cdot h} \quad (6.5)$$

where  $h$  denotes the time step and coefficient  $q$  denotes a correction factor for the integration method used. The derivative of the slip  $\dot{\zeta}_x$  is limited according to:

$$\dot{\zeta}_x = \begin{cases} \dot{\zeta}_x & \text{if } \dot{\zeta}_{x,min} \leq \dot{\zeta}_x \leq \dot{\zeta}_{x,max} \\ \dot{\zeta}_{x,max} & \text{if } \dot{\zeta}_x > \dot{\zeta}_{x,max} \\ \dot{\zeta}_{x,min} & \text{if } \dot{\zeta}_x < \dot{\zeta}_{x,min} \end{cases} \quad (6.6)$$

Equations (6.5) and (6.6) represent a constraint to one of the state variables. The coefficient  $q$  chosen is such that the constraint is as stiff as possible allowed by the integration method and time step. Table 6.2 presents the values of coefficient  $q$ , and the relative error in the constraint equation for three integration methods. The 4<sup>th</sup> order RUNGE-KUTTA method is the method used for the numerical simulations in this thesis. The relative error of the constraint equation of 27% means that an error made by this constraint is reduced to 27% for each time step.

**Table 6.2:** *The parameters of the constraint equation.*

integration method	coefficient $q$ [-]	error after 1 time step
1 <sup>st</sup> order EULER	1.0000	0 %
2 <sup>nd</sup> order HEUN	1.0000	50 %
4 <sup>th</sup> order RUNGE-KUTTA	0.6265	27 %

The method described above is most suitable for a fixed step integration routine. A variable step integration routine uses the time step  $h$  to control the error made by the integration. A small desired integration error will forced the step size  $h$  to become small. According to the constraint equation, the maximum value of the

derivative of a state variable is increases with decreasing the time step (*cf.* Eq. 6.5). which might not lead to a small (desired) error in the integration.

### Model 3: Filtering the longitudinal deformation

The filtering of the longitudinal deformation is based on the stretched string theory developed for the lateral deflection of the tyre [80]. Even though this theory was specifically developed for the lateral tyre responses its principle may also be used for the longitudinal tyre responses. Takahashi *et al.* applied the theory for the analysis of cornering on uneven roads [86,106,107]. He had difficulties in stabilising the numerical routine. Recently, Higuchi *et al.* [39,40] introduced an adapted approach for the numerical calculations which seems to be promising.

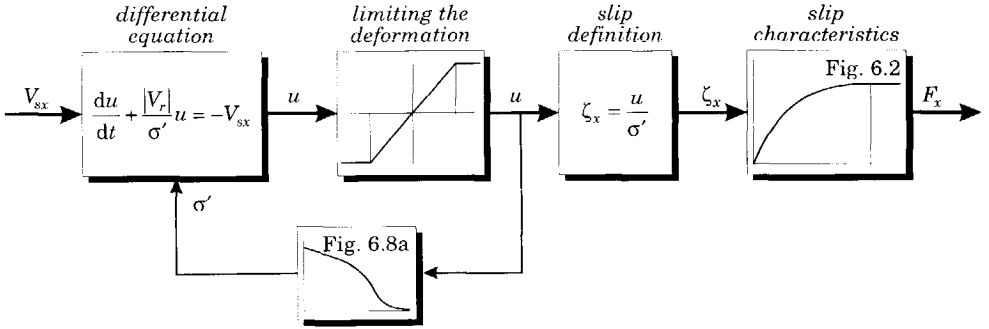


**Figure 6.7:** The calculation scheme of pragmatic tyre model 3.

The calculation scheme for this method is presented in Figure 6.7. The equations of this method read:

$$\sigma' = f(u, F_z) \quad (6.7a)$$

$$\zeta_x = \frac{u}{\sigma'} \quad (6.7b)$$

$$F_x = brush(\zeta_x, F_z, \mu) \quad (6.7c)$$

$$\frac{du}{dt} + \frac{|V_r|}{\sigma'} u = -V_{sx} \quad (6.7d)$$

$$u_{min} \leq u \leq u_{max} \quad (6.7e)$$

Although the differential equation (6.7d) is very similar to the previously introduced differential equations (6.2d) and (6.3b), the values of the relaxation



lengths are different. Therefore the relaxation length used in this scheme is denoted by an additional *prime*. According to the string theory [86], the relaxation length  $\sigma'$  can be expressed as:

$$\sigma' = \frac{\sigma_0}{C_{\kappa 0}} \frac{F_x}{\zeta_x} \quad (6.8)$$

where  $\sigma_0$  and  $C_{\kappa 0}$  are the relaxation length and slip stiffness at zero slip, respectively. Higuchi *et al.* [39] showed that the time constant of the first order differential equation (Eq. 6.7d) is not equal to relaxation length  $\sigma'$  divided by the velocity  $V_r$ . To obtain this time constant the differential equation is linearised: the deformation and relaxation length are written as small variations (denoted by a tilde) on top of constant values (denoted by a subscript 0).

$$\frac{d\tilde{u}}{dt} = -|V_{r0} + \tilde{V}_r| \cdot \frac{u_0 + \tilde{u}}{\sigma'_0 + \tilde{\sigma}'} - (V_{sx0} + \tilde{V}_{sx}) = -|V_{r0} + \tilde{V}_r| \cdot \left( \frac{u_0}{\sigma'_0} + \frac{\tilde{u}}{\sigma'_0} - \frac{u_0 \tilde{\sigma}'}{\sigma'^2_0} \right) - (V_{sx0} + \tilde{V}_{sx}) \quad (6.9)$$

The relaxation length  $\sigma'$  depends on both the deformation  $u$  and the vertical force  $F_z$  (cf. Eq. 6.7a). Thus small variations in the relaxation length can be expressed as:

$$\tilde{\sigma}' = \frac{\partial \sigma'}{\partial u} \tilde{u} + \frac{\partial \sigma'}{\partial F_z} \tilde{F}_z \quad (6.10)$$

We simplify the analysis by assuming that the variations in vertical load are zero. Using  $u_0 = -\sigma'_0 V_{sx0}/|V_{r0}|$ , expression (6.9) becomes:

$$\frac{d\tilde{u}}{dt} = -\frac{|V_{r0}|}{\sigma'_0} \left( 1 - \frac{u_0}{\sigma'_0} \frac{\partial \sigma'}{\partial u} \right) \tilde{u} - \tilde{V}_r \operatorname{sgn}(V_{r0}) \frac{u_0}{\sigma'_0} - \tilde{V}_{sx} \quad \text{if } \dot{F}_z = 0 \quad (6.11)$$

In the equations above is the partial derivative of the relaxation length  $\sigma'$  with respect to the deformation  $u$ :  $(\partial \sigma' / \partial u)$  is introduced. This derivative is negative if the deflection  $u$  is positive. We now define the actual relaxation length  $\sigma$  (without prime) as the time constant of the linearised system multiplied by the rolling velocity:

$$\sigma = \tau \cdot |V_{r0}| = \sigma'_0 \cdot \left( 1 - \frac{u_0}{\sigma'_0} \frac{\partial \sigma'}{\partial u} \right)^{-1} \quad (6.12)$$

Using  $u_0/\sigma'_0 = -V_{sx0}/|V_{r0}|$ , Equation (6.11) now takes the form (if  $\dot{F}_z = 0$ ,  $\tilde{V}_r = -\tilde{V}_{sx}$ ):

$$\frac{d\tilde{u}}{dt} + \frac{|V_{r0}|}{\sigma} \tilde{u} = -\frac{V_{x0}}{V_{r0}} \tilde{V}_{sx} \quad (6.13)$$

In the further analysis we will omit the subscript 0 for the constant values in the notation. The actual relaxation length  $\sigma$  is only equal to the relaxation  $\sigma'$  if the longitudinal deformation  $u$  is zero. The derivative of the relaxation length  $\sigma'$  with respect to  $u$  can be expressed as:

$$\frac{\partial \sigma'}{\partial u} = \frac{\partial \sigma'}{\partial F_x} \frac{dF_x}{du} = \frac{\partial \left( \frac{\sigma_0}{C_{\kappa 0}} \frac{F_x}{\zeta_x} \right)}{\partial F_x} \frac{dF_x}{du} = \frac{\sigma_0}{C_{\kappa 0}} \left( \frac{\partial F_x}{\partial F_x} \frac{1}{\zeta_x} - \frac{\partial \zeta_x}{\partial F_x} \frac{F_x}{\zeta_x^2} \right) C_x = \frac{1}{\zeta_x} \left( 1 - \frac{\partial \zeta_x}{\partial F_x} \frac{F_x}{\zeta_x} \right) \quad (6.14)$$

Using this result yields the expression for the actual relaxation length  $\sigma$  (note that  $\zeta_x = u/\sigma'$ ):

$$\sigma = \sigma' \cdot \left( 1 - \frac{u}{\sigma'} \frac{\partial \sigma'}{\partial u} \right)^{-1} = \sigma' \cdot \left( \frac{\partial \zeta_x}{\partial F_x} \frac{F_x}{\zeta_x} \right)^{-1} = \frac{\sigma_0}{C_{\kappa 0}} \frac{\partial F_x}{\partial \zeta_x} \quad (6.15)$$

This means that the actual relaxation length  $\sigma$  connected with the time constant of the differential equation (Eq. 6.13) equals the original definition of the relaxation length (Eq. 5.53). As a consequence we may conclude that the time constants of the transient responses to slip variations (if  $\dot{F}_z = 0$ ) are equal to each other, even though the values of the relaxation lengths  $\sigma'$  and  $\sigma$  in the differential equations (6.7d) and (6.13) differ.

Figure 6.8 shows the relaxation length  $\sigma'$  as function of the deformation  $u$ , and the deformation as function of the longitudinal slip. The shape of the latter curve is similar to the stationary slip characteristics, because the deformation of the tyre is proportional to the longitudinal force. After the peak in the curves of Figure 6.8b, the response of the tyre becomes infinitely fast as the time constant becomes zero. Takahashi *et al.* reported stability problems during numerical simulations close to complete sliding [86,107]. He also needed an iteration procedure to solve the slip, relaxation length, and force from equations (6.7b,c) and (6.8).

To avoid the instabilities, Higuchi *et al.* [39] and Takahashi *et al.* [107] proposed a correction for the deformation vs. slip characteristic such that the deformation keeps rising at increasing slip. Recently, Higuchi [40] proposed to alter the relaxation length vs. deformation characteristic rather than the deformation vs. slip characteristic. A similar approach is used in this study. The relaxation length vs. deformation characteristic is replaced by a new formula which was found by trial and error:

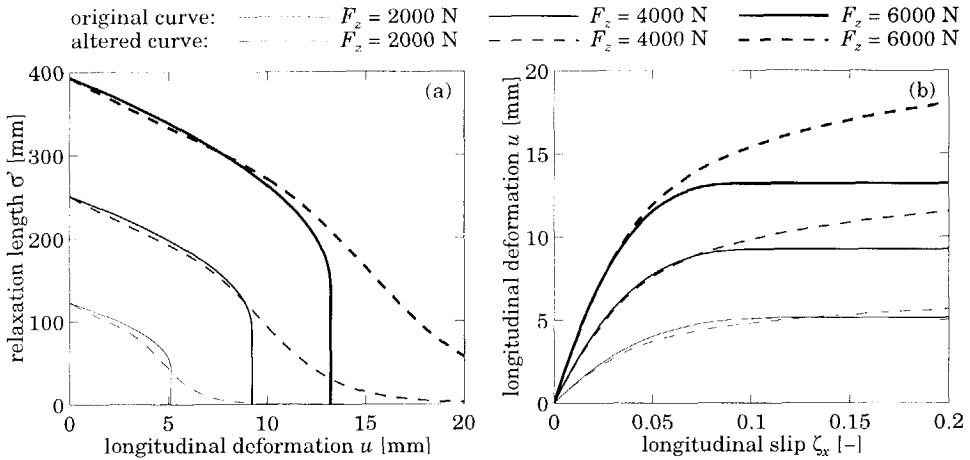
$$\sigma' = \sigma_0 \cdot \frac{\exp\left(-13 \frac{|u|}{\mu \sigma_0}\right)}{1 + 23 \left(\frac{|u|}{\mu \sigma_0}\right)^6} \quad (6.16)$$

Figure 6.8 presents the altered curves as well. The altered curve deviates from the original characteristics at high levels of slip and deformation. Using this formula has two advantages: First, the time constant will never become zero; and second, the relaxation length  $\sigma'$  is calculated directly from the deformation  $u$  without using an iteration procedure.

This model can also be used in zero velocity conditions, however, the longitudinal deformation may become too large. Therefore maximum and minimum allowed tyre deformations which depend on the maximum and minimum allowed longitudinal slips are introduced:

$$u_{max} = \sigma' \cdot \zeta_{x,max} \quad , \quad u_{min} = \sigma' \cdot \zeta_{x,min} \quad (6.17)$$

The method used to limit the longitudinal deformation is similar to the method of limiting the longitudinal slip employed in model 2.



**Figure 6.8:** The relaxation length  $\sigma'$  according to the stretched string theory; the original curve (Eq. 6.8), and the altered curve (Eq. 6.16).

#### Model 4: Contact model and sidewall flexibility

The fourth model is rather similar to the string theory. To solve the tyre deformation more easily, an additional mass in the contact patch is added. Both Pacejka *et al.* [88], and Gim *et al.* [31] used this approach to study the tyre transient responses for pure slip and combined slip conditions. Van der Jagt *et al.* applied this method to study of the effects of road unevennesses on ABS operation [44].

The disadvantage of the proposed models [31,44,88] is that the slip angle  $\alpha$  and longitudinal slip  $\kappa$  of the contact patch are used as input into the stationary slip characteristics, resulting in models which cannot handle zero velocity conditions. Therefore, a new pragmatic model is proposed: the carcass deformation is represented by a mass-spring system, and the transient response of the tread elements in the contact patch is represented by a slip model similar to the pragmatic model 2. The equations of pragmatic model 4 read:

$$\sigma_c = f(\zeta_{cx}, F_z) \quad (6.18a)$$

$$F_x = brush(\zeta_{cx}, F_z, \mu) \quad (6.18b)$$

$$m\ddot{u} + k\dot{u} + cu = F_x \quad (6.18c)$$

$$V_{c,sx} = V_{sx} + \dot{u} \quad (6.18d)$$

$$\sigma_c \frac{d\zeta_{cx}}{dt} + |V_{cr}| \zeta_{cx} = -V_{c,sx} \quad (6.18e)$$

$$\zeta_{cx,min} \leq \zeta_{cx} \leq \zeta_{cx,max} \quad (6.18f)$$

where, the situation in the contact patch is denoted by the subscript  $c$ . The carcass deflection is denoted by  $u$ , the carcass stiffness is denoted by  $c$ . A small amount of damping is added to avoid extensive vibrations of the mass  $m$ . Note:  $\ddot{u}$  is an approximation of the actual acceleration and the frequency of the excitation should be below the natural frequency of the mass-spring system. The calculation scheme is shown schematically in Figure 6.9.

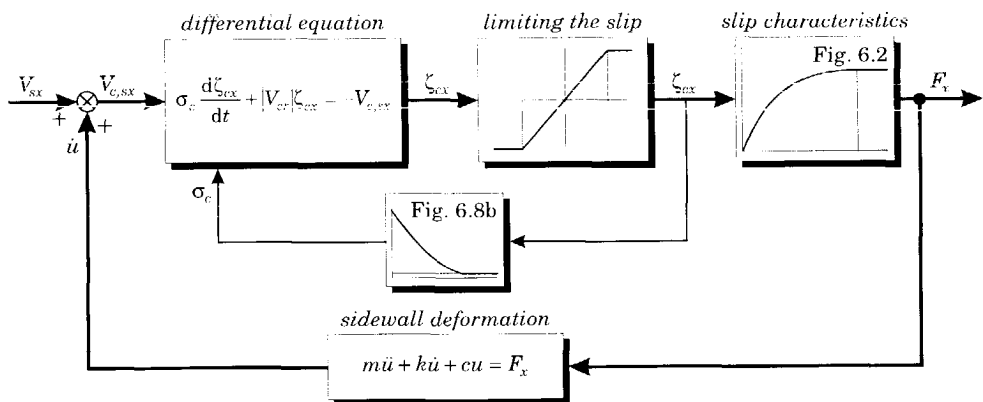


**Figure 6.9:** The calculation scheme of pragmatic tyre model 4.

The relaxation length  $\sigma_c$  of the slip model of the contact patch is much shorter than the total relaxation length  $\sigma$  of the tyre. The relaxation length  $\sigma_c$  decreases

with increasing slip and is also defined as the ratio between the actual slip stiffness and the slip stiffness at free rolling multiplied by the relaxation length of the contact patch model at free rolling  $\sigma_{c0}$ :

$$\sigma_c = \frac{\sigma_{c0}}{C_{\kappa 0}} \frac{\partial F_x}{\partial \zeta_{cx}} = \sigma_{c0} \frac{C_{\kappa}}{C_{\kappa 0}} \quad (6.19)$$

The slip stiffnesses  $C_{\kappa}$  and  $C_{\kappa 0}$  of the contact patch model are identical to the slip stiffnesses of the total tyre. The relaxation length  $\sigma_{c0}$  of the contact model at free rolling is equal to half the contact length  $a$ . Figure 6.10 presents the relaxation length of the contact patch model as function of force and slip.

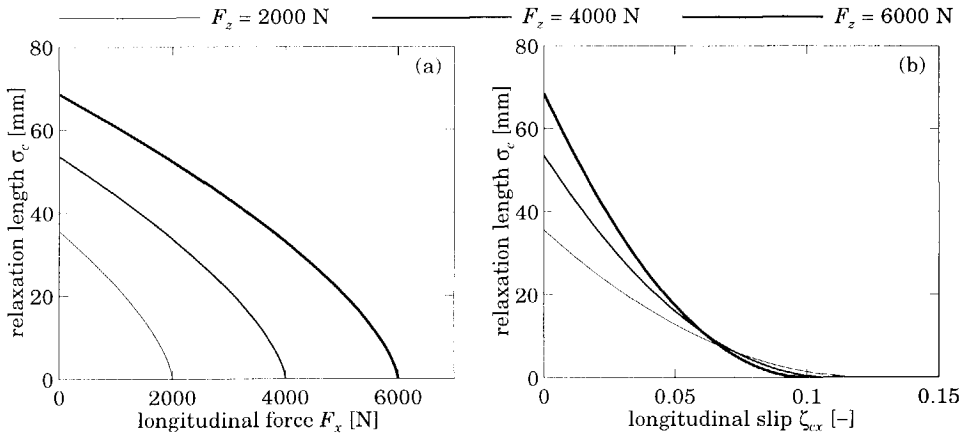


**Figure 6.10:** *The relaxation length of the contact model as function of the longitudinal force, and as function of the longitudinal slip.*

The contact model of model 4 is similar to model 2 (slip filtering) with a shorter relaxation length ( $\sigma_c$  instead of  $\sigma$ ). Accordingly, this contact model can be used at zero velocity and it does not show a transient response to vertical load variations. The influence of varying  $F_z$  in the contact model may be disregarded here because most of the influence is covered by the introduction of the carcass longitudinal compliance. A contact model according to model 3 (deformation filtering) would give more accurate results, especially at varying  $F_z$ . This approach is not used because it needs the altered curves for the relaxation length (*cf.* Eq. 6.16).

### 6.3 Discussion of the simulation results of the pragmatic models

The responses of the four pragmatic tyre models, which were introduced in the previous section are evaluated by comparing them to the responses of the discrete brush model. This model, which is called *physical* model, was developed in Chapter 5. The parameters used are given in Table 5.1. The responses of the pragmatic models are not compared to transient measurements because it is difficult to separate experimental longitudinal transient tyre responses from the dynamic tyre responses. The optimal pragmatic tyre model will be added to the rigid ring tyre model in Chapter 7. The rigid ring tyre model including the contact model is validated for various kinds of excitation of the tyre in Chapters 9 through 11.

The models were validated for non-linear conditions: large variations of longitudinal slip (Figure 6.11), large variations of vertical load and friction coefficient (Figure 6.12), and with simulations for zero velocity conditions (Figure 6.13). The simulations were performed for three wavelengths ( $\lambda = 0.25, 1$ , and 4 metre). The variations at 4 metre wavelength are almost quasi-statically. The 0.25 metre wavelength is very short, approximately as long as the tyre relaxation length at 4000 N vertical load. To be able to compare the results for various wavelengths, the travelled distance of the tyre is normalised by the wavelength. The models were initialised by applying the excitation signal over a length of two times the relaxation length at free rolling  $\sigma_0$  plus one wavelength  $\lambda$  of the excitation signal. The responses presented were obtained from simulations over an additional length of one wavelength.

**Table 6.3:** *The 6 investigated excitations of the tyre.*

input variation	vertical load [N]		friction coefficient [–]		longitudinal slip [%]		Figure
	$F_{z0}$	$\Delta F_z$	$\mu_0$	$\Delta\mu$	$\zeta_{x0}$	$\Delta\zeta_x$	
$V_x$ variations	4000	0	1.0	0	4.0	3.6	6.11a
$V_r$ variations	4000	0	1.0	0	4.0	3.6	6.11b
$F_z$ variations	4000	3600	1.0	0	4.0	0	6.12a
$\mu$ variations	8000	0	0.5	0.45	4.0	0	6.12b
$x$ variations	4000	0	1.0	0	$\times^1$	$\times^1$	6.13a
$\theta$ variations	4000	0	1.0	0	$\times^1$	$\times^1$	6.13b

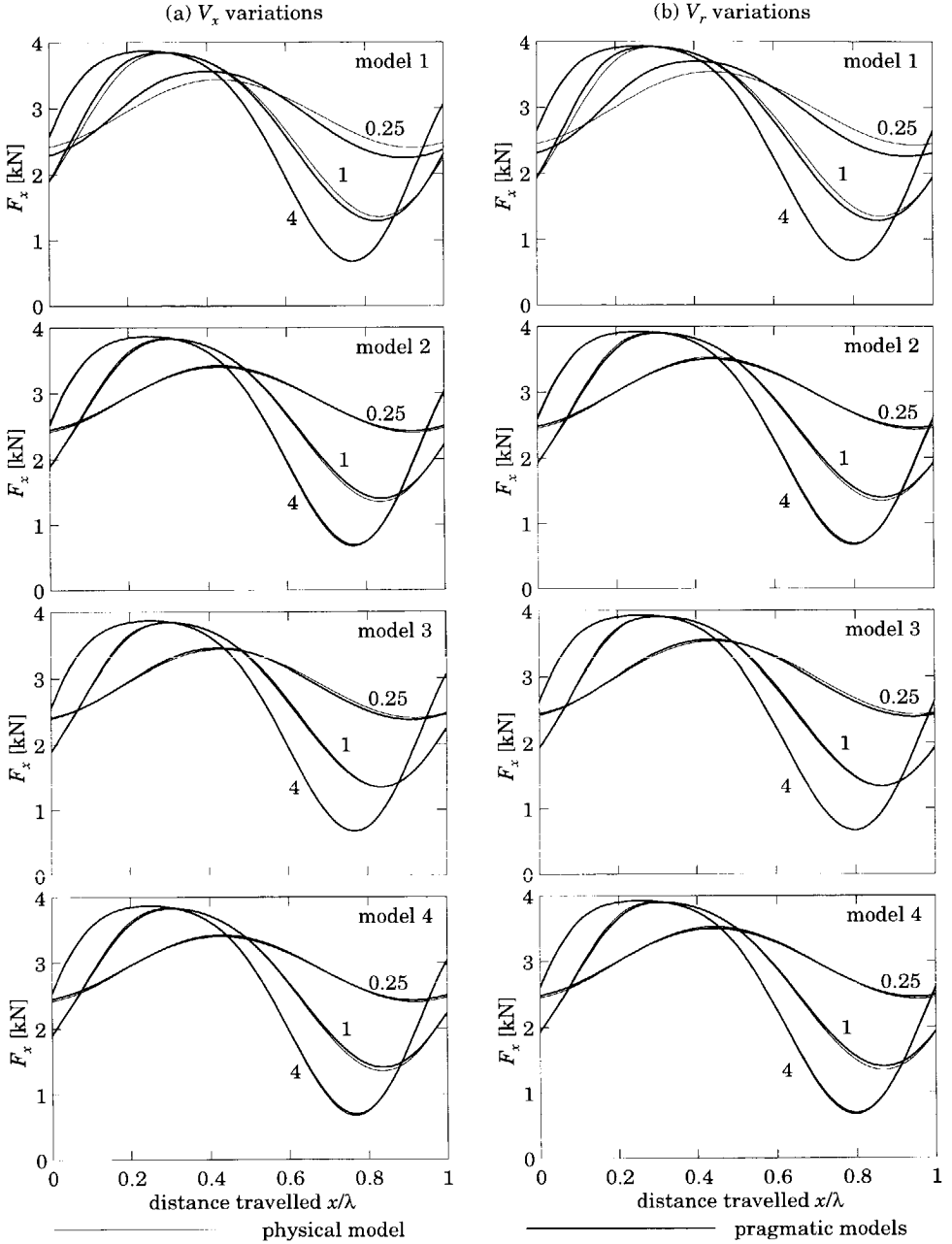
<sup>(1)</sup> slip is not defined at zero velocity.

Table 6.3 shows the conditions during the simulations. The average conditions are denoted by a subscript 0, and the variations by  $\Delta$ . The variations in slip, vertical load and friction coefficient are 90% of the average value. The amplitudes of the displacement  $x$  or the rim angle  $\theta$  at zero velocity are so large that full sliding occurs.

Figure 6.11 presents the results for large variations of slip velocity. Two situations were investigated: variation in longitudinal velocity  $V_x$  at constant rolling velocity  $V_r$ ; and variations of  $V_r$  at constant  $V_x$ . These two situations are chosen because the rolling velocity appears in the differential equations (Eq. 6.2d, 6.3b, 6.7d, and 6.18e). Nevertheless, the responses to  $V_x$  variations are similar to the responses to  $V_r$  variations. The responses of all four pragmatic models represent the responses of the physical model well.

Figure 6.12a presents the simulated responses to vertical load variations, which variations generally result from road undulations or vertical vibrations of the wheel. The simulated responses are very similar to the measured response of the lateral force at constant side slip angle and variations of vertical load [86,106,107,114].

The responses of model 1 to vertical load variations corresponds reasonable well with the responses of the physical tyre. The relaxation length  $\sigma_1$  (Eq. 6.2b) of this model permits the model to react quickly enough during the increase of  $F_z$ . The relaxation length  $\sigma_2$  (Eq. 6.2b) forces the model to react quickly at decreasing  $F_z$ . Otherwise the delayed longitudinal force would become larger than the maximum friction force. Model 2 does not show any transient response to the variations in vertical load as the load variations influence the longitudinal force variations directly only through the stationary characteristics (Eq. 6.3d). Model 3 (filtering of the deformation) represents the physical model best. At shorter wavelengths the longitudinal force approaches the maximum friction force ( $\mu F_z$ ). Model 4 reacts slightly too quickly to vertical load variations because the transient response to load variations is represented by carcass compliance only, and not by the transient response of the contact slip model. As stated previously, better results can be achieved by a contact model that filters the longitudinal deformation in the contact zone rather than the slip in the contact zone.



**Figure 6.11:** The responses of the models to slip variations.  
 wavelength  $\lambda = 0.25, 1, 4$  metre.  $\zeta_{x0} = 4.0\%$ ,  $\Delta\zeta_x = 3.6\%$



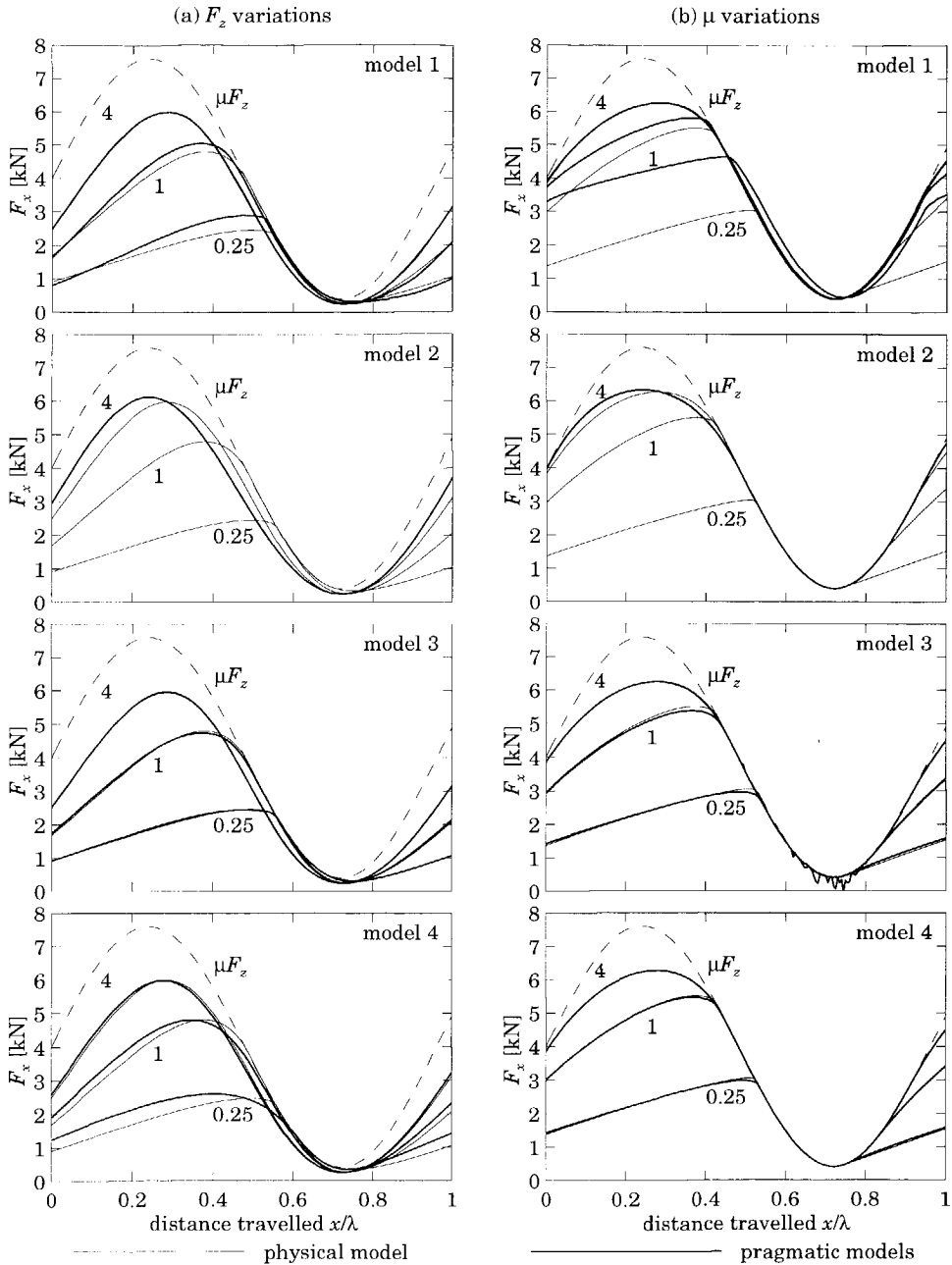


**Figure 6.12:** The responses of the model to vertical load or friction coefficient variations, wavelength  $\lambda = 0.25, 1, 4$  metre. Constant slip  $\zeta_{x0} = 4\%$ .

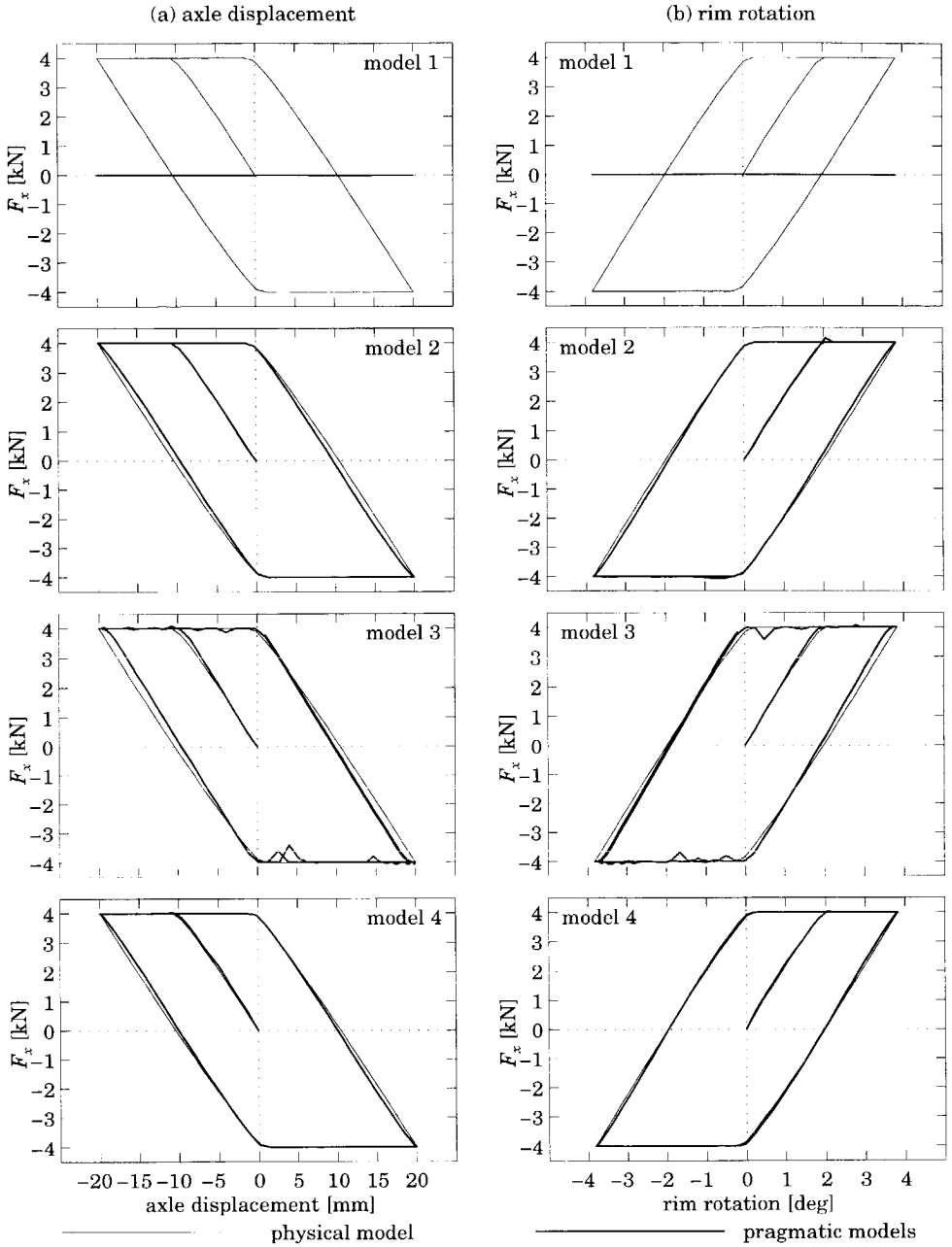


**Figure 6.13:** *The responses of the models at zero velocity conditions.*

The tyre responses to friction coefficient variations are presented in Figure 6.12b. The responses of models 2, 3 and 4 to friction coefficient variation are similar to the responses of these models to vertical load variations: model 2 does not show a transient response, and the responses of model 3 and 4 are rather good. It is very striking to see that the responses of model 1 to friction coefficient variations has deteriorated with respect to the responses of this model to load variations. The reason for this deterioration is the chosen condition: constant slip of 4%, constant vertical load of 8000 N and a varying friction coefficient ( $\mu=0.05-0.95$ ). At low values of the friction coefficient, the constant slip of 4% is already in the full-sliding range. Consequently, the relaxation length  $\sigma_1$  (cf. Eq. 6.2b) becomes very small and the longitudinal reaction is almost without delay. The responses of model 1 to vertical load variations will also deteriorate when the constant slip for the load variations is larger chosen (above 7%). The problem of model 1 is that without  $\sigma_1$  the model reacts too slowly with increasing vertical load or friction coefficient. A model with  $\sigma_1$ , on the other hand, reacts too fast at slip values close to full sliding.

Figure 6.13 presents the tyre response at zero velocity conditions. Figure 6.13a shows the response to a forward and backward displacement of the wheel axle of a non-rotating wheel. Figure 6.13b shows the forward and backward rotation of the rim with fixed axle positions. The amplitudes of the axle displacement and rim rotation are large enough to obtain full sliding.

Model 1 is not able to simulate the zero velocity condition because the longitudinal slip (Eq. 6.2a) cannot be calculated. Models 2,3 and 4 represent the zero velocity conditions rather well. The responses of models 2 and 4 are slightly better than the response of model 3 because the slip vs. deformation characteristic of model 3 was altered (see Figure 6.8) to ensure numerically stable integrations.

Figure 6.13 shows that the tyre force is proportional to the displacement until full sliding occurs. If the wheel motion changes direction the longitudinal force decreases immediately. The longitudinal forces of the pragmatic models 2,3 and 4 also react immediately to the change in the motion because the longitudinal slips (Eq. 6.3c and 6.18f) and the longitudinal deformation (Eq. 6.7e) were limited. Otherwise, the force vs. displacement characteristics would follow the same characteristics for forward and backward axle displacement. For small wheel motions (*i.e.* full sliding does not occur) the limitation is not necessary, and the force vs. displacement variations follows the same characteristic for forward and backward axle displacements.

The results of the study of the optimal pragmatic tyre model are summarised in Table 6.4. Models 3 and 4 are able to handle all situations, model 1 cannot be used in zero velocity conditions, and model 2 does not show a transient response to vertical load and friction coefficient variations. Model 3 has the best overall performance, but this model has two disadvantages. First, the relaxation length in the differential equation (Eq. 6.7d) divided by the velocity is not equal to the time constant of the transient response. This means that time constants obtained from experiments (*cf.* Section 9.2) cannot be used directly to represent the relaxation length of this model. Second, the longitudinal deformation vs. relaxation length characteristics had to be altered by trial and error to obtain a numerically stable model.

**Table 6.4:** *The performances of the four pragmatic tyre models.*

pragmatic tyre model	slip variations	vertical load & friction variations	zero velocity conditions	numerical consistency
1 Filtering the force	+	+/-	-	+
2 Filtering the slip	++	-	++	+
3 Filtering the deformation	++	++	+	+/-
4 Mass-spring system	++	+	++	+

The overall performance of model 4 is slightly poorer than the performance of model 3. The disadvantage of model 4 is that an additional second order differential equation is needed to solve the displacement of the mass in the contact patch.

In Chapter 7 the equations of the dynamic tyre model are developed. In this model the pragmatic model 4 will be used as a contact model because of the numerical stability is better than that of model 3. In the dynamic tyre model of Chapter 7, the tyre tread-band is modelled as a rigid ring and the carcass deformations are represented by the displacement of the rigid ring. This means that the additional mass of model 4 can be avoided as the contact model can be added directly to the ring model.

## 6.4 Basic influence of a relaxation system on tyre dynamics

The main effect of longitudinal and lateral carcass flexibilities that may be modelled using the relaxation length, is the phase lag of the force with respect to the imposed slip. For the in-plane case, a special effect is observed. This effect concerns the damping of the first natural mode of vibration of the tyre.

The transient responses of the tyre to slip and load variations could be approximately represented by a first order differential equation (Eq. 6.1). Such a differential equation can be represented by a spring and a damper in series. This system is named a *relaxation system*, as it represents the relaxation length behaviour of the tyre.

Figure 6.14 presents the relaxation length models for both the in-plane and out-of-plane tyre responses. The longitudinal and lateral tyre stiffnesses are denoted by  $C_x$  and  $C_y$ , and the longitudinal and lateral tyre slip stiffnesses are denoted by  $C_k$  and  $C_{F\alpha}$ . Even though for both directions the relaxation length systems are very similar, the system boundaries may be selected differently: the motion of the rim is prescribed for the out-of-plane model (steer angle  $\psi$ ) while the torque acting on the rim (drive or brake torque  $M_y$ ) may be prescribed for the in-plane model. These conditions reflect the typical boundary conditions for the wheel of a moving vehicle.

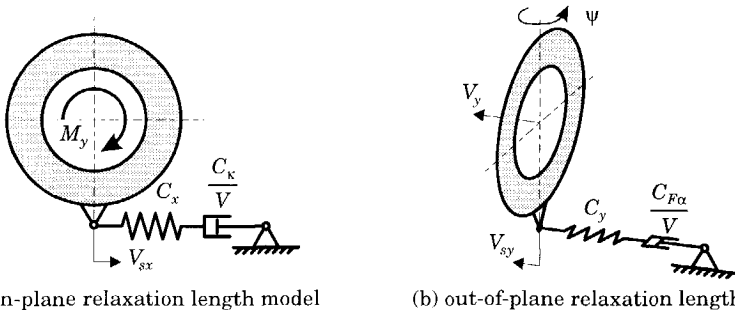


**Figure 6.14:** The differences between in-plane and out-of-plane transient tyre models.

The difference between boundary conditions for the in-plane and the out-of-plane model has two effects:

1. As long as wheel lock is avoided, the average value of the longitudinal force  $F_x$  multiplied by the tyre radius is always equal to the applied constant brake torque  $-M_y$ . Vertical load variations have little influence on the average

longitudinal force. The lateral force, on the other hand, is influenced strongly by variations in vertical load at constant slip angle. The adverse effects have been the subject of several studies [86,107].

2. The relaxation length system has a big influence on the relative damping of the in-plane modes of vibration of the tyre because the motion of the rim is not prescribed.

To illustrate the influence of the relaxation length system on the free in-plane tyre dynamics, two mass spring systems are considered: A 'normal' mass-spring-damper system with spring and damper parallel to each other, depicted in Figure 6.15a, and a 'mass-relaxation' system with spring and damper in series, depicted in Figure 6.15b. The system of Figure 6.15b corresponds to the situation below or close to the first natural frequency (typically 20-40 Hz) of the system where the rim and tyre rotate in-phase on the tangential carcass flexibility between the rim and the contact zone. This mode is defined as the 'in-phase rotational mode' in Chapter 8.

The analysis presented in this section is not intended to analyse the in-phase rotational mode in detail but is used to show the influence of the relaxation system on the tyre dynamics in terms of natural frequency and damping. The predicted behaviour appears to correspond with that of the in-plane rigid ring model of Chapter 7.

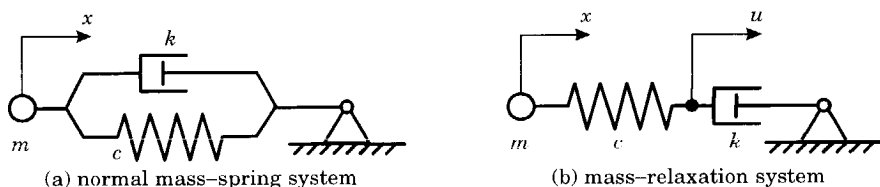


**Figure 6.15:** Two mass-spring systems. (a) a normal mass-spring system with the damper and spring parallel and (b) a relaxation system with the damper and spring in series.

Both the normal mass-spring system and the mass-relaxation system have three parameters: the overall longitudinal stiffness of the tyre, the damping coefficient and an equivalent mass. The stiffness  $c$  of the relaxation model results from all springs of the rigid ring model placed in series:

$$c = \left( \frac{1}{C_x} + \frac{1}{c_{cx}} \right)^{-1} \quad (6.20a)$$

The damping coefficient  $k$  equals the slip stiffness divided by the velocity.

$$k = C_\kappa / V \quad (6.20b)$$

The mass  $m$  of the model equals the modal mass of this mode of vibration. It involves the moments of inertia of the rim and the tyre ring and the mass of the tyre ring.

### Normal mass-spring system

The equation of motion of the normal mass-spring system reads:

$$m\ddot{x} + k\dot{x} + cx = 0 \quad (6.21)$$

where the longitudinal displacement of the mass is denoted by  $x$ . The characteristic equation becomes:

$$m\lambda^2 + k\lambda + c = 0 \quad (6.22)$$

The solutions  $\lambda_{1,2}$  of the characteristic equation are:

$$\lambda_{1,2} = -\kappa_n \omega_{n0} \pm \omega_{n0} \sqrt{\kappa_n^2 - 1} \quad (6.23)$$

The natural frequency of the undamped system  $\omega_{n0}$  and dimensionless damping coefficient  $\kappa_n$  are introduced:

$$\omega_{n0}^2 = \frac{c}{m} \quad \kappa_n = \frac{k}{2m\omega_{n0}} = \frac{k}{2\sqrt{mc}} \quad (6.24)$$

### Mass-relaxation system

In addition to the equation of motion of the mass  $m$ , the mass-relaxation system needs the equation for the force equilibrium between the spring and damper:

$$m\ddot{x} = c(u - x), \quad k\dot{u} = c(x - u) \quad (6.25)$$

where  $x$  denotes the longitudinal displacement of the mass and  $u$  denotes the displacement of the connection point between the spring and the damper. The characteristic equation of this set of equations becomes:

$$\lambda(mk\lambda^2 + mc\lambda + kc) = 0 \quad (6.26)$$

This characteristic equation has three solutions:

$$\lambda_{1,2} = -\kappa_r \omega_{r0} \pm \omega_{r0} \sqrt{\kappa_r^2 - 1}, \quad \lambda_3 = 0 \quad (6.27)$$

The frequency  $\omega_{r0}$  and dimensionless damping coefficient  $\kappa_r$  are introduced

$$\omega_{r0}^2 = \frac{c}{m} \quad \kappa_r = \frac{mc}{2\sqrt{km \cdot kc}} = \frac{\sqrt{mc}}{2k} \quad (6.28)$$

The natural frequencies of the normal mass-spring system (Eq. 6.24) and mass-relaxation system (Eq. 6.28) are equal to each other. Conversely, the values of relative damping are very different: the relative damping of the mass-relaxation system is inversely proportional to the relative damping of the normal mass-spring system.

To conclude, the first in-plane mode of vibration of the tyre can be approximated by the mass-relaxation system of Figure 6.15b. The relative damping of the mode of vibration is inversely proportional to the damping coefficient  $k$ . From Equation (6.20b) we can see that the relative damping of this mode of vibration is proportional to the velocity and inversely proportional to the slip stiffness. Indeed, the measured tyre responses to brake torque variations (*cf.* Chapter 9) and to road unevennesses (*cf.* Chapter 10) do show this effect.



# 7

## Development of the Rigid Ring Tyre Model

---

### 7.1 Introduction

The study with the physical tyre model in Chapter 5 showed that the longitudinal force generated in the tyre does not instantaneously follow slip variations. This phenomenon was characterised in Chapter 6 by the relaxation length. This approach, however, is valid only for low frequencies as the inertia properties of the tyre cannot be neglected at higher frequencies.

In this chapter the *rigid ring model* is developed. This model contains those modes of vibration of the tyre in which the tyre ring itself remains rigid and circular. In other words, the tyre ring moves as a rigid body with respect to the rim. The valid frequency range of this model is limited to frequencies higher than the first natural frequencies of the tyre, where the natural modes correspond to the rigid ring modes, but sufficiently below the higher natural frequencies of the flexible modes of vibration of the ring.

The out-of-plane rigid ring model was first introduced by Pacejka [81] in 1973 and later, following a different concept, by Meier-Dörnberg and Strackerjan [67,104]. Gerhard [28] and Werner [29] Fritz employed the latter model successfully for representing measured tyre responses to axle height, steer angle and camber angle variations up to 20 Hz. Laermann [56] added a discrete contact

patch model to the rigid ring dynamics. He studied the effect of load variations at constant slip angle on the lateral force and the self aligning moment responses. Oertel [77] used a rigid ring in his study on the influence of different contact models. Ammon *et al.* [4] used a rigid ring model in a multi body simulation of the vehicle motions.

The tyre models for the study of the in-plane vibrations vary in complexity. The simplest approach, where the tyre-wheel system is represented by one rigid body (of rim and large part of the tyre) and flexibility of the lower part of the carcass, is able to represent the lowest natural frequency of the tyre-wheel system [23,37,44]. The valid frequency range of these tyre models can be increased by adding the rotational degree of freedom of the tyre belt [72,121,122], its longitudinal degree of freedom [53], and its vertical degree of freedom [3,15,105]. These in-plane tyre models are used to study power-hop vibrations in a power driveline [37,72], dynamic tyre responses on uneven roads [15], and ABS operations [44,121,122]. It is striking to see that the in-plane flexible ring model, introduced by Tielking in 1965 [109], is much older than the simpler rigid ring models.

The in-plane rigid tyre ring model, depicted in Figure 7.1, represents a pneumatic tyre-wheel system. The model consists of four components: the tyre tread-band, the tyre sidewalls with pressurised air, the rim, and a contact model. The rigid ring model is able to represent those modes of the tyre where the shape of the ring remains circular: the rotation of the ring and a horizontal and vertical displacement of the ring. Therefore, the tread-band or belt is modelled as a rigid circular ring with three degrees of freedom: the displacements in longitudinal direction and in vertical direction and the rotation about the wheel axis (y-axis).

The rim is modelled as a rigid body that can rotate freely about the wheel axis. The tyre belt and the rim are connected through the third component: the sidewalls with pressurised air. This component is modelled as a horizontal, a vertical and a rotational spring and damper. The fourth component is the contact model. This model represents a vertical residual stiffness and a slip model. This slip model is based on the pragmatic tyre model 4 developed in Chapter 6.

The rigid ring model only represents the first modes of vibration of the tyre. The influences of the higher modes (which are called the *flexible* modes in Chapter 8) are neglected as we are not interested in higher frequency tyre dynamics. The influences of the flexible modes on the static deformation of the tyre cannot be neglected: each individual mode will deform statically and the deformation of all modes causes flattening of the tyre if it is standing on the road. To obtain a correct static stiffness of the rigid ring model a residual stiffness

between the tyre ring and the road surface is introduced. This residual stiffness accounts for the static deformation of all the higher order flexible modes.

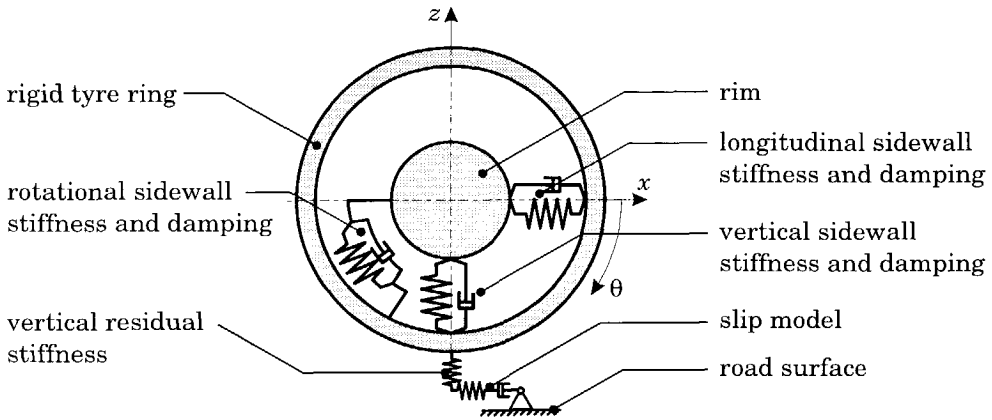


**Figure 7.1:** *The basic tyre model. The tyre is modelled as circular rigid ring, supported on an elastic foundation. A contact model is added.*

It appears that the horizontal and rotational stiffnesses belonging to the first modes already produce a sufficiently accurate longitudinal tyre stiffness, so that an additional tangential residual stiffness does not seem to be needed. If for any reason whatsoever, such a tangential residual stiffness is needed, the additional flexibility can be easily accomplished by increasing the relaxation length of the contact model. However, as stated in the previous chapter, the used contact model reacts directly to vertical load variations. This effect was disregarded as the relaxation length of the contact model was relatively short in comparison to the relaxation length of the total tyre. If the relaxation length of the contact model is increased to represent a tangential residual stiffness, the direct response of the contact model to vertical load variations can no longer be disregarded. To solve this problem, the contact model should be replaced by a contact model based on model 3 of the previous chapter.

Section 7.2 presents the first steps in the development of the rigid ring model: the dynamics and stability of the freely rotating rigid ring. The tyre-road interface is added to the model in Section 7.3. Section 7.4 presents the addition of the last item of the model: the motion of the rim. The linearisation of the rigid ring model is presented in Section 7.5. These equations are needed to apply techniques for linear models. The results of previously presented studies will be used for the model development: the static tyre properties (Chapter 2), the

stationary slip characteristics (Chapter 3), the tyre-road interface on an uneven road (Chapter 4), and the transient tyre responses (Chapters 5 and 6).

The present chapter presents only the development of the rigid ring model. In the subsequent chapters the model is validated by experiments. Section 7.6 presents an overview of the validation of the model and the parameter assessment. The mode shapes of the model are validated with experimental modal analysis in Chapter 8. The dynamic behaviour of the rigid ring model is validated for braking in Chapter 9 and for rolling over road unevenness in Chapter 10 and finally for axle height variations in Chapter 11.

## 7.2 The dynamics of a rotating free tyre-wheel system

This section presents the equations of motion and the dynamics of a non-loaded rotating tyre-wheel system. This system is modelled as a rigid rim and a rigid tyre ring connected through distributed sidewall stiffnesses. The tyre ring has three degrees of freedom in the wheel plane: the horizontal and vertical displacement of the tyre ring and the rotation of the tyre ring about the  $y$ -axis. The three in-plane motions of the rim can still be designated: either as input to the system, or as additional degrees of freedom of the system.

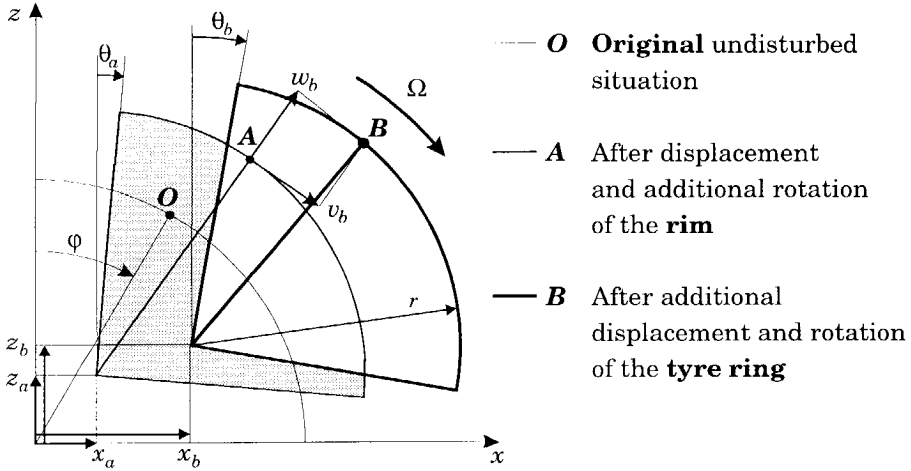
### Equations of motion of a rotating ring on an elastic foundation

Figure 7.2 presents the displacements of a point on the tyre ring in the fixed coordinate system  $(x, z)$  at different stages of the system motion: points  $O$ ,  $A$  and  $B$ . The tyre-wheel system rotates at constant angular speed  $\Omega$  about the wheel axis and point  $O$  is the position of a point on the tyre ring with radius  $r$  after this constant rotation. The angle of this undisturbed rotation is denoted by  $\varphi$  ( $\dot{\varphi} = \Omega$ ). Point  $A$  is a point on the tyre ring after the displacement of the axle  $x_a$  and  $z_a$  and the additional rotation of the rim  $\theta_a$ . The position after the tyre ring displacements is indicated by  $B$ . The horizontal and vertical positions of situation  $B$  are defined by  $x_b$  and  $z_b$  and the rotation by  $\theta_b$ .

The positions of the rim and axle are denoted by symbols showing the subscript  $a$ , and the positions of the tyre ring by the subscript  $b$ . In the next section a contact model is added to the rigid ring model. In the contact model the subscript  $c$  is provided.

The model of the tyre deformation introduced in Figure 7.2 is slightly different from that of the tyre deformations depicted in Figure 4.4. First of all in

Chapter 4 the flexible ring model was considered, while in this chapter the rigid ring model is developed. Secondly, here rim rotation results from two contributions: the angle  $\varphi$  due to constant rotation and the small variation  $\theta_a$ , while in Chapter 4 the total angle of rotation of the rim was represented by the angle  $\varphi$ . Thirdly, the variables  $v_b$  and  $w_b$  here denote the tangential and radial components of the deformation of the tyre sidewalls, rather than the tangential and radial positions of the tyre sidewalls.



**Figure 7.2:** The displacement of a point on the tyre ring including the deformation of the tyre sidewall.

The tangential  $v_b$  and radial  $w_b$  components of the deformation of the tyre sidewall are equal to the difference between the positions of points  $A$  and  $B$ :

$$\begin{bmatrix} v_b \\ w_b \end{bmatrix} = \begin{bmatrix} \cos(\varphi + \theta_a) & -\sin(\varphi + \theta_a) & r \\ \sin(\varphi + \theta_a) & \cos(\varphi + \theta_a) & 0 \end{bmatrix} \begin{bmatrix} x_b - x_a \\ z_b - z_a \\ \theta_b - \theta_a \end{bmatrix} \quad (7.1)$$

Or:

$$\underline{v}_b = \mathbf{Q}(\underline{x}_b - \underline{x}_a) \quad (7.2)$$

where  $\mathbf{Q}$  denotes the transformation matrix from the fixed to the rotating coordinate system and the deformations and positions are written as:

$$\underline{v}_b = [v_b \quad w_b]^T, \quad \underline{x}_a = [x_a \quad z_a \quad \theta_a]^T, \quad \underline{x}_b = [x_b \quad z_b \quad \theta_b]^T \quad (7.3)$$

The time rate of change of the tyre sidewall deformation reads:

$$\dot{\underline{v}}_b = \underline{Q}(\dot{\underline{x}}_b - \dot{\underline{x}}_a) + \dot{\underline{Q}}(\underline{x}_b - \underline{x}_a) \quad (7.4)$$

with:

$$\dot{\underline{Q}} = \frac{d\underline{Q}}{dt} = (\underline{\Omega} + \dot{\theta}_a) \begin{bmatrix} \sin(\varphi + \theta_a) & \cos(\varphi + \theta_a) & 0 \\ -\cos(\varphi + \theta_a) & -\sin(\varphi + \theta_a) & 0 \end{bmatrix} \quad (7.5)$$

The distributed tangential and radial foundation stiffness matrix  $\underline{C}_{bv}$  and damping matrix  $\underline{K}_{bv}$  are:

$$\underline{C}_{bv} = \begin{bmatrix} c_{bv} & 0 \\ 0 & c_{bw} \end{bmatrix}, \quad \underline{K}_{bv} = \begin{bmatrix} k_{bv} & 0 \\ 0 & k_{bw} \end{bmatrix} \quad (7.6)$$

where  $c_{bv}$  and  $c_{bw}$  are the stiffnesses and  $k_{bv}$  and  $k_{bw}$  are the damping coefficients of the tyre sidewalls per unit of length in tangential and radial directions, respectively. The internal forces  $\underline{f}_{bv}$  per unit of length oriented in the rotating frame are equal to the stiffness times the deformation plus the damping coefficients times the deformation velocity:

$$\underline{f}_{bv} = \underline{C}_{bv}\underline{v}_b + \underline{K}_{bv}\dot{\underline{v}}_b \quad (7.7)$$

Figure 7.3 shows the transformation between the rotating and fixed coordinate system. The forces and moments per unit of length oriented in the global frame become:

$$\begin{bmatrix} f_{bx} \\ f_{by} \\ m_{by} \end{bmatrix} = \begin{bmatrix} \cos(\varphi + \theta_a) & \sin(\varphi + \theta_a) \\ -\sin(\varphi + \theta_a) & \cos(\varphi + \theta_a) \\ r & 0 \end{bmatrix} \begin{bmatrix} f_{bv} \\ f_{bw} \end{bmatrix} \quad (7.8)$$

Whereby the internal torques due to unequal stiffnesses in radial and tangential direction are neglected. Integrating the distributed force over the entire circumference of the tyre and substituting expressions (7.4) and (7.7) yields the total sidewall force  $\underline{F}_b$  acting on the belt in the fixed coordinate system:

$$\underline{F}_b = \underbrace{\int_0^{2\pi} \underline{Q}^T \underline{C}_v \underline{Q} (\underline{x}_b - \underline{x}_a) r d\varphi}_1 + \underbrace{\int_0^{2\pi} \underline{Q}^T \underline{K}_v \underline{Q} (\dot{\underline{x}}_b - \dot{\underline{x}}_a) r d\varphi}_2 + \underbrace{\int_0^{2\pi} \underline{Q}^T \underline{K}_v \dot{\underline{Q}} (\underline{x}_b - \underline{x}_a) r d\varphi}_3 \quad (7.9)$$

Solving the first and second integral of Equation (7.9) gives the matrices  $\underline{C}_b$  and  $\underline{K}_b$  of the overall sidewall stiffnesses and damping coefficients, respectively:

$$\underline{C}_b = \begin{bmatrix} \pi r(c_{bv} + c_{bw}) & 0 & 0 \\ 0 & \pi r(c_{bv} + c_{bw}) & 0 \\ 0 & 0 & 2\pi c_{bv} r^2 \end{bmatrix}, \quad \underline{K}_b = \begin{bmatrix} \pi r(k_{bv} + k_{bw}) & 0 & 0 \\ 0 & \pi r(k_{bv} + k_{bw}) & 0 \\ 0 & 0 & 2\pi k_{bv} r^2 \end{bmatrix} \quad (7.10)$$

The third integral of equation (7.9) on the other hand, gives a matrix  $\mathbf{G}_b$  with off-diagonal elements, providing a coupling between the vertical and the longitudinal tyre ring displacements:

$$\mathbf{G}_b = (\dot{\theta}_a + \Omega) \begin{bmatrix} 0 & -\pi r(k_{bv} + k_{bw}) & 0 \\ \pi r(k_{bv} + k_{bw}) & 0 & 0 \\ 0 & 0 & 0 \end{bmatrix} \quad (7.11)$$

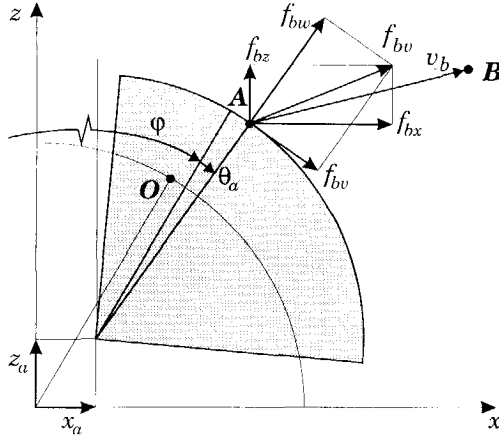


**Figure 7.3:** The sidewall forces oriented in the global (fixed) frame and in the rotating frame.

The equations of motion of the tyre belt motion read:

$$\mathbf{M}_b \ddot{\mathbf{x}}_b = -\mathbf{F}_b = -\mathbf{C}_b(\dot{\mathbf{x}}_b - \dot{\mathbf{x}}_a) - \mathbf{K}_b(\mathbf{x}_b - \mathbf{x}_a) - \mathbf{G}_b(\mathbf{x}_b - \mathbf{x}_a) \quad (7.12)$$

The mass matrix  $\mathbf{M}_b$  is defined as:

$$\mathbf{M}_b = \begin{bmatrix} m_b & 0 & 0 \\ 0 & m_b & 0 \\ 0 & 0 & I_{by} \end{bmatrix} \quad (7.13)$$

where  $m_b$ ,  $I_{by}$  are the mass and moment of inertia of that part of the tyre that is considered to move together with the tyre ring. Now, the total equations of motion of the free (non-loaded) rotating tyre ring model read:

$$m_b \ddot{x}_b + k_b(\dot{x}_b - \dot{x}_a) + c_b(x_b - x_a) - k_b(\Omega + \dot{\theta}_a)(z_b - z_a) = 0 \quad (7.14a)$$

$$m_b \ddot{z}_b + k_b(\dot{z}_b - \dot{z}_a) + c_b(z_b - z_a) + k_b(\Omega + \dot{\theta}_a)(x_b - x_a) = 0 \quad (7.14b)$$

$$I_{by} \ddot{\theta}_b + k_{b\theta}(\dot{\theta}_b - \dot{\theta}_a) + c_{b\theta}(\theta_b - \theta_a) = 0 \quad (7.14c)$$

Here the rim motion may be considered as a given time-dependent input to the tyre system, or this motion may result from the rim equations of motion. The stiffnesses and damping coefficients of the tyre sidewalls are introduced in the equations of motion of the tyre belt:

- translational sidewall stiffness:  $c_b = \pi r(c_{bv} + c_{bw})$  (7.15a)

- translational sidewall damping constant:  $k_b = \pi r(k_{bv} + k_{bw})$  (7.15b)

- rotational sidewall stiffness:  $c_{b\theta} = 2\pi c_{bv}r^3$  (7.15c)

- rotational sidewall damping constant:  $k_{b\theta} = 2\pi k_{bv}r^3$  (7.15d)

### The dynamic stability of a free rotating tyre ring

The equations of motion of a rotating system can be described in both the rotating frame and a fixed frame. Both descriptions refer to the same dynamic system. To study the dynamic stability of the rotating tyre ring the equations of motion of a simplified system are derived in both the rotating and the fixed frame.

In general, a damper has a stabilising effect on the dynamic behaviour of a system. The rotating damper is responsible for the coupling terms  $(-k_b\Omega z_b)$  and  $(k_b\Omega x_b)$  in equation (7.14) and might have a destabilising effect. To study the stability of the rotating tyre the theory of *rotor dynamics* is applied. Figure 7.4 shows a simplified model of the free rotating tyre: it depicts the horizontal and vertical displacements of the rotating tyre ring. In this analysis the rotational degree of freedom of the tyre is neglected ( $\dot{\theta}_b = 0$ ) as its influence on the stability of the rotating system is assumed to be small. Furthermore, the translational motions of the rim are set equal to zero.

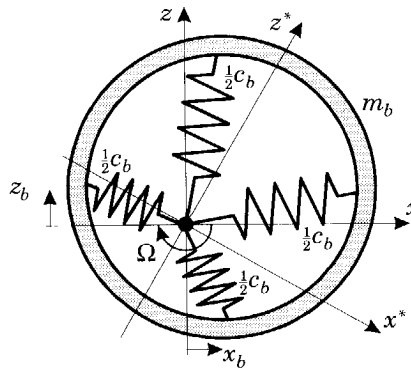


**Figure 7.4:** The simplified model used to study the stability of the rotating tyre.



The simplified tyre model is analogous to the *Jeffcott* rotor, the standard model used to study rotor dynamics [30,57]. The *Jeffcott* rotor, however, is a simplified model of a high-speed rotor that retains many of the essential characteristics of rotating systems. The *Jeffcott* rotor consists of a rotationally symmetrical body, carried by a flexible symmetrical structure that rotates about a rigidly supported bearing. The equations of the *Jeffcott* rotor can be applied directly to the simplified tyre model.

The equations of motion of the mass  $m_b$  in the fixed coordinate system  $(x, z)$  result from Equation (7.14) after setting  $x_a, z_a, \theta_a$  and  $\theta_b$  equal to zero:

$$\begin{aligned} m_b \ddot{x}_b + k_b \dot{x}_b + c_b x_b - k_b \Omega z_b &= 0 \\ m_b \ddot{z}_b + k_b \dot{z}_b + c_b z_b + k_b \Omega x_b &= 0 \end{aligned} \quad (7.16a)$$

The equations of motion in the rotating coordinate system  $(x^*, z^*)$  read [30]:

$$\begin{aligned} m_b \ddot{x}_b^* + k_b \dot{x}_b^* + (c_b - m_b \Omega^2) x_b^* + 2m_b \Omega \dot{z}_b^* &= 0 \\ m_b \ddot{z}_b^* + k_b \dot{z}_b^* + (c_b - m_b \Omega^2) z_b^* - 2m_b \Omega \dot{x}_b^* &= 0 \end{aligned} \quad (7.16b)$$

Both sets of equations represent the same system. The differences between the representations are the Coriolis and centrifugal forces in Equation (7.16b) and the coupling factors  $k_b \Omega$  in Equation (7.16a). The solutions  $\lambda$  of the characteristic equation of the equations in the non-rotating frame read:

$$\begin{aligned} \lambda_{1,2} &= -\kappa \omega_0 \pm j \sqrt{(1 - \kappa^2) \omega_0^2 + 2j\kappa \omega_0 \Omega} \\ \lambda_{3,4} &= -\kappa \omega_0 \pm j \sqrt{(1 - \kappa^2) \omega_0^2 - 2j\kappa \omega_0 \Omega} \end{aligned} \quad (7.17a)$$

while the solutions  $\lambda^*$  in the rotating frame become:

$$\begin{aligned} \lambda_{1,2}^* &= -(\kappa \omega_0 - j\Omega) \pm j \sqrt{(1 - \kappa^2) \omega_0^2 + 2j\kappa \omega_0 \Omega} \\ \lambda_{3,4}^* &= -(\kappa \omega_0 + j\Omega) \pm j \sqrt{(1 - \kappa^2) \omega_0^2 - 2j\kappa \omega_0 \Omega} \end{aligned} \quad (7.17b)$$

The natural frequency of the non-rotating system  $\omega_0$  and the dimensionless damping coefficient  $\kappa$  are introduced:

$$\omega_0 = \sqrt{c_b/m_b} \quad , \quad \kappa = \frac{1}{2} k_b / \sqrt{m_b c_b} \quad (7.18)$$

The relative damping of tyre vibrations is very small, only a few percent. So, the natural values can be approximated for small values of damping:

$$\lambda_{1,4} = -\kappa(\omega_0 + \Omega) \pm j\omega_0 \quad , \quad \lambda_{2,3} = -\kappa(\omega_0 - \Omega) \pm j\omega_0 \quad (7.19a)$$

and:

$$\lambda_{1,4}^* = -\kappa(\omega_0 + \Omega) \pm j(\omega_0 + \Omega), \quad \lambda_{2,3}^* = -\kappa(\omega_0 - \Omega) \pm j(\omega_0 - \Omega) \quad (7.19b)$$

Even though the natural values of Equations (7.19) represent the same system they differ. The frequencies in the rotating system are frequencies relative to the observer moving together with this rotating coordinate system. Since the velocity of rotation is  $\Omega$  the frequencies are also shifted by this rotational velocity.

Another effect of the rotation of the system is the distribution of the damping over the two modes of vibration: the relative damping of  $\lambda_{1,4}$  becomes larger and the relative damping of  $\lambda_{2,3}$  becomes smaller at increasing (positive)  $\Omega$ . Finally, at the critical velocity  $\Omega_{crit}$  the latter mode becomes unstable [30] as the real parts of  $\lambda_{2,3}$  and  $\lambda_{2,3}^*$  become positive. For high negative rotational velocities, the real parts of  $\lambda_{1,4}$  and  $\lambda_{1,4}^*$  become positive. The absolute value of the critical rotational velocity  $\Omega_{crit}$  equals the tyre natural frequency  $\omega_0$ .

In rotor dynamics studies the damping in the rotating system is often termed the *internal damping*, in contrast to the damping in a non-rotating frame: the *external damping*. In our tyre model the internal damping results from the tyre sidewall damping ( $k_b$ ) and the external damping results from damping in the suspension and damping in the contact patch. The derivation of the equations of a system with external and internal damping is beyond the scope of this thesis. The interested reader is referred to [30,57]. While the influence of the internal damping is destabilising above the critical speed, the influence of the external damping is always stabilising. The external damping will shift the critical speed to a higher value depending upon the ratio between the internal and external damping. If there is sufficient external damping, the system will not experience an unstable motion until it is run at a very high speed [57].

With the parameters used (see Table 7.1 at the end of this Chapter) the rotating damper causes the free rotating tyre to become unstable above 500 km/h. If the tyre is loaded on the road the critical velocity may rise up to 1000 km/h due to the damping influence of the slip model. Fortunately, the tyre concerned has a speed rating V, with a restricted maximum velocity of 240 km/h, in this velocity range the model will always be stable. The influence of the rotation in the permitted velocity range (0-240 km/h) is rather small.

The real limitations of the operating range of tyres are not related to the destabilising influence of the internal damping. The maximum velocities of tyres are primarily caused by excessive tyre temperatures due to hysteresis (*i.e.* rolling resistance). At very high velocities the rolling resistance may become excessive due to another dynamic effect: the formation of standing waves that involves flexible modes of the belt [93]. Finally, the high tensions in the tyre due to

centrifugal forces may become responsible for another cause of damage to the tyre.

### 7.3 The dynamics of the tyre touching the road surface

Two forces are generated at the tyre-road interface: the normal force  $F_{cN}$  to carry the vehicle weight and the tangential force  $F_{cT}$  for traction and braking. The expressions of the rigid ring dynamics (7.14) if the tyre rolls on a road surface at a slope denoted by the angle  $\beta$  become:

$$m_b \ddot{x}_b + k_{bx}(\dot{x}_b - \dot{x}_a) + c_{bx}(x_b - x_a) - k_{bz}(\Omega + \dot{\theta}_a)(z_b - z_a) = \cos(\beta)F_{cT} + \sin(\beta)F_{cN} \quad (7.20a)$$

$$m_b \ddot{z}_b + k_{bz}(\dot{z}_b - \dot{z}_a) + c_{bz}(z_b - z_a) + k_{bx}(\Omega + \dot{\theta}_a)(x_b - x_a) = -\sin(\beta)F_{cT} + \cos(\beta)F_{cN} \quad (7.20b)$$

$$I_{by} \ddot{\theta}_b + k_{b\theta}(\dot{\theta}_b - \dot{\theta}_a) + c_{b\theta}(\theta_b - \theta_a) = -r_e F_{cT} + M_{cy} \quad (7.20c)$$

As discussed in Section 3.7, the tangential force in the contact patch can be assumed to act at a distance  $r_e$  below the wheel centre. Therefore, the effective rolling radius  $r_e$  is used in Equation (7.20c) to transform the force into a torque acting on the tyre ring. The rolling resistance is modelled as an additional torque  $M_{cy}$  acting from the road on the tyre ring.

Although the freely rotating ring is completely symmetrical (Eq. 7.14), the expressions of the tyre rotating on the road may be made asymmetrical (Eq. 7.20): they have different stiffnesses and damping coefficients for vertical and longitudinal directions. The reason for the possibly introduced asymmetry is the greater freedom in estimating parameter values for obtaining vertical and longitudinal tyre dynamics closer to experimental evidence. Nevertheless, it is thought best to avoid this asymmetry, especially if the rigid ring model is applied in a multi body simulation code. For these simulations the tyre ring and rim are both modelled as rotating rigid bodies. This implies that the sidewall springs and dampers rotate together with the rotating tyre and rim.

The rigid ring model standing on the road has three modes of vibration, as discussed in Section 8.5: the vertical mode, where the tyre ring moves in vertical direction, or to be more precise: where the tyre ring moves in the direction normal to the road. The other two modes are rotational modes: one where the tyre ring rotates in-phase with the rim, and the other where the tyre ring rotates in anti-phase with the rim. The natural frequencies of these modes of vibration were estimated from brake experiments (Chapter 9) and cleat experiments (Chapter 10).

These experiments showed that the tyre natural frequencies (in the range 0-100 Hz) decrease with the velocity. Other studies report the same dependency of the measured tyre natural frequencies on velocity [15,53,68,111,112]. Bruni *et al.* [15] used cleat experiments to identify the natural tyre frequencies. They found that the frequencies of the vertical mode, the in-phase rotational mode and the anti-phase rotational mode decrease with velocity in the investigated velocity range 20-140 km/h. Kobiki *et al.* [53] found that the frequency of the anti-phase rotation dropped from 89 to 84 Hz when the velocity increases from 0 to 40 km/h. Mills *et al.* [68] excited the wheel axle longitudinally: the longitudinal frequencies decreased by 15% in the velocity range 0-60 km/h. Ushijima *et al.* [111] excited the tyre by using a hammer and a road obstacle. They found that the frequency of the vertical mode of vibration decreased by 15% in the velocity range 0-80 km/h. Finally, Vinesse [112] measured the reaction forces at the hub. He identified the same three modes of vibration that are presented in Section 8.5. He concluded that the natural frequencies of the rotating tyre are significantly lower than the frequencies of the standing tyre. Furthermore, his research showed that the frequency of the anti-phase rotational mode decreases with the velocity in the investigated velocity range of 25-55 km/h.

Simulations with the rigid ring model with constant parameters did not show the decrease in the natural frequencies with the velocity. To obtain this influence, some parameters of the model have to be made velocity dependent. We decided to make the sidewall stiffnesses velocity dependent because these stiffnesses have the largest influence on the tyre natural frequencies. The vertical sidewall stiffness is much larger than the vertical residual stiffness: thus the influence of the residual stiffness on the frequencies is relatively small. Conversely, the longitudinal and rotational sidewall stiffnesses are much smaller than the effective tangential stiffness resulting from the slip model. This effective tangential stiffness in the contact zone appears to be so large that it forces the centre of rotation of the rotational modes to lie approximately in the contact zone. Consequently, the frequencies of these rotational modes are hardly influenced by the actual value of the effective tangential stiffness in the contact zone.

To summarise, the sidewall stiffnesses are made velocity dependent. For this the variable  $Q_v$  is introduced. This variable  $Q_v$  is a measure for the deformation velocity of the tyre sidewalls due to the rotation and deformation of the tyre. It is proportional to the rotational tyre velocity and the total displacement of the tyre ring relative to the rim.

$$Q_v = \left| \left( \Omega + \dot{\theta}_a \right) \right| \cdot \sqrt{(x_b - x_a)^2 + (z_b - z_a)^2} \quad (7.21)$$

The sidewall stiffnesses are now made dependent on the square root of the variable  $Q_V$ :

$$c_{bx} = c_{bx0} \left( 1 - q_{bVx} \sqrt{Q_V} \right) \quad (7.22a)$$

$$c_{bz} = c_{bz0} \left( 1 - q_{bVz} \sqrt{Q_V} \right) \quad (7.22b)$$

$$c_{b\theta} = c_{b\theta 0} \left( 1 - q_{bV\theta} \sqrt{Q_V} \right) \quad (7.22c)$$

where the additional subscript 0 denotes the sidewall stiffnesses for a non-rotating tyre, and  $q_{bVx}$ ,  $q_{bVz}$ , and  $q_{bV\theta}$  indicate the contributions of the velocity dependence to the three sidewall stiffnesses. The results presented in Chapter 9 and 10 show that the tyre model with the velocity dependent sidewall stiffnesses is in agreement with the measurements.

### The normal force

If the tyre is loaded on a road surface large deformations of the tyre may occur near the contact patch and a finite contact length arises. The total deformation of the tyre is much larger than the displacement of the rigid ring. Therefore, the vertical residual stiffness  $c_{rz}$  is introduced to obtain the correct overall vertical tyre stiffness. The normal force in the contact patch  $F_{cN}$  is equal to the residual deformation of the tyre times the residual stiffness. The measurements of the vertical tyre stiffnesses in Chapter 2 showed some non-linearities of the vertical tyre stiffness:

- the increase in the total vertical tyre stiffness is slightly more than proportional to the vertical tyre deflection [26].
- the vertical forces arise only if the tyre deflection is positive.
- the vertical tyre stiffness increases with velocity [22,26].
- the tyre radius increases with increasing velocity due to the centrifugal force resulting in an increase in the vertical force for a fixed hub [26].

These effects yielded the following expression for the steady-state vertical tyre force vs. deflection characteristic on a flat road surface:

$$F_z = (1 + q_{V2} |\Omega|) \left\{ q_{Fz2} (\rho_{z0} + \Delta r)^2 + q_{Fz1} (\rho_{z0} + \Delta r) \right\} \quad (2.7a)$$

with:

$$\Delta r = q_{V1} \Omega^2 \quad (2.7b)$$

Here,  $q_{V1}$  is a parameter for the influence of the centrifugal force on the tyre radius  $\Delta r$  and  $q_{V2}$  for the increase in vertical tyre stiffness with velocity;  $q_{Fz1}$  and

$q_{Fz2}$  are the coefficients of the second order polynomial for the vertical force as function of the vertical tyre deformation  $\rho_{z0}$ .

The residual stiffness in series with the vertical sidewall stiffness  $c_{bz}$  (which decreases with velocity, cf. expression 7.22b) should result in the total vertical stiffness from expression (2.7). Neglecting the higher order terms, a third order polynomial is introduced for the vertical force due to the residual tyre deflection:

$$F_{cN} = q_{Fzr3}\rho_{zr}^3 + q_{Fzr2}\rho_{zr}^2 + q_{Fzr1}\rho_{zr} \quad \text{if } \rho_{zr} > 0 \quad (7.23a)$$

$$F_{cN} = 0 \quad \text{if } \rho_{zr} < 0 \quad (7.23c)$$

with:

$$\Delta r = q_{V1}\Omega_a^2 \quad (7.23c)$$

$$\rho_{zr} = z_w - z_b + \Delta r \quad (7.23d)$$

where  $z_w$  denotes the height of the road. On short wavelength unevennesses, the actual height of the road surface  $z_w$  should be replaced by the height  $w$  of the effective road surface. The rotational velocity  $\Omega$  of the original expressions (2.7) has been replaced by the rotational velocity of the rim  $\Omega_a (= \Omega + \dot{\theta}_a)$ . The residual vertical deformation  $\rho_{zr}$  is introduced. The coefficients  $q_{Fzri}$  of the residual polynomial as functions of the coefficients of the total polynomial  $q_{Fzi}$  and the vertical sidewall stiffness  $c_{bz}$  become:

$$q_{Fzr1} = c_{bz} \frac{q_{Fz1}(1 + q_{V2}|\Omega_a|)}{c_{bz} - q_{Fz1}(1 + q_{V2}|\Omega_a|)} \quad (7.24a)$$

$$q_{Fzr2} = c_{bz} \frac{(c_{bz} \cdot q_{Fz2} + q_{Fzr1} \cdot q_{Fz2})(1 + q_{V2}|\Omega_a|)}{(c_{bz} - q_{Fz1}(1 + q_{V2}|\Omega_a|))^2} \quad (7.24b)$$

$$q_{Fzr3} = 2c_{bz} \frac{q_{Fzr2} \cdot q_{Fz2}(1 + q_{V2}|\Omega_a|)}{(c_{bz} - q_{Fz1}(1 + q_{V2}|\Omega_a|))^2} \quad (7.24c)$$

The last influence on the vertical force to be treated, is that of the horizontal force. At high levels of brake force and constant axle height, the vertical force appears to decrease owing to the horizontal displacement of the contact patch. The tangential deformation  $\rho_x$  results from the longitudinal and the rotational sidewall deformations:

$$\rho_x = (x_b - x_a) - r_0(\theta_b - \theta_a) \quad (7.25)$$

The decrease in actual radial deflection of the residual spring is modelled as a quadratic function of  $\rho_x$ . The expression of the residual radial deflection (7.23d) is replaced by:

$$\rho_{zr} = z_w - z_b + \Delta r - q_{F_{cx}} \rho_x^2 \quad (7.26)$$

with  $q_{F_{cx}}$  the parameter concerned.

### The tangential force

Chapter 6 describes four pragmatic tyre models for the longitudinal tyre forces that were developed and tested. The model with the best overall performance was model 4 presented in Figure 6.9. The disadvantage of this model was that additional equations were needed to solve the tyre sidewall deformation. This disadvantage has now changed into a major advantage: for the rigid ring model only a slip model for the contact patch is needed as the deformations of the sidewalls are already represented by the displacements of the rigid ring (Eq. 7.20). The limiting of the slip of the contact model is used here as well.

The transient response of the contact model can be represented by the first order differential equation for the longitudinal slip  $\zeta_{cx}$  in the contact patch:

$$\sigma_c \dot{\zeta}_{cx} + |V_{cr}| \zeta_{cx} = -V_{c,sx} \quad (6.18e)$$

where  $\sigma_c$  denotes the relaxation length of the contact model,  $V_{cr}$  the linear rolling velocity of the tyre ring, and  $V_{c,sx}$  the slip velocity of the belt in the contact zone. The slip velocity is equal to the difference between the velocity  $V_{cT}$  of the centre of the ring oriented parallel to the road surface and the linear rolling velocity of the ring  $V_{cr}$ :

$$V_{c,sx} = V_{cT} - V_{cr} = (\cos(\beta)\dot{x}_b - \sin(\beta)\dot{z}_b) - r_e(\Omega + \dot{\theta}_b) \quad (7.27)$$

where the effective rolling radius  $r_e$  is represented by a third order polynomial of the square root of the normal contact force plus the contribution  $\Delta r$ , which is the increase in tyre radius due to centrifugal forces acting on the tyre ring:

$$r_e = q_{re3}\sqrt{F_{cN}^3} + q_{re2}\sqrt{F_{cN}^2} + q_{re1}\sqrt{F_{cN}} + q_{re0} + \Delta r \quad (3.27)$$

The tangential force in the contact zone  $F_{cT}$  results from the stationary slip characteristic:

$$F_{cT} = F_{cT}(\zeta_c, F_{cN}, \mu) \quad (7.28)$$

The slip characteristics used are those of the brush type model (*cf.* Eq. 3.16). Appendix B discusses the changes needed for the application of the Magic Formula model (*cf.* Eq. 3.18). The inputs to the stationary slip characteristics are the slip in the contact zone  $\zeta_{cx}$ , the normal force in the contact zone  $F_{cN}$ , and the tyre-road friction coefficient  $\mu$ . The relaxation length  $\sigma_c$  of the contact model was

defined as the ratio between the local slip stiffness  $C_{\kappa}$  ( $= \partial F_{cx} / \partial \zeta_{cx}$ ) and the slip stiffness at free rolling  $C_{\kappa 0}$  multiplied by the relaxation length  $\sigma_{c0}$  of the contact patch model at free rolling:

$$\sigma_c = \frac{\sigma_{c0}}{C_{\kappa 0}} \frac{\partial F_x}{\partial \zeta_{cx}} = \sigma_{c0} \frac{C_{\kappa}}{C_{\kappa 0}} \quad (6.19)$$

To ensure numerical stability, the minimum value of this relaxation length has to be limited. As stated in the introduction of the present chapter, no additional tangential residual stiffness is needed. Then the relaxation length  $\sigma_{c0}$  of the contact model at free rolling equals half the contact length  $a$  which can be expressed as a polynomial of the square root of the normal force in the contact zone (cf. Eq. 2.5):

$$a = q_{a2} \sqrt{F_{cN}^2} + q_{a1} \sqrt{F_{cN}} \quad (7.29)$$

If on the other hand, a tangential residual stiffness is needed, the relaxation length of the contact model will be longer than half the contact length.

The total relaxation length of the tyre  $\sigma$  is not a parameter of the model, but may rather be considered as a property. Its value results from all the longitudinal flexibilities of the model, as presented in Figure 7.5. The influence of the translational ( $c_{bx}$ ) and rotational ( $c_{b\theta}$ ) sidewall stiffnesses is much greater than the influence the relaxation length  $\sigma_c$  of the contact model.

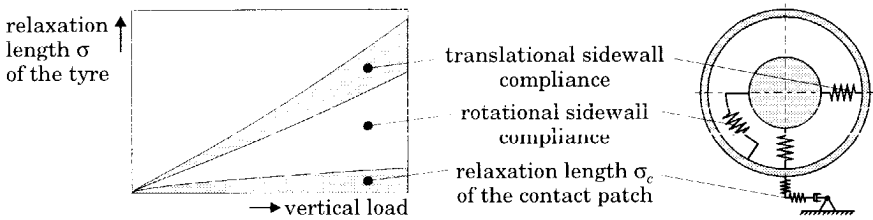
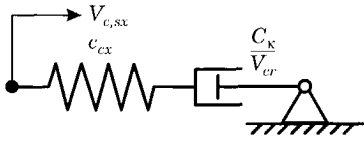


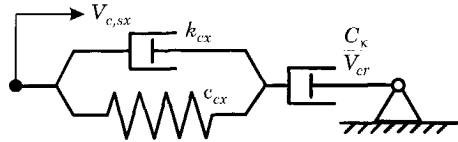
**Figure 7.5:** Contributions of the compliances of the rigid ring model to the total relaxation length of the tyre model.

The relaxation length contact model influences the relative damping of the modes of vibration strongly. When the rotating velocity  $V_{cr}$  approaches zero, the relative damping of a mass-relaxation system (see Section 6.4) becomes zero as well. Simulations at very low velocity showed that the relative damping of the simulated response is too low in comparison to measured tyre responses. Therefore, the original contact model, depicted in Figure 7.6a, is replaced by a contact model including tread element damping depicted in Figure 7.6b.





(a) original contact model



(b) contact model with tread element damping

**Figure 7.6:** Modelling of the damping of the tread elements.

Equation (6.18e) is replaced by:

$$\left( \sigma_c + \frac{k_{cx}}{c_{cx}} |V_{cr}| \right) \dot{\zeta}_{cx} + |V_{cr}| \zeta_{cx} = -V_{c,sx} - \frac{k_{cx}}{c_{cx}} \dot{V}_{c,sx} \quad (7.30)$$

where  $k_{cx}$  denotes the damping coefficient of the tread elements. The relaxation length of the model remains  $\sigma_c$ . The influence of the tread element damping is assumed to decrease with the velocity. Furthermore, the tread element damping is assumed to be proportional to the tread element stiffness. Hence, the ratio between tread element damping and tread element stiffness  $c_{cx}$  is defined as:

$$\frac{k_{cx}}{c_{cx}} = \frac{q_{kc1}}{1 + q_{kc2} |V_{cr}|} \quad (7.31)$$

The model with tread element damping shows the appropriate relative damping at very low velocities.

Section 8.5 shows that the rigid ring model including the contact model has three modes of vibration which can be observed in the measured tyre responses. However, the fourth mode of the model, the horizontal mode, cannot be observed in the measurements. The horizontal mode is the mode of the model with the highest natural frequency (100-140 Hz) and it has very small damping at low velocities. The relative damping of this mode increases by the introduction of the tread element damping. The resulting larger relative damping has two positive effects: first, the unwanted vibrations of the mode are damped rather quickly; and second, the larger damping puts less restrictions to the step size of the numerical integration process.

## Rolling resistance

The rolling resistance is modelled as an external torque  $M_{cy}$  acting from the road on the tyre ring:

$$M_{cy} = -r_c f_r F_{cN} \cdot \text{sgn}(\Omega + \dot{\theta}_b) \quad (7.32)$$

where  $f_r$  denotes the rolling resistance coefficient. If the rotational tyre ring velocity changes sign, the rolling resistance torque changes sign as well. Close to zero rotational velocity expression (7.32) does not predict the appropriate rolling resistance torque. Rather than using this expression directly, the rolling resistance torque is modelled as a dry friction torque and expression (7.32) represents the maximum possible rolling resistance torque. The equations of the dry friction rolling resistance torque are similar to the equations of the dry friction brake torque and will be discussed in Section 7.4.

Both the rolling resistance and rotating damper forces (see Section 7.2) originate from the hysteresis forces in the tyre sidewalls. Nevertheless, the two effects are dealt with separately in the model: the damping factors ( $k_{bx}$ ,  $k_{bz}$ ,  $k_{b\theta}$ ) are directly connected with the tyre sidewall and are used to obtain the appropriate relative damping of the modes of vibration (see Chapters 9 and 10); the rolling resistance moment is assumed to act directly on the ring and is estimated from the stationary slip characteristics (in Chapter 3).

### The tyre-road interface on short wavelength unevenness

The enveloping properties of tyres on short wavelength unevenness were discussed in Chapter 4. The result of Chapter 4 was that the rather complex tyre-road interface on these unevennesses could be represented by a single-point contact model on an effective road surface. The effective road surface could be represented by the effective plane height  $w$  and the effective plane angle  $\beta$ :

$$w = \frac{f\left(x_b - \frac{1}{2}\lambda_{imp}\right) + f\left(x_b + \frac{1}{2}\lambda_{imp}\right)}{2} \quad (7.33a)$$

$$\beta = \frac{f\left(x_b + \frac{1}{2}\lambda_{imp}\right) - f\left(x_b - \frac{1}{2}\lambda_{imp}\right)}{\lambda_{imp}} \quad (7.33b)$$

with,

$$\lambda_{imp} = q_{bf2}a^2 + q_{bf1}a \quad (7.33c)$$

where  $f$  is the expression of the basic function which may be given as a look-up table. The longitudinal shift of these basic functions, denoted by  $\lambda_{imp}$ , is expressed as a second order polynomial in half the contact length  $a$ . The value of  $\lambda_{imp}$  is somewhat smaller than  $2a$ . The relatively fast variations in road plane angle  $\beta$  will generate additional slip velocities in the contact patch (*cf.* Eq. 4.24); therefore expression (7.27) is replaced by:

$$V_{c,sx} = \cos(\beta)\dot{x}_b - \sin(\beta)\dot{z}_b - r_e(\Omega + \dot{\theta}_b) + \rho_z \frac{d\beta}{dt} \quad (7.34)$$

with  $\rho_z$  defined as the total vertical tyre deformation:

$$\rho_z = w - z_a + \Delta r - q_{Fcx}\rho_x^2 \quad (7.35)$$

The effective road plane angle  $\beta$  depends on the state variables. During numerical simulations it is not possible to calculate the derivative of a variable. Rather than differentiating directly, the derivative of  $\beta$  is estimated from a high pass filter with time constant  $\tau$ . The frequency response function of the high pass filter is given by:

$$H = \frac{j\omega}{1 + j\omega\tau} \quad (7.36)$$

At low frequencies, the output of this filter is approximately equal to the derivative of the input. At higher frequencies, the output is limited. The cut-off frequency of this filter should be higher than the natural frequencies of the model. Then in the frequency range of the model, the filter will give the derivative of the input. The estimated derivative  $\dot{\beta}_{est}$  of the road plane angle reads:

$$\dot{\beta}_{est} = (\beta - \beta_{est})/\tau \quad (7.37)$$

## 7.4 The rotation wheel and the application of a brake torque

Horizontal  $x_a$  and vertical  $z_a$  rim motions are given as input to the model. The rotation of the rim about the wheel axis is treated as an additional degree of freedom to the model:

$$I_{ay}\ddot{\theta}_a + k_{b\theta}(\dot{\theta}_a - \dot{\theta}_b) + c_{b\theta}(\theta_a - \theta_b) = M_{ay} \quad (7.38)$$

where  $I_{ay}$  denotes the moment of inertia of the rim and the rotating parts of the brake system, and  $-M_{ay}$  denotes the brake torque. This torque is oriented in a direction opposite to the rim rotational velocity  $\Omega + \dot{\theta}_a$ . Note that  $\Omega$  represents the undisturbed speed of revolution of the rim. The brake is modelled as a dry frictional element, which means that at very large levels of brake torque the wheel becomes locked. This is rather difficult to model as the rim angle  $\theta_a$  is a state variable that cannot be removed easily during simulation. Therefore, the optimal wheel deceleration is calculated to get wheel lock at the end of the time

step considered. This method is similar to the method introduced in Section 6.2 for limiting the slip of pragmatic model 2.

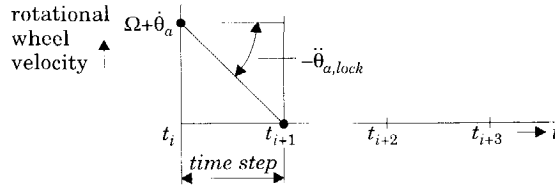


**Figure 7.7:** The optimal wheel deceleration to get wheel lock.

The approach is shown graphically in Figure 7.7. At the beginning of an integration step (from time  $t_i$  to  $t_{i+1}$ ), the rim has the rotational velocity  $\Omega + \dot{\theta}_a$ . The optimal acceleration of the wheel  $\ddot{\theta}_{a,lock}$  can be calculated so that the rotational rim velocity equals zero (i.e. wheel lock) at the end of this integration step:

$$\ddot{\theta}_{a,lock} = -\frac{\Omega + \dot{\theta}_a}{q \cdot h} \quad (7.39)$$

where  $h$  denotes the time step and  $q$  denotes a correction factor that depends on the integration method used. The values of coefficient  $q$  are given in Table 6.2. The brake torque  $M_{ay}$  needed to obtain wheel lock at the end of the integration step is given by:

$$M_{ay} = I_{ay} \ddot{\theta}_{a,lock} + k_{b\theta}(\dot{\theta}_a - \dot{\theta}_b) + c_{b\theta}(\theta_a - \theta_b) \quad (7.40)$$

Now, we have to check whether the dry friction in the disc brake is able to generate this torque:

$$M_{ay} = \begin{cases} M_{ay} & \text{if } -M_{ay,fric} \leq M_{ay} \leq M_{ay,fric} \\ M_{ay,fric} & \text{if } M_{ay} > M_{ay,fric} \\ -M_{ay,fric} & \text{if } M_{ay} < -M_{ay,fric} \end{cases} \quad (7.41)$$

## 7.5 The linearised equations of motion for constraint axle motion

The non-linear rigid ring model developed in the previous sections can be used for non-linear time simulations. Other techniques, like frequency response function, modal analysis, require a linearised model. In this section the non-linear equations of motion will be linearised. The vertical and horizontal axle motions will be constrained:  $x_a = 0$ ,  $z_a = 0$ . This choice is not essential, but this fits the

experimental conditions on the rotating drum test stand (*cf.* Chapter 8, 9 and 10). The non-linear equations may now be linearised by writing the state variables as small variations additional to the stationary values which represent the considered undisturbed state of operation:

$$x_b = x_{b0} + \tilde{x}_b \quad (7.42a)$$

$$z_b = z_{b0} + \tilde{z}_b \quad (7.42b)$$

$$\theta_a = \theta_{a0} + \tilde{\theta}_a \quad (7.42c)$$

$$\theta_b = \theta_{b0} + \tilde{\theta}_b \quad (7.42d)$$

$$\zeta_{cx} = \zeta_{cx0} + \tilde{\zeta}_{cx} \quad (7.42e)$$

The inputs to the model are considered to be small as well: the road surface is assumed to be level with small slope variations; and the brake torque is assumed to vary around an average value:

$$z_w = \tilde{z}_w \quad (7.43a)$$

$$\beta = \tilde{\beta} \quad (7.43b)$$

$$M_{ay} = M_{ay0} + \tilde{M}_{ay} \quad (7.43c)$$

The effective rolling radius becomes:

$$r_e = r_{e0} + \tilde{r}_e, \quad \tilde{r}_e = \eta \tilde{F}_{cN} + \tilde{r}_{ec} \quad (7.44)$$

where  $\eta$  represents the load dependency of the effective rolling radius and  $\tilde{r}_{ec}$  the additional effective rolling radius variation resulting from the road unevennesses (*cf.* Eq. 4.38b). Now, the linearised equations of motion of the tyre-wheel system from Equations (7.20, 6.18e, 7.27, 7.38) with  $k_b = k_{bx} = k_{bz}$  and  $c_b = c_{bx} = c_{bz}$  become:

$$m_b \ddot{\tilde{x}}_b + k_b \dot{\tilde{x}}_b + c_b \tilde{x}_b - k_b \Omega \tilde{z}_b - k_b \dot{\tilde{\theta}}_a z_{b0} = \tilde{F}_{cT} + F_{cN0} \tilde{\beta} \quad (7.45a)$$

$$m_b \ddot{\tilde{z}}_b + k_b \dot{\tilde{z}}_b + c_b \tilde{z}_b + k_b \Omega \tilde{x}_b + k_b \dot{\tilde{\theta}}_a x_{b0} = \tilde{F}_{cN} - F_{cT0} \tilde{\beta} \quad (7.45b)$$

$$I_{ay} \ddot{\tilde{\theta}}_a + k_{b\theta} (\tilde{\theta}_a - \tilde{\theta}_b) + c_{b\theta} (\tilde{\theta}_a - \tilde{\theta}_b) = \tilde{M}_{ay} \quad (7.45c)$$

$$I_{by} \ddot{\tilde{\theta}}_b - k_{b\theta} (\tilde{\theta}_a - \tilde{\theta}_b) - c_{b\theta} (\tilde{\theta}_a - \tilde{\theta}_b) = -r_{e0} \tilde{F}_{cT} - \tilde{r}_e F_{cT0} + \tilde{M}_{cy} \quad (7.45d)$$

$$\sigma_e \ddot{\tilde{\zeta}}_{cx} + r_{e0} \Omega \tilde{\zeta}_{cx} = -\dot{\tilde{x}}_b + r_{e0} \dot{\tilde{\theta}}_b + \tilde{r}_e \Omega \quad (7.45e)$$

The linearised normal force variation in the contact patch equals the overall residual vertical deformation multiplied by the residual vertical stiffness plus a small contribution  $\xi_c$  from the horizontal shift of the contact point:

$$\tilde{F}_{cN} = c_{cz}(\tilde{z}_w - \tilde{z}_b) + c_{cz}\xi_c(\tilde{x}_b - r_{e0}\tilde{\theta}_b + r_{e0}\tilde{\theta}_a) \quad (7.46)$$

The quadratic term  $\rho_x^2$  in expression (7.26) has been linearised for small variations of the tangential deflection around the average value ( $\xi_c = -2q_{F_{xz}}\rho_{x0}$ ). The variation in the longitudinal force depends on the variation of slip in the contact patch and on the variation of the vertical force. The rate of increase in slip force with increasing vertical load at a given slip is indicated by:  $\xi_\kappa$ . The expression of the variation of the longitudinal force in the contact patch reads:

$$\tilde{F}_{cT} = C_\kappa \tilde{\zeta}_{cx} + \xi_\kappa \tilde{F}_{cN} \quad (7.47)$$

Or,

$$\tilde{F}_{cT} = C_\kappa \tilde{\zeta}_{cx} + c_{cz}\xi_\kappa(\tilde{z}_w - \tilde{z}_b) + c_{cz}\xi_\kappa\xi_c(\tilde{x}_b - r_{e0}\tilde{\theta}_b + r_{e0}\tilde{\theta}_a) \quad (7.48)$$

The rolling resistance torque variation reads:

$$\tilde{M}_{cy} = -r_{e0}f_r\tilde{F}_{cN} = -r_{e0}f_rc_{cz}(\tilde{z}_w - \tilde{z}_b) - r_{e0}f_rc_{cz}\xi_c(\tilde{x}_b - r_{e0}\tilde{\theta}_b + r_{e0}\tilde{\theta}_a) \quad (7.49)$$

where the influence of the variations of the effective rolling radius  $\tilde{r}_e$  on the rolling resistance torque variations is neglected. Furthermore, the influences of the velocity dependency of the sidewall stiffnesses (Eq. 7.22) and the velocity dependency of the total vertical tyre stiffness (Eq. 7.23) are small and are neglected in this analysis. Five parameters have been defined:

$$\eta = \frac{dr_e}{dF_z} \quad \text{effective rolling radius variation with vertical load}$$

$$C_\kappa = \frac{\partial F_{cx}}{\partial \xi_{cx}} \quad \text{slip stiffness at given vertical load and longitudinal slip}$$

$$\xi_\kappa = \frac{\partial F_{cx}}{\partial F_{cz}} \quad \text{variation of } F_{cx} \text{ with load at vertical load and longitudinal slip}$$

$$c_{cz} = \frac{dF_{cz}}{dz_w} \quad \text{vertical residual stiffness}$$

$$\xi_c = \frac{\partial z_c}{\partial x_c} \quad \text{vertical deflection due to horizontal shift of the contact patch}$$

Finally, we introduce the composite parameters:

$$Q_x = c_{cz}\xi_\kappa \quad (7.50a)$$

$$Q_y = c_{cz}(r_{e0}\xi_\kappa + r_{e0}f_r + \eta F_{cT0}) \quad (7.50b)$$

$$Q_\zeta = c_{cz}\Omega\eta \quad (7.50c)$$

The contribution due to the composite parameters  $Q$ 's is rather small. The final set of linear equations becomes:

$$m_b \ddot{\tilde{x}}_b + k_b \dot{\tilde{x}}_b + c_b \tilde{x}_b - k_b \Omega \tilde{z}_b - k_b \tilde{\theta}_a z_{b0} = Q_x(\tilde{z}_w - \tilde{z}_b) + Q_x \xi_c(\tilde{x}_b - r_{e0} \tilde{\theta}_b + r_{e0} \tilde{\theta}_a) + C_\kappa \tilde{\zeta}_{cx} + F_{cN0} \tilde{\beta} \quad (7.51a)$$

$$m_b \ddot{\tilde{z}}_b + k_b \dot{\tilde{z}}_b + c_b \tilde{z}_b + k_b \Omega \tilde{x}_b + k_b \tilde{\theta}_a x_{b0} = c_{cz}(\tilde{z}_w - \tilde{z}_b) + c_{cz} \xi_c(\tilde{x}_b - r_{e0} \tilde{\theta}_b + r_{e0} \tilde{\theta}_a) - F_{cT0} \tilde{\beta} \quad (7.51b)$$

$$I_{ay} \ddot{\tilde{\theta}}_a + k_{b\theta}(\tilde{\theta}_a - \tilde{\theta}_b) + c_{b\theta}(\tilde{\theta}_a - \tilde{\theta}_b) = \tilde{M}_{ay} \quad (7.51c)$$

$$I_{by} \ddot{\tilde{\theta}}_b - k_{b\theta}(\tilde{\theta}_a - \tilde{\theta}_b) - c_{b\theta}(\tilde{\theta}_a - \tilde{\theta}_b) = -Q_y(\tilde{z}_w - \tilde{z}_b) - Q_y \xi_c(\tilde{x}_b - r_{e0} \tilde{\theta}_b + r_{e0} \tilde{\theta}_a) - r_{e0} C_\kappa \tilde{\zeta}_{cx} - \tilde{r}_{ce} F_{cT0} \quad (7.51d)$$

$$\sigma_c \ddot{\tilde{\zeta}}_{cx} + r_{e0} \Omega \tilde{\zeta}_{cx} = -\dot{\tilde{x}}_b + r_{e0} \dot{\tilde{\theta}}_b + Q_\zeta(\tilde{z}_w - \tilde{z}_b) + Q_\zeta \xi_c(\tilde{x}_b - r_{e0} \tilde{\theta}_b + r_{e0} \tilde{\theta}_a) + \tilde{r}_{ec} \Omega \quad (7.51e)$$

The linearised set of equations is used to calculate the modes of vibration in Chapter 8. In Chapter 9, these equations are used to calculate the frequency response function to brake torque variations. In Chapter 10, the linearised model is used to roll over short wavelength unevenness.

## 7.6 Validation of the model and parameter assessment

This section discusses briefly how the rigid ring model is validated in the subsequent chapters and how the dynamic parameters of the model are assessed in these chapters.

### Validation of the model

First of all, the mode shapes of the rigid ring model are validated in Chapter 8. That chapter presents the modes of vibration of a non-rotating tyre which were assessed experimentally by applying the experimental modal analysis technique. The modes in the frequency range 0-250 Hz are compared to the modes of the flexible ring model. The modes in the frequency range 0-100 Hz are used to validate the rigid ring model. Furthermore, Chapter 8 presents the influence of various boundary conditions on the modes of the rigid ring model.

Chapters 9, 10 and 11 present the dynamic tyre response to brake torque variations, road unevennesses and axle height oscillations at constant brake torque, respectively. The experiments presented in these chapters are used to

estimate the parameters of the model and to validate the model for a number of severe conditions.

Chapter 9 shows that the model provides a good representation of the dynamic tyre response to large brake torque, successive steps in brake torque (Section 9.3), braking with wheel lock (Section 9.4) and braking to stand-still of both the tyre and the drum (Section 9.5). The model with the parameters obtained from the small random variations represents the non-linear tyre responses to large brake torque variations rather well. A validation of the model structure shows that the ratio of the slip stiffness and all tangential stiffnesses in series (sidewall stiffnesses and tread element stiffness) equals the relaxation length of the total tyre obtained from the experiments.

In Chapter 10 the tyre model is validated rolling over short wavelength road unevennesses. The effective road surface, assessed in Chapter 4, is used as excitation of the model rather than the actual road surface. Chapter 10 shows that the effective inputs can be used, also at higher velocities and during braking.

Chapter 11 presents responses of a tyre subjected to a constant brake torque during axle height oscillations. The responses of the model during very severe conditions are rather good: large variations in axle height in which the vertical force decreases to such an extent that wheel lock occurs, including the case where the tyre loses contact with the road.

### Stationary and basic parameters

The mass of the tyre and the rim were measured directly. The masses and moments of inertia of the parts of the tyre that move together with the rigid ring or the rim were obtained from cutting the tyre into five pieces and estimating the mass properties of each piece (*cf.* Section 2.5). To obtain the total value of  $I_{ay}$  (the moment of inertia of the tyre-wheel system that rotates together with the rim) the moment of inertia of the rotating parts of the tyre test stand should be added to the moment of inertia of the rim:

- *cleat and brake* test stand, all rotating parts:  $0.57 \text{ kg m}^2$
- *cleat and brake* test stand, the rotating parts except brake system:  $0.41 \text{ kg m}^2$
- *measurement tower*, all rotating parts:  $0.51 \text{ kg m}^2$

The contact length parameters were obtained from contact prints of a non-rotating tyre (*cf.* Section 2.2). The relaxation length of the contact patch at free rolling  $\sigma_{c0}$  is equal to half the contact length. The parameters to represent the vertical tyre stiffness and tyre radius growth as function of the velocity were estimated from the stationary rolling experiments at constant axle height



(*cf.* Section 2.4). The parameters of the effective rolling radius were obtained from a rolling experiment at very low velocity (*cf.* Section 3.7). These parameters, together with the growth of the tyre free radius obtained from the vertical tyre stiffness experiments, can accurately represent the effective rolling radius at higher velocities.

The parameters of the stationary slip characteristics were obtained from the slowly increasing brake torque. For the brush model, besides the contact length  $a$  and vertical load  $F_z$  only two additional parameters are needed: the tread element stiffness per unit of length  $c_{ep}$  and the coefficient of friction  $\mu$ . The tread element stiffness corresponds well with the estimated slip stiffness from FRFs to brake torque variations around an average brake torque (*cf.* Section 9.2). The friction coefficient, on the other hand, is not constant. Its value depends highly on operating condition (velocity, tyre temperature, time).

During the experiments with stationary rolling of a non-braked tyre at constant axle height the (small) longitudinal reaction forces were measured as well. From these forces the rolling resistance coefficient was estimated. The resulting value is hardly changing with the velocity in the range 25-143 km/h. The value of the rolling resistance coefficients is in agreement with the offset of stationary slip characteristic measured on the road.

### Dynamic parameters

It is important that excitation of the tyre for the estimation of the dynamic parameters (sidewall stiffness and damping coefficients) is realistic since the tyre stiffness and damping depend on the amplitude and frequency of excitation and on the tyre temperature. Consequently, the excitations applied on the test stands have to be comparable to the excitations of the tyre running in a vehicle. It is assumed that the relatively small random brake torque variations around an average value of brake torque (*cf.* Section 9.2) and the cleat excitations (*cf.* Chapter 10) may be applied for assessing the dynamic parameters. The linearised tyre rigid ring model (*cf.* Eq. 7.51) was used to estimate the tyre parameters.

The experiments that provided the most accurate method for estimating the parameters used random brake torque variations. Two kinds of Frequency Response Functions were used: the FRF of longitudinal force to brake torque variations and the FRF of longitudinal force to wheel slip variations. Even though the responses of the rigid ring model represent the measured tyre responses rather well, the difference in calculated and simulated amplitude of the anti-

phase rotational mode is so large that an optimisation method based on the difference between the measured FRFs and calculated FRFs could not be used to estimate the parameters of the model. Therefore, the parameters were estimated by using an indirect approach. First, the tyre properties which characterise the dynamic responses were obtained from the measurements:

- natural frequency of the in-phase rotational mode
- natural frequency of the anti-phase rotational mode
- relative damping of the in-phase rotational mode
- relative damping of the anti-phase rotational mode
- slip stiffness
- total relaxation length of the tyre

Second, the following parameters of the model were estimated from these properties:

- translational sidewall stiffness  $c_b$
- rotational sidewall stiffness  $c_{b\theta}$
- translational sidewall damping  $k_b$
- rotational sidewall damping  $k_{b\theta}$
- tread element stiffness per unit of length  $c_{cp}$

First, the parameters were estimated for each operating condition (average brake torque, velocity and constant axle height). The results showed that the sidewall stiffnesses decrease with increasing velocity. The coefficients which represent this influence (*cf.* Eq. 7.22) were estimated in a second fit where the properties of the tyre obtained from experiments at all conditions were used. The three coefficients of this equation are assumed to be equal to each other. The resulting value of the tread element stiffness  $c_{cp}$  corresponds well to the value obtained from the stationary slip characteristics.

The tyre sidewall stiffnesses and damping coefficients and the tread element damping could also be obtained from the cleat experiments. The variation in the parameter values thus obtained was rather large as auto spectral densities of the responses were used rather than the frequency response functions. In contrast to the brake experiments, an optimisation method based on the differences in simulated spectral densities and measured spectral densities could not be used.

To conclude, the brake experiments were preferred for estimating the sidewall stiffness and damping coefficients. Nevertheless, it is thought to be very important to validate the natural frequency of the vertical mode of the model (with parameters obtained from brake experiments) against the measured natural frequency obtained from the cleat experiment.

**Table 7.1a:** *The parameters of the rigid ring tyre model.*

description	symbol	unit
mass of tyre ring	$m_b$	kg
moment of inertia that moves with rim	$I_{ay}$	kg m <sup>2</sup>
moment of inertia that moves with tyre ring	$I_{by}$	kg m <sup>2</sup>
translational sidewall damping	$k_b$	Ns/m
rotational sidewall damping	$k_{b\theta}$	Nms/rad
translational sidewall stiffness (at $\Omega=0$ )	$c_{b0}$	N/m
rotational sidewall stiffness (at $\Omega=0$ )	$c_{b\theta 0}$	Nm/rad
longitudinal tread stiffness per unit of length	$c_{cp}$	N/m <sup>2</sup>

**Table 7.1b:** *The parameters of the polynomials and miscellaneous coefficients of the rigid ring tyre model.*

Half contact length $a$ as function of vertical load $F_z$				(Eq. 2.5)
$q_{a1}$	[m/ $\sqrt{N}$ ]	$q_{a2}$	[m/N]	
Vertical tyre stiffness $C_z$ as function of deflection $\rho_z$ and velocity $\Omega$				(Eq. 2.7)
$q_{Fz1}$	[N/m]	$q_{Fz2}$	[N/m <sup>2</sup> ]	$q_{V1}$ [m/s <sup>2</sup> ] $q_{V2}$ [s]
Rolling resistance coefficient $f_r$ as function of the velocity $\Omega$				(Eq. 3.22)
$q_{fr0}$	[–]	$q_{fr1}$	[s/m]	$q_{fr4}$ [s <sup>2</sup> /m <sup>2</sup> ]
Effective rolling radius $r_e$ as function of vertical load $F_z$				(Eq. 3.27)
$q_{re0}$	[m]	$q_{re1}$	[m/ $\sqrt{N}$ ]	$q_{re2}$ [m/N] $q_{re3}$ [m/ $\sqrt{N}^3$ ]
Decrease of tyre sidewall stiffnesses as function of velocity $\Omega$				(Eq. 7.22)
$q_{bVx}$	[ $\sqrt{s}/\sqrt{m}$ ]	$q_{bVz}$	[ $\sqrt{s}/\sqrt{m}$ ]	$q_{bV\theta}$ [ $\sqrt{s}/\sqrt{m}$ ]
Tread element damping $k_{cx}$ as function of the velocity $V_{cr}$				(Eq. 7.31)
$q_{kc1}$	[s]	$q_{kc2}$	[s/m]	
Decrease in radial deflection with longitudinal deflection				(Eq. 7.26)
$q_{Fcx}$	[1/m]			

### The parameters of the rigid ring model

Table 7.1a lists the parameters of the rigid ring model and Table 7.1b lists the coefficients of the polynomials used. These tables do not show the values of the parameters for reasons of confidentiality. The simulations presented in Chapters

9 through 11 were performed with one set of parameters. No additional changes in the parameter values were needed to simulate the tyre response at the different operating conditions. However, there is one exception: braking with wheel-lock presented in Section 9.4. When the tread element damping is included in the model, the vibrations of the tyre are strongly damped. A model without the tread element damping shows the appropriate damping at wheel-lock. Therefore, the results of the simulations presented in Section 9.4 were performed without tread element damping ( $q_{kc1}=0$ ).

### **Experiments which cannot be used for estimating the parameters of the rigid ring model**

The tyre stiffnesses obtained from the experiments are very sensitive to the operating conditions. These stiffnesses cannot be obtained from experiments with a non-rotating tyre. The stiffnesses which result from experiments in which the forces are measured after the tyre has settled are too low:

- total vertical tyre stiffness of the tyre standing on the road (*cf.* Table 2.2).
- total longitudinal tyre stiffnesses of the tyre standing on the road (*cf.* Section 2.4).
- tyre sidewall stiffnesses which were measured directly inside a test drum (*cf.* Table 4.3).

The stiffnesses which result from experiments in which the non-rotating tyre is excited dynamically with relatively large amplitudes are slightly too high:

- total vertical tyre stiffness of the tyre standing on the road, obtained from sinusoidal axle height variations (*cf.* Table 2.3a).

The stiffnesses which result from experiments where the non-rotating tyre is excited dynamically with very small amplitudes are much too high:

- total vertical tyre stiffness of the tyre standing on the road, obtained from random axle height variations (*cf.* Table 2.3b).
- tyre sidewall stiffnesses obtained from modal analysis (*cf.* Table 8.2).

# 8

## Modal Analysis of Tyre In-Plane Vibrations

---

### 8.1 Introduction

The rigid ring model, developed in the previous chapter, represents the in-plane vibrations of tyres in the frequency range 0-80 Hz. These in-plane vibrations are generally excited by road irregularities, brake torque fluctuations, axle height oscillations and tyre non-uniformities. The dynamic responses of the rigid ring model due to these excitations are validated in the laboratory by special experiments conducted with the *cleat and brake* test stand and *tyre measurement tower* described in Appendix A. In the subsequent chapters the setup and results of these tests are discussed: Chapter 9 concerns the responses to brake torque variations; Chapter 10 the responses to road unevenness and Chapter 11 the responses to axle height oscillations. For the validation of the model the responses of reaction forces and velocities are measured at the wheel axis. The modal analysis technique is applied in this chapter to link the natural frequencies of the tyre-wheel with the accompanying mode shapes.

Section 8.2 presents the experimental modal analysis of a non-rotating tyre for two boundary conditions: a free (non-loaded) tyre with the horizontal and vertical positions of the spindle axis fixed and a tyre loaded on the road. The tyre is excited by a hammer and the responses are measured on the tyre

circumference in tangential and radial direction with accelerometers. The mode shapes and the resonance frequencies are assessed from the measured frequency response functions.

The results of the experimental modal analysis are first compared to the modes of the *flexible ring* tyre model, which has been used in Chapter 4 for the tyre rolling over short wavelength road unevennesses. This model, presented in the PhD Thesis of Gong [32], describes the deformation of the tyre tread-band accurately in the frequency range 0-300 Hz. The *flexible ring* model is used to obtain more of the insight into differences between the modes of a free tyre and the modes of a standing tyre. This model is also used to identify modes which were hard to measure accurately. In particular modes of vibration with little difference in frequencies are difficult to distinguish and identify in the tests (*cf.* modes  $n=1$  and  $n=2$  of the standing tyre in Figure 8.3).

The modes of vibration of the tyre can be classified into *rigid* modes and *flexible* modes. The *rigid* modes refer to those vibrations of the tyre in which the tyre tread-band moves as a rigid body supported on springs. The *flexible* modes, on the other hand, show deformations of the tyre tread-band.

The last section of this chapter presents the modes of vibration of the *rigid ring* tyre model. In this model, developed in the previous chapter, the tyre tread-band is modelled as a rigid body connected with springs to the rim. The frequency range of this model is limited to 80 Hz and this model shows only the *rigid* modes of the tyre. In that section the rigid ring tyre model is used to study the influence of vertical load, rotational velocity and brake force on the modes of vibrations.

Table 8.1 presents a chronological survey of literature on experimental and theoretical analysis of tyre in-plane vibrations. The following items of interest are considered:

- **Tyre construction.** The research on the analysis of tyre vibrations started in the 60s focusing on the differences between the then standard bias ply tyres and the new radial tyres [17,68,89,109]. The radial tyre with its stiff construction of the tread-band, has 6-8 modes in the frequency range of 0-300 Hz. The bias ply tyre, on the other hand, shows only the two lowest modes.
- **Rotational velocity.** The rotational velocity generates centrifugal and Coriolis accelerations. The centrifugal force increases the pre-tension in the tyre tread-band, resulting in higher frequencies of the flexible modes of vibration. The measured frequencies of the rigid modes, however, are significantly lower at higher velocities [68,97,111,112,113]. The rotating tyre complicates the modelling of the tyre system as transformations between the rotating and fixed coordinate system are needed.

**Table 8.1:** *Survey of literature on the analysis of tyre in-plane tyre vibrations.*

reference	tyre type		velocity  non-rotating rotating	boundary conditions						model used  FEM ring modal	experiments					
	radial ply	bias ply		spindle		patch			modal holography spindle cleat							
				free	pinned		rim fixed	suspension						free	fixed	
Chiesa [17]	• •	• •	• •				•		•						•	
Tielking [109]	•		• •		•				•		•					
Böhm [12]	•		•		•				•	•			•			
Mills [68]	• •	•	• •			• •			• •						• •	
Potts [89]	• •	•	•		•				•					•		
Potts [90]	• •	•	•		•				•					• •	•	
Potts [91]	•		•		•		•		•	•			•		•	
Soedel [103]	•		•		•				•	•						
Kung [54]	•		•		•				•				•			
Kung [55]	•		•				•		•		•					
Richards [95]	•		•	•	•	•	•		•	•			•			
Ushijima [111]	•		• •			• •			•			•			• •	
Vinasse [112,113]	• •		• •			• •			•	•			•			
Deneuvy [21]	•		•		•				•	•			•			
Zhang [124]	•		•		•		•		•			•			•	
Huang [42]	•		•		•				•				•			
Huang [42,43]	•		• •		•				•	•						
Gong [33]	•		• •	•	•	•	•		•	•						
Scavuzzo [97]	•		•				•		•				•			
Fejes [27]	•		•		•				•				•			
Bannwitz [9]	•		•		•				•	•					•	
Kim [50]	•		•		•				•							
Negrus [76]	•		•	•	•				•	•			•			

- **Spindle boundary conditions.** The in-plane tyre resonance frequencies are highly dependent on the boundary conditions of the contact patch and the spindle [95]. The most common spindle boundary conditions are: (1) a free wheel; (2) a pinned wheel: the vertical and horizontal motion of the spindle are constrained, but the rim may rotate freely about the spindle-axis; (3) a fixed wheel: the rim is also fixed in rotation and (4) the wheel in an actual vehicle suspension. The spindle boundary conditions affect only the rigid body modes of the tyre.
- **Contact patch boundary conditions.** The ground contact destroys the symmetry of the tyre structure and leads to mathematical complications because the circumferential mode components can no longer be simply expressed by harmonic functions [103]. This non-symmetry causes the resonance peaks to split into double peaks [21,42,112,113]. The lowest resonance frequencies of the double peaks are approximately equal to the frequencies of the unloaded tyre while the highest frequencies of the double peaks are a little higher than the frequencies of the free tyre. Some researchers performed incomplete modal analysis [76]. They did not recognise the splitting of the resonances and drew the wrong conclusion that all frequencies of the tyre standing on the road are higher than the frequencies of the free tyre.
- **Theoretical modal analysis.** Various models have been used to model the in-plane vibrations of pneumatic tyres. The Finite Element Models (FEM) describe the tyre geometry in detail. The influences of non-linearities of the tyre due to large deformations can be modelled accurately. The constraints due to the finite contact length can easily be added [95,124]. The disadvantages of FEM are that it takes a lot of effort to build accurate models and simulations are time consuming. The ring model introduced by Tielking [109] is an elegant model. This model uses a circular beam supported on an elastic foundation to represent the motion of the tread-band of a pneumatic tyre in the plane of the wheel. Tielking introduced the assumption of in-extensibility of the circular beam which simplifies the equations. The mode shapes of the ring model are found by expanding the tread-band deformation in a Fourier series. The third type of model uses a direct modal representation of the tyre from experimental data without using a theoretical model. The measurements are represented directly by the modal parameters of the model [124].
- **Experimental modal analysis.** The classic modal analysis is performed by exciting the tyre with a hammer or a shaker and measuring accelerations at several points on the tyre circumference. This method can be used for non-



rotating tyres only. Holography has been used to identify the mode shapes of a rotating tyre as well. A third method is based on the excitation of the tyre in the contact patch or at the spindle and measuring the reaction forces at the spindle. This method shows the natural frequencies of the tyre only and not the corresponding mode shapes. The last method is the excitation of the tyre by road unevenness (*e.g.*, cleats) and measuring the force responses at the spindle. Ushijima [111] used force transducers mounted under the cleat to measure the excitation forces as well.

## 8.2 Experimental modal analysis

The basic idea of experimental modal analysis is the excitation of a structure by a measurable dynamic force and measuring the dynamic responses at several points of the structure. In this section the Single Input Multiple Output technique (SIMO) is used: the structure is excited at one point. This technique can be used to identify structures with little damping and clear mode shapes. The Frequency Response Functions (FRFs) obtained show the resonance frequencies of the structure. The mode shapes may be determined from the gains at the resonance frequencies at several points of the structure.

### Experimental setup

The tyre and rim are mounted on a spindle on the *cleat and brake* test stand (*cf.* Appendix A). The wheel can rotate freely about its axis of revolution. The spindle motions in vertical and horizontal directions have been constrained to zero. The tyre was tested for two situations: the tyre not in contact with the drum and the tyre standing on the drum at 4000 N pre-load.

The easiest, fastest and thus most widely used excitation technique for modal analysis measurement is impact excitation. The system is excited by an impulse force generated by a hammer hitting the system. Figure 8.1a shows the points and directions of excitation used: radial on the tyre surface (point 3), tangential on the tyre surface (points 1 and 3), and tangential on the rim (point 12).

The impact force is measured by piezo electric transducers located at various points on the tyre circumference. The excitations have been evaluated by the frequency contents of the inputs signal. For an accurate estimation of the FRFs, the energy should ideally be distributed uniformly over the frequency range of interest. Best results were obtained with a plastic tip on top of the hammer and a

small piece of aluminium mounted on the tyre at the point of impact. A relatively small impulse was used to ensure a linear response of the tyre.

The accelerometers were attached to the tyre surface with heated beeswax, which is an easy, light and stiff connection. Figure 8.1b shows the positions and orientations of the accelerometers. The responses in both radial and tangential directions were measured at ten locations along the tyre circumference. The responses at point 11 could not be measured: this point lies at the centre of the contact patch of the loaded tyre; the free tyre could not be lifted clear of the drum sufficiently to mount an accelerometer at this position.

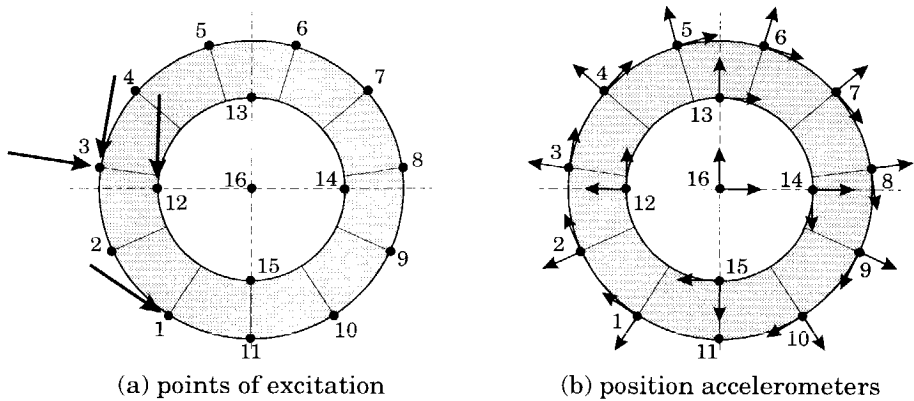


**Figure 8.1:** *Experimental setup: (a) the positions and directions of the force excitations and (b) the positions and orientations of the accelerometers.*

The rim is expected to rotate as a rigid body in the frequency range of interest. Therefore, the responses of the rim were measured at four points (12-15) only. Finally, the response was also measured at point (16) on the frame to which the spindle is attached.

The duration of a single measurement was two seconds at 512 Hz sampling rate. Each measurement was repeated five times to improve the signal to noise ratio and to enable the estimation of the coherence functions. Although the impact excitation technique is known to be the most simple excitation type, it is very hard to control precisely the intensity and direction of the impacts with hand-held excitation hammers. So, the estimated coherence functions were used to evaluate the validity of each measurement.

## The Frequency Response Functions

The total number of measured responses was 30. The estimated FRF  $H_i(\omega)$  and coherence function  $\Gamma_i(\omega)$  of the  $i^{\text{th}}$  response are defined by:

$$H_i(\omega) = \frac{S_{FX_i}(\omega)}{S_{FF}(\omega)} \quad (8.1a)$$

$$\Gamma_i(\omega) = \sqrt{\frac{|S_{FX_i}(\omega)|^2}{S_{X_iX_i}(\omega) \cdot S_{FF}(\omega)}} \quad (8.1b)$$

where  $S_{FX_i}(\omega)$ ,  $S_{X_iX_i}(\omega)$  and  $S_{FF}(\omega)$  are the averaged cross spectral density, the auto spectral density of the  $i^{\text{th}}$  response and the auto spectral density of the excitation force, respectively. Figure 8.2 shows the estimated frequency response function at the radial driving point (3) for the two boundary conditions. The FRF for the free tyre clearly shows five resonances in the frequency range 100-250 Hz. The natural frequencies are determined from the positions of peaks and the degree of damping is estimated from the width of the peaks. The gain of the resonance can be found from the height of the peak. It is interesting to observe that the boundary condition in the contact patch of the standing tyre leads to doubling of the number of resonance peaks, and the height of the peaks varies considerably.

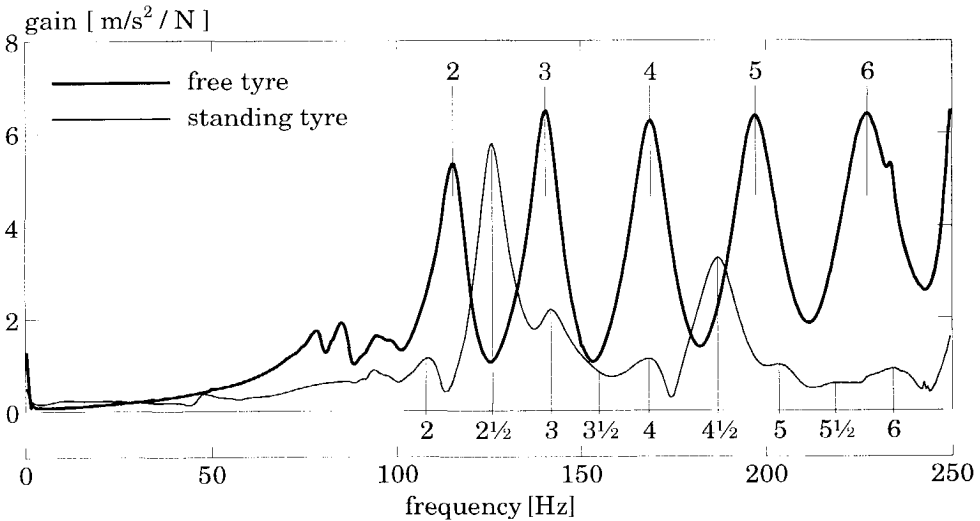


**Figure 8.2:** Measured frequency response functions in radial direction at point 3 due to a radial excitation at point 3 for two boundary conditions.

### Estimating the mode shapes

Figure 8.2 shows the frequency response function measured at the radial driving point. Thirty FRFs were measured which showed the same resonance frequencies with different gains. The mode shapes are related to these gains. Furthermore, four sets of experiments were performed with four different points of excitation.

The sharp peaks in the measured FRFs show that the tyre has little damping. Furthermore, each resonance peak may be considered to represent a distinct Single Degree Of Freedom system (SDOF), since the resonance frequencies are well separated. Consequently, we may assume that the vibrations in the region of resonance frequencies represent normal modes of the tyre. Using this approximation the modal FRF  $G_n(\omega)$  may be expressed in terms of the FRF of a SDOF system:

$$G_n(\omega) = \frac{\omega_{0n}^2}{\omega_{0n}^2 + 2j\kappa_n\omega\omega_{0n} - \omega^2} \quad (8.2)$$

where  $\omega_{0n}$  denotes the natural frequency of the SDOF system and  $\kappa_n$  the relative damping. The total response function  $H_i(\omega)$  of the tyre at point  $i$  is equal to the sum of all modal response functions multiplied by the modal amplitudes  $a_{i,n}$ :

$$H_i(\omega) = \sum_{n=1}^m a_{i,n} G_n(\omega) \quad (8.3)$$

where  $n$  denotes the mode number and  $m$  the number of modes used. The modal amplitude  $a_{i,n}$  is defined as the normalised inner product of the  $i^{th}$  response and the  $n^{th}$  modal response in a narrow frequency range around the resonance frequency:

$$a_{i,n} = \frac{\overline{G_n(\omega)}^T H_i(\omega)}{\overline{G_n(\omega)}^T G_n(\omega)} \quad (0.95 \omega_{0n} < \omega < 1.05 \omega_{0n}) \quad (8.4)$$

The degree of fit is expressed by defining an error function  $E_{i,n}$ :

$$E_{i,n} = \|H_i(\omega) - a_{i,n} G_n(\omega)\| \quad (0.95 \omega_{0n} < \omega < 1.05 \omega_{0n}) \quad (8.5)$$

The total error  $E_n$  then reads:

$$E_n = \sum_{i=1}^{n_r} E_{n,i} \quad (8.6)$$

where  $n_r$  is the number of measured FRFs. The total error  $E_n$  was minimised by fitting the optimal values for natural frequency  $\omega_{0n}$  and relative damping  $\kappa_n$ . Using this method all modes are fitted individually but the responses of all 30

measurements are used at the same time. Figure 8.3 in Section 8.4 present the resulting mode shapes. A cubic interpolation between the measured points is used to obtain smooth mode shapes.

The responses at point 11, located at the underside of the tyre, could not be measured. In the case of the free tyre, the amplitude at this point was estimated from the amplitudes of the adjacent points. If the tyre stands on the road, point 11 is located at the centre of the contact patch and the amplitude at this point is set equal to zero. Section 8.4 discusses the results in detail.

### 8.3 Theoretical modal analysis using the flexible ring model

The flexible ring model introduced in Chapter 4 (*cf.* Figure 4.3), consists of a circular ring representing the tyre tread-band, a mass representing the rim, circumferentially distributed radial and tangential springs representing the tyre sidewalls and pressurised air. The deformation of the flexible ring was represented by a set of partial differential equations with derivatives with respect to time  $t$  and angular position  $\theta$  (*cf.* Eq. 4.1).

As in the analysis presented in Chapter 4, the *Modal Expansion Method* is used to simplify the analysis. In contrast to the analysis presented in Chapter 4, the equations of the flexible ring model will not be simplified by the introduction of the *in-extensibility assumption* (*cf.* Eq. 4.3), even though this assumption is usually valid for radial tyres [32]. The *in-extensibility assumption* leads to a total pressure distribution (*cf.* Eq. 4.7) which is a combination of the tangential and radial pressure distributions. The total pressure distribution makes a discrimination between tangential and radial constraints in the contact patch difficult. When the *in-extensibility assumption* is not used, expression (4.5) of the tangential  $v_b$  and radial  $w_b$  displacements of the flexible ring takes the form:

$$v_b(\theta, t) = \sum_{n=0}^{+\infty} a_n(t) \cos n\theta + b_n(t) \sin n\theta, \quad w_b(\theta, t) = \sum_{n=0}^{+\infty} c_n(t) \cos n\theta + d_n(t) \sin n\theta \quad (8.7)$$

where  $a_n(t)$ ,  $b_n(t)$ ,  $c_n(t)$  and  $d_n(t)$  are the generalised modal displacements. Substituting Equations (8.7) into (4.1), multiplying the resulting equations by  $\cos(n\theta)$  and  $\sin(n\theta)$ , and integrating these equations over  $2\pi$  yields the equations of motion of the modal displacements  $\underline{x}_n$ :

$$\mathbf{M}_n \ddot{\underline{x}}_n + \mathbf{C}_n \dot{\underline{x}}_n = \underline{F}_n \quad (n = 0, 1, 2, 3, \dots) \quad (8.8)$$

where  $\mathbf{M}_n$ , and  $\mathbf{C}_n$  are the modal mass matrix and modal stiffness matrix, respectively, and  $\underline{F}_n$  are the generalised modal forces. To obtain this result, the

orthogonality of the sine and cosine functions was used. The modal equations, the generalised modal displacements, the modal forces and the modal parameters read for  $n \geq 1$ :

$$\mathbf{M}_n \ddot{\mathbf{x}}_n + \mathbf{C}_n \dot{\mathbf{x}}_n = \mathbf{F}_n \quad (8.9a)$$

$$\mathbf{x}_n = [a_n \quad b_n \quad c_n \quad d_n]^T \quad (8.9b)$$

$$\mathbf{F}_n = [\xi_{cv,n} \quad \eta_{cv,n} \quad \xi_{cw,n} \quad \eta_{cw,n}]^T \quad (8.9c)$$

$$\mathbf{M}_n = \begin{bmatrix} m_{bn} & 0 & 0 & 0 \\ 0 & m_{bn} & 0 & 0 \\ 0 & 0 & m_{bn} & 0 \\ 0 & 0 & 0 & m_{bn} \end{bmatrix} \quad (8.9d)$$

$$\mathbf{C}_n = \begin{bmatrix} C_{bv,n} & 0 & 0 & -C_{bvw,n} \\ 0 & C_{bv,n} & C_{bvw,n} & 0 \\ 0 & C_{bvw,n} & C_{bw,n} & 0 \\ -C_{bvw,n} & 0 & 0 & C_{bw,n} \end{bmatrix} \quad (8.9e)$$

The zeroth order modes are slightly different: We only have two modal displacements  $a_0$  and  $c_0$  because the sine terms are zero for  $n=0$ . Furthermore, the equation of the rim (4.1e) is added to the zero order modes. The modal equations read for  $n=0$ :

$$\mathbf{M}_0 \ddot{\mathbf{x}}_0 + \mathbf{C}_0 \dot{\mathbf{x}}_0 = \mathbf{F}_0 \quad (8.10a)$$

$$\mathbf{x}_0 = [a_0 \quad c_0 \quad \theta_a]^T \quad (8.10b)$$

$$\mathbf{F}_0 = [\xi_{cv,0} \quad \xi_{cw,0} \quad M_{ya}]^T \quad (8.10c)$$

$$\mathbf{M}_0 = \begin{bmatrix} m_{b0} & 0 & 0 \\ 0 & m_{b0} & 0 \\ 0 & 0 & I_{ay} \end{bmatrix} \quad (8.10d)$$

$$\mathbf{C}_0 = \begin{bmatrix} C_{bv,0} & 0 & -rc_{bv} \\ 0 & C_{bv,0} & 0 \\ -2\pi r^2 c_{bv} & 0 & 2\pi r^3 c_{bv} \end{bmatrix} \quad (8.10e)$$

Introduced in the modal representation of the flexible ring model are the modal stiffnesses  $C_{v,n}$ ,  $C_{vw,n}$  and  $C_{w,n}$ :

$$C_{bv,n} = \frac{EI}{r^4} n^2 + \frac{EA}{r^2} n^2 + c_{bv} \quad (8.11a)$$

$$C_{bvw,n} = \frac{EI}{r^4} n^3 + \frac{EA}{r^2} n \quad (8.11b)$$

$$C_{bw,n} = \frac{EI}{r^4} n^4 + \frac{EA}{r^2} + c_{bw} + \frac{p_0 b_R}{r} (n^2 - 1) \quad (8.11c)$$

the modal masses  $m_{bn}$ :

$$m_{bn} = \rho A \quad (8.12)$$

and the generalised forces  $\xi_{cv,n}$ ,  $\eta_{cv,n}$ ,  $\xi_{cw,n}$  and  $\eta_{cw,n}$ :

$$\xi_{cv,0} = \frac{1}{2\pi} \int_0^{2\pi} q_{cv} d\theta, \quad \xi_{cv,n} = \frac{1}{\pi} \int_0^{2\pi} q_{cv} \cos n\theta d\theta \quad (n = 1, 2, 3, \dots) \quad (8.13a)$$

$$\eta_{cv,0} = 0, \quad \eta_{cv,n} = \frac{1}{\pi} \int_0^{2\pi} q_{cv} \sin n\theta d\theta \quad (n = 1, 2, 3, \dots) \quad (8.13b)$$

$$\xi_{cw,0} = \frac{1}{2\pi} \int_0^{2\pi} q_{cw} d\theta, \quad \xi_{cw,n} = \frac{1}{\pi} \int_0^{2\pi} q_{cw} \cos n\theta d\theta \quad (n = 1, 2, 3, \dots) \quad (8.13c)$$

$$\eta_{cw,0} = 0, \quad \eta_{cw,n} = \frac{1}{\pi} \int_0^{2\pi} q_{cw} \sin n\theta d\theta \quad (n = 1, 2, 3, \dots) \quad (8.13d)$$

To analyse the modes of the unloaded tyre, the generalised forces are set to zero. The mode shapes of the flexible ring tyre model are shown in Figure 8.4 in Section 8.4. There they will be discussed in relation with the experimentally found results.

### The tyre-road interface

If the tyre is loaded on the road surface, large deformations of the tyre occur and a finite contact length arises. In the contact patch the deformation of the tyre ring is prescribed by the flat road surface. The new boundary condition has changed the structure of the system. We could use the partial differential equations (4.1) and perform the *Modal Expansion Method* again with these new boundary conditions. Instead, the modes of the free tyre model will be used and the equations that describe the forces in the contact patch are added.

The displacement of the tyre ring in the contact patch equals all modal displacements multiplied by their modal shapes. The forces generated in the contact patch, which depend on the displacements in the contact patch, are fed back into the model. This destroys the modal structure of the free tyre model, resulting in new modes that are linear combinations of the free tyre modes.

The modified ring model, introduced in Figure 4.5, is used for the analysis. In this model the flexibility of the tread rubber is added. The differences with

respect to the discrete simulation model presented in Section 4.3 are that in this chapter:

- the tread elements are modelled in the contact patch only.
- the *in-extensibility assumption* is not used
- the model is linear: the tread elements are only modelled in the contact zone; all tread elements adhere to the road surface; the non-linearity of the sidewall stiffnesses is neglected.

The radial and tangential displacements of the tyre ring in the contact patch are calculated for a finite number of contact points  $n_e$ :

$$v_{b,i} = \sum_{n=0}^m a_n \cos n\theta_i + b_n \sin n\theta_i, \quad w_{b,i} = \sum_{n=0}^m c_n \cos n\theta_i + d_n \sin n\theta_i \quad (8.14)$$

where  $m$  denotes the number of modes used. The angular position  $\theta_i$  of the contact points is defined by:

$$\theta_i = \frac{1}{2}\pi + \left( \frac{2i}{n_e} - 1 \right) \frac{a}{r} \quad i = 0, 1, 2, \dots, n_e \quad (8.15)$$

The vertical and horizontal displacements read:

$$x_{b,i} = -\sin \theta_i \cdot v_{b,i} + \cos \theta_i \cdot w_{b,i} \quad (8.16a)$$

$$z_{b,i} = -\cos \theta_i \cdot v_{b,i} - \sin \theta_i \cdot w_{b,i} \quad (8.16b)$$

The vertical and horizontal forces per unit of length equal the displacements multiplied by the tread stiffnesses:

$$q_{cx,i} = -c_{cpx} \cdot x_{b,i} \quad (8.17a)$$

$$q_{cz,i} = -c_{cpz} \cdot z_{b,i} \quad (8.17b)$$

where  $c_{cpx}$  and  $c_{cpz}$  are the horizontal and vertical tread stiffnesses per unit of length, respectively. Since the tread element stiffnesses only play a role in the contact patch, the stiffnesses are termed *horizontal* and *vertical* rather than *tangential* and *radial*. The radial and tangential forces acting on the tyre ring read:

$$q_{cv,i} = -\sin \theta_i \cdot q_{cx,i} - \cos \theta_i \cdot q_{cz,i} \quad (8.18a)$$

$$q_{cw,i} = \cos \theta_i \cdot q_{cx,i} - \sin \theta_i \cdot q_{cz,i} \quad (8.18b)$$

Combining the equations for the vertical and horizontal displacements of the ring in the contact patch (cf. Eq. 4.16) and the vertical and horizontal forces in the contact patch (cf. Eq. 4.17 and 4.18) gives radial and tangential forces in the contact patch in terms of the radial and tangential displacements:



$$q_{cv,i} = -(c_{cpx} \sin^2 \theta_i + c_{cpz} \cos^2 \theta_i) \cdot v_i + \sin \theta_i \cos \theta_i (c_{cpx} - c_{cpz}) \cdot w_i \quad (8.19a)$$

$$q_{cw,i} = \sin \theta_i \cos \theta_i (c_{cpx} - c_{cpz}) \cdot v_i - (c_{cpx} \cos^2 \theta_i + c_{cpz} \sin^2 \theta_i) \cdot w_i \quad (8.19b)$$

The forces  $q_{cv,i}$  and  $q_{cw,i}$  at position  $\theta_i$  depend on the deformations  $v_i$  and  $w_i$ . These deformations are summations of all the modal deformations according to Equation (8.14). As we consider only a finite number of points in the contact patch, rather than a continuous description, the integral for the generalised modal force (Equation 8.13) changes into summations of the forces in the contact points considered:

$$\xi_{cv,0} = \Delta\theta \frac{1}{2\pi} \sum_{i=1}^{n_c} q_{cv,i}, \quad \xi_{cv,n} = \Delta\theta \frac{1}{\pi} \sum_{i=1}^{n_c} q_{cv,i} \cos n\theta_i \quad (n = 1, 2, 3, \dots) \quad (8.20a)$$

$$\eta_{cv,0} = 0, \quad \eta_{cv,n} = \Delta\theta \frac{1}{\pi} \sum_{i=1}^{n_c} q_{cv,i} \sin n\theta_i \quad (n = 1, 2, 3, \dots) \quad (8.20b)$$

$$\xi_{cw,0} = \Delta\theta \frac{1}{2\pi} \sum_{i=1}^{n_c} q_{cw,i}, \quad \xi_{cw,n} = \Delta\theta \frac{1}{\pi} \sum_{i=1}^{n_c} q_{cw,i} \cos n\theta_i \quad (n = 1, 2, 3, \dots) \quad (8.20c)$$

$$\eta_{cw,0} = 0, \quad \eta_{cw,n} = \Delta\theta \frac{1}{\pi} \sum_{i=1}^{n_c} q_{cw,i} \sin n\theta_i \quad (n = 1, 2, 3, \dots) \quad (8.20d)$$

The equations are now rearranged according to Equations (8.9) and (8.10) resulting in the final set of equations of the tyre standing on the road:

$$\begin{bmatrix} \mathbf{M}_0 & 0 & \cdots & 0 \\ 0 & \ddots & 0 & \vdots \\ \vdots & 0 & \ddots & 0 \\ 0 & \cdots & 0 & \mathbf{M}_m \end{bmatrix} \begin{bmatrix} \ddot{\mathbf{x}}_0 \\ \vdots \\ \vdots \\ \dot{\mathbf{x}}_m \end{bmatrix} + \begin{bmatrix} \mathbf{C}_0 & 0 & \cdots & 0 \\ 0 & \ddots & 0 & \vdots \\ \vdots & 0 & \ddots & 0 \\ 0 & \cdots & 0 & \mathbf{C}_m \end{bmatrix} \begin{bmatrix} \mathbf{x}_0 \\ \vdots \\ \vdots \\ \mathbf{x}_m \end{bmatrix} = \begin{bmatrix} \mathbf{F}_0 \\ \vdots \\ \vdots \\ \mathbf{F}_m \end{bmatrix} \quad (8.21)$$

where the forces  $\mathbf{F}_n$  on the right hand side of the Equation (8.21) depend on all modal displacements. This indicates that these equations have lost their diagonal shape and we can perform a transformation into a new diagonal shape. The result is a set of new modes which are linear combinations of the modes of the original model. Figure 8.4 shows the resulting mode shapes.

## 8.4 Comparison of the experimental findings with the theoretical results using the flexible ring model

### The free tyre

In Figure 8.3 the left half shows the mode shapes obtained from the experimental modal analysis of the free tyre. This figure results from various excitations. Mode 0 can be identified from a tangential excitation on either the tyre or the rim. Modes 1 can be identified from a radial or tangential excitation on the tyre circumference. The higher order modes can be identified only from a radial excitation on the tyre circumference. The relative damping, which is difficult to assess accurately, ranges from 2.5% to 4.5%. The mode number  $n$  equals half the number of nodes of the mode shape. The frequency of mode 0 is 113 Hz. This frequency will drop to 68 Hz if the rotation of the rim is also constrained. From this case onwards the frequencies of the modes will always increase with the mode number. Note that the rim will not rotate at these higher modes.

The in-plane modes of vibration occur only up to  $n=8$ . The highest frequency ( $n=8$ ) is approximately 250 Hz. Higher frequencies belong to sidewall waves and are strongly damped [118].

**Table 8.2:** *The parameters of the flexible ring and the rigid ring model.*

parameter	symbol	value	unit
bending stiffness tyre ring	$EI$	4.0	$\text{N m}^2$
extensional stiffness tyre ring	$EA$	$4.9 \cdot 10^6$	N
tyre ring radius	$r$	0.300	m
inside tyre width	$b_0$	0.152	m
inflation pressure	$p_0$	$2.2 \cdot 10^5$	$\text{N/m}^2$
tangential sidewall stiffness	$c_{bv}$	$6.49 \cdot 10^5$	$\text{N/m}^2$
radial sidewall stiffness	$c_{bw}$	$1.93 \cdot 10^6$	$\text{N/m}^2$
horizontal tread stiffness	$c_{cpx}$	$25 \cdot 10^6$	$\text{N/m}^2$
vertical tread stiffness	$c_{cpz}$	$75 \cdot 10^6$	$\text{N/m}^2$
moment of inertia rim	$I_{ay}$	0.35	$\text{kg m}^2$
mass density tyre ring	$\rho A$	3.81	$\text{kg/m}$
half the contact length (at $F_z = 4000 \text{ N}$ )	$a$	0.0535	m
number of tread elements in contact	$n_e$	100	—
number of modes	$m$	30	—

In Figure 8.4 the left half shows the modes of the flexible ring model of the free tyre. The parameters used are given in Table 8.2. Although, the measured frequencies have been used to estimate the parameters, the calculated frequencies of the higher order modes are lower than measured. The calculated mode shapes, on the other hand, represent the measured mode shapes rather well.

All higher order modes are double, they can be imagined as modes, which have similar shape and frequency, of which the nodes and anti-nodes have been interchanged. Combining both modes can result in a mode in any direction. If the tyre is excited by a hammer, it will only show those modes of vibration in the direction of the excitation. In other words, the excitation will always take place in an anti-node of the mode shapes, which enables accurate estimations of the mode shapes.

### **The tyre standing on the road.**

The boundary condition of the flat road surface forces the two identical modes for each mode number to split [21,42,112,113]: both the mode shapes and the frequencies are no longer identical. The orientation of the modes is not arbitrary; they are clearly subdivided into symmetrical (with respect to the vertical axis) and anti-symmetrical modes. This effect complicates the measurements because the excitations are generally not in the anti-nodes. This means that less energy is transmitted into the modes, making the estimation of the mode shapes more difficult. The excitation may even occur in a node of the mode shape. Then this specific mode shape cannot be identified using this excitation. Accordingly, it is important that the excitations should take place at several locations on the tyre, to ensure a proper identification of all modes. The effect is illustrated in Figure 8.2 where the gains of the modes of the free tyre are approximately equal to each other and the gains of the modes of the loaded tyre vary considerably.

The right halves of Figures 8.3 and 8.4 show the modes of the tyre standing on the road. Mode 0 is a rigid body rotation of the rim and the tyre. Modes 1,2,3, and 4 are almost identical to the free tyre case. A small rotation of the rim is added to the free tyre modes to make the horizontal deformation in the contact patch equal to zero.

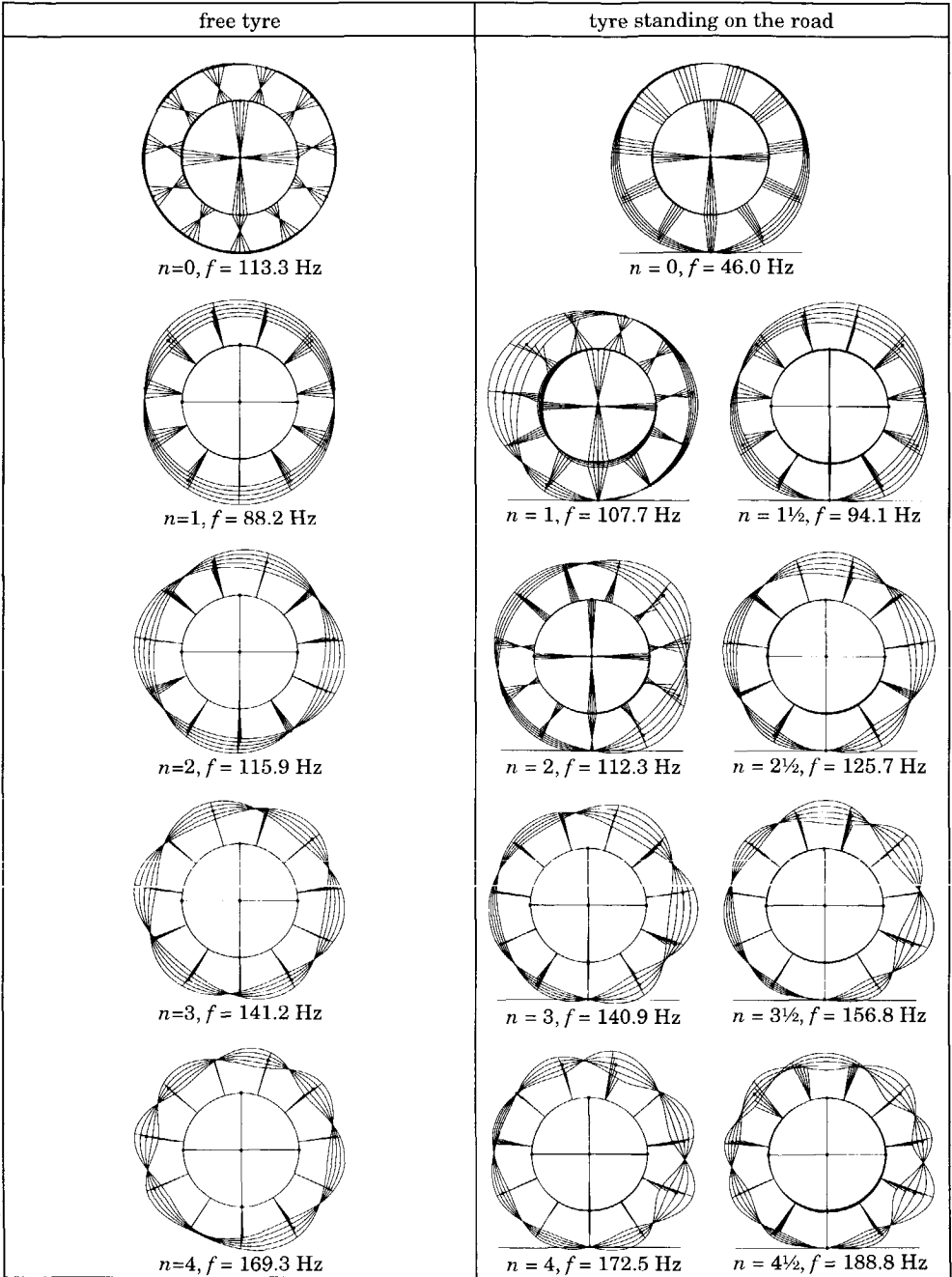


**Figure 8.3:** *The modes of the tyre from the experimental modal analysis.*

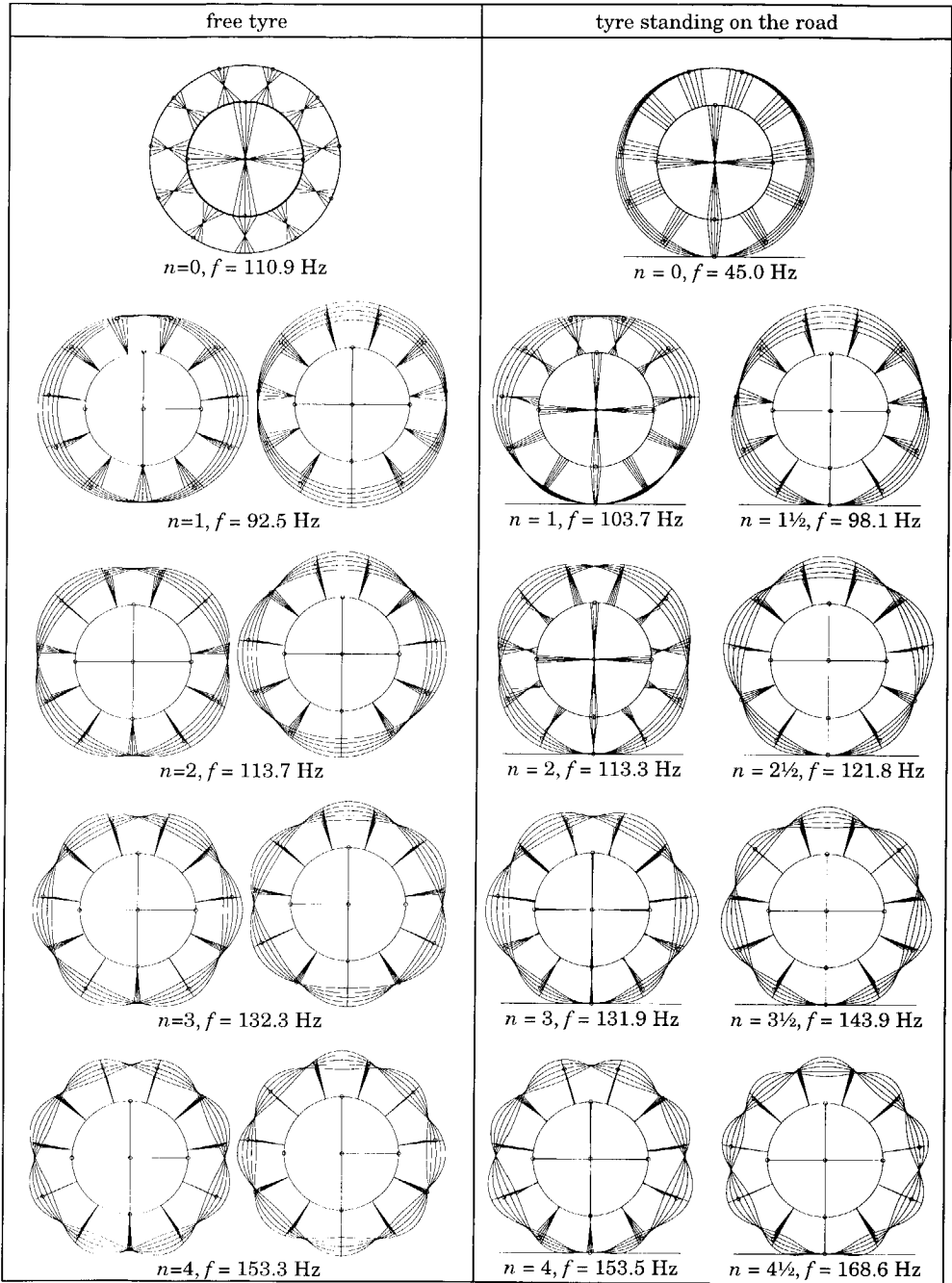


**Figure 8.4:** *The modes of the tyre from the flexible ring model.*

The standing tyre also shows modes different from the free tyre case: mode numbers  $1\frac{1}{2}$ ,  $2\frac{1}{2}$ ,  $3\frac{1}{2}$ , and  $4\frac{1}{2}$ . Although this mode numbering (using halves) is rather uncommon it still fits the original definition: the mode number  $n$  equals half the number of nodes of the mode shape. Consequently, a mode with 5 nodes has a mode number of  $2\frac{1}{2}$ . Also the frequency of mode  $2\frac{1}{2}$  is approximately equal to the average value of the frequencies of mode 2 and 3.

Figure 8.5 shows the frequencies of the modes as function of the mode number. The open circles are the frequencies of the free tyre. The filled circles are the frequencies of the tyre standing on the road. This figure shows that the frequencies of the higher order modes of the flexible ring model deviate from the measured frequencies.

The frequencies above mode number 1 are all situated on a single line regardless of whether they belong to the free or to the standing tyre case. The frequencies of modes  $1\frac{1}{2}$ ,  $2\frac{1}{2}$ ,  $3\frac{1}{2}$ , and  $4\frac{1}{2}$  fall precisely between the frequencies of modes 1, 2, 3, 4, and 5. Figure 8.5 shows that the natural frequency is inversely proportional to the distance between two nodes of the mode shapes of the Figures 8.3 and 8.4. The figure shows some discrepancies for mode number 0 and 1. The reason is the rotational degree of freedom of the rim, which influences the frequencies of the rigid modes.

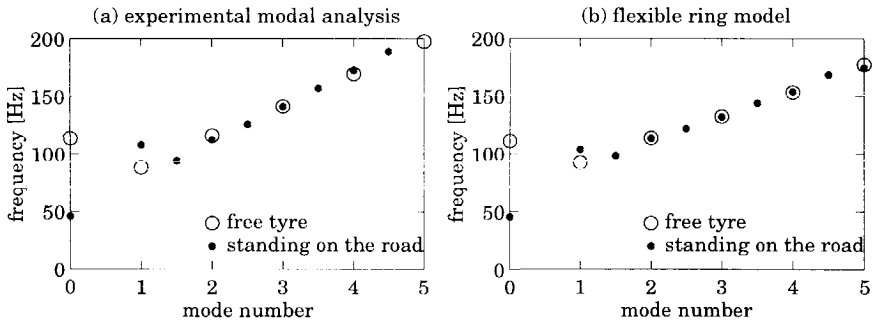


**Figure 8.5:** *The natural frequencies of the tyre as function of the mode number for two different boundary conditions.*

The experimentally and theoretically obtained mode shapes of the tyre (*cf.* Figures 8.3 and 8.4) correspond well to the mode shapes of the tyre presented in the literature: the modes of the free tyre [12,27,103,109], the symmetrical modes of the standing tyre [21,43,103,112,113] and the anti-symmetrical modes of the standing tyre [21,112,113].

## 8.5 Theoretical modal analysis using the rigid ring model

This section presents the modes of the *rigid ring* model, which was developed in the previous chapter. First, these modes will be compared with the results of the experimental modal analysis; and second, the influence of the boundary conditions of these modes will be investigated.

The natural frequencies of the modes obtained from experimental modal analysis are much higher than the frequencies obtained from the dynamic experiments presented in Chapters 9, 10 and 11 where the tyre actually rolls over the drum surface. A possible reason is that the brake system was not mounted during the modal analysis experiments so that the moment of inertia of the rotating parts was higher for the dynamic experiments on the drum than for the experimental modal analysis. However, after we had corrected the natural frequencies for the difference in the moment of inertia of the rotating parts we still noticed that the stiffnesses obtained from the dynamic experiments are 30% lower than the stiffnesses obtained from the experimental modal analysis.

There are two other reasons for the difference in frequencies: First, the measured frequencies of the rigid modes are significantly lower at higher velocities [68,97,111,112,113]. Second, the amplitude of vibration during the brake and cleat experiments is much higher than during the modal analysis experiments and the stiffness of rubber is velocity and amplitude dependent. Consequently, for comparison of the modes of the rigid ring model with the results of the experimental modal analysis (see Figure 8.6) the parameters of Table 8.2 are used, and for comparison with the dynamic experiments (see Figures 8.7 through 8.9) the parameters of Table 7.1 are used.

The equations of motion of the *rigid ring* model have been derived in Chapter 7. In this model the tyre ring can move as a rigid body with respect to the rim. The tyre has three degrees of freedom: the horizontal displacement  $x_b$ , the vertical displacement  $z_b$  and the rotation  $\theta_b$ . The rim has one degree of freedom: the rotation  $\theta_a$ . The contact with the road is modelled with a vertical residual stiffness and a horizontal slip model. The linearised equations of motions (Eq. 7.51) at non-rolling conditions ( $\Omega=0$ ), with zero average brake torque ( $Q_x=Q_y=Q_z=0$ ) and no excitation ( $\beta=z_r=M_{ay}=0$ ) become:

$$m_b \ddot{x}_b + k_b \dot{x}_b + c_b \ddot{x}_b - k_b \ddot{\theta}_a z_{b0} = C_\kappa \ddot{\zeta}_{cx} \quad (8.22a)$$

$$m_b \ddot{z}_b + k_b \dot{z}_b + (c_b + c_{cz}) \ddot{z}_b = 0 \quad (8.22b)$$

$$I_{ay} \ddot{\theta}_a + k_{b\theta} (\ddot{\theta}_a - \ddot{\theta}_b) + c_{b\theta} (\dot{\theta}_a - \dot{\theta}_b) = 0 \quad (8.22c)$$

$$I_{by}\ddot{\tilde{\theta}}_b - k_{b\theta}(\tilde{\theta}_a - \tilde{\theta}_b) - c_{b\theta}(\dot{\tilde{\theta}}_a - \dot{\tilde{\theta}}_b) = -r_{e0}C_{\kappa}\tilde{\zeta}_{cx} \quad (8.22d)$$

$$\sigma_c\ddot{\tilde{\zeta}}_{cx} + r_{e0}\Omega\tilde{\zeta}_{cx} = -\dot{\tilde{x}}_b + r_{e0}\dot{\tilde{\theta}}_b \quad (8.22e)$$

The parameters of the rigid ring model are related to the parameters of the flexible ring model (*cf.* Eq. 7.15, 3.10, 6.19):

$$\text{translational sidewall stiffness:} \quad c_b = \pi r(c_v + c_w) \quad (8.23a)$$

$$\text{translational sidewall damping constant:} \quad k_b = \pi r(k_v + k_w) \quad (8.23b)$$

$$\text{rotational sidewall stiffness:} \quad c_{b\theta} = 2\pi c_v r^3 \quad (8.23c)$$

$$\text{rotational sidewall damping constant:} \quad k_{b\theta} = 2\pi k_v r^3 \quad (8.23d)$$

$$\text{slip stiffness:} \quad C_{\kappa} = 2c_{cpx}a^2 \quad (8.23e)$$

$$\text{relaxation length contact patch:} \quad \sigma_c = a \quad (8.23f)$$

$$\text{mass of tyre belt:} \quad m_b = 2\pi r\rho A \quad (8.23g)$$

$$\text{moment of inertia of tyre belt:} \quad I_{by} = 2\pi r^3\rho A \quad (8.23h)$$

The modes of the rigid ring model at zero average rotational speed ( $\Omega=0$ ) are presented in Figure 8.6, the parameters used are given in Table 8.2. As already stated, the rigid ring model shows only the rigid modes of the tyre. The modes of the rigid ring model represent the measured modes (Figure 8.3) rather well.

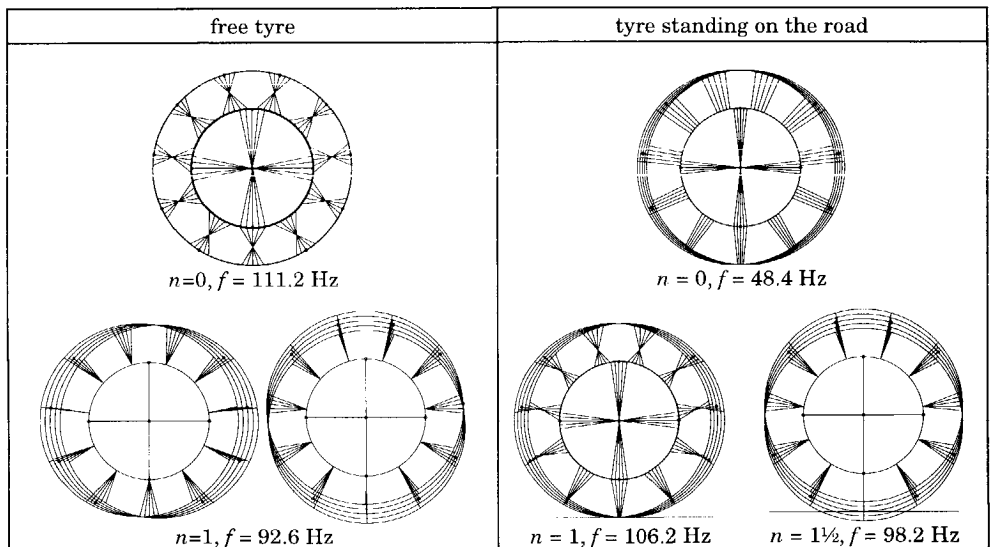


**Figure 8.6:** *The modes of the tyre from the rigid ring model; parameters obtained from the experimental modal analysis.*



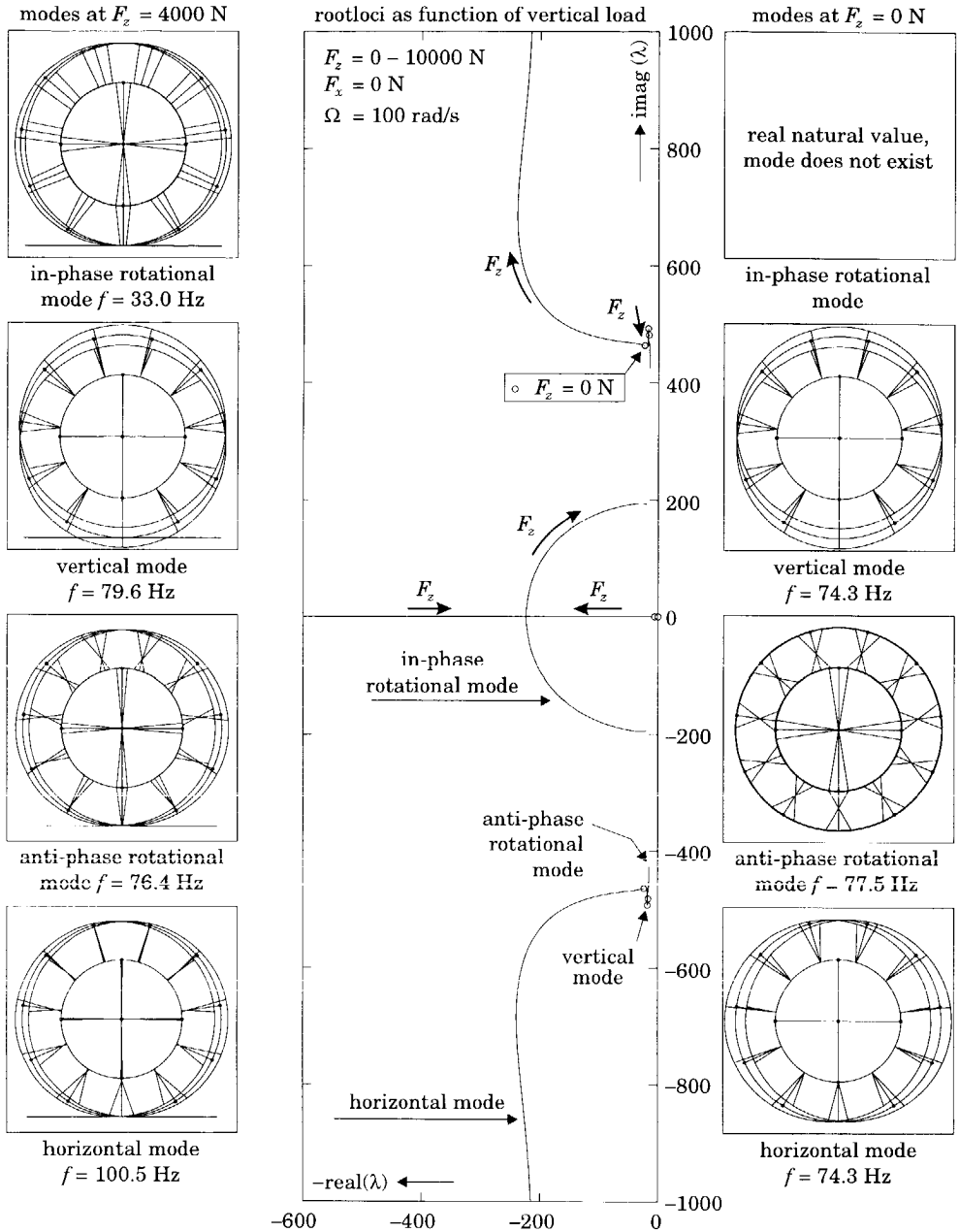
Figures 8.7 through 8.9 present the influence of the operational conditions (load, speed and brake force) on the modes of the rolling tyre. The parameters have been obtained from the dynamic experiments on the drum and are given in Table 7.1. Rather than using the mode numbering method, the individual modes are indicated by names. The mode number  $n=1$  will be called the vertical or horizontal mode of vibration, depending on the direction of the mode. The rotational modes will be referred to as: in-phase rotation of the rim and tyre belt (at 33 Hz) or anti-phase rotation (at 76 Hz) of these bodies.

Figure 8.7 presents the influence of the vertical load on the mode shapes and the roots of the model. The modes of the free tyre are presented on the right hand side of Figure 8.7. For this case we can identify three modes of vibration: the anti-phase rotational mode and a horizontal and vertical mode of vibration. The system does not show the fourth mode because the tyre and wheel may rotate freely about the spindle. This in fact corresponds to a natural frequency zero.

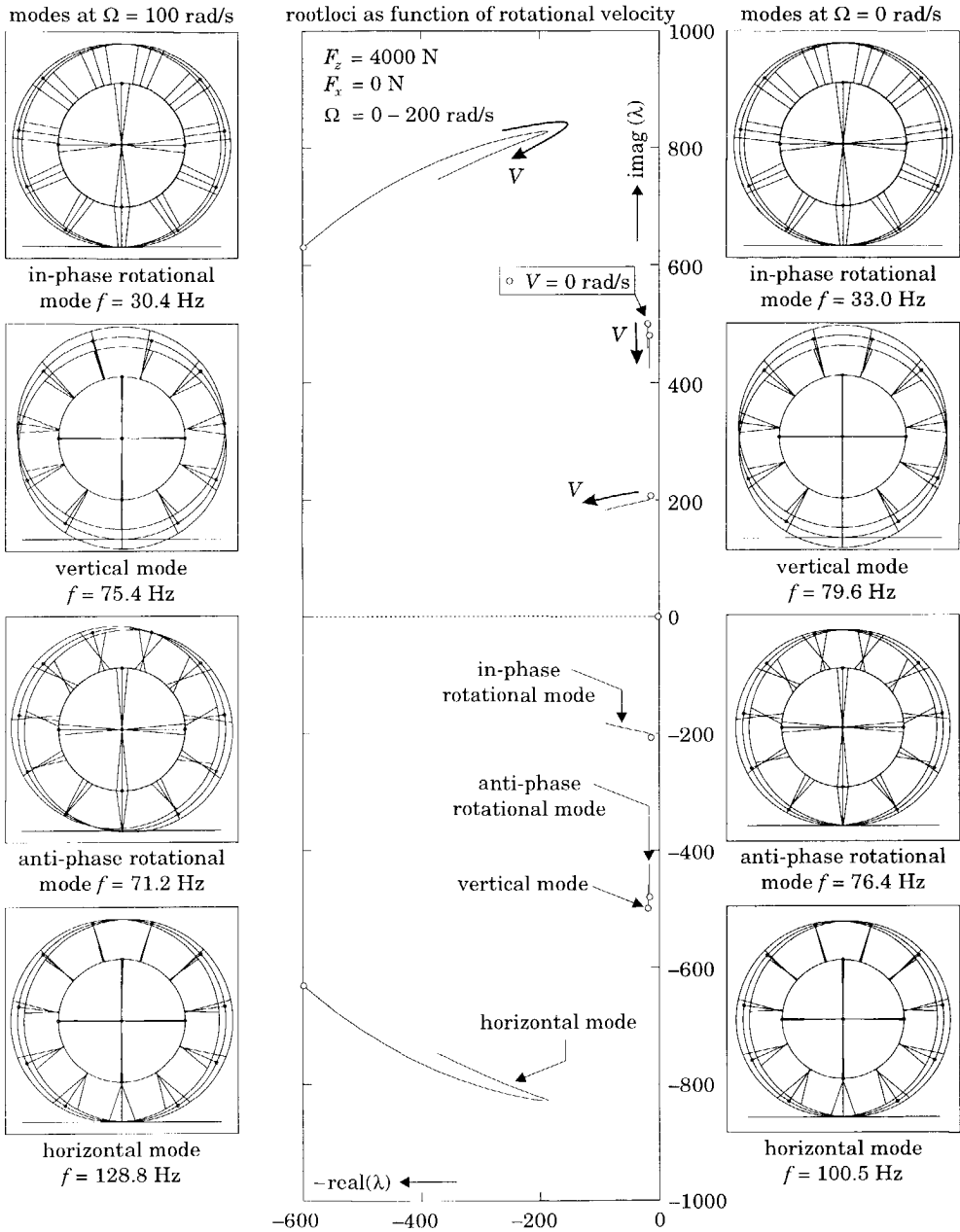
The modes of the standing tyre are presented on the left hand side of Figure 8.7. The free rotation of the wheel (at 0 Hz) has changed into the in-phase rotational mode at 33 Hz. The relative damping of this mode decreases with increasing vertical load. The frequency of the anti-phase mode decreases slightly with vertical load. The mode shape of this mode has changed considerably with respect to the free tyre mode: the horizontal displacement of the tyre in the contact patch becomes small. The horizontal mode at 74 Hz changes into a mode at 100 Hz. This mode is a vibration of the tyre ring on the tread elements in fore and aft direction, which constitutes the highest stiffness in the model.

Figure 8.8 presents the root loci of the tyre model as function of the velocity. The influence of the velocity on the modes is rather small. The relative damping of the in-phase rotational mode increases with velocity. The relative damping of the horizontal mode at zero velocity is high owing to the tread element damping (*cf.* Equations 7.30 and 7.31). The relative damping of this mode decreases with the velocity because the damping of the tread element decreases. At high velocity, on the other hand, the relative damping of this mode increases again owing to the damping resulting of the relaxation length contact model. Furthermore, the sidewall stiffnesses in the model decrease with velocity (*cf.* Eq. 7.22) resulting in lower frequencies at higher velocities.

The average brake force has much more influence. Its influence is opposite to the influence of vertical load. At very high levels of brake force, the slip stiffness in the contact patch approaches zero. This means that the horizontal constraint becomes less effective: the in-phase rotational mode disappears at high brake force levels and the horizontal mode becomes the free horizontal mode again.



**Figure 8.7:** The root loci and modes of vibration of the rigid ring tyre model as function of the vertical load.



**Figure 8.8:** The root loci and modes of vibration of the rigid ring tyre model as function of the rotational velocity.

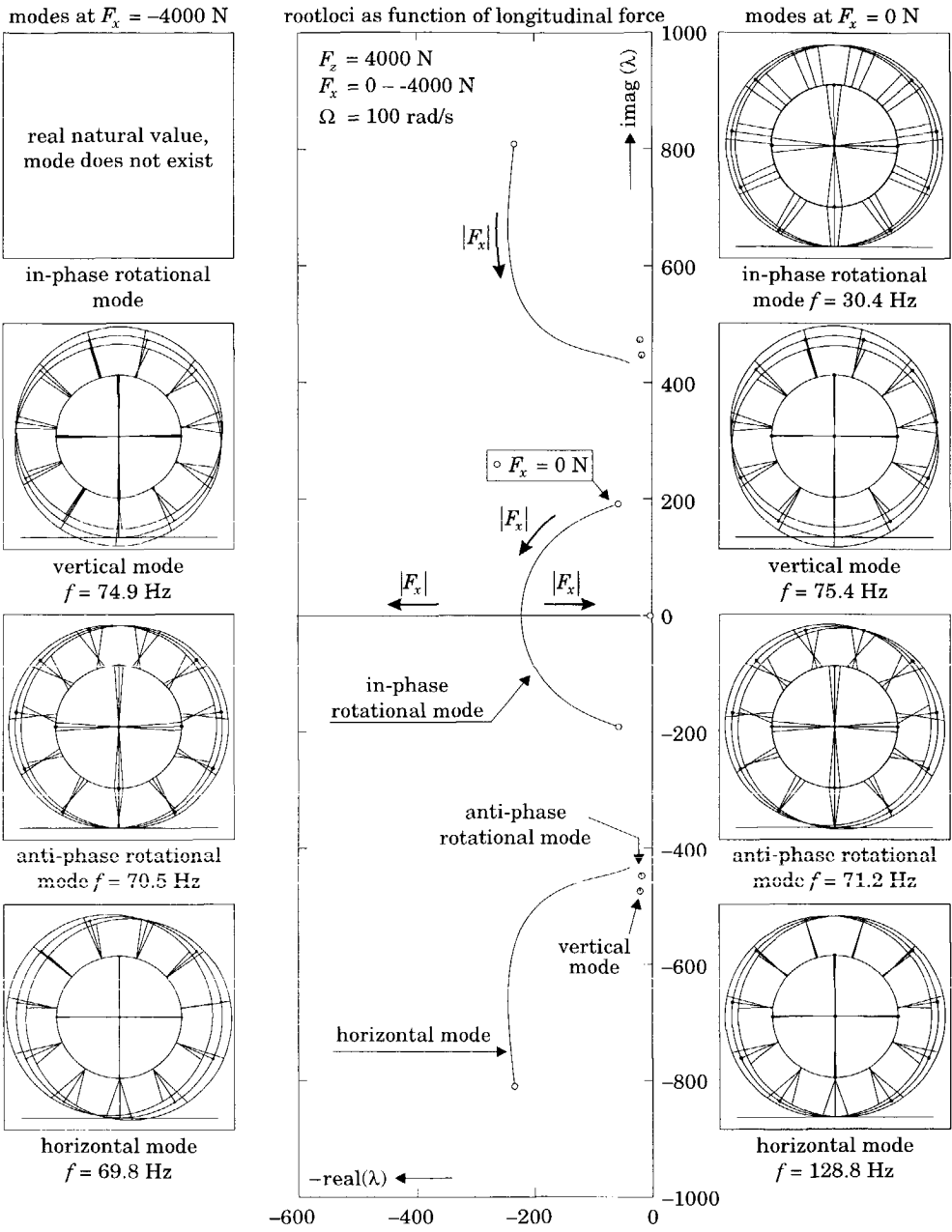


**Figure 8.9:** The root loci and modes of vibration of the rigid ring tyre model as function of the longitudinal force ( $F_x$  is negative during braking).

# 9

## Dynamic Tyre Responses to Brake Torque Variations

---

### 9.1 Introduction

The tyre model described in Chapter 7 is able to generate the typical tyre vibrations in the frequency range 0-80 Hz. In this frequency range the tyre tread-band behaves as a rigid body with respect to the rim. Consequently, the model is called *rigid ring* model. Above 80 Hz the tread-band shows deformations during vibration. These modes of the tyre, which are called the *flexible modes* are presented in the previous chapter.

There are several sources of tyre in-plane vibrations: brake torque fluctuations, road unevennesses, horizontal and vertical wheel oscillations, and tyre non-uniformities. The tyre model, developed in Chapter 7, will be validated for most of these excitations. This chapter presents the dynamic tyre response to brake torque variations, the next chapter treats the response to road unevennesses, and Chapter 11 deals with the response to axle height oscillations.

Most research into the dynamic tyre response to brake pressure variations has been done within the context of Anti-lock Brake System (ABS) development. The main task of ABS is to maintain the longitudinal slip within a small range about the maximum of the brake force vs. slip curve. In order to achieve this goal

the pressure in the wheel brake cylinder is modulated by the ABS, resulting in rapid brake pressure variations.

The Anti-lock Brake System was successfully introduced by Bosch in 1978 [60]. In the 70s fundamental research was carried out into hardware requirements for ABS: the optimal rise time of the brake pressure, the delay time of components [35,59]. The ABS uses the rim velocity to monitor the longitudinal slip of the tyre. Tyre vibrations affect the monitoring of slip, especially, the longitudinal wheel hop mode and the in-phase rotational vibration of the tyre and wheel cause problems. The tyre vibrations can be induced by road unevennesses and it is well known that the performance of ABS deteriorates on very rough roads [44,66,96,108,116].

The dynamic tyre responses due to brake torque variations can be investigated in the frequency domain and in the time domain. The frequency domain is generally used to study the linear tyre responses, while the time domain can be used to study both the linear and the non-linear tyre response. In Section 9.2 the measured Frequency Response Functions (FRFs) are used to estimate the parameters of the rigid ring model. The simulations in the time domain are used to study the non-linear behaviour of the model, its robustness and the agreement with experimental findings (Section 9.3, 9.4 and 9.5).

The measured frequency response functions of brake force to brake torque are similar to the ones found by Kobiki *et al.* [53]. They studied the interior booming noise caused by tyre vibrations and measured the frequency response functions of the longitudinal force over the brake torque in the frequency range up to 120 Hz. Kobiki *et al.* identified two modes of vibration of the tyre in this frequency range. They used a rigid ring model to simulate the dynamic tyre behaviour in a power train-suspension model. Using a simple simulation model Zellner studied the time and frequency responses of several subsystems of the ABS and of the tyre [123]. He performed his study not to gain knowledge about tyre behaviour, but as an analytical approach to ABS design.

The non-linear behaviour of the rigid ring tyre model has been validated in the time domain. This allows the use of large variations in slip, velocity and forces. The non-linear simulation model is based on the equations given in Sections 7.3 and 7.4. Figure 9.1 shows schematically the non-linearities of the model: (1) the non-linear slip characteristics and contact patch relaxation length; (2) the vertical load dependency of the loaded tyre radius  $r_l$  and the effective rolling radius  $r_e$ ; (3) the slight increase of the tyre radius due to the centrifugal force; (4) the horizontal shift of the contact point due to the influence of a

horizontal force on the vertical force; and (5) the dry friction in the disc brake. Of these, the two first non-linearities have the largest influence.

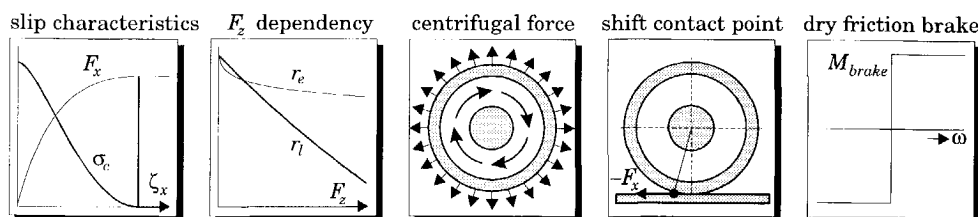


**Figure 9.1:** The major non-linearities of the simulation model of the tyre-wheel system.

Section 9.3 presents the non-linear responses of the tyre to successive step increases in brake pressure. These input signals are similar to the ones used by Van Zanten *et al.* [121,122]. They studied the tyre responses during ABS operation in a vehicle and simulated and measured the responses of the tyre to successive step increases in brake pressure. Their model consists of two rigid bodies with two degrees of freedom: the rotation of the rim and the rotation of the tyre (belt). The interface with the road was governed by individual tread elements.

The robustness of the rigid ring model was validated at zero velocity conditions. Simulations encounter numerical problems at low speed because the longitudinal speed of the wheel hub appears in the denominator of the expressions of both longitudinal and lateral slip [11]. The numerical stability of the rigid ring model was validated by using two brake manoeuvres: braking with wheel lock at constant drum velocity and braking to stand-still of both wheel and drum.

Section 9.4 presents a brake manoeuvre with wheel lock. During this experiment the drum velocity was constant and the brake pressure was increased rapidly, causing wheel lock. Bernard *et al.* developed a tyre model for both low-speed and high-speed calculations [11]. He modelled the longitudinal tyre transient behaviour by using a first order equation for the longitudinal slip with the longitudinal slip velocity as input (comparable to model 2 of Chapter 6). He proved that this model was numerically able to brake to stand-still even on a slope. But as soon as the velocity became zero the tyre showed large lightly damped vibrations. Section 9.5 presents a brake manoeuvre to stand-still of the drum.

## 9.2 Frequency Response Functions

The Frequency Response Functions (FRFs) were used to estimate the relevant parameters of the tyre. To estimate the FRFs the tyre-wheel-brake system was excited by small variations of brake pressure. The FRFs to brake pressure variations could not be established accurately because of non-linearities (*i.e.* a mechanical delay) in the brake system. Two kinds of FRFs could be estimated accurately: the response of the longitudinal force  $F_x$  to brake torque ( $-M_y$ ) variations and the response of the longitudinal force to wheel slip ( $\zeta_x$ ) variations. For the latter FRF the wheel slip is considered to be an input, even though the wheel slip is in fact a response of the tyre to the brake torque.

The goal of these experiments was to estimate the tyre parameters in different operating conditions. The experiments were carried out at three constant axle heights, corresponding to 2000, 4000 and 6000 N vertical load for the initially non-rotating tyre. One set of experiments was carried out at five velocities: 25, 39, 59, 92, 143 km/h and a small average brake torque. Another set of experiments was carried out at one velocity (25 km/h) and several average brake torques covering the entire slip characteristic. The total number of conditions investigated was 35. For each condition 10 measurements were averaged to enable the estimation of the coherence functions as well. The duration of each measurement was 16 seconds at 256 Hz sampling rate.

The standard deviation of the applied brake pressure was approximately 1 bar. Table 9.1a shows the resulting average brake torque and the standard deviation of the brake torque for the experiments with low average brake pressure (5 bar) and several velocities. Table 9.1b shows the values of brake torque for the experiments at various levels of average brake pressure and one velocity.

**Table 9.1a:** *The average values ( $\mu$ ) and standard deviations ( $\sigma$ ) of the applied brake torque variations at low average brake pressure (5 bar).*

V [km/h]	$F_z = 2000$ N		$F_z = 4000$ N		$F_z = 6000$ N	
	$\mu_{M_y}$ [Nm]	$\sigma_{M_y}$ [Nm]	$\mu_{M_y}$ [Nm]	$\sigma_{M_y}$ [Nm]	$\mu_{M_y}$ [Nm]	$\sigma_{M_y}$ [Nm]
25	121	20	129	23	128	24
39	129	22	130	24	123	23
59	121	22	120	22	124	23
92	106	20	107	20	113	22
143	106	21	97	20	97	20



**Table 9.1b:** *The average values ( $\mu$ ) and standard deviations ( $\sigma$ ) of the applied brake torque at  $V=25$  km/h and various levels of brake pressure.*

brake pressure	$F_z = 2000$ N		$F_z = 4000$ N		$F_z = 6000$ N	
	$\mu_{M_y}$ [Nm]	$\sigma_{M_y}$ [Nm]	$\mu_{M_y}$ [Nm]	$\sigma_{M_y}$ [Nm]	$\mu_{M_y}$ [Nm]	$\sigma_{M_y}$ [Nm]
low	121	20	129	23	128	24
	213	17	324	20	416	20
⧿	319	19	529	19	701	22
	399	11	704	16	966	15
high	477	11	872	10	1190	15
			1030	11	1410	12

The piezo electric force transducers used in the *cleat and brake* test stand could only accurately measure variations in the forces and not the static components. In Section 2.3 the vertical force of a rolling tyre at constant axle height was measured by using the *measurement tower*. These experiments showed that the increase in the vertical force due to the rotation cannot be neglected. The values of the vertical force presented in Table 2.4b will be used in this chapter as the average vertical force in the given operating (axle height and velocity) condition.

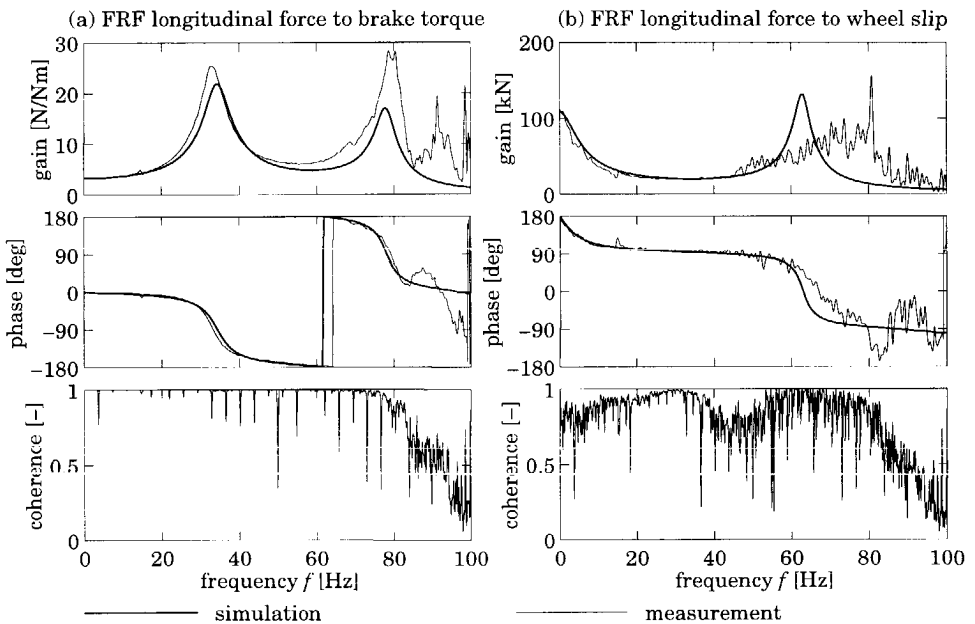
It was rather difficult to control the tyre temperature during the experiments. The increase in the tyre temperature was minimised by alternately measuring for 16 seconds and cooling during a period of free rolling. For severe conditions (high velocity, large vertical load and large average brake torque) the ratio between cooling time and measuring time was as large as 10 to 1.

Figure 9.2a shows one of the measured and simulated FRFs of longitudinal force to brake torque variations. These FRFs clearly show two modes of vibration of the tyre. The first mode is the in-phase rotational mode; and the second one is the anti-phase rotational mode. The estimated coherence functions show that the measured FRFs are valid until 80 Hz. To represent the measured FRFs, the linearised model (*cf.* Eq. 7.51) does not include the moment of inertia between the applied brake torque (at the disc brake) and the measured brake torque (at the brake torque sensor in the intermediate shaft). The measured and simulated FRFs are similar to the ones presented by Kobiki [53].

The FRFs of the longitudinal force to slip variations ( $\zeta_x = -V_{sx}/V_r$ ) are shown in Figure 9.2b. This figure presents the FRF of a system with a different boundary condition than that of the FRF of Figure 9.2a. In Figure 9.2a the brake torque was used as input to the system; thus the rotational velocity of the wheel was not prescribed. In Figure 9.2b, on the other hand, the wheel velocity is considered to

be the input to this system; thus the rotational velocity of the wheel was prescribed. Consequently, the resonance frequencies of Figure 9.2a and Figure 9.2b do not match.

From the FRF to slip variations (Figure 9.2b) two important tyre properties can be found: the slip stiffness which can be estimated from the amplitude of the FRF at zero frequency and the overall relaxation length of the tyre which can be estimated from the phase shift in the frequency range 0–30 Hz. Note that this frequency is much smaller than the first resonance frequency (approximately 65 Hz) of the system with the given boundary conditions. The coherence functions show that these measured FRFs could not be estimated very accurately in the frequency range up to 80 Hz.



**Figure 9.2:** The measured and simulated frequency response functions.

Conditions:  $F_{z0} = 4000$  N,  $F_{x0} = 450$  N,  $V = 25$  km/h.

The simulated and measured frequency response functions are compared in Figure 9.2 as well. The model represents the in-phase rotational mode very well (see Figure 9.2a). The simulated amplitude of the anti-phase rotational mode is lower than the measured amplitude. For some reason, the excitation of the anti-phase mode of the real tyre is larger than the excitation of this mode in the

model. According to the phase diagram we can see that the relative damping of the simulation is equal to the value of damping obtained from measurements.

The model represents the measured FRF of force to slip variations well in the frequency range 0-50 Hz, see Figure 9.2b. This figure shows the correct course of the phase angle up to 90 degrees owing to the modelling of a relaxation length system, and a mode of vibration corresponding to the natural vibration of the belt of the loaded tyre when the rotation of the rim is prescribed. The simulation clearly shows this mode at 63 Hz. The measured amplitude hardly reveals this mode, but from the phase diagram we can identify this mode at 65 Hz.

The dynamic parameters of the rigid ring model (sidewall stiffnesses  $c_b$ ,  $c_{b\theta}$  sidewall damping coefficients  $k_b$ ,  $k_{b\theta}$  and the tread element stiffness per unit of length  $c_{cp}$ ) were not estimated directly from the measured FRFs. First the most important response properties of the dynamic brake performance of the tyre were estimated. The parameters of the model are estimated from these properties. The following properties of the tyre responses were estimated:

- natural frequency of the in-phase rotational mode (from FRF  $F_x/M_y$ )
- natural frequency of the anti-phase rotational mode (from FRF  $F_x/M_y$ )
- relative damping of the in-phase rotational mode (from FRF  $F_x/M_y$ )
- relative damping of the anti-phase rotational mode (from FRF  $F_x/M_y$ )
- slip stiffness (from FRF  $F_x/\zeta_x$ )
- overall relaxation length of the tyre (from FRF  $F_x/\zeta_x$ )

In Figures 9.3 through 9.5 the results from measurements are indicated with a little circle. The results of the simulations (with the parameters of Table 7.1) are presented with full lines. Two sets of parameters were used to show the influence of the velocity dependency of the sidewall stiffnesses. The bold lines represent the rigid ring model as described in Sections 7.3 and 7.4, thus including the velocity dependent sidewall stiffnesses (*cf.* Eq. 7.22). The thin lines represent a model with constant sidewall stiffnesses ( $q_{bVx}=0$ ,  $q_{bVz}=0$ ,  $q_{bV\theta}=0$ ).

Figure 9.3 shows the tyre properties as function of the vertical load. It is shown that the slip stiffness  $C_k$  increases with the vertical load. This corresponds with measured stationary slip characteristics (*cf.* Section 3.5). Apparently, the overall relaxation length  $\sigma$  increases proportionally with the slip stiffnesses, which corresponds with theoretical findings.

The damping of the in-phase rotational mode decreases with increasing vertical load. This effect is strengthened by the influence of the average brake force. An average brake force is needed to be able to excite the tyre with brake torque variations. At very small levels of vertical load, the average brake torque becomes so large that sliding in the contact patch occurs. This increases the

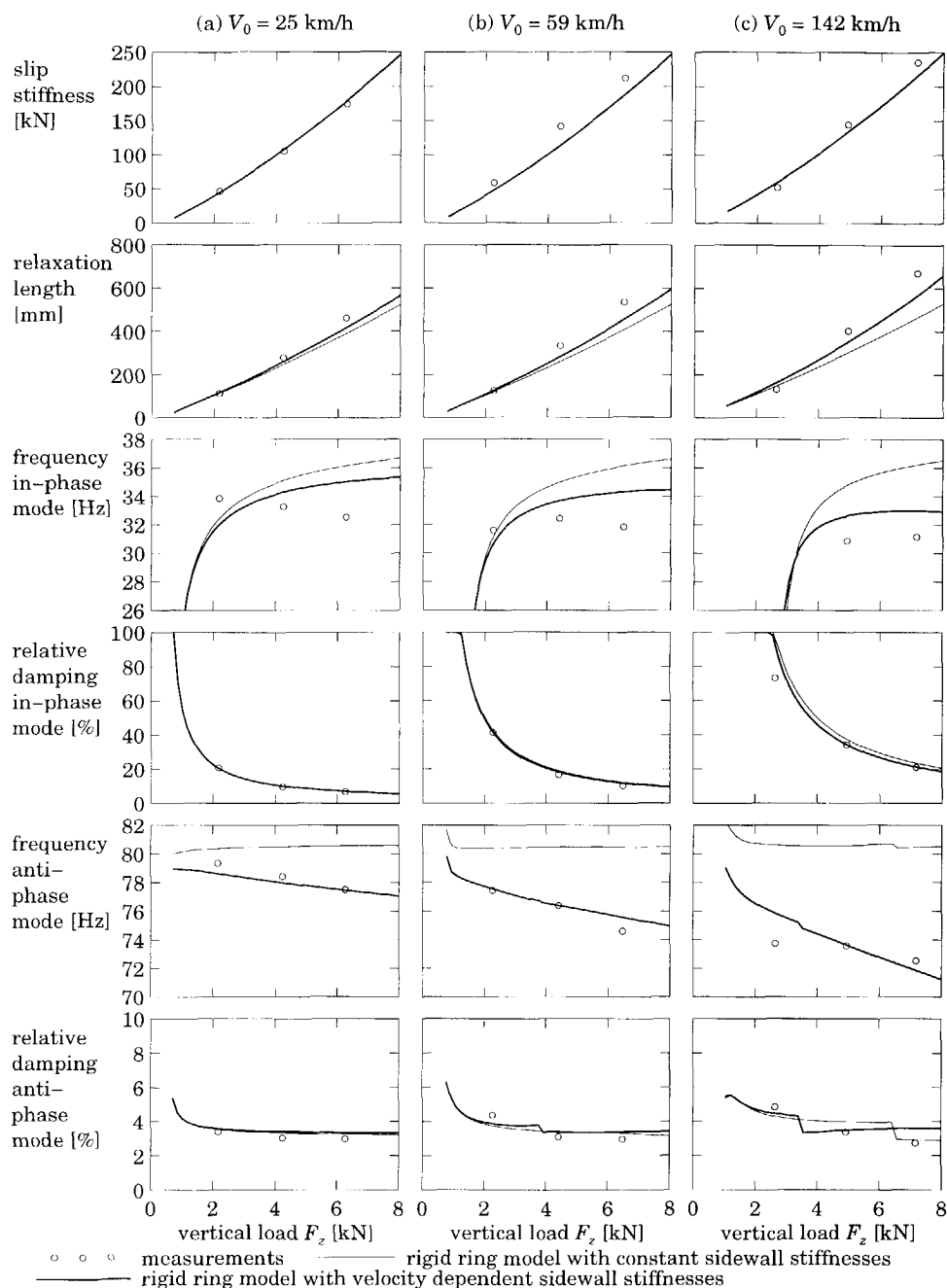
relative damping of this mode of vibration as well. The increasing damping lowers the natural frequency of vibration.

The vertical mode of vibration is defined to be the mode which has the largest amplitude of the vertical motion of the ring. When the moment of inertia of the brake system is omitted, the difference between the natural frequency of the anti-phase mode and of the vertical mode becomes small. Then the vertical mode and the anti-phase rotational mode may interchange at increasing vertical load. This phenomenon causes the jumps in the simulated frequency and damping graphs.

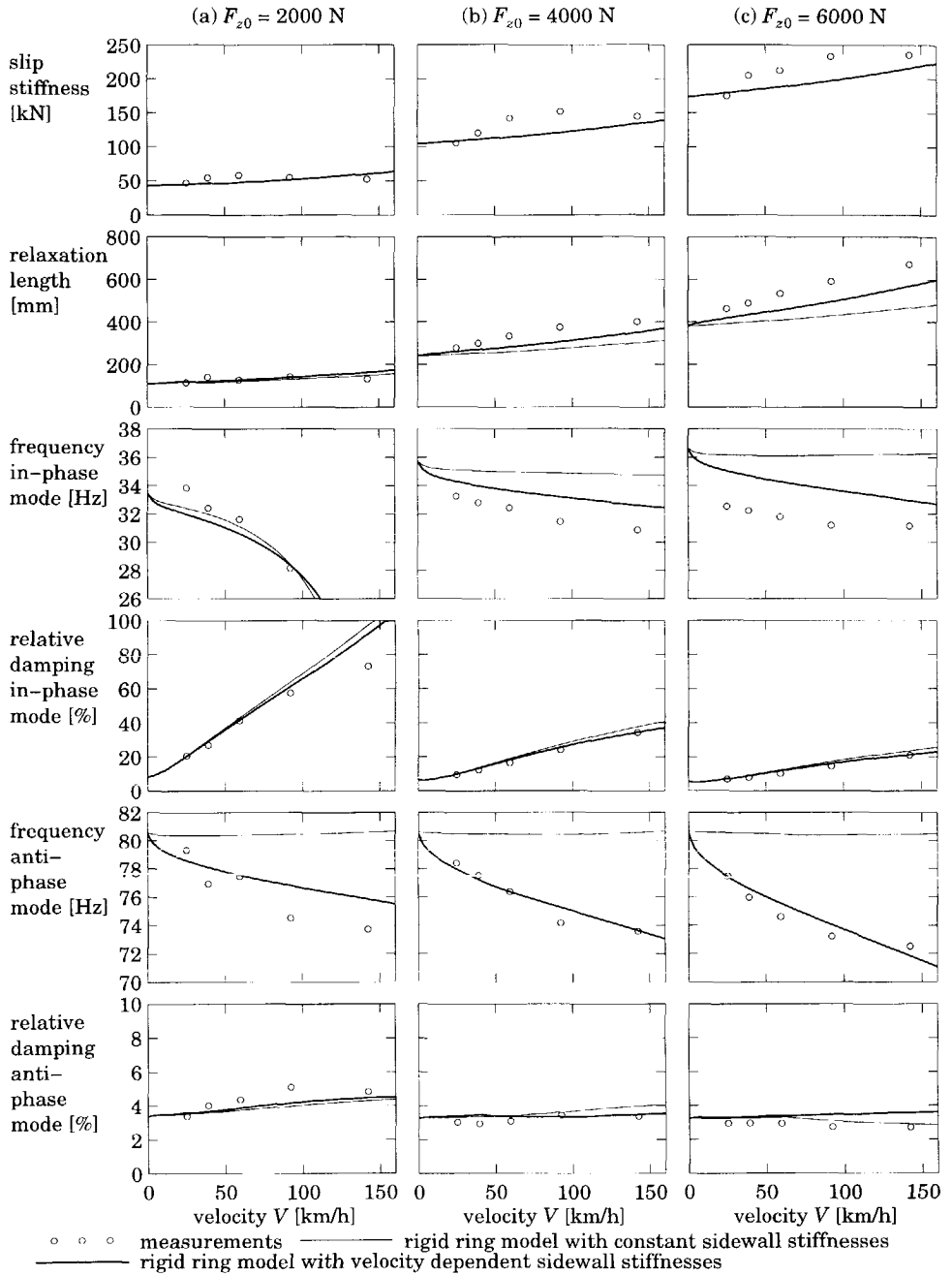
Figure 9.4 shows the tyre properties as functions of the velocity for three constant axle heights. The slip stiffness and relaxation length increase slightly with the velocity. The reason for this is that the experiments were carried out at constant axle height and the vertical load increases with velocity (*cf.* Table 2.4b). The damping of the in-phase rotational mode increases with velocity as predicted in Section 6.4. The natural frequency of the anti-phase rotational mode decreases with velocity. The simulations with the velocity dependent sidewall stiffnesses represent the measurements much better than the simulations with constant sidewall stiffnesses.

Figure 9.5 shows the tyre properties as functions of the average brake force. The average brake force varied between a small value and a value close to the peak value of the slip characteristics. When the average brake force increased the vibrations occurred around a point further on the slip characteristic curve. The slip stiffness, which is defined as the local derivative of the slip characteristics, will decrease with increasing slip. At very high levels of brake force the damping of the in-phase rotational mode increases rapidly and the natural frequency decreases. The natural frequency of the anti-phase mode decreases slightly with increasing brake force. This effect hardly be observed in the simulations.

In the subsequent sections the tyre responses are analysed in the time domain. The natural frequencies found from these of the responses do not correspond directly with the resonance frequencies presented in the Figures 9.3, 9.4 and 9.5. In these figures, the resonances of the FRF of longitudinal forces with respect to the measured brake torque are presented. The brake torque sensor is mounted on the intermediate shaft between wheel system and brake system (*cf.* Appendix A.1). This means that the moment of inertia concerned in these FRFs is the moment of inertia between the brake torque sensor and the longitudinal reaction force at the wheel bearings (thus excluding the brake system). From the subsequent section onwards the tyre dynamics are considered in the time domain. The moment of inertia of all rotating parts (thus including the brake system) must be taken into account.



**Figure 9.3:** The tyre properties as function of the vertical load ( $F_{x0} = 400 \text{ N}$ ).



**Figure 9.4:** The tyre properties as function of the velocity ( $F_{x0} = 400$  N).

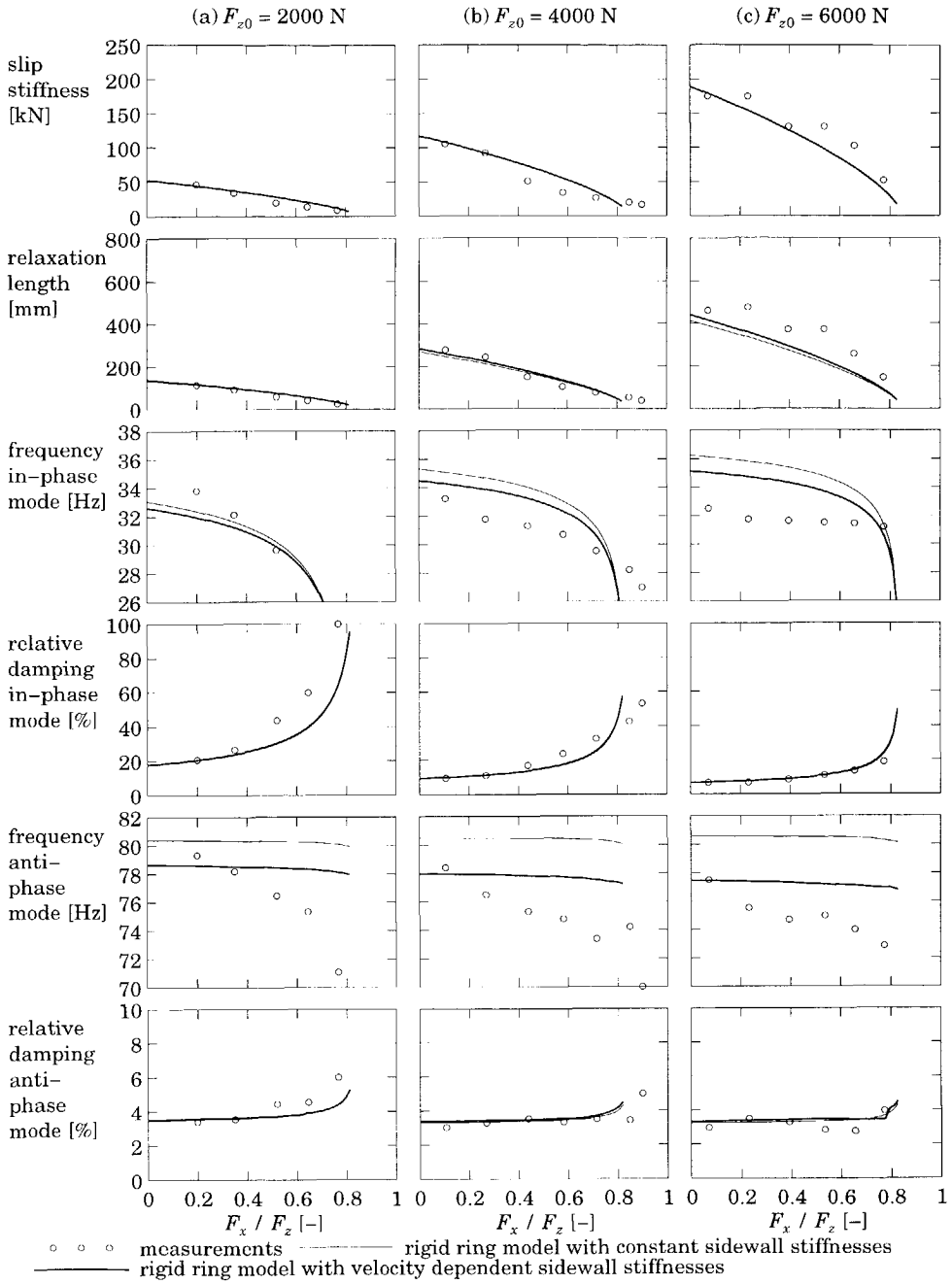


**Figure 9.5:** The tyre properties as function of average brake force ( $V=25$  km/h).

### 9.3 Braking with successive steps in brake pressure

As illustrated in the previous section, the tyre properties vary with speed, vertical load and brake torque. The linearised tyre model was used to estimate the tyre parameters from these tyre properties in each condition. In this section, the estimated parameter values are used in a non-linear simulation model of the tyre. The parameters which depend on the operating conditions are represented by the coefficients of the polynomials shown in Table 7.1b. The behaviour of the tyre model is validated by using variations in wheel slip and longitudinal force covering the entire slip curve.

The tyre was excited by stepwise increases of brake pressure until the peak in the slip characteristics is reached. The experiments were carried out at three axle heights: corresponding to 2000, 4000 and 6000 N vertical load for an initially non-rotating tyre and at five velocities: 25, 39, 59, 92 and 143 km/h. Fifteen conditions were investigated. The duration of each measurement was 4 seconds at 1024 Hz sampling rate. The filter frequency was 400 Hz. To reduce the influence of noise, the measurements were averaged 10 times. The measured brake torque was used as input for the non-linear simulation model.

Figures 9.6 and 9.7 show the measured and simulated responses of the tyre for two different speeds. From  $t$  is 0 to 2 seconds the brake pressure is increased stepwise. The dominant oscillation, that is the in-phase rotational mode at 33 Hz, is excited by each step in brake pressure. These oscillations are shown clearly in the dynamic force vs. slip characteristics. After a few oscillations a new steady-state value of the slip characteristics is found. At the end of the series of steps when wheel lock almost occurs, the wheel velocity decreases rapidly.

Figures 9.6 and 9.7 show the influence of the velocity on the tyre dynamics. The relative damping of the in-phase rotational mode increases at higher velocity (see also Figure 9.4). The friction coefficient is also affected: the tyre temperature increases at higher velocity and thus the friction coefficient increases as well. A further effect, which is not shown in the Figure 9.6 and 9.7, is the increase in vertical load of the rolling tyre at constant axle height.

Figures 9.8 and 9.9 represent the measurements and simulations for all 15 investigated conditions in a convenient manner. For comparison the dynamic force vs. slip characteristics are given and the longitudinal force is normalised by the vertical force. The values of the vertical force used for the normalisation are not the values for a non-rotating tyre (2000, 4000, 6000 N), but the values obtained from fitting the measurements of stationary rolling at constant axle heights as presented in Table 2.4b. Now, the y-axis represents the used portion of



friction coefficient present between tyre and drum. The friction coefficient increases from 0.6 at 25 km/h till 0.8 at 143 km/h.

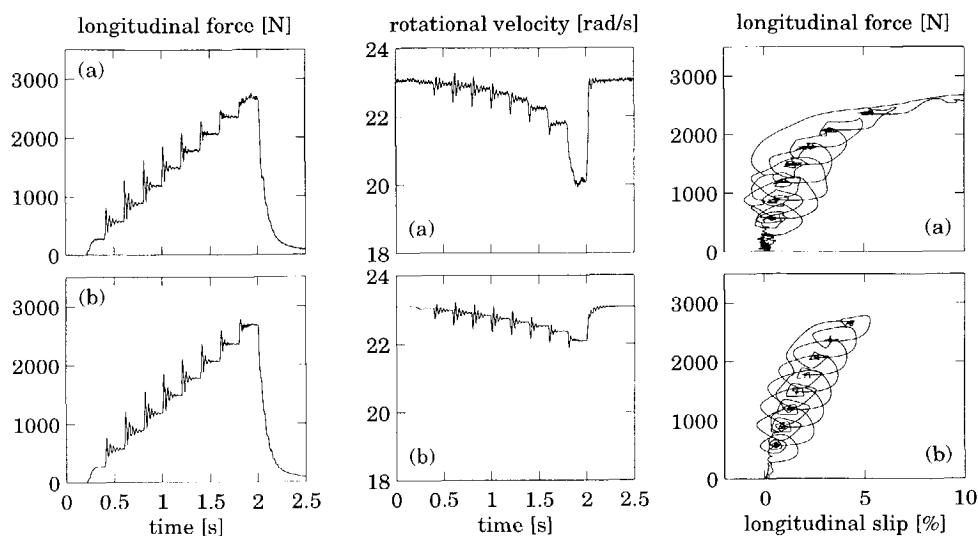


**Figure 9.6:** Tyre response on successive step increases of brake pressure.

$F_{z0} = 4000 \text{ N}$ ,  $V = 25 \text{ km/h}$ , (a) measurements, (b) simulation.

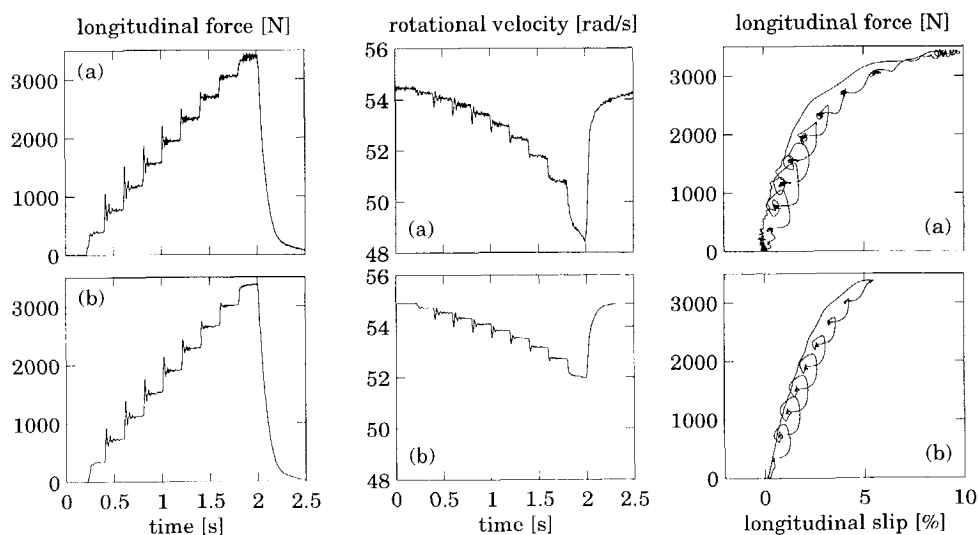


**Figure 9.7:** Tyre response on successive step increases of brake pressure.

$F_{z0} = 4000 \text{ N}$ ,  $V = 59 \text{ km/h}$ , (a) measurements, (b) simulation.

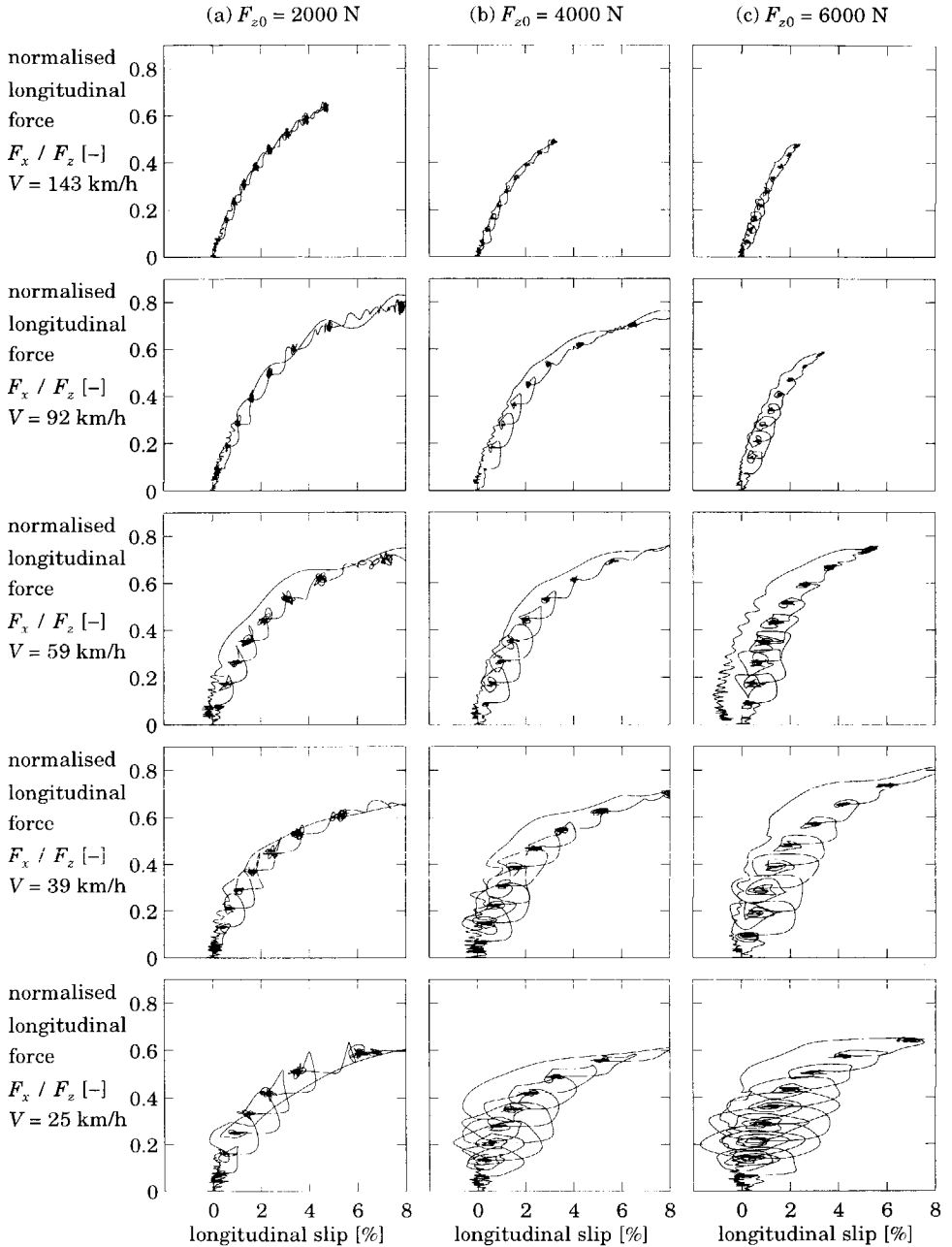


**Figure 9.8:** Measured step responses at five velocities and three axle heights.

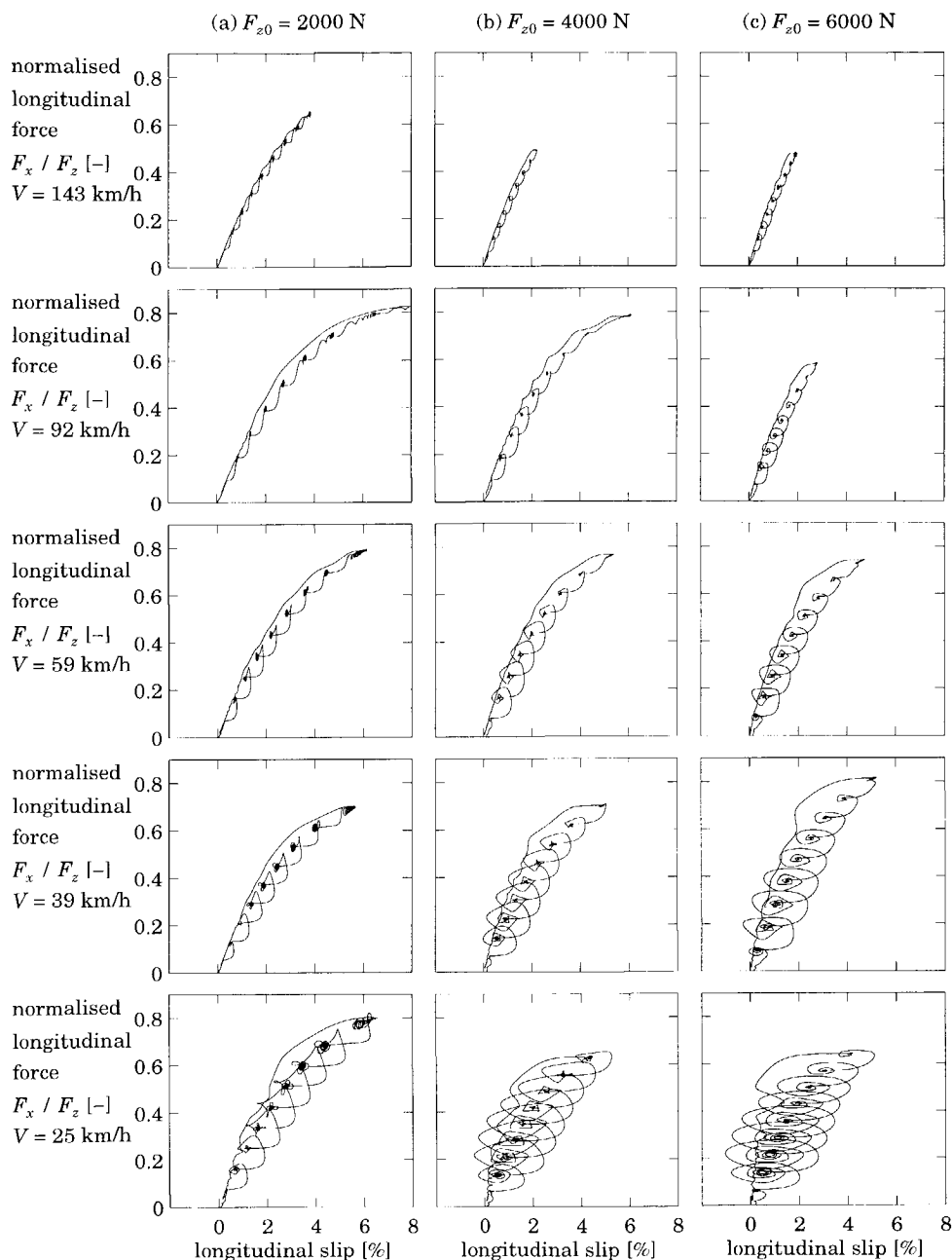


**Figure 9.9:** Simulated step responses at five velocities and three axle heights.

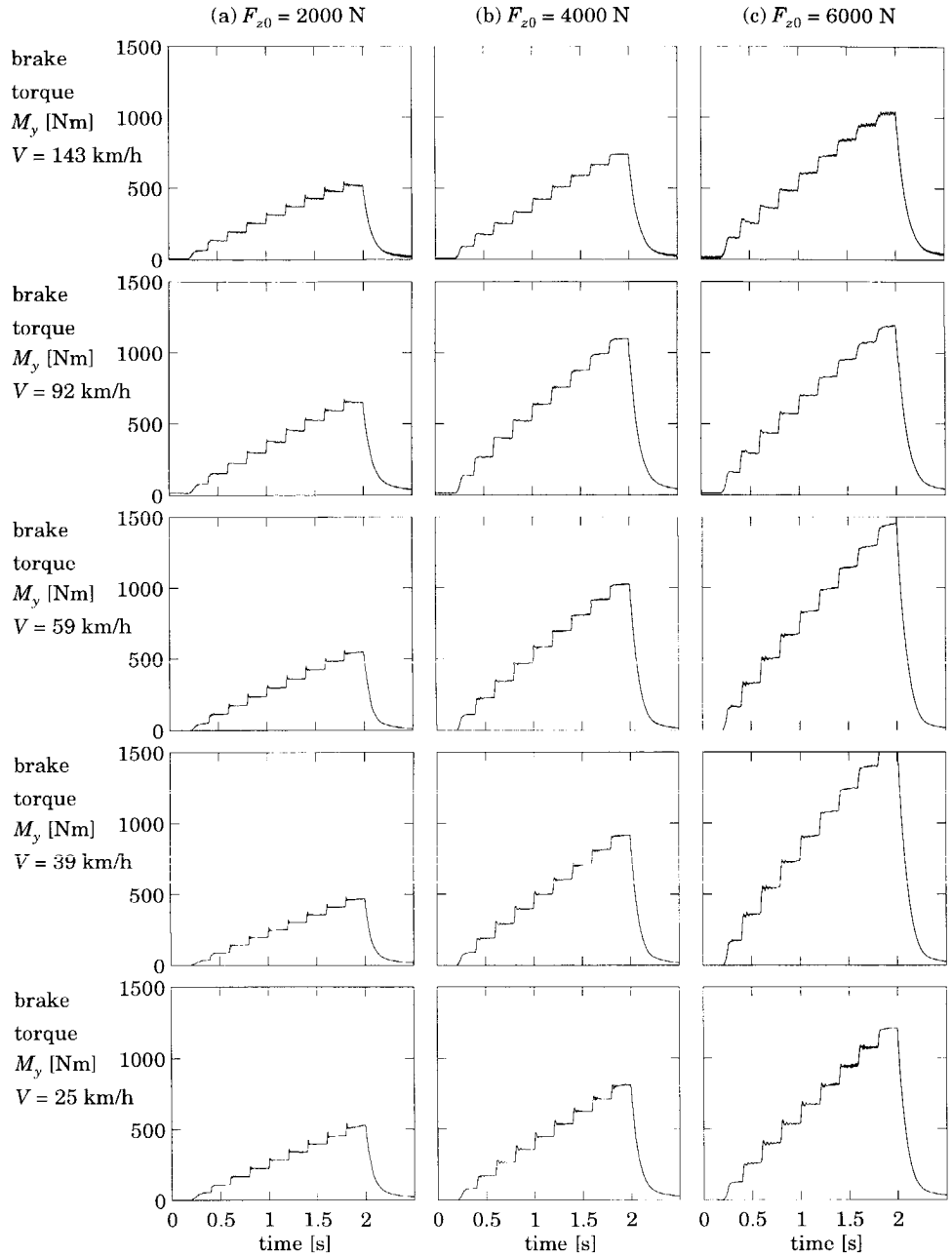


**Figure 9.10:** Measured brake torque at five velocities and three axle heights.

The model represents the measurements reasonably well. The input to the model is the measured brake torque, see Figure 9.10. The results achieved by the rigid ring model with a single-point contact tyre-road interface including the contact patch relaxation length are comparable with the results achieved with tyre models showing distributed deflections over the contact length [121,122].

At high levels of slip the model deviates from the measurements. This is because the used slip characteristics (of brush model) do not represent the measured slip characteristics accurately enough. The performance of the model will improve if a better representation of the measured slip characteristics (*e.g.* according to Magic Formula) is used.

## 9.4 Braking with wheel lock

The tyre model has also been validated for a brake manoeuvre resulting in wheel lock and spinning up again. This manoeuvre is not used to validate the tyre model properties themselves, but to validate the numerical stability of the simulation model. Two numerical problems may show up at wheel lock owing to the possible integration of theoretical slip to minus infinite and the dry friction characteristic of the brake system.

The experiments have been performed at three axle heights and at one velocity only (25 km/h). From  $t = 0.5$  to 1.5 seconds the brake pressure is kept at a high level causing wheel lock within 0.25 seconds. In contrast to all previous brake measurements, no averaging is performed. In the previous experiments, the brake pressure signals were generated by a computer. Measurements could be averaged easily because the excitation signal could be repeated. During the wheel lock experiments the brake pressure is kept constant at a high level. The tyre vibrations are not directly excited by the brake pressure changes. The tyre is excited by two abrupt changes in the rotational velocity: directly after wheel lock occurs and at spinning up of the wheel. The timing of these events depends highly on the friction between tyre and road.

Figure 9.11 presents the measured tyre response. The brake torque increases proportionally with the brake pressure until wheel lock occurs. The measured brake torque consists of two contributions: the torque resulting from the horizontal force generated in the contact patch and the torque needed to accelerate and decelerate the wheel. At wheel lock the deceleration of the wheel becomes abruptly zero causing a drop in measured brake torque. During wheel lock the brake torque is sufficient to maintain this condition.

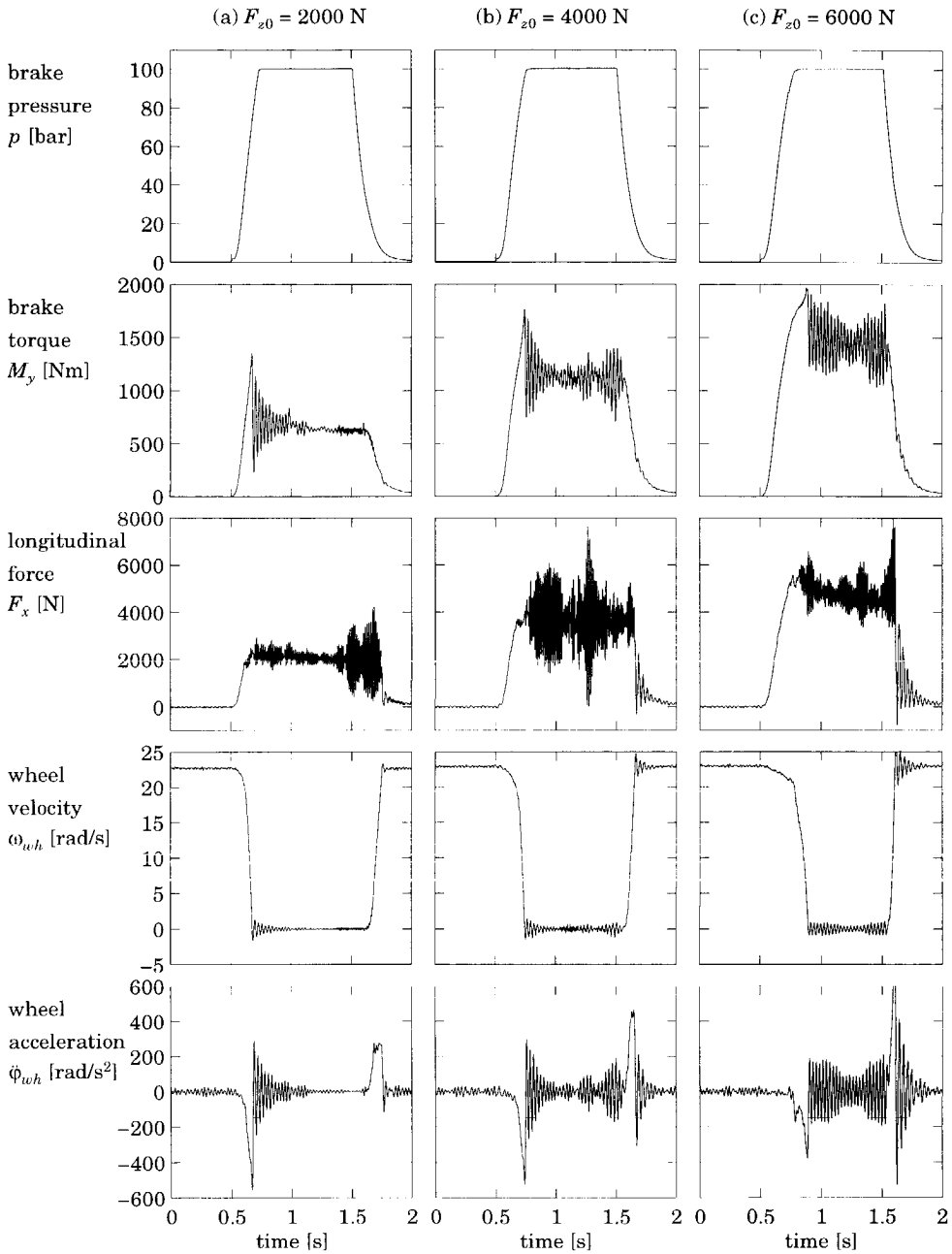


**Figure 9.11:** Measured brake response with wheel lock.

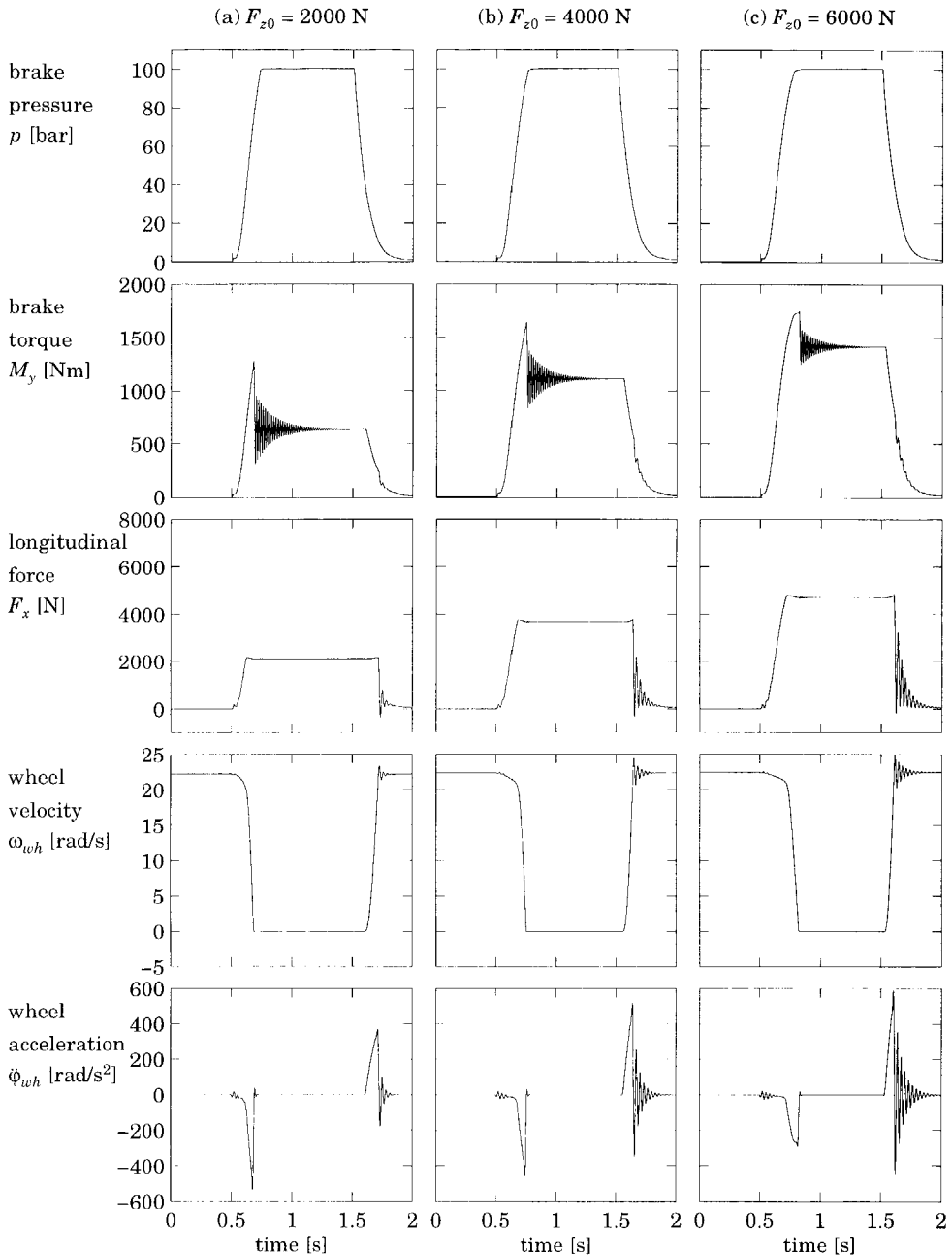


**Figure 9.12:** Simulated brake response with wheel lock.

The wheel acceleration was obtained by numerically differentiating the wheel velocity. Just before wheel lock occurs the wheel velocity decreases rapidly, resulting in a large negative peak in the wheel acceleration. At spinning up of the wheel the velocity increases rapidly causing a large positive peak of the wheel acceleration. The measured wheel velocity and wheel acceleration signals indicate that the motion of the wheel was not constrained completely. This is probably due to flexibility between the wheel and the brake system.

Figure 9.12 presents the simulated brake response. For these simulations the brake torque was not used as input, because of the fact that especially during wheel lock the measured brake torque must be regarded as a response of the tyre wheel-system rather than as an input to the system. Therefore, the brake pressure was used as input for the simulation model. The frictional force generated in the brake system depends on the applied brake pressure and the wheel velocity. The constraint equations used are given in Section 7.4.

The model represents the measurements rather well. We see wheel lock within 0.25 seconds. The constraint equation for the brake system operates well. The rotational velocity of the wheel is exactly zero during wheel lock. The tyre model generates a constant force during wheel lock. At spinning up of the wheel the simulations show the same vibrations as the measurements.

Section 6.2 introduces in the model limitation of the longitudinal slip at full sliding. This limitation prevents the integration of the slip to plus or minus infinity. If this limitation would not be employed in the model, the simulated spinning up of the wheel would be delayed.

The abrupt change in wheel deceleration causes a vibration of the tyre. The simulated frequency of this vibration is higher than the measured frequency. This is probably caused by the flexibility between the brake system and the wheel. This flexibility decreases the overall stiffness between brake system and contact patch.

Owing to the use of the model with a constant friction coefficient the model does not show the stick-slip behaviour which is shown very severely in the measurements. However, a model with a decreasing friction coefficient at full sliding shows only small vibrations and not the severe vibrations exhibited in the experiments.



## 9.5 Braking to stand-still

The rigid ring tyre model has also been validated for a brake manoeuvre to stand-still. This is in contrast to all previous experiments, where the electric motor of the drum was used to maintain a constant drum velocity.

We may see the rotating drum as the mass of a vehicle and the tyre is used to slow down the drum. The goal of this experiment was to validate the tyre model at varying velocity and to check the numerical stability of the model at zero drum velocity. The difference between the tyre rotating on a drum and the tyre rotating in a vehicle is that the longitudinal force in the contact patch is used to slow down the drum, rather than the reaction force at the axle slowing down the vehicle.

This experiment has been done only at one axle height, corresponding to 6000 N vertical load, because the moment of inertia of the drum is relatively large. Only at high levels of vertical load can the tyre produce enough longitudinal force to slow down the drum within a reasonable time span.

A periodic brake pressure signal was chosen, each brake cycle consisted of one second free rolling, followed by two seconds of successive step increases until maximum brake force, followed by one second free rolling. The initial velocity was 59 km/h and 8 brake cycles were used to brake the drum to a complete stand-still. The resulting measuring time was 32 seconds. Due to limitations of the data-acquisition system the 32 seconds measuring time was split into two 16 seconds intervals and the sampling rate was decreased from 1024 Hz to 512 Hz. Accordingly, the filter frequency was decreased from 400 Hz to 200 Hz. Figure 9.13a through 9.13d present the measured tyre and drum responses.

The drum is modelled as an equivalent moving mass  $m_{drum}$  slowed down by two forces: the longitudinal force generated in the tyre contact patch  $F_{cx}$  and an internal hysteresis force in the drum propulsion system  $F_{hyst}$ :

$$\dot{V}_{drum} = (F_{cx} - F_{hyst}) / m_{drum} \quad (9.1)$$

where  $V_{drum}$  denotes the velocity of the drum. The equivalent mass of the drum equals all moments of inertia of the drum and its subsystems such as motor, transmissions and brake systems. The value of the equivalent mass was estimated from the drum deceleration and the measured longitudinal reaction force in the wheel bearing during the successive step increases. The equivalent mass equals 3800 kg for the drum with transmission in third gear (maximum velocity 59 km/h).

During the free rolling intervals the drum decelerated considerably owing to internal friction in the drum propulsion system. This frictional force varied from 1000 N at 60 km/h to 400 N at 2 km/h. The influence of this friction is represented by the hysteresis force  $F_{hyst}$ :

$$F_{hyst} = (368.5 + 143.1 \cdot \sqrt{|V_{drum}|}) \cdot \text{sgn}(V_{drum}) \quad (9.2)$$

Obviously the hysteresis force is the maximum friction force generated in the drum propulsion system and it is acting in the direction opposite to the drum velocity. In the simulation model this force is modelled as a dry friction force with magnitude according to expression (9.2).

The brake pressure is used as input for the simulation model. At 10 km/h the disc brake produces 25 Nm brake torque at 1 bar brake pressure; at 60 km/h this value decreases to 17 Nm/bar.

Figures 9.13a through 9.13d compare the measured tyre response with the simulated tyre response. These figures clearly show the decrease of the relative damping of the in-phase rotational mode at decreasing velocity. A similar effect was found from the random brake pressure variations presented in Figure 9.4. The simulation represents the measurements rather well, except

At the end of both the simulation and the experiment a vibration of the drum can be seen. Here, the drum vibrates against the tangential tyre stiffness. The frequency of this vibration (1.7 Hz) results directly from the tangential stiffness of the tyre ( $C_{x,tot}=400000$  N/m) and the equivalent mass of the drum ( $m_{drum}=3600$  kg). The damping of these drum rotational vibrations is a result of the hysteresis forces.

## 9.6 Conclusions

The rigid ring model gives a satisfactory representation of the dynamic tyre responses to brake torque variations. The parameters of the model were successfully estimated from the measured frequency response functions. The tyre parameters should actually be taken as functions of the velocity, because the measured natural frequencies apparently decrease with velocity. A further improvement on the stationary performance of the model may be achieved by changing the brush characteristics into a better representation like the Magic Formula.

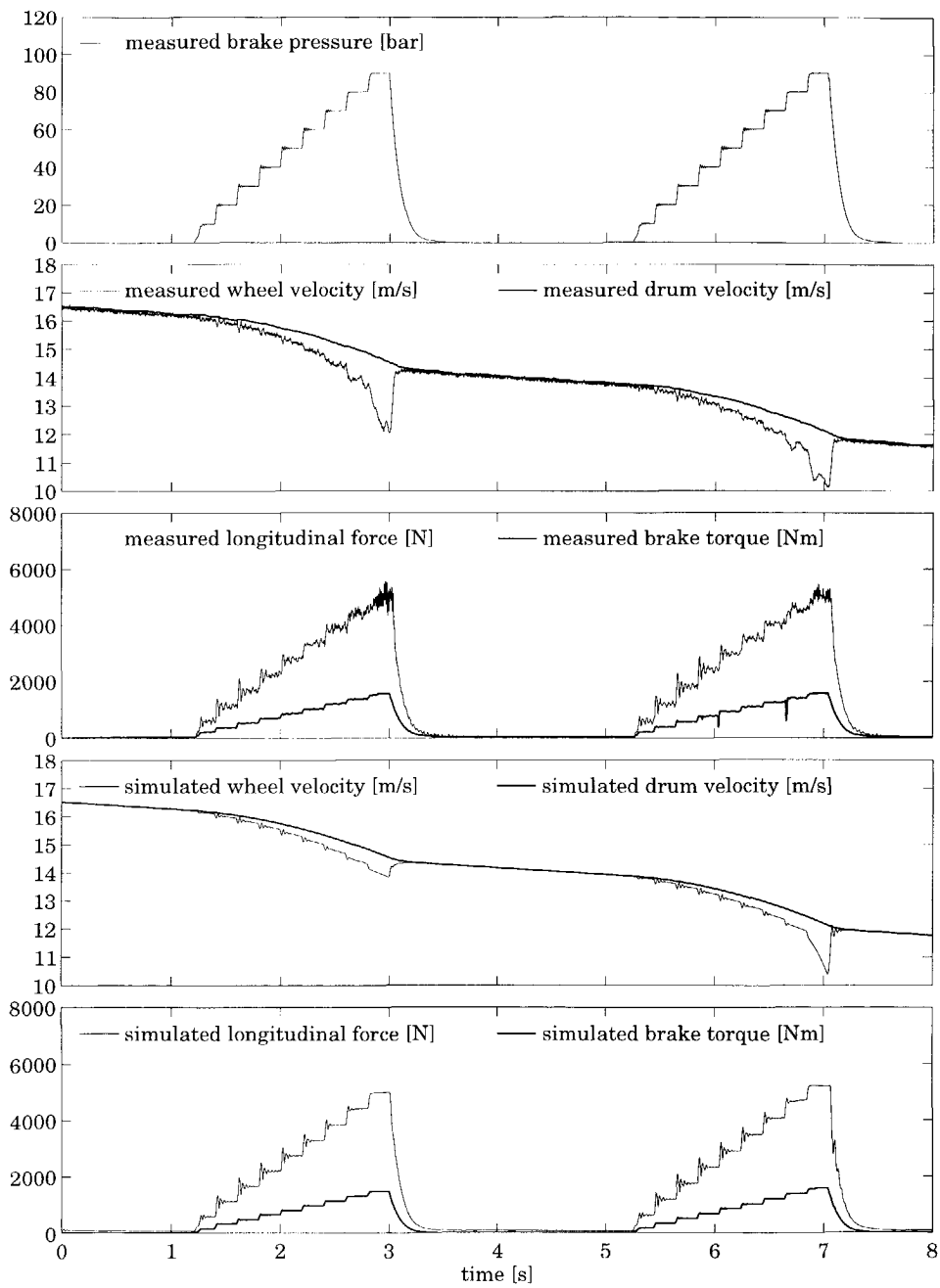


**Figure 9.13a** Measured and simulated braking to stand-still ( $t=0-8$  s).

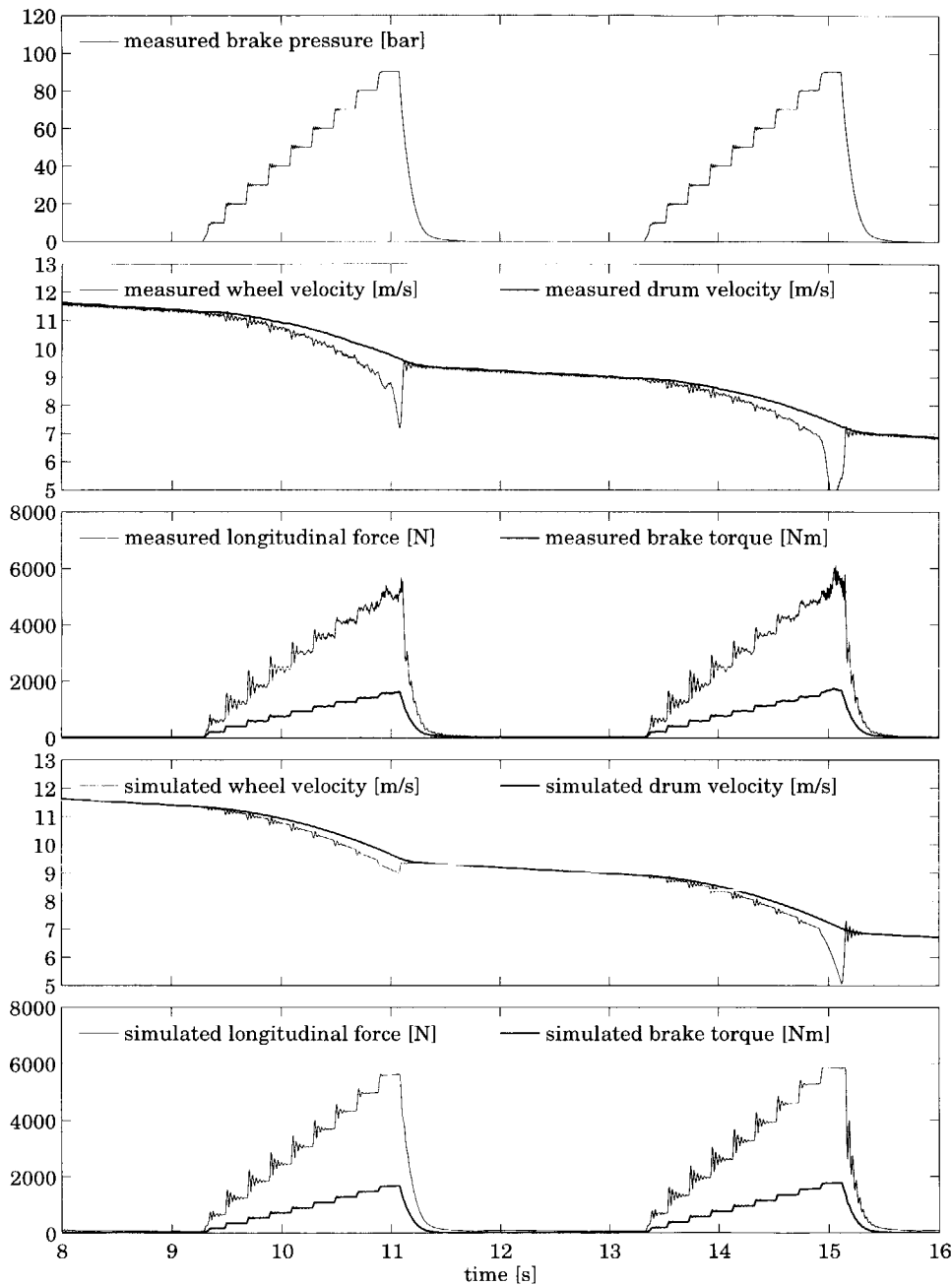


**Figure 9.13b** Measured and simulated braking to stand-still ( $t=8-16$  s).

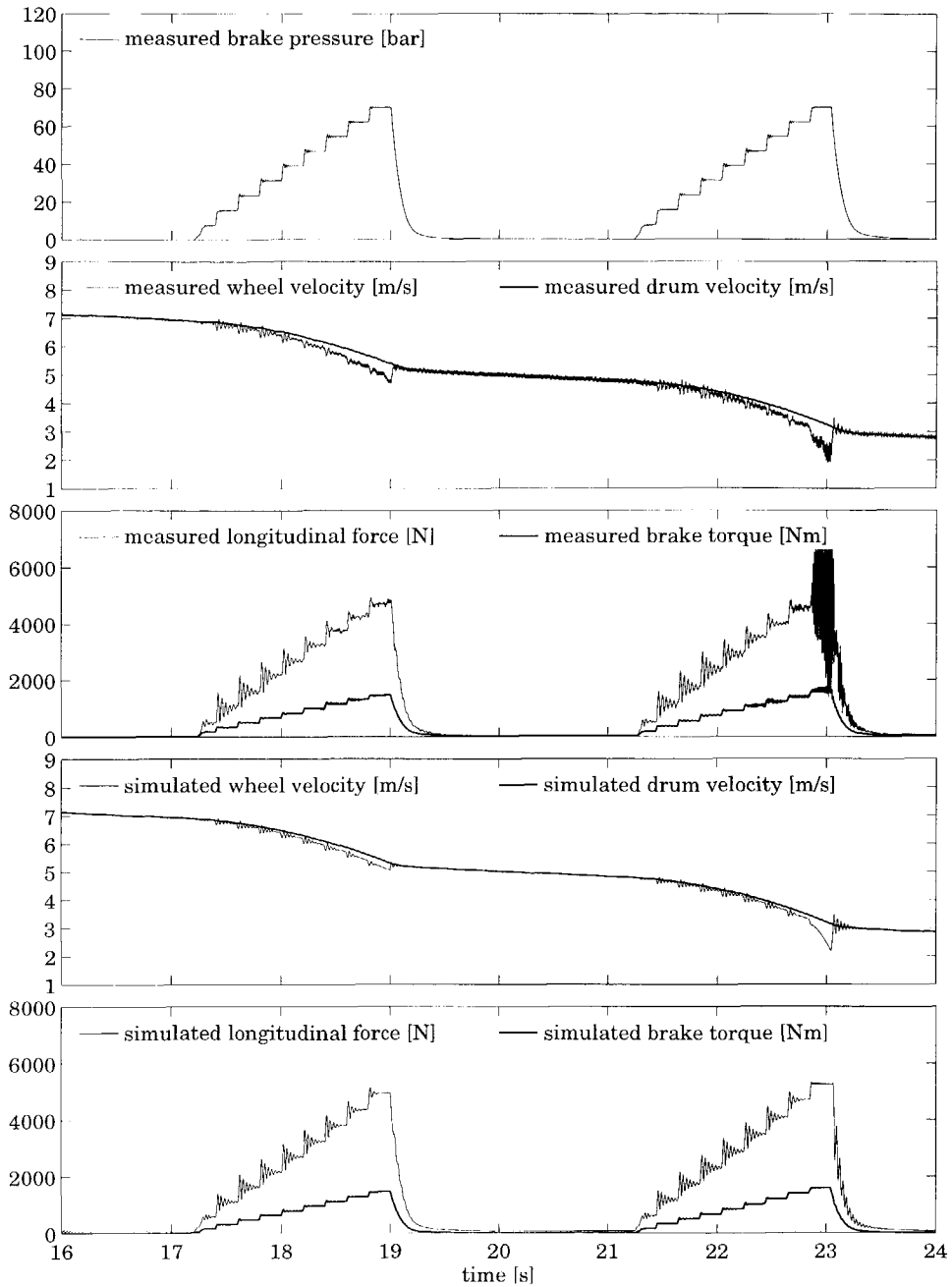


**Figure 9.13c** Measured and simulated braking to stand-still ( $t=16-24$  s).

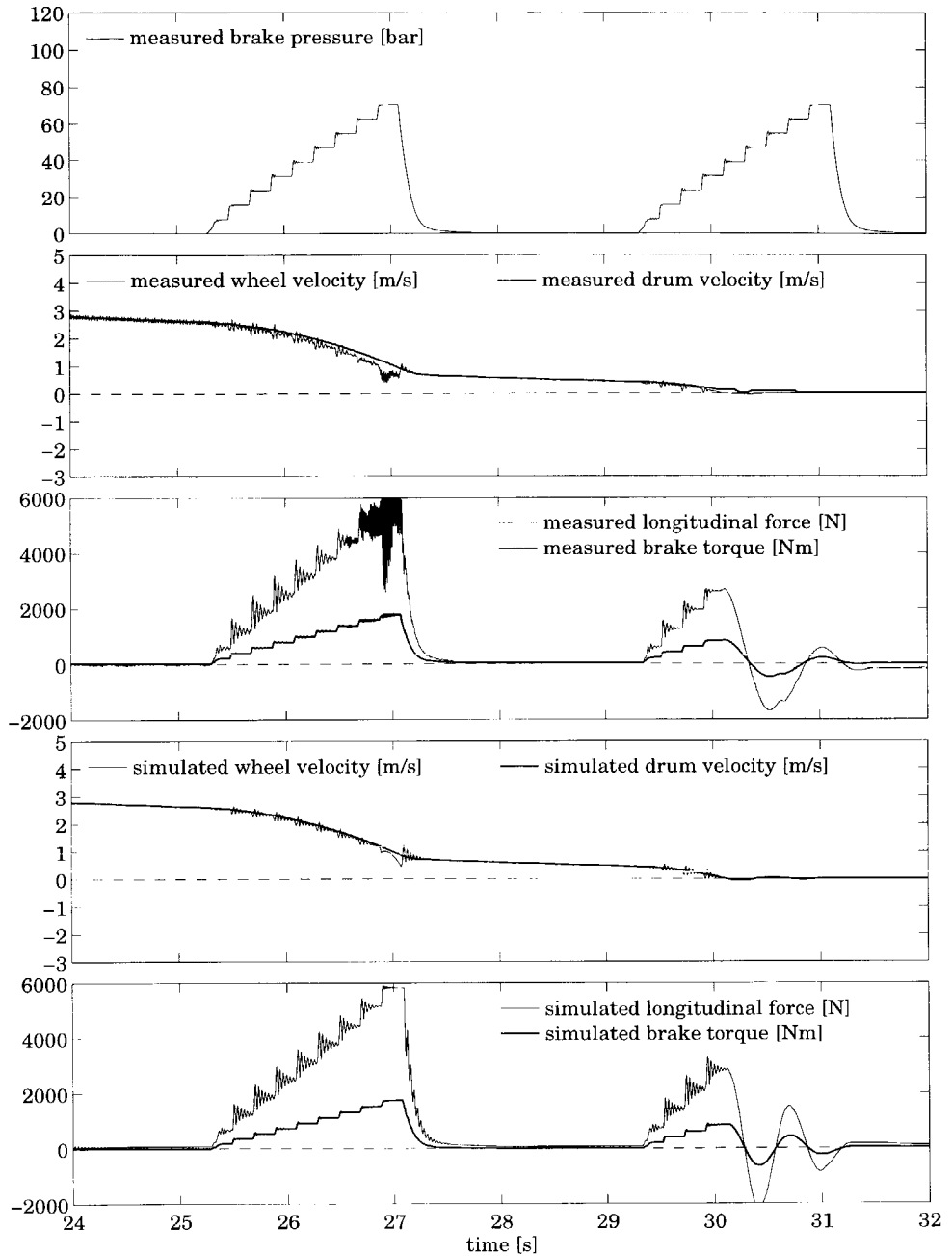


**Figure 9.13d** Measured and simulated braking to stand-still ( $t=24\text{--}32$  s).

# 10

## Dynamic Tyre Responses to Short Wavelength Road Unevennesses

---

### 10.1 Introduction

The study of vehicle dynamics on uneven road surfaces requires a mathematical tyre model to transform the road profiles into forces at the vehicle hub. With long wavelength road irregularities, the tyre-road interface may be governed by a single-point contact model. For short wavelength irregularities, on the other hand, a more detailed description of the tyre-road interface is necessary.

The approach used in this PhD study is to separate the tyre-road interface from the tyre dynamics, as shown schematically in Figure 10.1. In Chapter 4 an elaborated tyre model (the *flexible ring* tyre model) and extensive experiments were used to obtain the quasi-static excitation of the tyre on short wavelength irregularities. These quasi-static excitations were transformed into an effective road surface and can be used as input to the *rigid ring* tyre model. The advantage of this approach is that the dynamic simulations are relatively fast.

The flexible ring model (see Chapter 4 and 8) can also be used to calculate the dynamic tyre responses in short wavelength conditions. The exact obstacle shape can be used as input for such a model. However, this approach leads to unacceptably large simulation times.

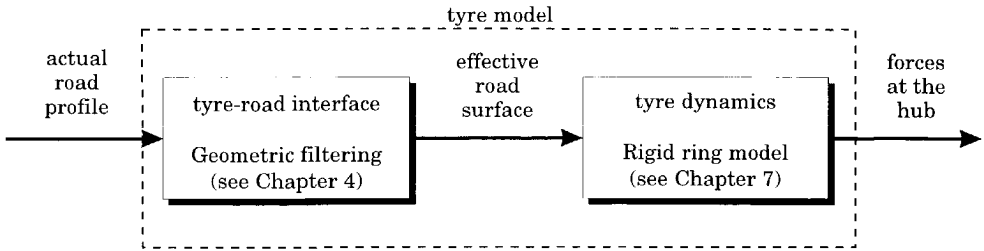


**Figure 10.1:** The transformation of the road profile to forces at the wheel hub.

Table 10.1 presents a chronological literature study of the dynamic tyre responses due to cleat impacts. These studies were generally performed to study either vehicle comfort properties [8,15,47,79], or vehicle durability properties [74,75]. For these studies it was important that the tyre simulations were relatively fast. The following items of interest are considered in Table 10.1:

- **Velocity.** The low velocity experiments, used either to validate the enveloping model, or to establish the effective excitation of the tyre in quasi-static conditions. A literature study of the enveloping properties of tyres has already been presented in Table 4.1.
- **Direction of the responses.** The longitudinal and vertical forces acting on the hub are important. This chapter presents the rotational wheel velocity and accelerations as well.
- **Boundary condition at the axle.** The boundary conditions for experiments carried out on a rotating drum test stand were generally pinned conditions; that is with constrained horizontal and vertical axle displacements. The tyre dynamics were identified from the forces acting on the hub. For experiments on a road surface a vehicle with a suspension was used and the horizontal and vertical accelerations of the hub were measured.
- **Input to the model.** Tyre models that describe tyre tread-band deformation in detail can use the actual shape of the obstacle as input. For simplified models effective excitations are used rather than the actual shape of the unevenness. Oldenettel *et al.* measured the vertical response at low velocity (2 km/h) and determined the frequency response function between the high and the low velocity excitation [79]. Ushijima *et al.* measured the excitation forces under the cleat and used these forces as excitation to the model.
- **Tyre model.** The Finite Element Models (FEM) have proven to be very successful in enveloping obstacles at high velocities. Oertel [78] and Eichler [24,25] used a 2-dimensional FEM. They increased the accuracy of the tyre-road interface by adding massless sensor points between the node points. The



2-dimensional FEMs are faster than full scale 3-dimensional FEM. Kao *et al.* [47] increased the simulation speed by reducing a 3-dimensional FEM to a modal representation with 8 fore/aft and vertical modes and 9 contact points. Bandel [8] also used a modal model with even less modes. Mousseau *et al.* used both a radial spring model and a 3-dimensional FEM; the relatively simple radial spring model could not predict the dynamic tyre forces [75].

- **Experiments.** The experiments were either carried out on a rotating test drum or with a vehicle on the road.

**Table 10.1:** Literature survey on dynamic tyre responses on short wavelength obstacles.

reference	velocity		direction response		axle		model input			dynamic tyre model					experiments	
	low	high	longitudinal	vertical	pinned	suspension	obstacle shape	basic function	contact forces	2D FEM	3D FEM	radial spring	modal model	rigid ring	on drum	on flat road
Kao [47]		•	•	•		•	•						•		•	
Bandel [8]	•	•	•	•	•			•					•		•	
Ushijima [111]				•	•				•				•		•	
Mousseau [75]	•	•	•	•	•		•				•	•			•	
Kamoulakos [46]		•	•	•	•		•				•				•	
Eichler [24,25]		•	•	•		•	•			•						•
Bruni [15]		•	•	•	•									•	•	
Oertel [78]		•	•	•	•		•			•					•	
Oldenettel [79]	•	•	•	•	•										•	

10.2 Experimental setup

The experiments were carried out on the *cleat and brake* test stand that is shown in detail in Appendix A. The tyre rotates on a drum with a diameter of 2.5 meter. The tyre was excited by obstacles which were mounted on the drum surface. The trapezoid cleat (obstacle 1) was created by mounting a metal strip to the drum. Obstacles 2 and 3 were created by mounting cylindrical shells on half the drum circumference, resulting in one positive and one negative step for each drum revolution. The fourth obstacle was created by mounting the shells along almost the entire drum circumference leaving a gap of 50 cm.

Obstacle 1, 2 and 3 are discussed in Chapter 4 for determining the effective inputs. The effective input of obstacle 4 ‘negative cleat’ can be composed from one negative and one positive step.

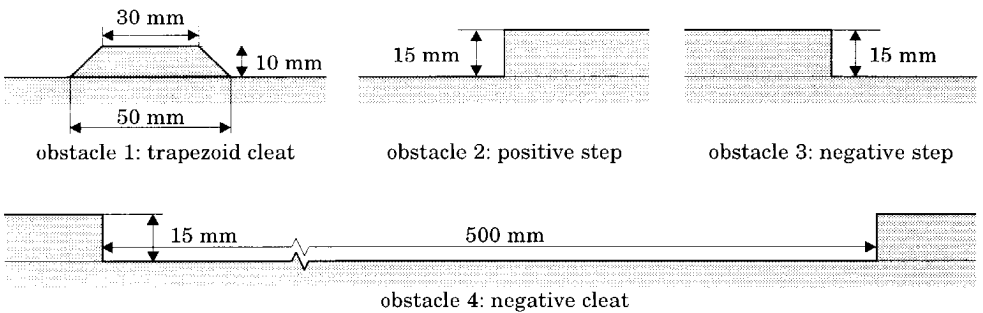


**Figure 10.2:** The four obstacles used.

The experiments were carried out at three constant axle heights, corresponding to 2000, 4000 and 6000 N vertical load for a non-rotating tyre measured on the undisturbed surface of the drum. The four obstacles are used to study the tyre dynamics after obstacle impact. After the obstacle is passed, the vertical load will tend to its average value while showing initial vibrations. For the tyre rolling over positive step obstacles 2 and 4, the average vertical load during vibration will be 3000 N larger due to the finally reached constant obstacle height of 15 mm. In other words, the experiments of the tyre rolling over obstacles 2 and 4 were effectively carried out at 5000, 7000 and 9000 N vertical load.

The experiments were carried out at three velocities: 25, 39 and 59 km/h. This choice of velocities resulted from the transmission ratios of the drum propulsion system. The maximum velocity was restricted owing to the large impact forces and the settling time of the tyre vibrations between two impacts. At

60 km/h the drum rotates at approximately one revolution per second. When the cylindrical shells are mounted on half the drum circumference, the time interval between the positive step and negative step is only 0.5 seconds. At higher velocities, the tyre has not reached a steady-state situation at the next cleat impact.

In total 36 experiments were carried out for a free rolling tyre (4 obstacles at 3 axle heights and 3 velocities). 96 experiments were carried out at various levels of constant brake torque to study cleat impacts on a braked tyre as well.

The wheel axle was fixed in a frame to constrain its vertical and horizontal motion. The reaction forces of the wheel were measured with piezo electric elements mounted above the wheel axle bearings. These sensors can only measure the variations of the force due to a drifting effect. As in the brake experiments, the vertical load at constant axle height will increase with increasing velocity. The exact values of vertical load in given operating conditions (axle height and velocity) are presented in Table 2.4b.

The other sensors were the wheel velocity sensor and the brake torque sensor. The brake torque sensor did not only measure the constant brake torque but also the torque needed to accelerate and decelerate the brake system in rotational direction. By dividing the variations in measured torque by the moment of inertia of the rotating parts between sensor and brake callipers, the rotational acceleration of the wheel could be obtained as well.

An optical cleat passage sensor was used to trigger the data acquisition system. Using this trigger it was possible to average the tyre responses reducing the influence of tyre non-uniformities and other sources of noise. The measurements were averaged 20 times for free rolling conditions and 10 times for braking conditions.

### **10.3 Natural frequencies obtained directly from the measurements**

This section presents the natural frequencies which were obtained directly from the experimental data without using tyre models or knowledge of the excitation of the tyre by unevennesses. The measured time signals were transformed into the frequency domain. The auto-spectral densities of the tyre responses are used rather than the frequency response functions, as the excitation is assumed to be unknown at this stage.

The measured auto-spectral density function in a narrow frequency band around an expected natural frequency is used to estimate this frequency. In this

narrow band the input signal is assumed to be of constant mean square density and the frequency can be estimated from the position of the peak and the relative damping from the sharpness of the peak. The method is not very accurate as the input spectrum is usually non-constant. The method used to estimate the natural frequency and damping from auto-spectral density functions is identical to the method used to estimate these quantities from a frequency response function, see Equations (8.2) through (8.5) in Section 8.2.

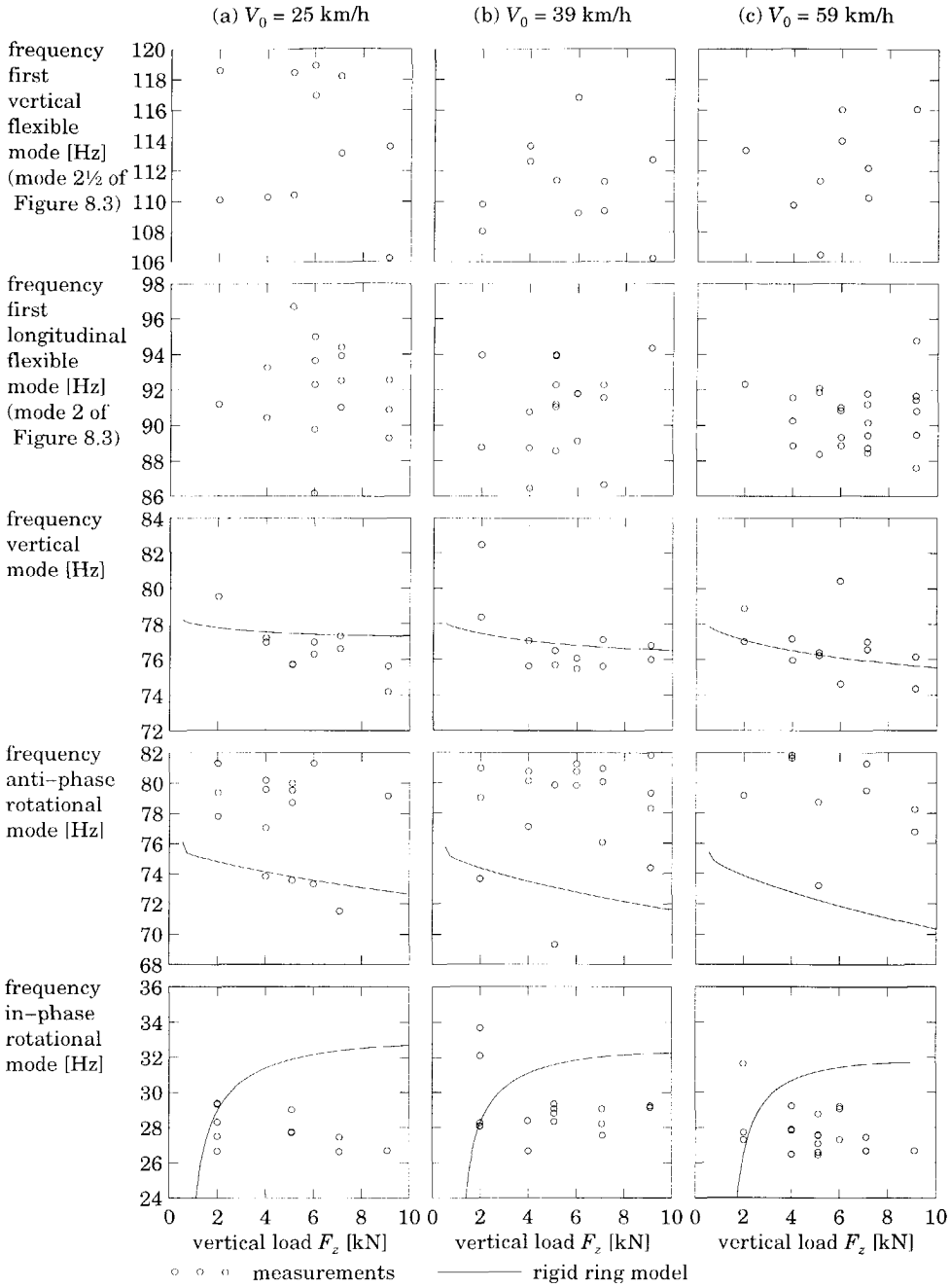
The results are presented in Figures 10.3 through 10.5 where the estimated frequencies are plotted as functions of vertical load, velocity or average brake force. Each estimated frequency is indicated by a small circle. Only data which is thought to be reasonable is presented in these figures: first, the relative error in the estimation (Eq. 8.5) should be small enough, second the estimated frequency should lie in a narrow band ( $\pm 10$  Hz), and third, the estimated damping should lie in a narrow band ( $\pm 5\%$ ) as well. From the data scatter it can be seen that this method is not very accurate for estimating tyre natural frequencies.

Table 10.2 presents the average frequencies of the five identified modes. The measured vertical force response shows two resonance frequencies: the vertical mode where the belt moves approximately as a rigid body at 76 Hz, which is in this thesis referred as *the* vertical mode of the tyre, and the first flexible mode in vertical direction (mode 2½ in the Figures 8.3 and 8.4).

**Table 10.2:** *The average natural frequencies obtained from the experiments.*

tyre-wheel mode	natural frequency	relative damping
first vertical flexible mode	111 $\pm$ 4 Hz	3 $\pm$ 2 %
first longitudinal flexible mode	91 $\pm$ 2 Hz	4 $\pm$ 2 %
the vertical mode	76 $\pm$ 3 Hz	5 $\pm$ 2 %
anti-phase rotational mode	74 $\pm$ 4 Hz	5 $\pm$ 2 %
in-phase rotational mode	28 $\pm$ 3 Hz	20 $\pm$ 13 %

Three measured signals were used to estimate the longitudinal and rotational tyre modes: the longitudinal force, the rotational wheel velocity and the rotational wheel acceleration. Three longitudinal and rotational resonance frequencies were obtained: the in-phase rotational mode at 28 Hz, the anti-phase rotational mode at 74 Hz, and the first flexible longitudinal mode, corresponding to mode 2 in Figures 8.3 and 8.4. The natural frequencies of the rigid ring tyre model which velocity dependent sidewall stiffnesses are depicted in Figures 10.3, 10.4, and 10.5 as well.



**Figure 10.3:** The tyre natural frequencies as function of the vertical load.

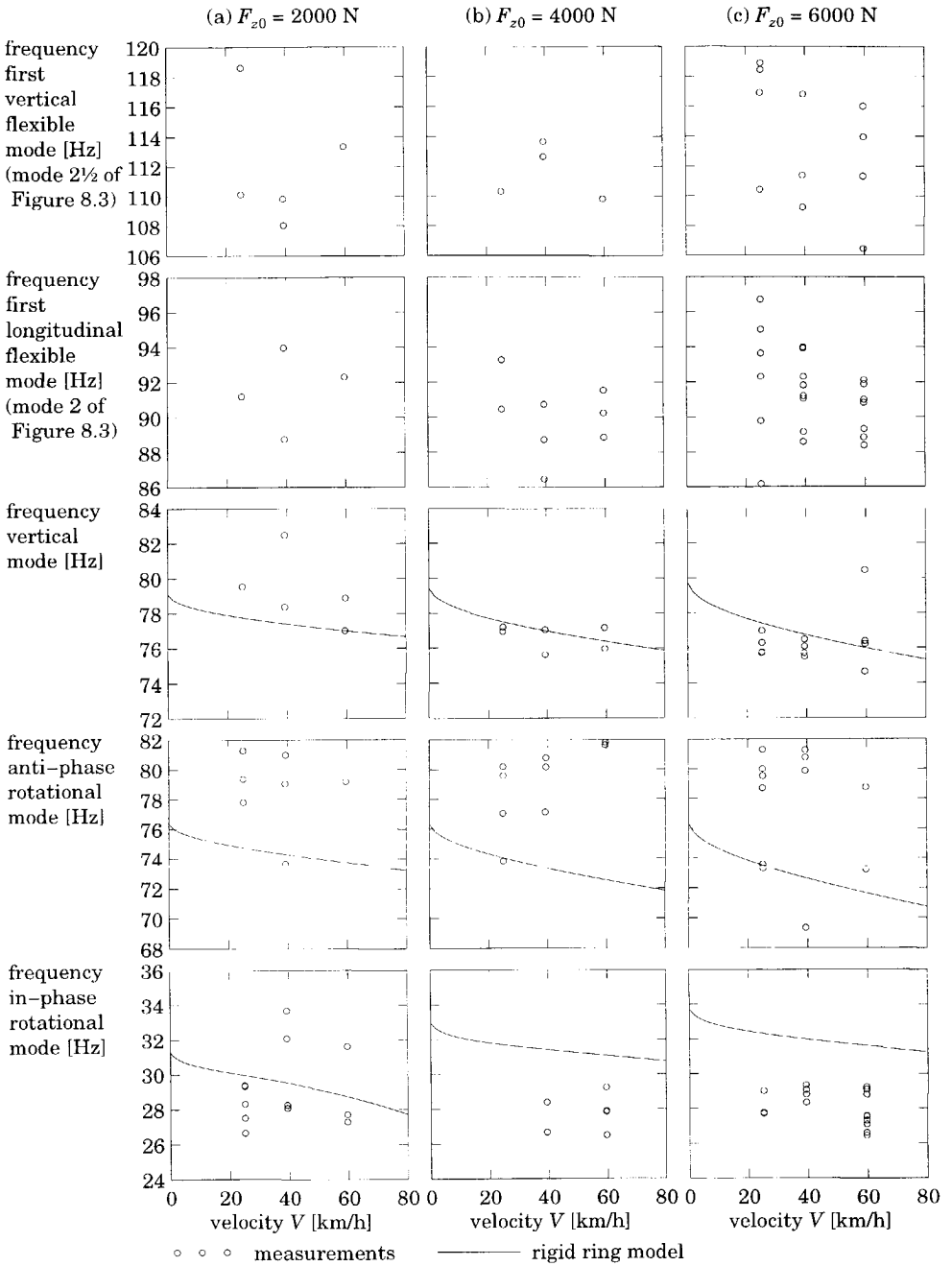


**Figure 10.4:** The tyre natural frequencies as function of the velocity.

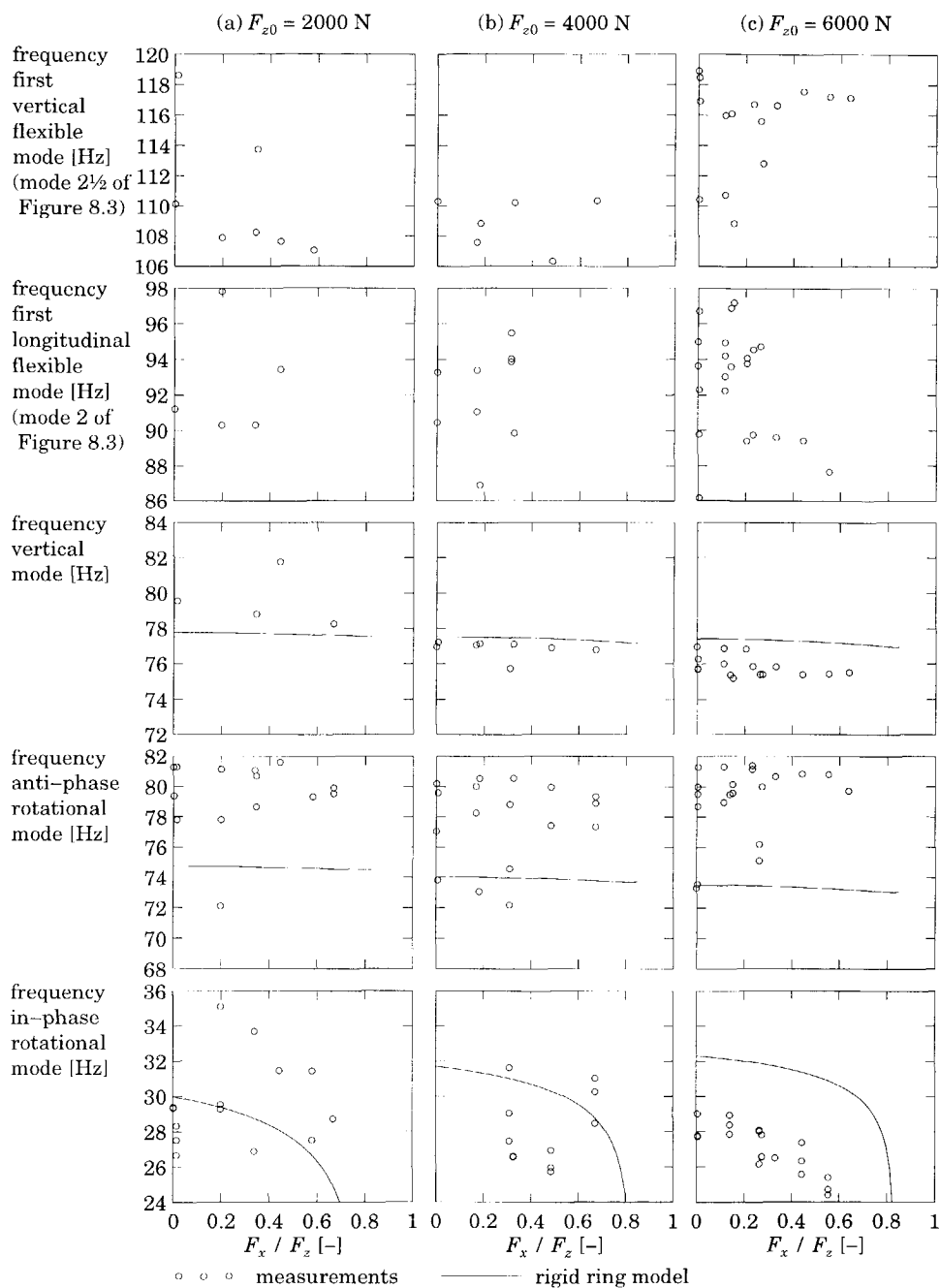


**Figure 10.5:** The tyre natural frequencies as function of the average brake force.

The relative damping of most modes varies between 3 and 5%. As already discussed in Section 9.2, the damping of the in-phase rotational mode depends highly on the slip stiffness and the velocity.

### 10.4 Excitation of the tyre by the effective road surface

The effective road surface, introduced in Chapter 4, is used in Sections 10.5 through 10.8 as excitation of the rigid ring tyre model. This section presents the excitation of the effective road surface in the frequency domain by means of the auto spectral density functions. Two methods of modelling the excitation of the tyre by the effective road surface are considered the first method can be used at fixed axle height, and the second method can be used at varying axle height as well.

#### Spectral densities of the excitation of the effective road surface

The effective road surface is constructed from basic functions, resulting in unequally distributed energy in the frequency range. Figures 10.6 and 10.7 show the auto-spectral densities of the effective plane height and the effective plane angle as function of the velocity and undisturbed vertical load. The auto-spectral densities of the positive step (obstacle 2) are identical to the those of the negative step (obstacle 3) even though the signals in the time domain are mirrored. These figures illustrate that the excitation of the tyre is highly velocity and load dependent. We furthermore may distinguish *zeros* (*i.e.* frequencies with amplitude zero) in the signals. The zeros in the spectral densities will influence the identification of the tyre dynamics adversely: tyre natural frequencies cannot be identified if they coincide with a frequencies of a zero in the input spectrum.

If we divide the velocity by the frequency we can obtain the wavelengths of the zeros. It is most striking to see that the wavelengths of the zeros are not related directly to the overall length of the obstacles or the overall length of the effective inputs. To understand the mechanism of the origin of the zeros we have to return to Chapter 4 where the effective inputs were defined as convolutions of basic functions with impulse functions, as indicated in the Figures 4.15 and 4.16.



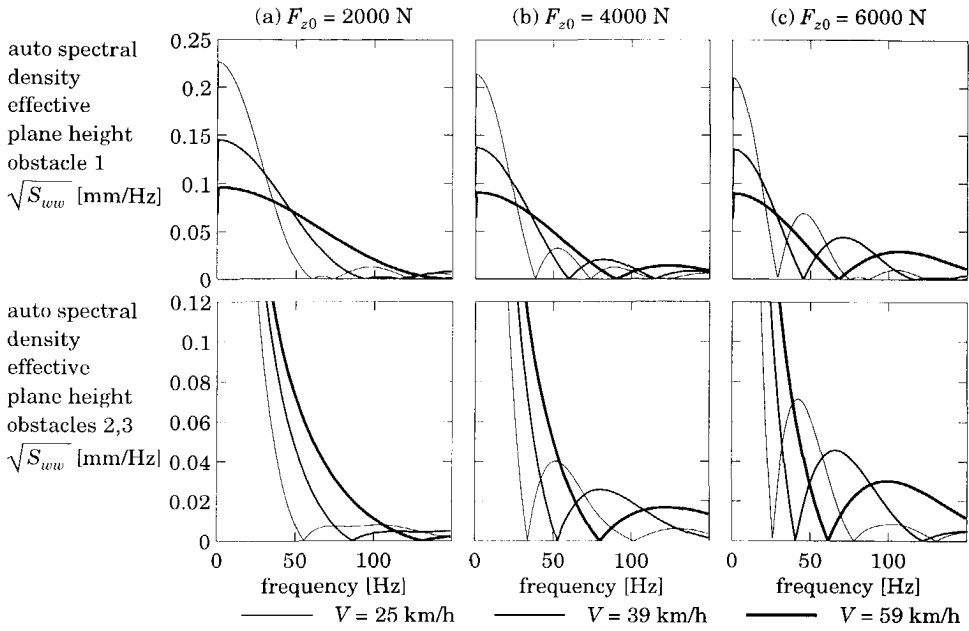


**Figure 10.6:** The auto spectral densities of the effective road plane height.

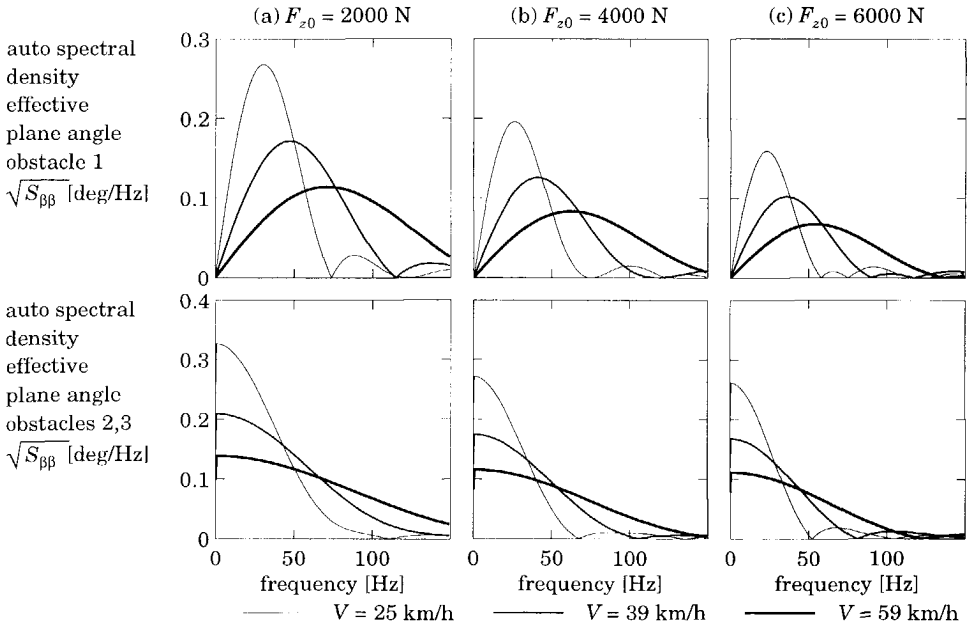


**Figure 10.7:** The auto spectral densities of the effective road plane angle.

A convolution of two functions in the time domain is identical to a multiplication of the Fourier transformed functions in the frequency domain. Thus, to identify the zeros in the responses, we may study the two Fourier transformed functions separately. Accordingly, the zeros in the effective road surface are related to either the basic functions or to the two shifted impulse functions.

Both the basic functions and the shifted impulse functions may generate a series of zeros in the auto-spectral densities of the effective road surface. Table 10.3 presents the expressions of the zeros as function of the length of the basic functions  $\lambda_{bf}$  and the shift of the impulse functions  $\lambda_{imp}$ . The length of the basic functions is independent of the vertical load. These shifts of these functions, which are slightly smaller than the contact length, increase with the vertical load.

The basic function for obstacle 1 (trapezoid cleat) is equal to half a sine wave. The effective plane height results from the convolution of the basic function with two positive impulse functions shifted over a distance  $\lambda_{imp}$ . The effective plane angle results from the convolution of the basic function with one negative and one positive impulse function shifted over the same distance.

The basic function of the obstacles 2 and 3 is represented by a quarter of a sine wave. This basic function does not provide any zeros in the power spectral densities. Accordingly, the zeros in the effective road surface of these obstacles are related to the shift in the impulse functions only.

**Table 10.3:** *The wavelengths of the zeros in the power spectral densities of the effective road plane height and effective road plane angle.*

obstacle number	effective input	wavelength zeros from		
		basic function	contact length	gap length
1	effective plane height	$\frac{2}{2n+1}\lambda_{bf}$	$\frac{2}{2n-1}\lambda_{imp}$	—
	effective plane angle	$\frac{2}{2n+1}\lambda_{bf}$	$\frac{1}{n}\lambda_{imp}$	—
2,3	effective plane height	—	$\frac{2}{2n-1}\lambda_{imp}$	—
	effective plane angle	—	$\frac{1}{n}\lambda_{imp}$	—
4	effective plane height	—	$\frac{2}{2n-1}\lambda_{imp}$	$\frac{1}{n}\lambda_{gap}$
	effective plane angle	—	$\frac{1}{n}\lambda_{gap}$	$\frac{1}{n}\lambda_{gap}$

Figures 10.6 and 10.7 do not present the auto-spectral densities of the effective road surface of obstacle 4 (negative cleat) as these spectra have too many zeros to depict the responses clearly. The effective road surface of obstacle 4 can be decomposed into the effective road surface of obstacle 3 (negative step) and obstacle 2 (positive step), or, in other words, into a convolution of the effective road surface of a step obstacle with shifted positive and negative impulse functions. This additional convolution will give zeros with parameter the length of the gap  $\lambda_{gap}$ . The length of the gap is large compared to the length of the basic functions  $\lambda_{bf}$  or the shift in these function  $\lambda_{imp}$ . This means that the frequencies of the zeros resulting from the length of the gap are much lower than the frequencies of the other zeros.

It is striking to see that most zeros (for obstacle 2, and 3 all zeros) depend only on the length of the contact patch. This means that changing the shape or height of the obstacles does not influence the positions of most zeros. To excite the tyre in a broad frequency range it is important to perform experiments at many axle heights and velocities rather than using many obstacle shapes.

The large number of zeros makes it almost impossible to estimate the frequency response functions of the tyre on an effective road surface. Only if the actual conditions match the expected conditions exactly, the zeros in the tyre responses will coincide with the zeros in the inputs. Therefore, in the subsequent sections the auto-spectral densities of the simulations are compared to auto-spectral densities of the measurements rather than using the frequency response functions.

Table 10.4 presents the parameters of the basic functions. The first two columns comprise the data from either the quasi-static experiments or the quasi-static simulations of Chapter 4. The quality of the fit of the dynamics responses (see next Sections) is influenced strongly, even though the difference in the parameter values between the various experiments is rather small. Processing the measured dynamic responses showed that the zeros in the auto-spectral densities of the tyre responses did not coincide exactly with the zeros in the input spectrum. For this reason, the parameters of the basic functions are altered such that the zeros in the input spectrum match the zeros in the dynamic responses best. The last column of Table 10.4 shows these altered values.

**Table 10.4:** *The parameters of the basic functions*

obstacle number	symbol parameter	measured quasi-static (see Chapter 4)	simulated quasi-static (see Chapter 4)	from dynamic tyre response
1	$\lambda_{bf}$	0.1432	0.1401	0.1510
	$\lambda_{imp}$ at $F_{z0} = 2$ kN	0.0624	0.0572	0.0700
	$\lambda_{imp}$ at $F_{z0} = 4$ kN	0.0906	0.0904	0.0920
	$\lambda_{imp}$ at $F_{z0} = 6$ kN	0.1231	0.1197	0.1140
2	$\lambda_{bf}$	0.0953	0.0949	0.0950
	$\lambda_{imp}$ at $F_{z0} = 2$ kN	0.0727	0.0625	0.0770
	$\lambda_{imp}$ at $F_{z0} = 4$ kN	0.1023	0.1025	0.1012
	$\lambda_{imp}$ at $F_{z0} = 6$ kN	0.1358	0.1331	0.1397
3	$\lambda_{bf}$	0.0985	0.0945	0.0950
	$\lambda_{imp}$ at $F_{z0} = 2$ kN	0.0665	0.0633	0.0770
	$\lambda_{imp}$ at $F_{z0} = 4$ kN	0.0939	0.1057	0.1012
	$\lambda_{imp}$ at $F_{z0} = 6$ kN	0.1274	0.1326	0.1397

### Excitation of a model at constant axle height

In Chapter 4 the quasi-static excitation of the tyre on short wavelength irregularities and constant axle height was transformed into an effective road surface (*cf.* Eq. 4.22a, 4.23a and 4.38b). Chapter 4 showed that effective inputs ( $\tilde{w}$ ,  $\tilde{\beta}$  and  $\tilde{r}_{cx}$ ) depend highly on obstacle shape and constant axle height. In this chapter the effective road surface is used as input to the rigid ring model. First, we will discuss the excitation of the linearised model running at constant axle height.

The variation in effective plane height  $\tilde{w}$  generates the vertical force variations  $\tilde{F}_{cz}$  in the contact patch through the radial residual stiffness  $c_{cz}$ :

$$\tilde{F}_{cz} = (\tilde{w} - \tilde{z}_b) \cdot c_{cz} \quad (10.1)$$

where  $\tilde{z}_b$  denotes the change in vertical position of the tyre ring. The tyre is excited longitudinally and rotationally by the effective plane angle variation and the effective rolling radius variations. The effective plane angle variation  $\tilde{\beta}$  results in a longitudinal force variations  $\tilde{F}_{cx}$  acting on the tyre ring:

$$\tilde{F}_{cx} = \tilde{\beta} F_{z0} \quad (10.2)$$

where  $F_{z0}$  denotes the vertical force on an undisturbed road surface. The additional effective rolling radius variations  $\tilde{r}_{ec}$  due to the short wavelength unevenness give additional slip velocities in the contact patch:

$$\tilde{V}_{c,sx} = \dot{x}_b - r_{e0}\ddot{\theta}_b + \eta\Omega\tilde{F}_{cz} + \tilde{r}_{ec}\Omega \quad (10.3)$$

The full set of linearised equations is given in expressions (7.51). The linearised model may be used to estimate the parameters at the given operating conditions.

### Excitation of the model at general conditions

The equations of motion of the non-linear simulation model of the rigid ring model are presented in Section 7.3. The tyre-road interface of this non-linear model on short wavelength unevennesses is employed in expressions (7.33) through (7.37). The non-linear model is designated to be used for vehicle simulations. It is obvious that the axle height is not constant during vehicle motions over uneven roads.

Chapter 4 showed that the shift of the basic functions can be expressed in terms of the axle height above the undisturbed road surface because the shift depends on the contact length and the contact length depends on the vertical tyre deformation. Consequently it is important that the height of the obstacles relative to the undisturbed road surface is small as the contact length of the tyre on the undisturbed road surface is used to determine the shift of the basic functions.

The undisturbed road surface may be easily determined for the experiments carried out on the rotating drum test stand in the laboratory: the height of the obstacles is small and the drum surface with no cleat mounted is defined as the undisturbed road surface. For the tyre running on a general road surface, on the other hand, it is considered difficult to determine the undisturbed road surface. Furthermore, the height road unevennesses of a general road cannot be assumed small with respect to the undisturbed road surface.

For the tyre running on a general uneven road surface it is thought to be easier to assess the alternative set of basic functions where the vertical load is kept constant at different levels rather than the axle height is kept constant at different levels. The shift of the basic functions now directly results from the contact length at the given level of vertical load. In Section 4.8 the effective inputs were obtained from simulations at constant vertical load rather than constant axle height. The analysis showed that the effective excitation of the tyre obtained from simulation with constant vertical load could also be represented by

shifted basic functions. Furthermore, the analysis in Section 4.8 showed that these basic functions depends on the obstacle shape and tyre radius, and the shift of these functions depends on the contact length  $a$ .

The original approach, depicted in Figure 10.1, will be replaced by the approach presented in Figure 10.8. The basic functions may be obtained off-line by using, for instance, the flexible ring model. In Section 4.8 an alternative approach was suggested, using the response of a rigid wheel. More research will be needed before this relative simple approach can be used.

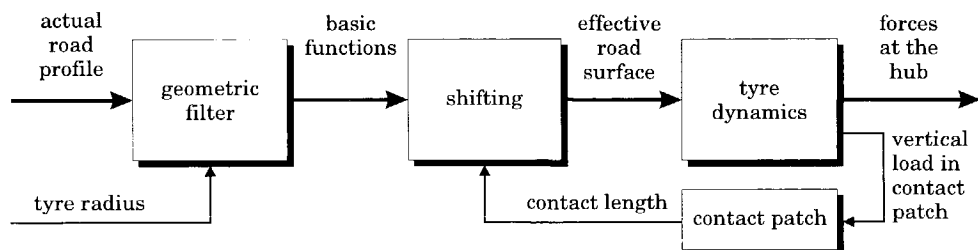


**Figure 10.8:** *The enhanced tyre-road interface.*

The vertical force in the contact area  $F_{cz}$  varies due to the road unevennesses and axle height variations. Consequently, the contact length  $2a$  will change and thereby influencing the effective excitation of the tyre. An iteration procedure is needed to solve for the shift  $\lambda_{imp}$  of the basic functions as this shift depends on the contact length (cf. Eq. 7.33), the contact length depends on the vertical force in the contact patch (cf. Eq. 7.29) and the vertical force depends on the effective plane height (cf. Eq. 7.23).

### Comparison with the measurements

In the subsequent sections results of test at constant axle heights are compared with simulations using the linearised and the non-linear rigid ring model. The basic functions for effective inputs assessed at constant axle height were used in connection with the linearised model. The alternative functions at constant vertical loads were employed in the non-linear model. Using the vertical tyre stiffness, the effective inputs defined at constant axle height can be transferred into the effective inputs defined at constant vertical load.

Section 10.5 presents the comparison between the measured vertical tyre responses and the simulated vertical tyre responses with the linearised rigid ring model. The subsequent section presents the longitudinal responses of the tyre.

Sections 10.7 and 10.8 present the influence of the obstacle shape and the average brake torque respectively. The goals of the research presented in these sections are: (1) to validate the rigid ring model, (2) to validate the method of replacing the actual road surface excitation of the tyre by effective road surface inputs; and (3) to estimate the parameters of the rigid ring tyre model. It should be noted that the parameter values of the model obtained from the frequency response functions to brake torque variations presented in Section 9.2 were considered most adequate and therefore used in the simulations.

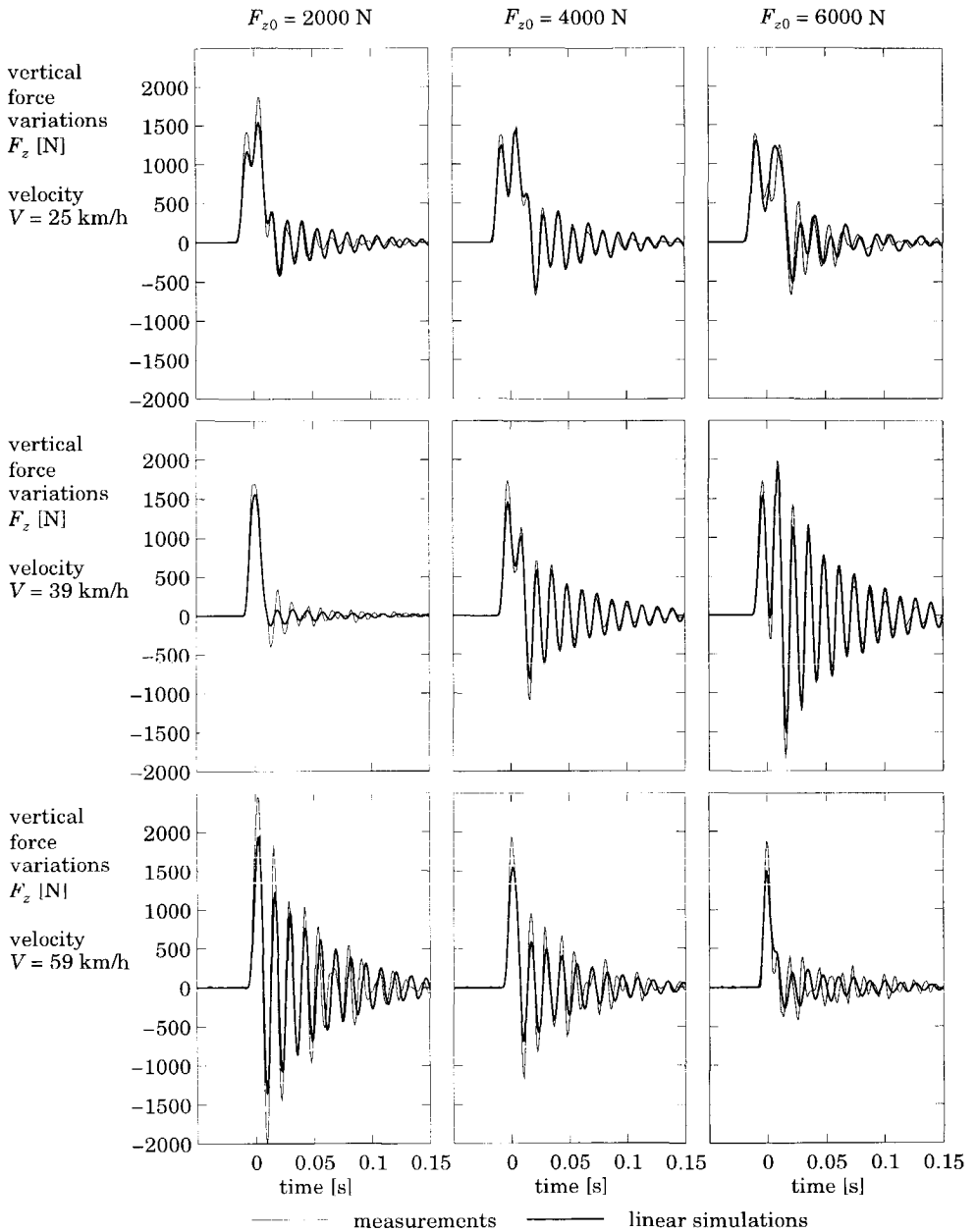
The figures in this chapter present a selection of the experiments conducted as it is not feasible to present the responses of all 128 conditions investigated. The time base is shifted such that at  $t=0$  the tyre is exactly on the centre of the obstacle.

Before we are able to compare the measurements with simulations we have to match the simulation conditions with the measurements. The most important factor is the exact timing of the cleat excitation. The highest frequency of interest is approximately 79 Hz. This represents a wavelength of 9 mm at the lowest velocity (25 km/h). Consequently, the accuracy of the cleat position measurement should be much smaller than 9 mm.

The cleat position is monitored by an optical sensor which generates an impulse like signal at cleat passage. Although this sensor is very useful for triggering the data acquisitions, it is not accurate enough for assessing the cleat position as the shape of this impulse like signal varies with the drum velocity. Therefore, the exact position of the cleat is used as an additional parameter in the parameter fit routine.

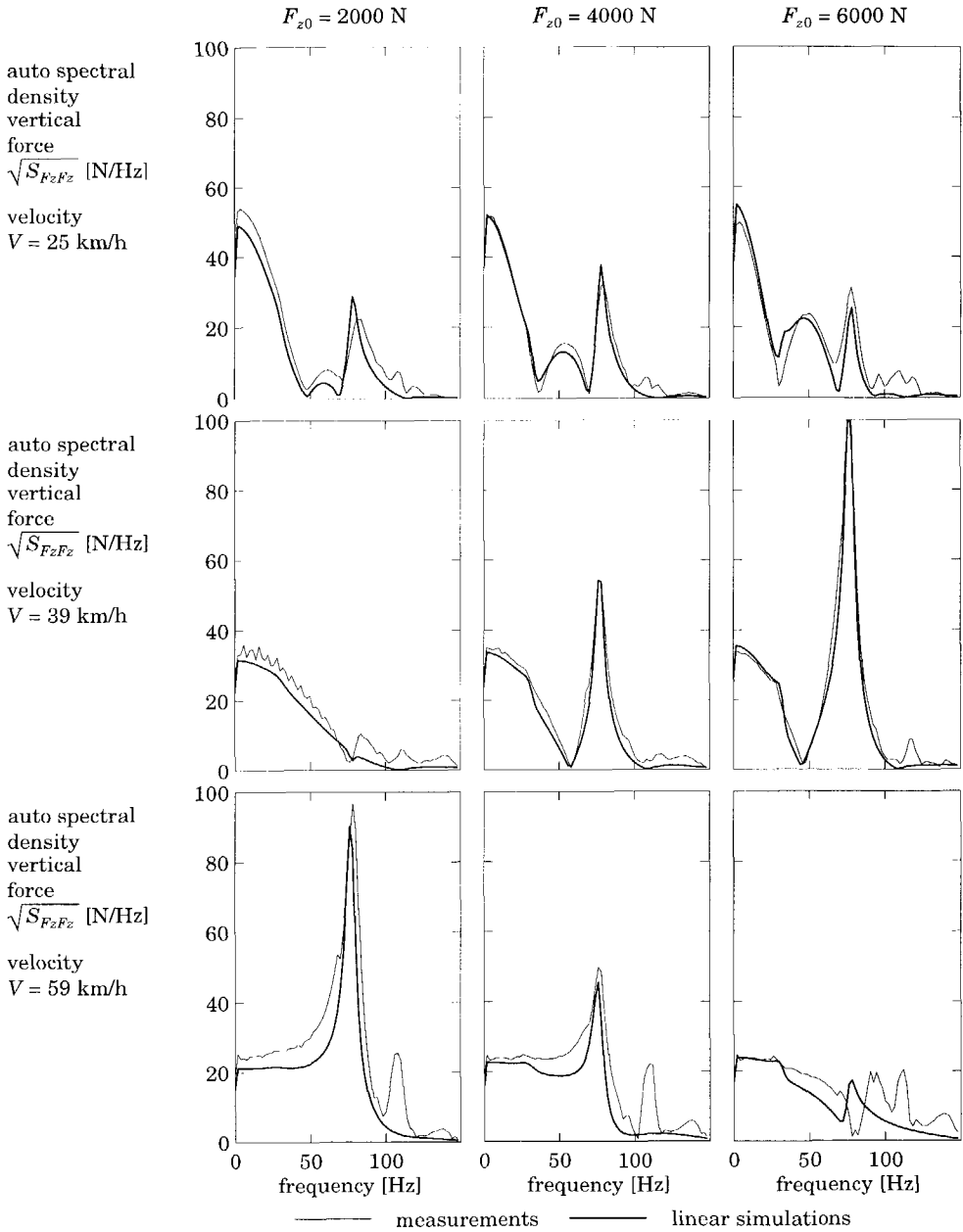
## 10.5 Vertical tyre responses to a trapezoid cleat

Figure 10.9 presents the measured and simulated responses of the vertical force for three axle heights corresponding to 2000, 4000 and 6000 N vertical load for the non-rotating tyre and three velocities: 25, 39 and 59 km/h. The time base is shifted such that at  $t=0$  the tyre is exactly on the centre of the obstacle. The simulations presented in this section were performed with the linearised rigid ring model. The vertical responses of the non-linear model are very similar to the presented responses of the linearised model.



**Figure 10.9:** The simulated (linear model) and measured time response of the vertical force of the tyre running over the trapezoid cleat.





**Figure 10.10:** The simulated (linear model) and measured auto-spectral densities of the vertical force of the tyre running over the trapezoid cleat.

The response of the vertical force at low velocity is a combination of the excitation of the tyre by the unevenness (*i.e.* the effective plane height) and free tyre vibration with a natural frequency of 76 Hz after cleat passage. At higher velocities the excitation of the tyre in the vertical direction will become more impulse like.

The shape of the auto-power spectral density function of the vertical force (see Figure 10.10) is very much related to the auto-power spectral density functions of the effective plane height (see Figure 10.6). The amount of vibration after cleat impact depends highly on the velocity and vertical load. At 2000 N, 25 km/h and 6000 N, 59 km/h the vertical mode of vibration is hardly excited because the natural frequency of this mode coincides with a zero in the input spectrum. At 6000 N, 39 km/h and 2000 N, 59 km/h, on the other hand, the tyre shows large vertical vibrations after cleat impact as the input spectrum contains much energy at 76 Hz.

We may distinguish the same zeros (*i.e.* frequencies where the amplitude is zero) in the spectrum of the vertical force as in the spectrum of the effective plane height. For example at 25 km/h the zeros related to the length of one basic function and are independent of the vertical load: 70 and 115 Hz. The other zeros in the frequency range 0-150 Hz at 25 km/h are related to the contact length and shift with the vertical load: from 55 Hz at 2000 N, 35 Hz at 4000 N, to 30 Hz at 6000 N. At higher velocities the frequencies of all zeros will shift to higher values.

Figures 10.9 and 10.10 show that the rigid ring model with the effective road surface as input describes the vertical tyre dynamics rather well in the frequency range up to 100 Hz. Above this frequency the model deviates from the measurements because the higher order modes are not taken into account in the rigid ring model. The frequencies of the higher order can be identified from the high velocity experiments at 110 Hz and 140 Hz. These frequencies probably correspond to the first two modes of vibration where the belt does not keep its circular shape during vibration (modes  $2\frac{1}{2}$  and  $3\frac{1}{2}$  of Figures 8.3 and 8.4).

The results of the measured and simulated vertical responses of the tyre at constant axle height running over a trapezoid cleat corresponds to the studies presented in literature [8,46,78,79]. The response of the vertical force at constant axle height is rather similar to the response of the vertical hub acceleration of the wheel in a vehicle suspension [25,47]. Oldenettel *et al.* [79] studied the influence of the velocity on the shape of the frequency spectrum of the vertical force. They found similar results compared to those presented in Figure 10.10: the excitation of the tyre depends highly on the velocity and the zeros in the spectrum shift with the velocity. Oldenettel *et al.* showed that a mode of vibration could only be

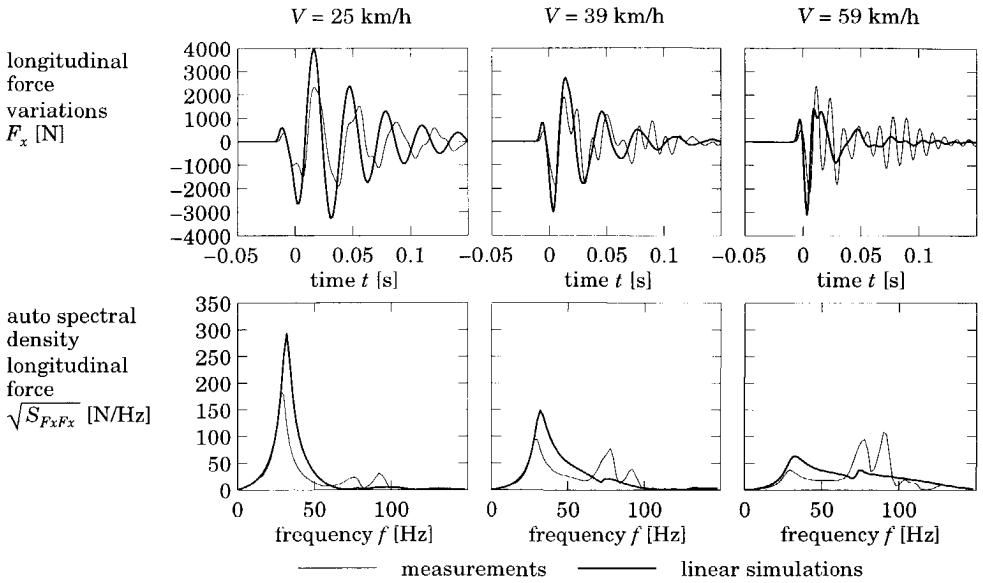
identified when the natural frequency did not coincide with the frequency of a zero in the input spectrum [79].

## 10.6 Longitudinal tyre responses to a trapezoid cleat

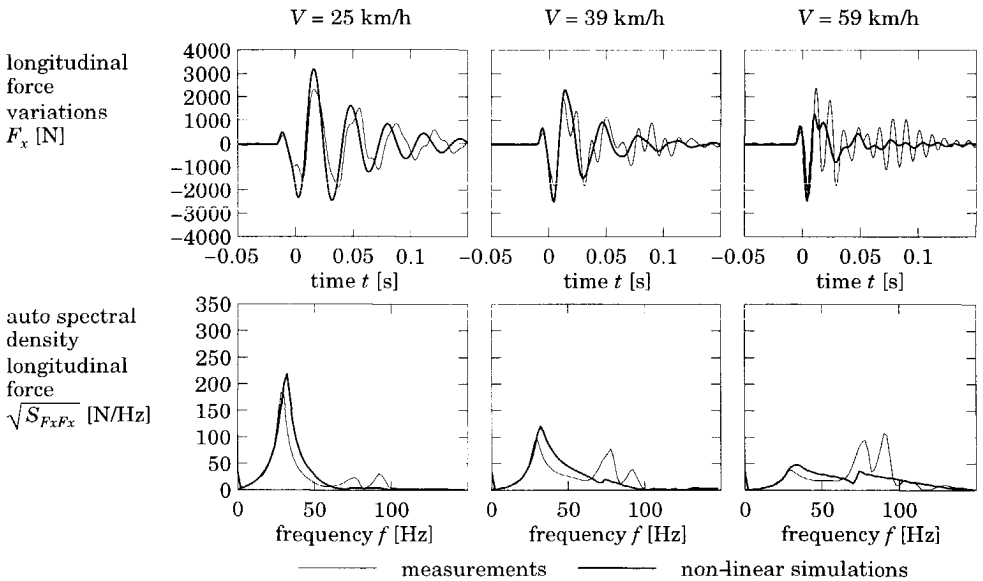
The longitudinal force variations, the rotational wheel velocity and accelerations represent the tyre dynamics in longitudinal and rotational directions. The influence of effective plane angle variations is relatively small; the effective rolling radius variations are much more important. The resulting slip velocity variations generate longitudinal forces in the contact patch. These longitudinal force variations accelerate and decelerate the wheel in rotational direction.

Figure 10.11 compares the measured longitudinal forces with the simulations of the linearised tyre model in the time and frequency domain. This figure shows that the linearly simulated forces are much larger than the measured forces. The reason for this difference is the constant slip stiffness of the linearised model. During cleat impact, large horizontal forces arise in the contact patch: the peak values of the longitudinal force can be up to 40% to 90% of the vertical force. The longitudinal slip stiffness during cleat impact will become much smaller owing to these large longitudinal forces. Therefore it cannot be assumed that the slip stiffness is constant.

The non-linear simulation model represents the measurements much better, see Figure 10.12. In this model the slip stiffness decreases with increasing longitudinal force, resulting in a smaller excitation of the longitudinal vibrations of the tyre. Furthermore, the effective excitation according to the scheme presented in Figure 10.8 is used, which means that the effective inputs depend on the vertical force in the contact patch. In other words, the condition that the axle height was constant was not used in the non-linear simulation model. All the simulation results presented from this point onwards were obtained by using the non-linear simulation model.



**Figure 10.11:** Comparison between the measured response and the response of the linear model at  $F_{z0} = 4000$  N.



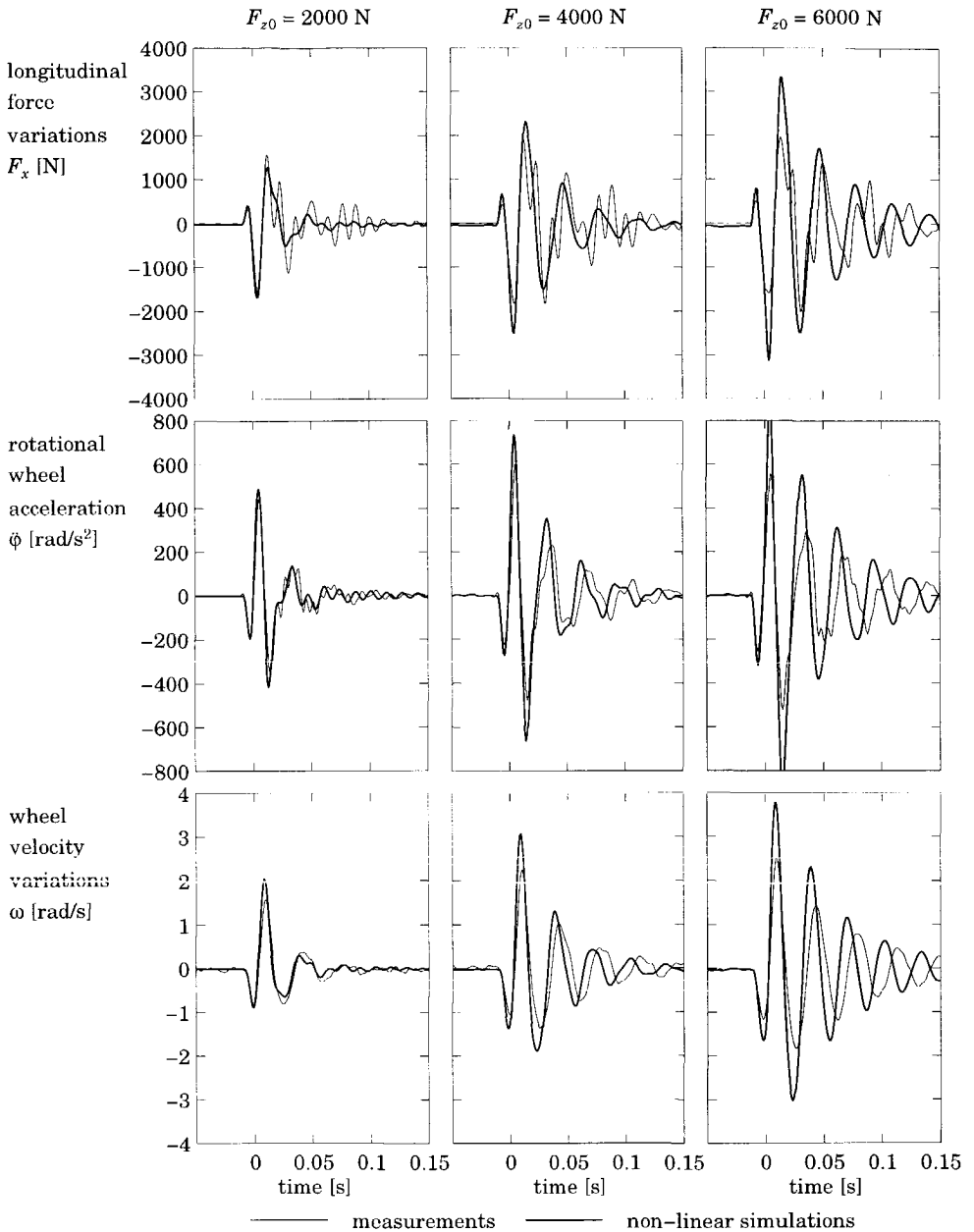
**Figure 10.12:** Comparison between the measured response and the response of the non-linear simulation model at  $F_{z0} = 4000$  N.

It is interesting to see that the first small peak in both the measured and simulated responses of longitudinal force is oriented in the positive rather than the negative direction. According to the road plane angle variations, the first peak in the longitudinal force should be negative. But, as stated before, the influences of the rotational velocity variations of the wheel are much more important than the variations of the effective plane angle. The effective rolling radius increases rapidly if the tyre hits the trapezoid cleat (*cf.* Figures 4.10 and 4.11), resulting in a negative slip velocity according to the definition of Equation (3.2). This negative slip velocity generates the first positive peak in the response of the longitudinal force.

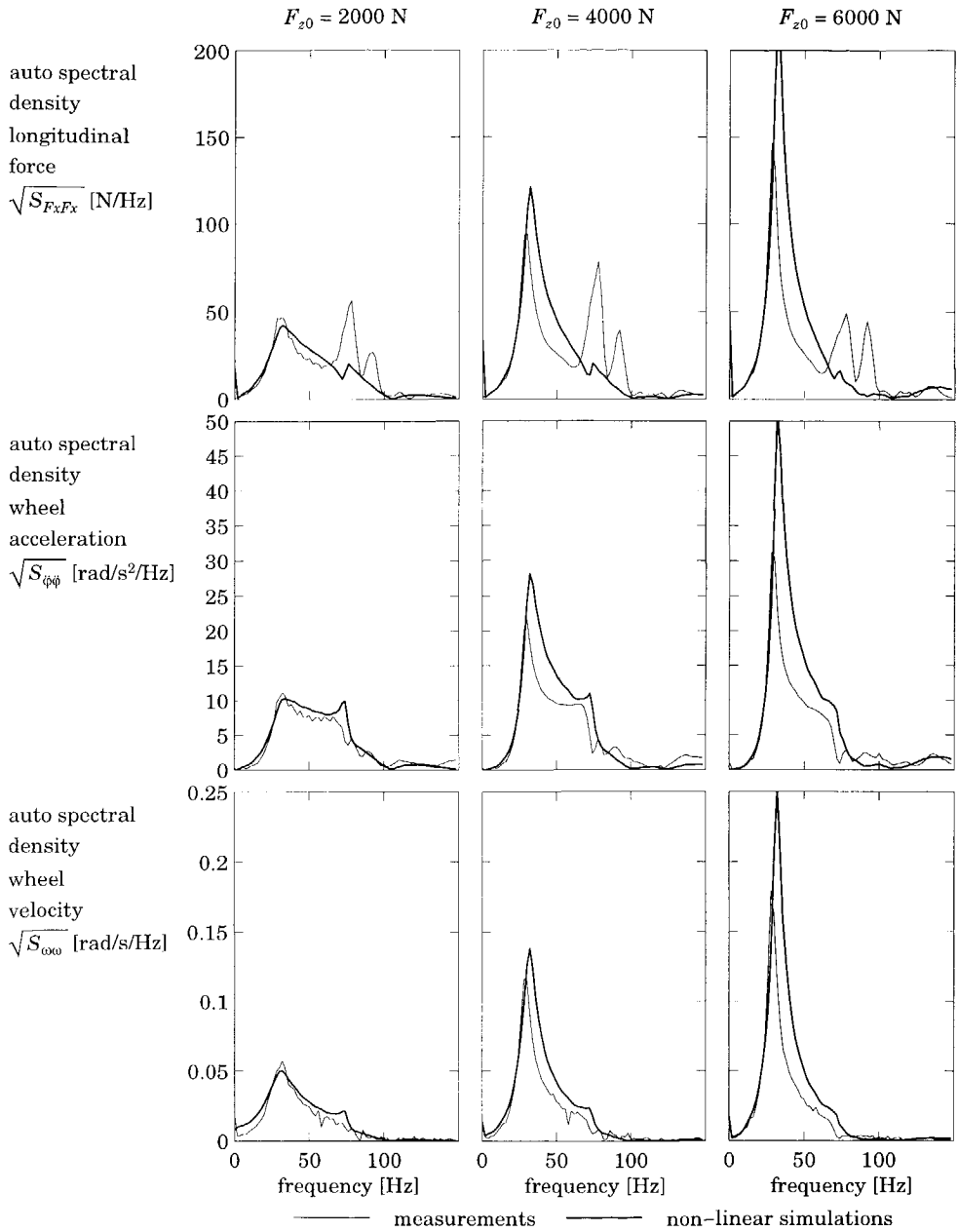
The first positive peak in the longitudinal force is also found in other experimental studies [8,25,75,79]. The same effect is also represented by the finite element models of Mousseau [75] and Eichler [25], where the actual shape of the obstacle was used as input. The modal model of Bandel [8] with the effective plane angle as input showed this first peak as well.

Figure 10.13 presents the measured and simulated longitudinal tyre responses: the variations in longitudinal force at the wheel axle, the variations in rotational velocity of the rim and the rotational acceleration of the rim. The literature studied by the author presents only the dynamic responses of the longitudinal forces [8,15,25,46,47,75,78,79]. The rotational wheel velocity and wheel acceleration provide additional information to validate the dynamic tyre model.

Figure 10.14 shows the measured and simulated auto spectral densities of the longitudinal responses. The measured spectral density of the longitudinal force shows three modes of vibration in the frequency range 0-100 Hz: the in-phase rotational model at 31 Hz, the anti-phase rotational mode at 72 Hz, and a resonance at 90 Hz. The last mode, which is not represented by the rigid ring model, is the first flexible mode in longitudinal direction: mode 2 of Figures 8.3 and 8.4. Bruni *et al.* erroneously identified the first flexible mode as the horizontal mode of the rigid ring model [15]. This horizontal mode results from the horizontal constraint in the contact patch of the rigid ring model (*cf.* Section 8.5) and cannot be found in measurements (*cf.* Figure 8.3). The measured time response of the longitudinal force (Figure 10.13) shows a beating phenomenon as the difference in frequencies between the anti-phase rotational mode (72 Hz) and the first flexible mode (90 Hz) is rather small.



**Figure 10.13:** *The measured and simulated time responses of the longitudinal force, wheel acceleration and wheel velocity at  $V = 39 \text{ km/h}$ .*



**Figure 10.14:** The measured and simulated frequency responses of the longitudinal force, wheel acceleration and wheel velocity at  $V = 39 \text{ km/h}$ .

The measured rotational wheel velocity and rotational wheel acceleration show only two modes in the frequency range 0-100 Hz: the in-phase rotational mode at 31 Hz and the anti-phase rotational mode at 72 Hz. This is consistent with the modal analysis results presented in Chapter 8, where the amplitude of the wheel rotation decreases rapidly with increasing mode number.

Both the measurements and the simulations show that the in-phase rotational mode is the most important mode of vibration at low velocity. At higher velocity, the relative damping of this mode increases and the other modes of vibration become more important. Unfortunately, the simulated amplitude of the vibrations of the anti-phase rotational mode is too low compared to the measured tyre vibrations. This effect was already observed at the brake torque variations in Section 9.2.

To provide insight into the longitudinal excitation of the tyre the Frequency Response Functions (FRF) of the linearised model are examined. Figure 10.15a presents the FRF of the longitudinal force  $F_x$  and rotational wheel acceleration  $\ddot{\phi}_a$  with respect to the effective plane angle variations. These FRFs clearly show the two modes of vibration in longitudinal direction: the in-phase rotational mode at 31 Hz and the anti-phase rotational mode at 72 Hz.

Figure 10.15b presents the FRF of the longitudinal force  $F_x$  and rotational wheel acceleration  $\ddot{\phi}_a$  with respect to the effective rolling radius variations. These FRFs are the most important ones, since the influence of the effective rolling radius variations is much larger than the influence of the effective plane angle variations. These FRFs, presented in Figure 10.15b, do not show a clear resonance at 72 Hz. First, the phase difference between the response of the force and the rotational acceleration is 180 degrees, rather than the 0 degree according to the natural mode of vibration; and second, the peaks in the FRFs do not coincide exactly with the natural frequency: the peak frequency of the force is somewhat greater and the peak frequency of the acceleration is somewhat smaller than the natural frequency. This difference between peak frequencies can also be seen in the measured and simulated auto-spectral densities, see Figure 10.14.

At higher values of vertical load the relative damping of the in-phase rotational mode decreases. Furthermore, the slip stiffnesses increase with increasing vertical load, resulting in greater excitation of the tyre due to the effective rolling radius variations. Both effects can be seen in the measured and simulated tyre responses, see Figures 10.13 and 10.14.



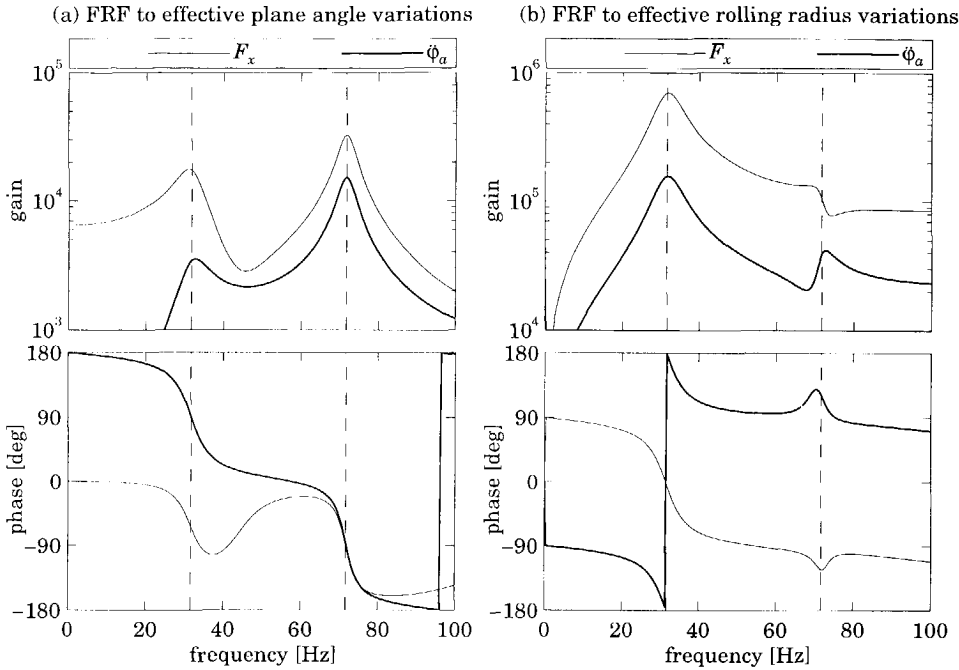


**Figure 10.15:** *The simulated frequency response functions of tyre response due to the effective plane angle and the effective rolling radius variations.*

## 10.7 Tyre responses to other obstacle shapes

This section discusses briefly the influence of the obstacle shape on the tyre responses. The measurements and simulations with the non-linear model were performed for all obstacle shapes depicted in Figure 10.2. Figure 10.16 presents the tyre vibrations for one vertical load and velocity after rolling over the positive step (obstacle 2), the negative step (obstacle 3), and the negative cleat (obstacle 4). The time bases of the responses are shifted such that the negative step takes place at  $t=0$  s, and the positive step takes place at  $t=0.042$  s. The negative cleat causes a negative step at  $t=0$  s and a positive step at  $t=0.042$  s. The negative cleat is not only a realistic road unevenness (e.g. a pothole), but is also chosen to prove the superposition principle.

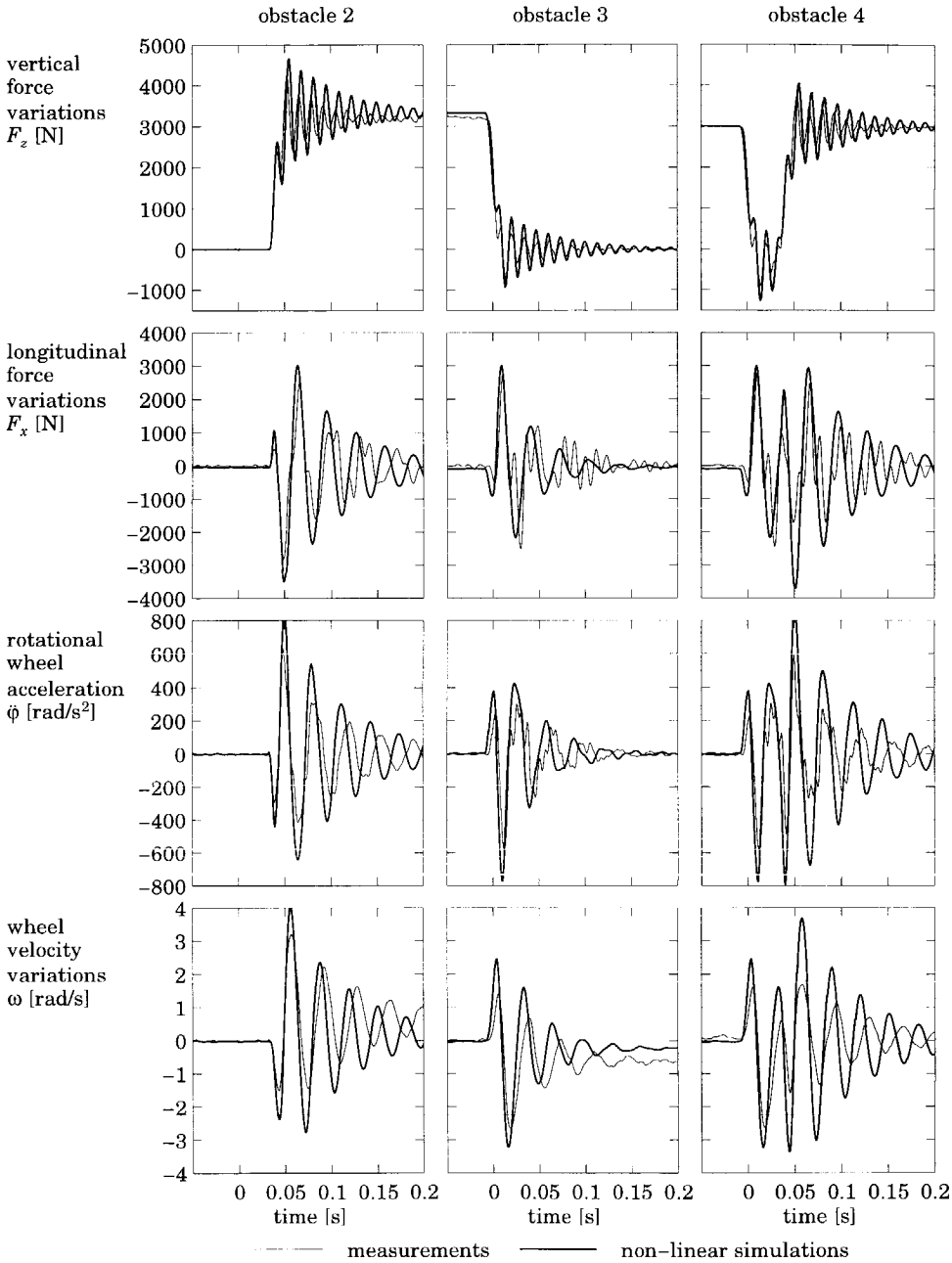


**Figure 10.16:** *The responses of the free rolling tyre at  $F_{z0} = 4000 \text{ N}$  and  $V = 39 \text{ km/h}$ : influence of obstacle shape.*

At first sight one might think that the responses for the positive and the negative step should be identical. However, this is not true as the vertical load increases roughly from 4000 N to 7000 N for the positive step and decreases from 7000 N to 4000 N for the negative step, and most of the tyre vibrations take place after the cleat impact. Consequently, after a positive step the vibrations take place at a much larger vertical load than the vibrations after a negative step. The damping of the in-phase rotational mode is strongly influenced by the average vertical load.

The vertical tyre responses (top graphs of Figure 10.16) show the vertical mode of vibration at 76 Hz. The other graphs represent the longitudinal and rotational tyre responses. The longitudinal force, rotational wheel acceleration and velocity clearly show the in-phase rotational mode at 31 Hz. The relative damping of this mode after the negative step is much larger than after the positive step, owing to the difference in average vertical load. Another influence of the step change in vertical load is the increase or decrease in effective rolling radius: the rotational wheel velocity that is finally achieved increases slightly after a positive step and decreases slightly after a negative step.

## 10.8 Tyre responses during braking

This section presents the responses of a constantly braked tyre rolling over obstacles. This situation is in contrast to the results presented in the previous sections, where only a free rolling tyre was considered. Braking the tyre will not only influence the modes of vibration as presented in the root-loci of Figure 8.9, but it is also a severe condition for the rigid ring tyre model. Obviously, the non-linear simulation model has to be used for these severe conditions.

Experiments and simulations of a braked tyre were performed for four obstacle shapes, three velocities and three axle heights. Figures 10.17 and 10.18 present a selection of the performed experiments: the responses at one velocity, one axle height, and three levels of constant brake torque. The brake torque level varies from free rolling (very low values of brake torque) to large levels of brake torque (close to wheel lock). The value of the brake torque  $M_y$  is indicated in the upper right corner of the graphs.

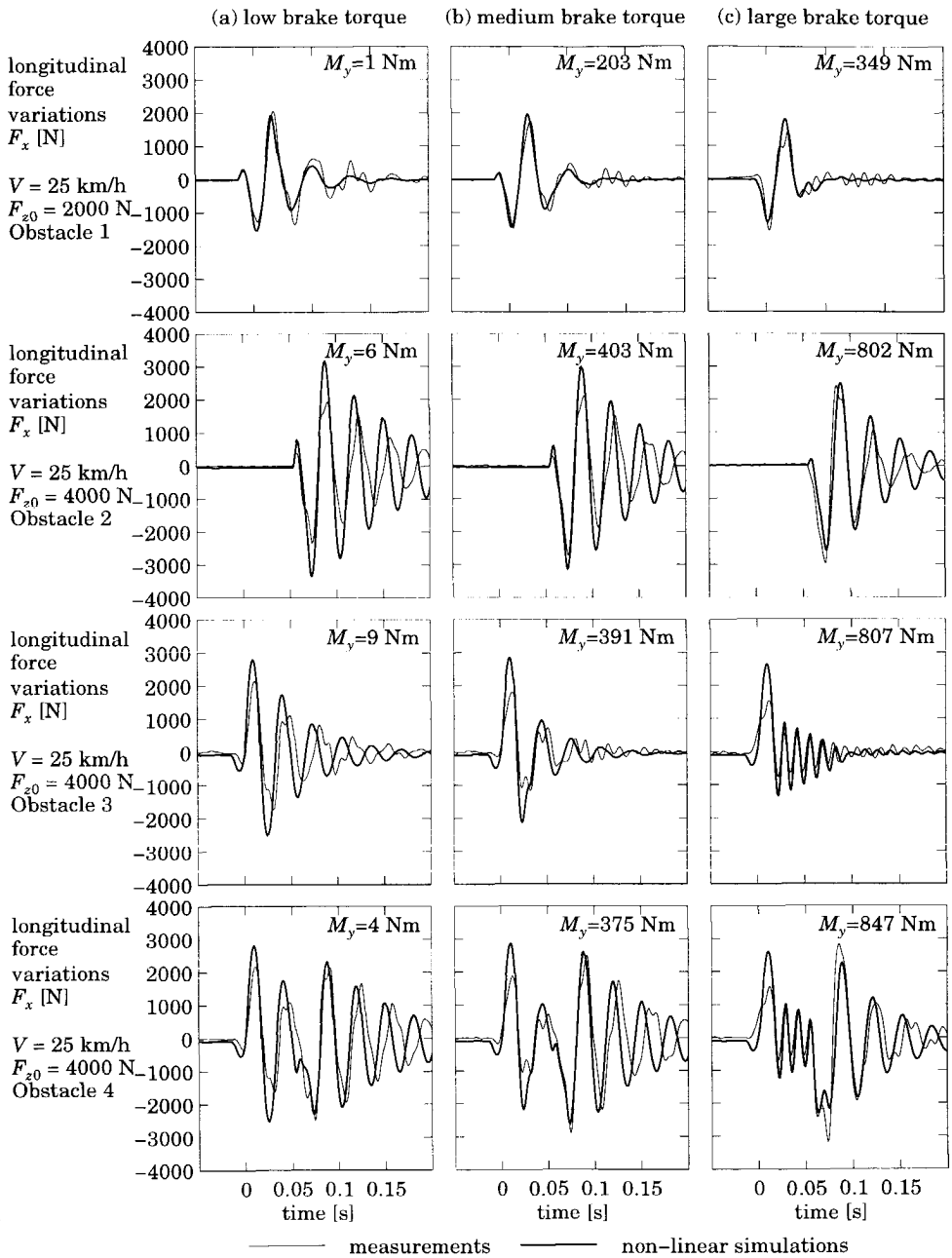


**Figure 10.17:** *The influence of the average brake torque on the response of the longitudinal force.*

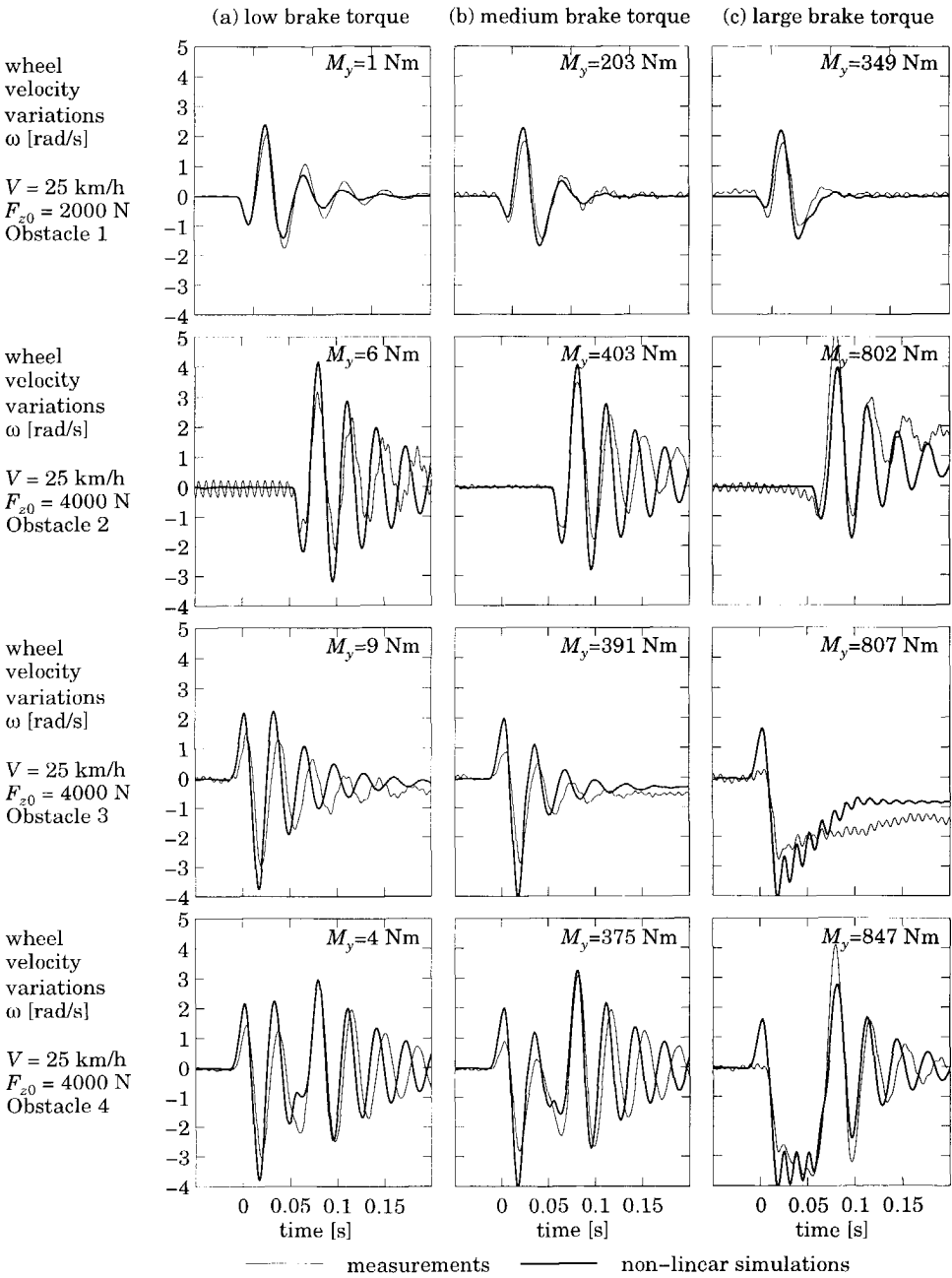


**Figure 10.18:** *The influence of the average brake torque on the response of the rotational wheel velocity.*

During rolling over short wavelength obstacles, the contact between tyre and road may be divided into more than one small contact patch rather than one large contact patch. Deformed tread elements moving from one contact patch to another will lose their deformation. A tread element entering a new contact patch needs some time to build up a new deflection.

The tyre-road interface of the rigid ring model is governed by a single-point for the vertical excitation and a relaxation length contact model. The relaxation length concept is based on a finite contact length and the input to the relaxation length model is the slip velocity of a single point (point *S*). The multiple contact patches due to the obstacle shape are not represented by this model. Nevertheless, this model is able to represent a braked tyre rolling over a short wavelength obstacle in an approximate way.

Figure 10.17 presents the responses of the longitudinal force and Figure 10.18 presents the responses of the wheel velocity. The responses of the rotational wheel acceleration are not presented as these responses are very similar to the responses of the longitudinal force. The responses of the vertical force are not shown either, as these responses are hardly influenced by the average brake torque.

The uppermost graphs of Figures 10.17 and 10.18 present the measured and simulated responses of the tyre rolling over the trapezoid cleat. These graphs present the results of the trapezoid cleat at 2000 N load rather than 4000 N because the attachment of cleat to the drum restricted the maximum brake torque. A brake torque level close to wheel lock could only be achieved at 2000 N vertical load.

The major influence of an average brake torque is the decrease in the slip stiffness resulting in an increase in the damping of the in-phase rotational mode. The amplitude of the tyre responses to the trapezoid cleat is hardly affected by the brake torque. The first small peak in the force response is oriented in the positive direction and results from the sudden increase in the effective rolling radius, as already discussed in Section 10.6. The amplitude of this first peak, which is related to the slip stiffness, decreases with increasing brake torque.

The second row of graphs of Figures 10.17 and 10.18 presents the tyre responses to the second obstacle: the positive step. The tyre vibrations take place after the positive step, thus at 7000 N average vertical load rather than 4000 N. The large brake torque (which results in a situation close to wheel lock at 4000 N) is effectively a medium brake torque at 7000 N. Simultaneously, the relative damping of the in-phase rotational mode does not increase as much. The

wheel velocity increases after the step because at higher values of vertical load less slip is needed to obtain the same longitudinal force.

The average brake torque has a larger influence on the negative step than on the positive step because the vibrations for the negative step take place at 4000 N. At the high level of brake torque, the tyre produces approximately the maximum possible longitudinal force and the slip stiffness approaches zero. This results in a supercritically damped in-phase rotational mode. Another effect is that the vertical tyre vibration at 76 Hz influences the generation of the longitudinal force in the contact patch.

The responses of the tyre rolling over the fourth obstacle constitute a combination of the negative and positive step. The damping of the in-phase vibration after the negative step is much larger than the vibration after the positive step. For these situations one really needs the non-linear simulation model that has been employed.

Summing up: the non-linear rigid ring model is able to simulate simultaneous braking and rolling over obstacles. Unfortunately, these results could not be compared to other studies, as there no such studies are available in the literature.

## 10.9 Simulations with non-constraint axle height

As stated in Section 10.4 the effective inputs assessed at constant vertical loads can be used for simulations where the axle height is not constant. This section will show the results of simulations where the axle is mounted in a suspension. In these simulations the height of the vehicle body was constant and the axle could only move in vertical direction. The parameters of the suspension are: mass of the axle  $m_a = 13$  kg, vertical stiffness of the suspension  $c_{az} = 20000$  N/m, vertical damping coefficient suspension  $h_{az} = 1700$  Ns/m.

Figure 10.19, 10.20 and 10.21 show the results of the simulations: the vertical forces in tyre and suspension, and the vertical motions of the tyre and the axle. Unfortunately we are not able to validate the simulations with experiments since the experiments were only carried out at constant axle height. The height of the vehicle body is constant during the simulations and at the start of the simulation the tyre is load on the road ( $F_z = 4000$  N). At low velocity the axle follows approximately the vertical profile of the road surface and the variations in vertical load are small. At high velocity, the vertical axle motion is excited strongly resulting in a large variation in the forces.

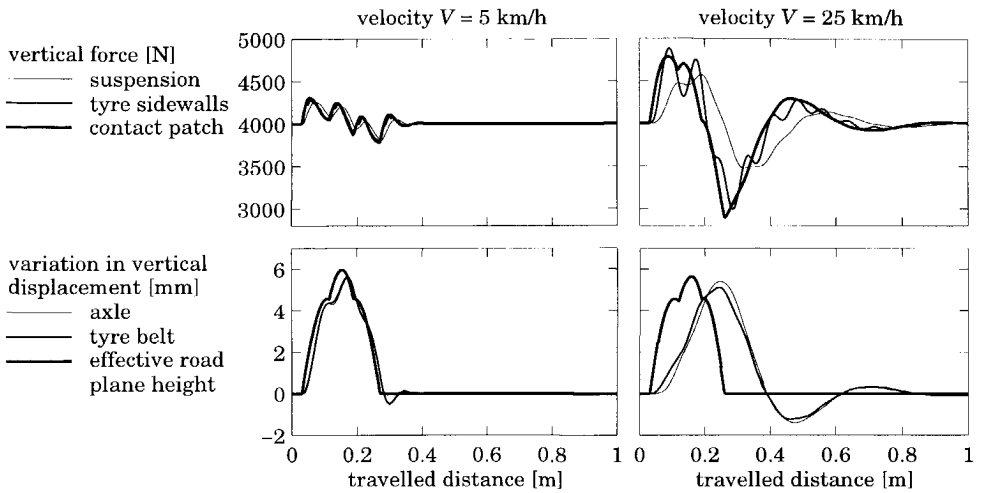


**Figure 10.19:** *The vertical tyre response of the tyre rolling over obstacle 1 with axle mounted in a suspension.*

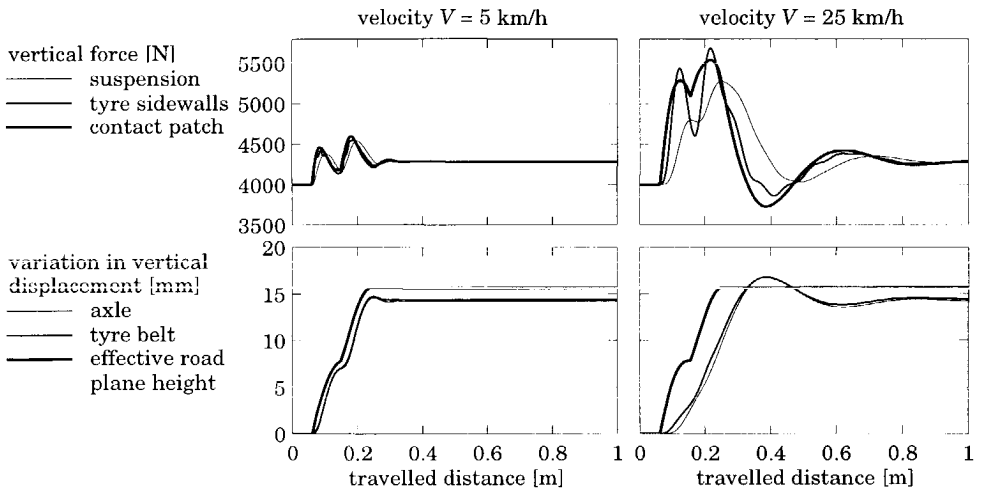


**Figure 10.20:** *The vertical tyre response of the tyre rolling over obstacle 2 with axle mounted in a suspension.*



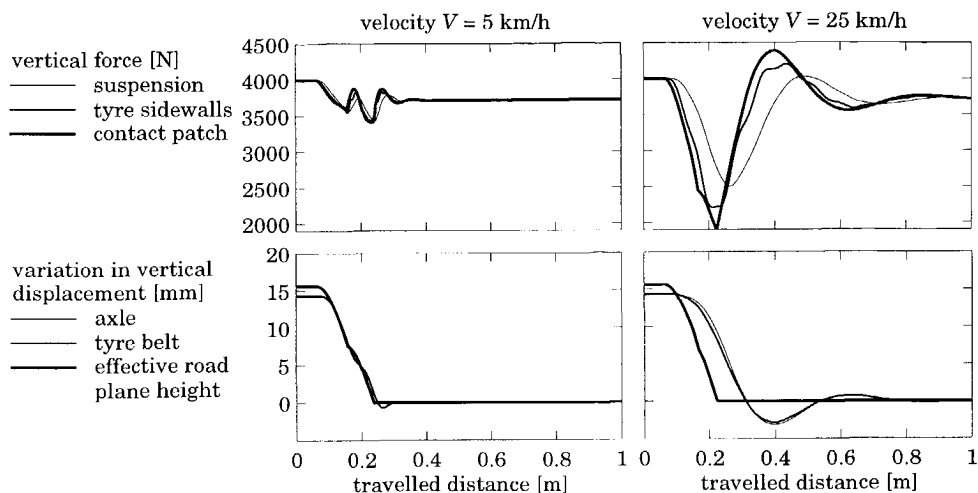


**Figure 10.21:** *The vertical tyre response of the tyre rolling over obstacle 3 with axle mounted in a suspension.*

The simulations show that the method of assessing the effective input can be used with a moving axle.



# 11

## Dynamic Tyre Responses to Axle Height Oscillations While Braking

---

### 11.1 Introduction

This chapter presents the responses of a tyre subjected to a constant brake torque during variations of the axle height. Very severe conditions were also considered: axle height oscillations where the vertical force decreases to such an extent that wheel lock occurs, including the case where the tyre loses contact with the road.

For a tyre operating in a vehicle, axle height oscillations occur due to suspension travel of the wheel. Pacejka *et al.* studied the influence on the in-plane behaviour of a free rolling tyre to axle height oscillations [82]: slip variations occur owing to effective rolling radius variations as function of the vertical load (*cf.* Eq. 3.27). The slip velocity variations result in variations in longitudinal force. Another effect is the rolling resistance because the rolling resistance force is proportional to the vertical load. For a tyre subject to a constant brake torque, the variations in the longitudinal force are larger because the generated longitudinal force depends highly on vertical load.

It is well known that axle height oscillations during constant side slip angle have an adverse effect on the generated lateral forces [86,106,107]. Not only do large variations occur in the lateral forces, but the average value of the lateral force is also affected. In contrast, the average value of the longitudinal force at

constant brake torque is almost unaffected by the variation of the axle height as long as wheel lock does not occur. The reason for this is that the average longitudinal force in the contact zone has to counterbalance the average applied brake torque.

Force variations also occur owing to rotational accelerations of the wheel to achieve a new value of slip, since at high values of vertical load, less slip is needed to generate a longitudinal force than at low values of vertical load. To obtain these variations of wheel slip, the wheel has to be accelerated or to be decelerated in the rotational direction. In conclusion, there are four mechanisms that contribute to the variations of the longitudinal force to axle height oscillations:

- The variation of the effective rolling radius.
- The rolling resistance force.
- The load dependency of the slip stiffness.
- The forces needed to accelerate and decelerate the wheel in rotational direction.

The axle height experiments were not used to obtain the parameters of the rigid ring model. For the simulations, the parameter values obtained in the previous chapters were used (*cf.* Table 7.1). To be able to simulate the tyre responses in the most severe conditions (wheel lock) the following properties of the simulation model are important:

- The first order differential equation of the slip in the contact zone which can be used at zero velocity (*cf.* Eq. 6.18).
- The value of the slip is limited during wheel lock. Otherwise, the simulated spinning up of the wheel would occur much later (*cf.* Section 6.2).
- The brake torque that is modelled as a dry friction torque (*cf.* Section 7.4).
- The vertical force that is only generated in the contact patch if the vertical tyre deformation is positive (*cf.* Eq. 7.23).

The experiments were performed with the *measurement tower*, see Appendix A.2. In the test stand the wheel can be moved up and down by using a hydraulic cylinder. The reaction forces at the wheel axle bearings are measured with strain gauges. Owing to the relatively high mass of the test stand and strain gauged measuring hub, the maximum frequency range of operating is limited to 20 Hz. The other measured signals were: the displacement of the hydraulic cylinder, the rotational velocity of the wheel and the drum and the applied brake pressure. Unfortunately, the brake torque could not be measured. The constant value of the brake torque, which was needed for the simulation model, was estimated from the average value of the longitudinal reaction force.

## 11.2 Comparison of the results

### Tyre responses at an average axle height corresponding to 4000 N vertical load

Figures 11.1, 11.2 and 11.3 present the tyre response to large sinusoidal axle height variations around an average value corresponding to 4000 N vertical load. The amplitude of the axle height variation is 10 mm, which is equivalent to an amplitude of 2000 N vertical load. Four excitation frequencies were used: 1, 2, 4 and 6 Hz. For each excitation frequency the figures present one wavelength of the excitation signal. The vertical load presented has been corrected for the inertia of the measuring hub and the wheel, thus, the value in the figures represents the value of the vertical force in the contact zone. The top graphs of the figures present the vertical tyre deformation.

The inputs to the simulation model are the constant brake torque, the measured and filtered vertical axle displacement (which is equal to the negative value of the tyre deformation) and the vertical velocity (*cf.* Eq 7.20b) of the axle motion obtained by numerically differentiating the measured and filtered vertical axle displacement.

Figure 11.1 presents the responses for a tyre subjected to a small constant brake torque (6 bar brake pressure). Figure 11.2 presents the responses at large constant brake torque (28 bar) and Figure 11.3 presents the responses of a tyre subjected to a very large brake torque (43 bar), where the vertical force decreases to such an extent that wheel lock occurs.

At 1 Hz excitation frequency and low constant brake pressure (*cf.* Figure 11.1) the response of the longitudinal force is mainly caused by the rolling resistance, which is proportional to the vertical load (*cf.* Eq. 3.21). The response of the wheel velocity is caused by the load dependency of the slip stiffness and the load dependency of the effective rolling radius.

To accelerate or decelerate the wheel in the rotational direction additional longitudinal forces are needed in the contact zone: to accelerate the wheel an additional negative force is needed, and to decelerate the wheel an additional positive force is needed. The additional contributions of longitudinal force in the contact zone can be seen in the measured reaction force at the hub: at increasing vertical load, the rotational wheel velocity increases and the absolute value of the longitudinal force  $|F_x|$  increases. At higher excitation frequencies, the value of rotational wheel accelerations increases and thus the additional forces as well. This is clearly shown in the longitudinal force response of Figure 11.1: at 1 Hz

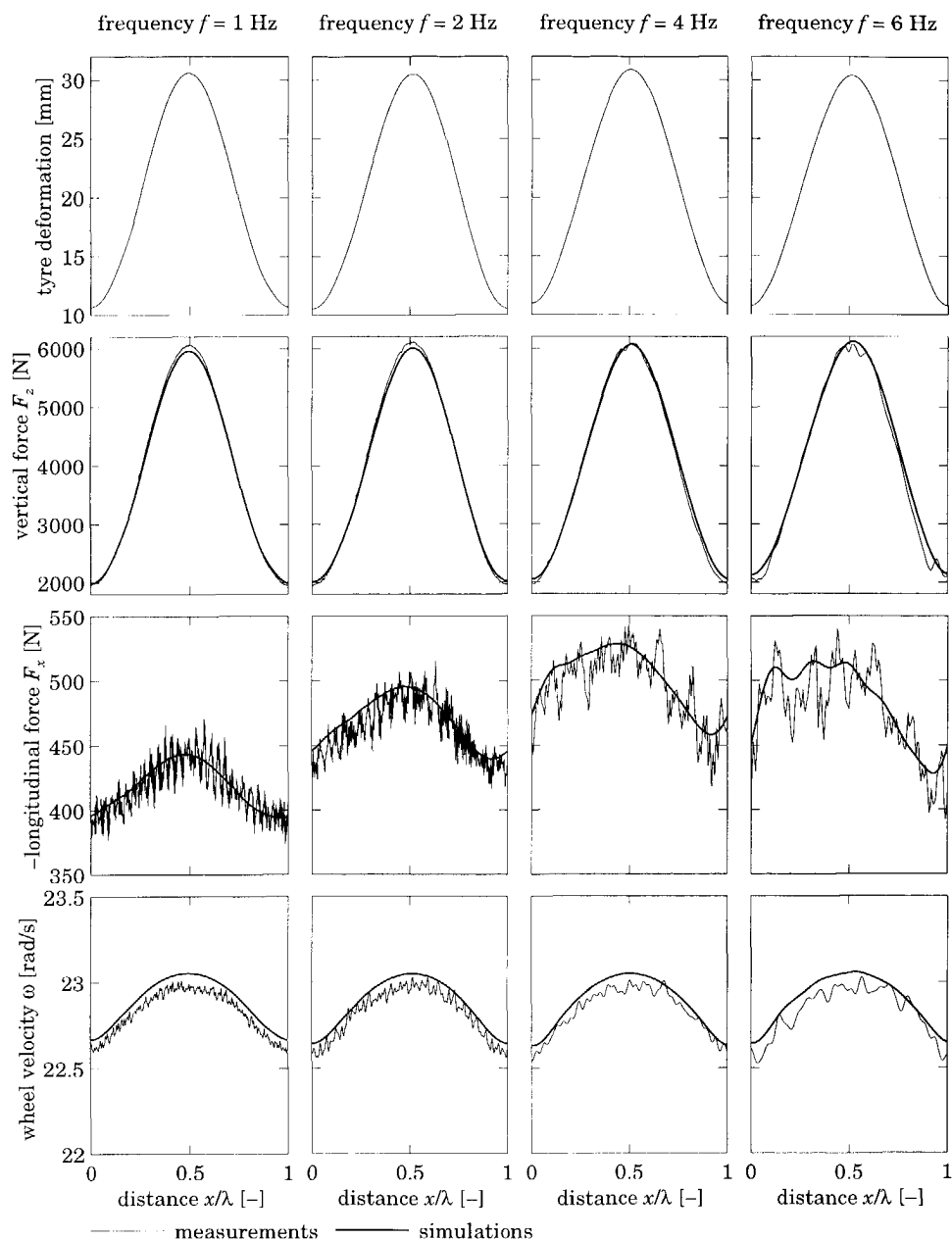
excitation frequency the response is symmetrical, at 4 and 6 Hz excitation frequency the force response is not symmetrical due to the acceleration and deceleration of the wheel.

Figure 11.2 presents the responses at a high constant brake torque. The rapid decrease of the rotational wheel velocity and decreasing vertical load indicate that full sliding occurs. The longitudinal forces also decrease with decreasing vertical load because the maximum longitudinal force is limited by the friction between tyre and road.

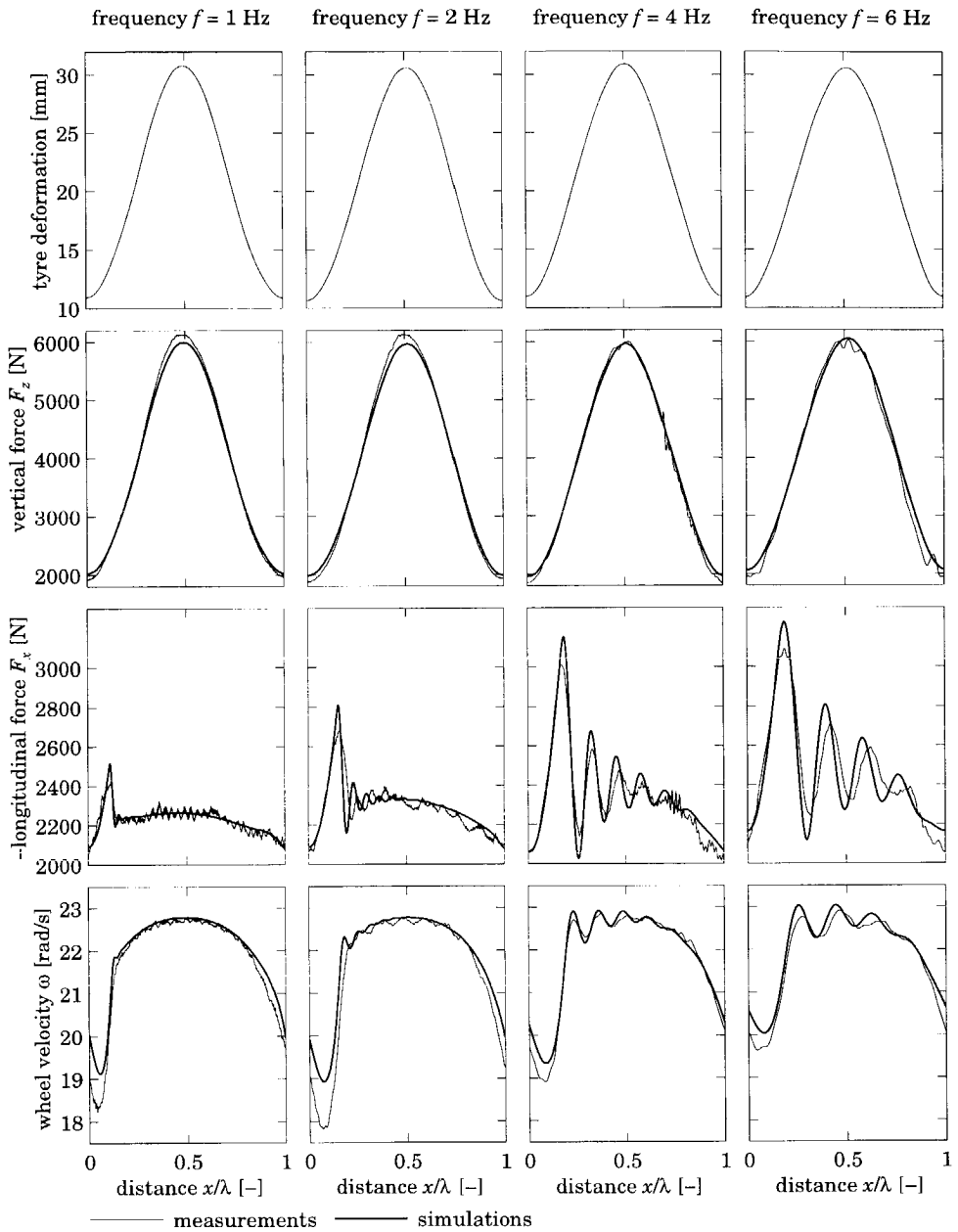
At the beginning of the increase in the vertical load, the wheel velocity is small and the slip is large. Consequently, the longitudinal force is equal to the friction coefficient multiplied by the vertical load ( $\mu F_2$ ). The longitudinal force increases rapidly with increasing vertical load as long as the slip is large. The increase in the longitudinal force stops abruptly when the wheel velocity has reached the original value again. Exactly at that point, the tyre shows the vibration corresponding to the in-phase rotational mode at 30 Hz.

Figure 11.3 shows the tyre response to a very severe operating condition. The very high constant brake pressure of 43 bar corresponds to an average reaction longitudinal force of 3300 N. This value is close to the average vertical load of 4000 N. The large brake torque causes wheel lock at the low values of vertical load. The rapid acceleration of the wheel causes more violent vibrations than those shown in the previous figure (*cf.* Figure 11.2).

Wheel lock only occurs if the wheel has enough time to reach wheel lock: at low frequency excitation wheel lock will occur, and at high frequency excitation wheel lock will not occur. The exact timing of wheel lock and spinning up of the wheel highly depends on the friction between tyre and road and the applied brake torque. Neither the friction between tyre and road nor the applied brake torque could be measured and they vary in time: the tyre temperature and disc brake temperature increase during the experiments. For the simulations these values have been estimated.



**Figure 11.1:** The measured and simulated responses to large variations of axle height and small constant brake pressure (6 bar).



**Figure 11.2:** The measured and simulated responses to large variations of axle height and high constant brake pressure (28 bar).



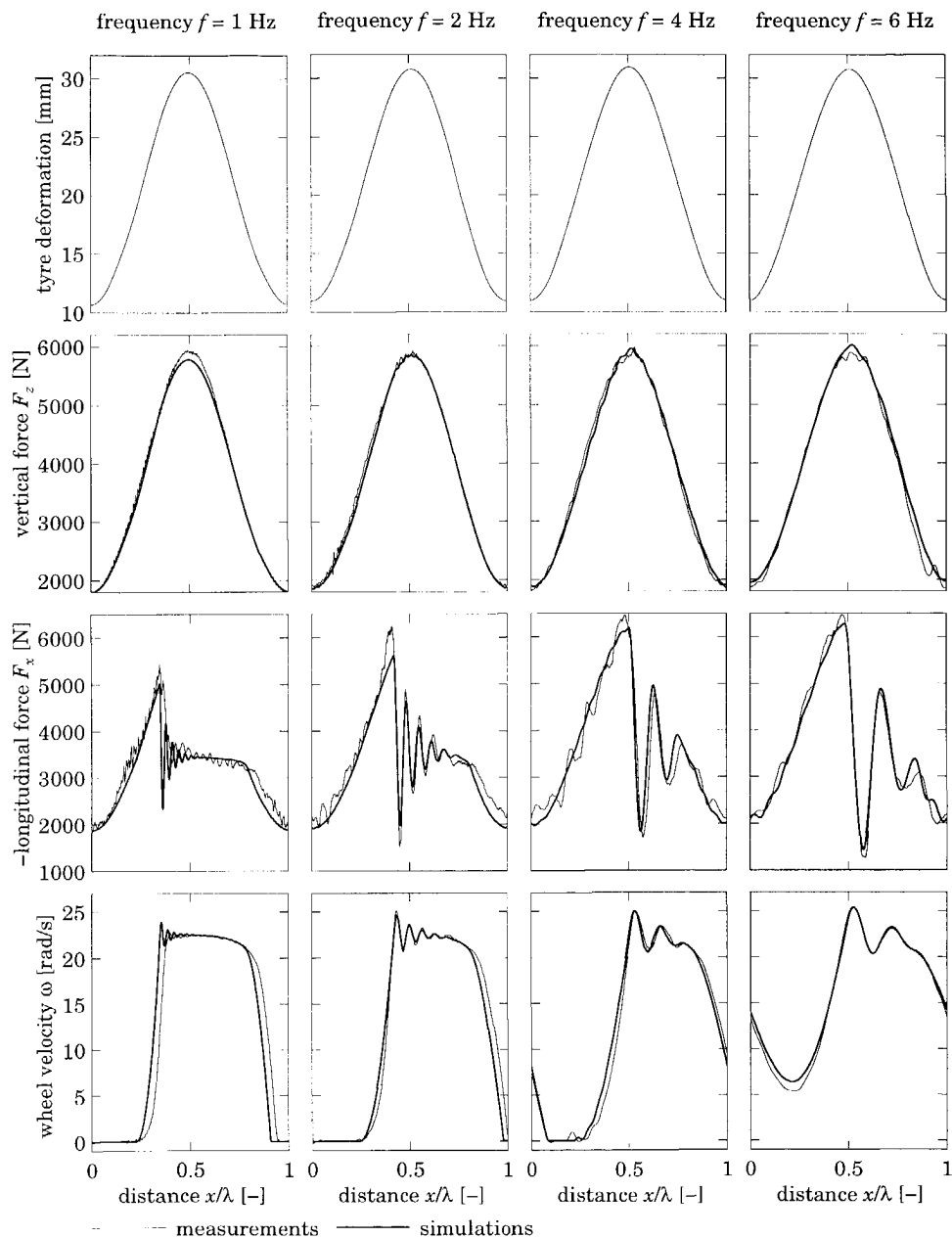


**Figure 11.3:** The measured and simulated responses to large variations of axle height and very high constant brake pressure (43 bar).

### **Tyre responses at an average axle height corresponding to 0 N vertical load**

One experiment was carried where the tyre loses contact with the road. The average value of the axle height chosen corresponds to the case where the tyre just touches the road without generating a vertical force. The amplitude of the axle height variations was equal to 10 mm. A relatively high average brake pressure (8 bar) was used.

Figure 11.4 presents the measured and simulated tyre responses. This figure shows that the tyre generates only a vertical force if the vertical tyre deformation is positive. Furthermore, the vertical tyre dynamics are excited by the sharp transitions in the vertical force.

The maximum longitudinal force is limited by the vertical force. If the tyre loses contact with the road, the longitudinal force becomes zero and the rotational wheel velocity decreases rapidly. At 1 and 2 Hz excitation, the wheel becomes locked. When the vertical load increases again, the wheel spins up and the in-phase rotational mode is excited.

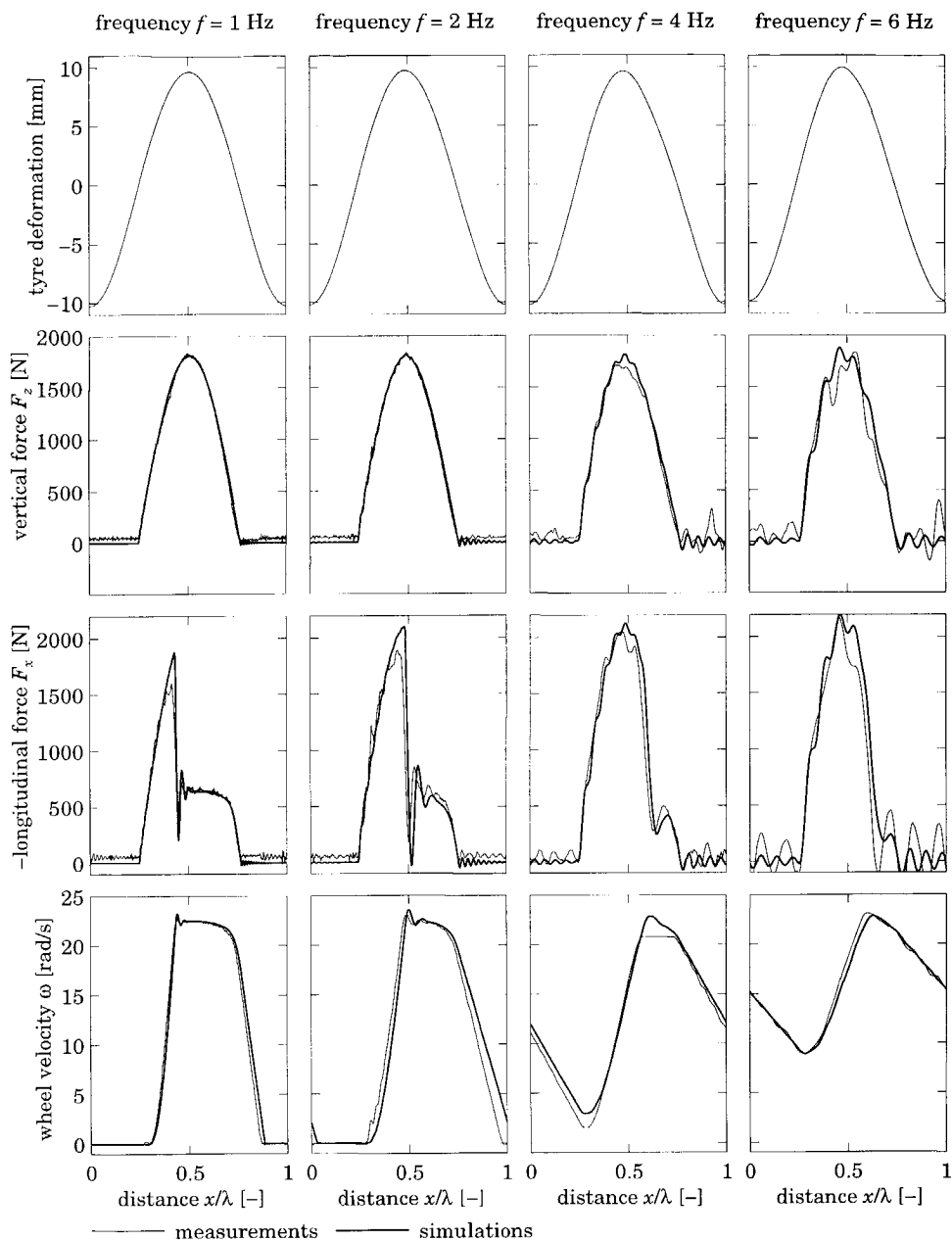


**Figure 11.4:** The measured and simulated responses to large variations of axle height where the tyre loses contact with the road, brake pressure=8 bar.



# 12

## Conclusions and Recommendations

---

### 12.1 The rigid ring model

The *rigid ring model* contains those modes of vibration of the tyre in which the tyre ring itself remains rigid and circular. In other words, the tyre ring moves as a rigid body with respect to the rim. The rigid ring for the in-plane tyre dynamic behaviour has three degrees of freedom: the horizontal and vertical motions and the rotation about the wheel axis. The motions of the ring are represented by three second order differential equations. The valid frequency range of the rigid ring model is limited to frequencies higher than the first natural frequencies of the tyre, where the natural modes correspond to the rigid ring modes, but sufficiently below the higher natural frequencies showing flexible modes of vibration of the ring. The experiments showed that the valid frequency range of the rigid ring model is 80 Hz for the longitudinal and rotational dynamics and 100 Hz for the vertical dynamics.

The relative damping of the in-phase rotational mode depends highly on the velocity, the vertical load and the amount of slip. This dependency can be easily explained by the influence of a relaxation length system on the tyre dynamics. The relative damping of all other tyre modes is low (3-5%) and almost independent of the operating conditions. The measured frequencies of the rigid

modes decrease significantly with increasing velocity. This effect has been reported in the literature [15,53,68,97,111,112,113]. At present there is no theoretical explanation for this effect available.

The tyre stiffnesses obtained from experiments with a non-rotating tyre cannot be used to represent the tyre dynamics of a rotating tyre. Instead, the experiments with a tyre rolling on the drum are to be used to estimate these parameters: the total vertical stiffness of the tyre was obtained from axle height oscillations for a rotating tyre; the sidewall stiffnesses and damping coefficients were obtained from brake experiments. The experiments with small random variations of brake torque around an average value used to estimate the frequency response functions proved to be a good method for estimating the dynamic parameters of the model. The cleat experiments are not needed to estimate the parameters, however, a single cleat experiment should be used to validate the frequency of the vertical mode of vibration of the tyre.

For the calculation of the transient responses in the contact zone a first order differential equation is used. In this contact model, the slip velocity is used as input rather than the slip. This means that the model can be used in zero velocity conditions. The first order differential equation provides a smooth transition from the response of a rotating tyre (force is proportional to the slip) to the response of a non-rotating tyre (force is proportional to the displacement). For a realistic response, the slip should be limited at zero velocity, otherwise, the first order differential equation may integrate the slip to plus or minus infinity. The slip characteristics for the contact model can be obtained from the slip characteristics based on the slip of the wheel and the reaction forces at the wheel.

The relaxation length contact model can be used to simulate the transient tyre responses also at short wavelengths. The model is able to simulate the transient responses even when more than one wavelength fit in the contact patch. Furthermore, the relaxation length contact model is able to represent the tyre rolling over short wavelength obstacles in an approximate way even if multiple contact patches arise due to the deformation of the tyre on the obstacle shape.

The overall relaxation length of the total tyre is not a parameter of the model but results from the tyre sidewall flexibilities and the relaxation length of the contact model. The expression of the longitudinal relaxation length of the complete tyre (longitudinal slip stiffness divided by the longitudinal stiffness) is similar to the expression for the lateral relaxation length (lateral slip stiffness divided by the lateral stiffness). The longitudinal relaxation length in the vertical load range considered is smaller than the lateral relaxation length. The ratio

between these relaxation lengths increases from 0.5 at 2000 N vertical load to 0.85 at 6000 N load. It is expected that a value of the vertical load exists where both relaxation lengths have the same value, since the longitudinal slip stiffness increases more than proportional to the vertical load and the lateral slip stiffness increases less than proportional to the vertical load.

The rigid ring model has been developed and validated for braking and free rolling conditions. It is assumed that the model will hold for driving conditions even though the definitions for slip during braking and during driving are not symmetrical. The rigid ring model has been validated for severe operating conditions: large brake torque variations including wheel lock of the wheel, rolling over short wavelength unevennesses while braking and large axle height variations while braking. The non-linear simulation model represents the tyre behaviour for these conditions rather well.

## 12.2 Tyre enveloping properties

The tyre enveloping properties were obtained from experiments at very low velocity of the tyre rolling at constant axle height over short wavelength road irregularities. These quasi-static tyre responses were also simulated using the *flexible ring* model. The flexible ring model consists of a flexible circular beam supported on an elastic foundation. When the non-linearity of the tyre sidewall stiffnesses is incorporated, the model is able to show an accurate response. Three effective inputs were defined to represent tyre enveloping properties:

- the effective plane height.
- the effective plane angle.
- the variation of the effective rolling radius.

The effective inputs are strongly dependent on the axle height and the obstacle shape. The effective inputs could be further decomposed into shifted basic functions. The effective plane height equals the sum of two positive shifted basic functions. The effective plane angle equals the sum of one positive and one shifted negative basic function. The effective rolling radius is related to the derivative of the effective plane angle with respect to the travelled distance. The influence of the obstacle shape on the effective inputs is governed by the basic functions, and the influence of the axle height (or average vertical load) is governed by the shift of the basic functions.

The effective inputs were used as excitation of the rigid ring model for dynamics simulations. The comparison of the simulated and measured responses

showed that the effective inputs can be used to excite the tyre also at higher velocities.

### 12.3 Recommendations for further research

Two sets of random brake experiments were carried out to estimate the tyre parameters: one set at low velocity and several levels of average brake torque and one set at several velocities and low average brake torque. To cover the entire operating range experiments at high velocity and high average brake torque should also be carried out. The experiments were carried out at one inflation pressure, but the influence of the inflation pressure on the tyre dynamic behaviour needs to be investigated as well.

The rigid ring model developed in this thesis has been validated for one tyre only. Consequently, it is important to validate the model structure for several types of tyres and sizes. It is expected that the basic structure of the rigid ring model does not need to be changed. However, some aspects of the tyre which are represented by polynomials (contact length and effective rolling radius as function of vertical load, velocity dependency of the parameters) might need some adaptation.

The stationary slip characteristics of the brush model have been used for the development and validation of the rigid ring model. Appendix B shows the changes of the model needed when the Magic Formula is used instead. However, the model has not been validated in combination with the Magic Formula. The limitation of the slip at velocities close to zero and the problems that arise with a characteristic showing a decreasing part need more attention.

The model development and the assessment of the parameters were based on the assumption that the dynamics of the tyre measured on a rotating drum test stand represent the dynamics of the tyre operating in a vehicle. This, even though the stationary slip characteristics on the drum and road differ considerably. Therefore, this assumption should be verified by testing the model on the road: measuring the reaction force of the tyre operating in a vehicle and comparing the results to simulations with the rigid ring model incorporated in a multi body vehicle simulation model. The model should also be tested for combined excitations: brake torque variations (*e.g.* ABS operation) on uneven roads in an actual vehicle (thus with the axle height not fixed).

The effective inputs obtained from the tyre enveloping properties can be represented by shifted basic functions. The comparison between the shape of the



basic functions and the response of a rigid wheel showed remarkable similarities. To be able to replace the rather cumbersome assessment of basic functions from either measurements or simulations with the flexible ring model, the benefits of using the rigid wheel motion should be investigated in greater detail.

The method of using effective road inputs (including effective rolling radius variations) has been validated for a number of short obstacles. The method should also be validated by using longer and smoother obstacles with wavelengths ranges from 10 cm to 1 m. Higher obstacles should also be considered. Nevertheless, it is expected that the method will hold also for longer wavelength unevennesses. At large wavelengths the effective inputs approach the actual geometrical surface quantities (height and slope) and the actual effective rolling radius occurring on a flat surface. It is important to further develop the method for general application on a random road surface. For such an application the present method of finding the effective inputs is too cumbersome.

The measurements and simulations showed that the effective rolling radius variations can be obtained from the other two effective inputs. This might be explained by theory. However, for a solid theoretical explanation, the influence of a varying road plane angle on the variation of the effective rolling radius needs more study. This can be done with simulation models that represent the effective rolling radius in a more accurate way than the flexible ring model used in this thesis (*e.g.* finite element models, or a flexible ring model where the height of the tread elements is not neglected [51]).

The dynamic response of the tyre to short wavelength unevennesses show the shortcomings of the model in the higher frequency range. The measured responses at higher velocities showed that the flexible modes have considerable amplitudes in the frequency range 80-150 Hz. At least one additional vertical flexible mode (at 90 Hz) and one additional longitudinal flexible mode (at 110 Hz) should also be incorporated into the model to obtain a more accurate model behaviour in the higher frequency range ( $> 60$  Hz). The inclusion of the first flexible modes at high velocity is important as the measurements showed beating phenomena probably originating from the rigid modes and the first flexible modes.



## Appendix

# A

### Experimental Setup

---

The experiments were carried out on the rotating drum test stand in the Vehicle Research Laboratory of the Delft University of Technology. On this test stand several test rigs can be mounted including the *cleat and brake* test rig and the *tyre measurement tower*. The drum was driven by an electric motor connected by means of two transmissions. The propulsion torque available to the drum depends on the transmission ratios. The choice of the velocities for the experiments (25, 39, 59, 92 and 143 km/h) was based on the characteristics of the electric motor and on the transmission ratios.

The drum has a steel surface. Even though a more realistic road surface (*i.e.* safety walk paper) generates better stationary slip characteristics, the tyre properties will quickly deteriorate due to excessive tread wear. Conversely, the stationary slip characteristics on a steel surface differ substantially from road measurements, but the dynamic tyre properties will be less effected.

#### A.1 Cleat and brake test stand

The tyre was mounted in the *cleat and brake* test rig which was placed on the drum test stand. The complete test stand is shown in Figure A.1. The tyre rolls over the rotating drum representing the road surface. This test stand is used to

examine the dynamic behaviour of the tyre in the frequency range 0-100 Hz. Obviously, the natural frequencies of the test stand must be sufficiently higher than the frequency range of interest.

The vertical axle height can be adjusted to load the tyre on the drum. During the measurements, the horizontal and vertical motions of the wheel axle are constrained. The reaction forces of the tyre are measured at both wheel bearings with piezo electric elements. These elements measure only the variations in the forces only and not the static components.

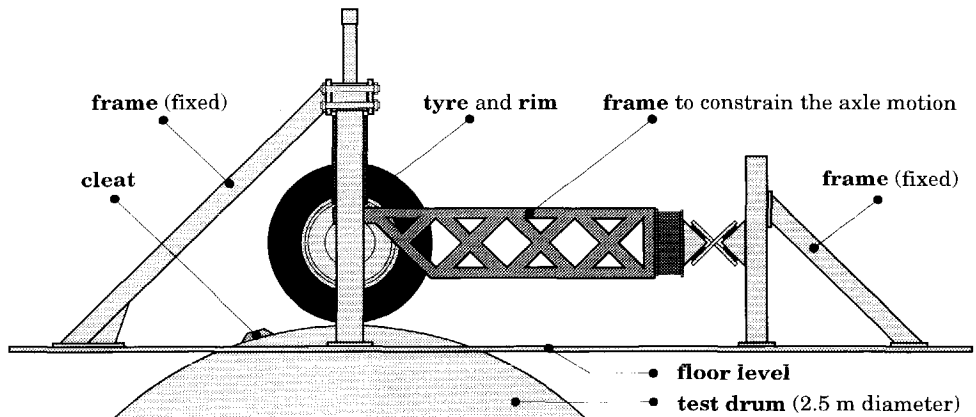


**Figure A.1a:** Schematic view of the cleat and brake test stand (side view).

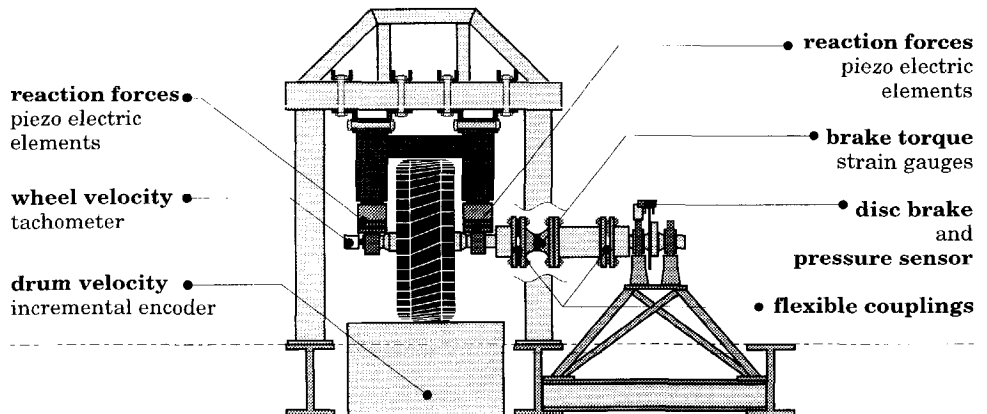


**Figure A.1b:** Schematic view of the cleat and brake test stand (front view).

The disc brake is mounted in a separate structure. The reaction forces of the brake are counterbalanced by the bearings of the brake shaft. The brake shaft

and the wheel shaft are connected with an intermediate shaft and two flexible couplings. These couplings are flexible in all directions except about the axis of revolution. This arrangement results in the application of a pure brake torque to the wheel without residual forces due to a possible offset in the alignment of the two shafts. The applied brake torque is measured with strain gauges in the coupling shaft.

To estimate the wheel slip, the wheel and drum velocities are measured. The wheel velocity is measured with a tachometer which has a good dynamic response. The generated signal showed a small ripple of 7 times the rotational velocity of the sensor. Therefore, the tachometer was connected through a gear with ratio varying between 5:1 at 25 km/h to 1:1 at 143 km/h to ensure that the frequency of the ripple was above 100 Hz. The drum velocity is measured with an incremental angle encoder that generates 2000 pulses each revolution. These pulses are converted into an analog signal by a frequency converter.

A hydraulic servo system is used to control the brake pressure. The servo valve is controlled by feedback of the difference between the measured and the desired brake pressure. The desired brake pressure signal is generated by a computer. This setup allows us to be flexible in the kind of brake torque excitations used: sinusoidal, block pulses, successive steps, random variations or sinusoidal sweeps.

Figure A.2 shows the hydraulic scheme. We may discern three pressures: the high pressure generated by a pump, the low pressure of the reservoir and the controlled pressure in the brake cylinder. The accumulator and pressure relief valve are used to maintain a constant high pressure.

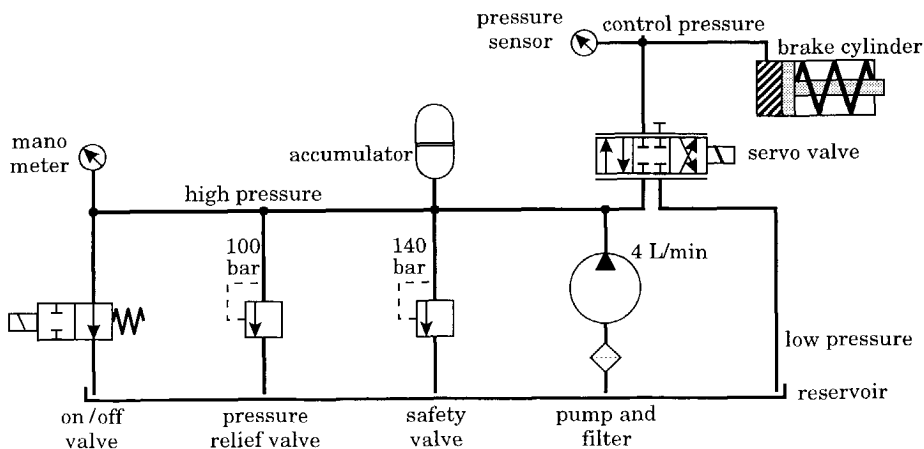


**Figure A.2:** The hydraulic scheme of the brake system.

The rotating part of the *cleat and brake* test stand can be seen as two systems connected by two flexible couplings and a coupling shaft (*cf.* Figure A.1). The brake system includes the brake disc, the rotating wheel-shaft and a part of the coupling shaft, and the wheel system includes the tyre, the rim, the rotating wheel-shaft and a part of the coupling shaft. The brake torque sensor is mounted in the coupling shaft between these two systems.

The moment of inertia of the wheel system was obtained from the difference in applied brake torque and the measured longitudinal reaction force multiplied by the tyre radius. The value of this moment of inertia was calculated from the ratio between the torque difference and the rotational acceleration (from differentiating the rotational velocity of the wheel). Obviously, only the low frequency components (0-5 Hz) were used. At higher frequencies tyre dynamics play a role.

The moment of inertia of the brake system was obtained from cleat experiments at free rolling. Due to the cleat passage, large rotational vibrations occur. The brake torque sensor measured the amount of torque needed to accelerate and to decelerate the brake system in rotational direction. The value of this moment of inertia was calculated from the ratio between the measured torque and the rotational acceleration (from differentiating the rotational velocity of the wheel).

### A.2 Tyre measurement tower

The *tyre measurement tower*, depicted in Figure A.3, can also be placed on the rotating drum test stand. This test stand was adapted for the experimental study of the combined slip tyre dynamics [65]. The tyre and measuring hub can be moved in the vertical direction, the excitation is controlled by a hydraulic cylinder. The wheel frame and the vertical cylinder are mounted on the top frame. The top frame is mounted on a large bearing, so that the entire rig can rotate about the vertical axle. The steer angle can be adjusted by a hydraulic cylinder. Obviously, for the in-plane experiments the steer angle was set to zero. The same hydraulic servo system of Figure A.2 was used to control the brake pressure.

The reaction forces at the wheel axle bearings are measured with strain gauges. The wheel velocity, the drum velocity and the applied brake pressure are measured with the same sensors, which can also be mounted on the *cleat and brake* pressure. The applied brake torque cannot be measured. Due to the

relatively high mass of the test stand and strain gauged measuring hub, the maximum frequency range of operating is limited to 20 Hz.

The moment of inertia of the rotating parts of the rim and brake system of the *measurement tower* was estimated from the time needed to achieve wheel lock of a wheel at a known level of constant brake torque.

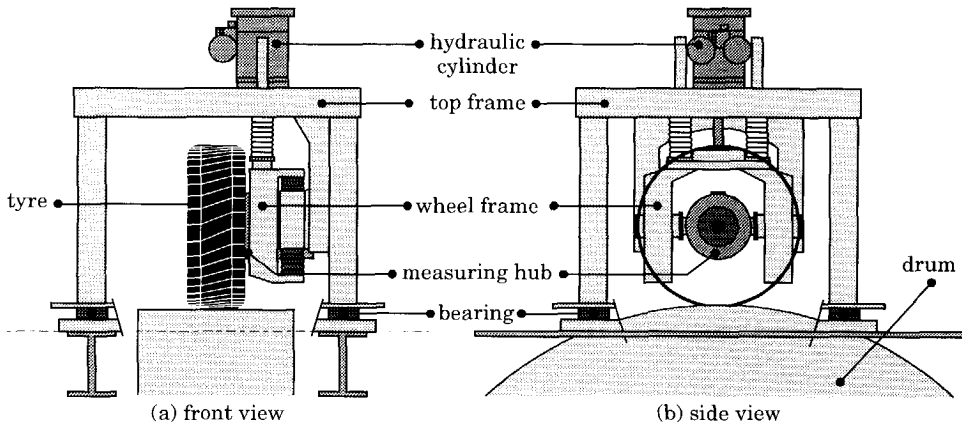


**Figure A.3:** The tyre measurement tower [65].

### A.3 Data acquisition and processing

Figure A.4 presents an overview of the data acquisition and the control system. The desired brake pressure signal and a trigger signal were generated by a personal computer equipped with a DA interface. A similar scheme is used for the axle height variations. A HP workstation with LMS CADA-X 2.6 software was used for the data acquisition and some basic signal processing (amplification and filtering). The filter frequency was set automatically to 0.4 times the sample frequency.

Most measurements were repeated 10 times and the average results were stored. The LMS software proved to be very powerful in estimating Frequency Response Functions (FRFs)

The off-line signal processing was performed in MATLAB 4.2c: Digital filtering, estimating natural frequencies and parameters. The non-linear simulations were also performed in MATLAB, using a fixed step 4th order RUNGE-KUTTA integration method.

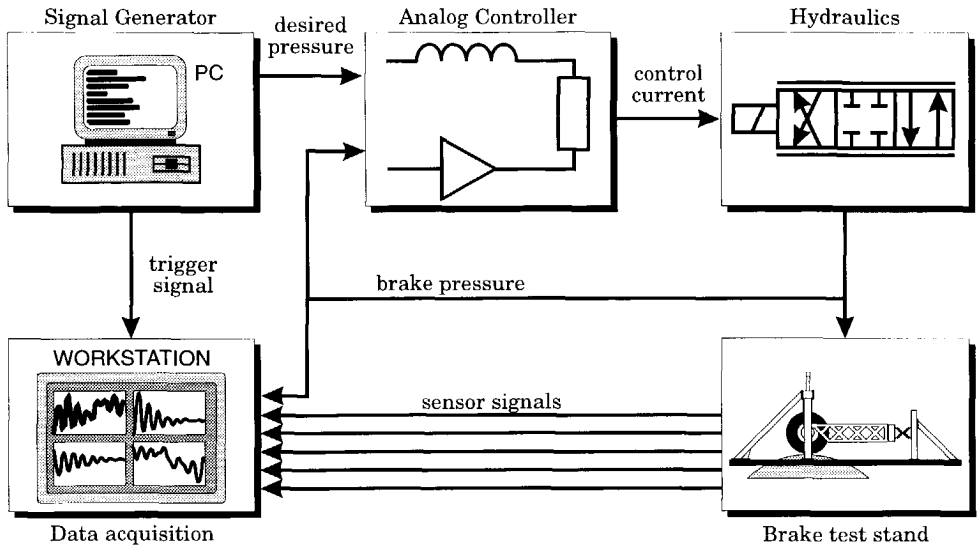


**Figure A.4:** Overview of the data acquisition and control system.



The contact model of the *rigid ring model* developed in this thesis was based on the brush model characteristics. In this appendix the changes to the model are discussed when the Magic Formula characteristics are used instead of the brush model characteristics. Figure B.1 depicts the stationary slip characteristics of the two models.

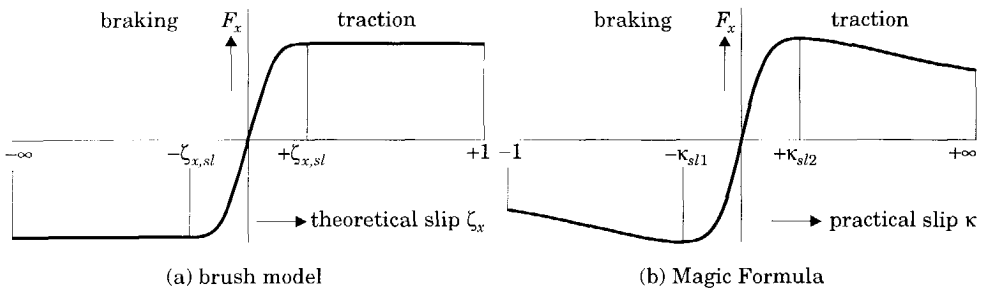


**Figure B.1:** Stationary slip characteristics.

One of the differences between the Magic Formula and the brush model is that the practical slip  $\kappa$  is generally used as input to the stationary slip characteristic of the Magic Formula while in this thesis the theoretical slip  $\zeta_x$  is used as input

for the stationary slip characteristic of the brush model. These slips are defined as:

$$\kappa = -\frac{V_{sx}}{V_x} \quad (3.3)$$

$$\zeta_x = -\frac{V_{sx}}{V_r} \quad (3.4)$$

where  $V_x$  denotes the forward velocity of the wheel axle,  $V_r$  denotes the rolling velocity of the wheel ( $= \Omega r_e$ ) and  $V_{sx}$  the slip velocity of the wheel. The equations of the contact model used read (cf. Eqs. 6.18e, 6.19 and 3.16):

$$\sigma_{c\zeta} \frac{d\zeta_{cx}}{dt} + |V_{cx}| \zeta_{cx} = -V_{c,sx} \quad (B.1a)$$

$$\sigma_{c\zeta} = \frac{\sigma_{c\zeta 0}}{C_{\kappa 0}} \frac{\partial F_x}{\partial \zeta_{cx}} \quad (B.1b)$$

$$F_{cx} = brush(\zeta_{cx}, F_{cx}, F_{cz}) \quad (B.1c)$$

where the additional subscript  $c$  is used to denote this situation in the contact model and  $\sigma_{c\zeta}$  denotes the relaxation length of the contact model,  $\sigma_{c\zeta 0}$  and  $C_{\kappa 0}$  denote the relaxation length of the contact model and the slip stiffness at free rolling and  $F_{cx}$  and  $F_{cz}$  denote the longitudinal and vertical forces in the contact patch. The theoretical slip in the contact patch  $\zeta_{cx}$ , which is used as input to the brush model characteristics, is found from the first order differential equation.

If the Magic Formula is used, the practical slip  $\kappa_c$  may be employed rather than the theoretical slip. Then the calculation scheme becomes:

$$\sigma_{c\kappa} \frac{d\kappa_c}{dt} + |V_{cx}| \kappa_c = -V_{c,sx} \quad (B.2a)$$

$$\sigma_{c\kappa} = \frac{\sigma_{c\kappa 0}}{C_{\kappa 0}} \frac{\partial F_x}{\partial \kappa_c} \quad (B.2b)$$

$$F_{cx} = MagicFormula(\kappa_c, F_{cx}, F_{cz}) \quad (B.2c)$$

The differences between the two calculation schemes is that the original scheme (Eq. B.1) uses the absolute value of the rolling velocity in the differential equation and the other approach (Eq. B.2) uses the absolute value of the forward velocity instead. To discriminate between both relaxation lengths of both approaches the additional subscripts  $\zeta$  and  $\kappa$  are used. The relaxation length of the second model is chosen such that the time constant of this differential equation is equal to the time constant of the original equation (Eq. B.1a):

$$\tau = \frac{\sigma_{c\kappa}}{|V_{cx}|} = \frac{1}{|V_{cx}|} \frac{\sigma_{c\kappa 0}}{C_{\kappa 0}} \frac{\partial F_x}{\partial \kappa_c} = \frac{1}{|V_{cx}|} \frac{\sigma_{c\kappa 0}}{C_{\kappa 0}} \frac{\partial F_x}{\partial \zeta_{xc}} \frac{\partial \zeta_{xc}}{\partial \kappa_c} = \frac{1}{|V_{cx}|} \frac{\sigma_{c\kappa 0}}{C_{\kappa 0}} \frac{\partial F_x}{\partial \zeta_{xc}} = \frac{\sigma_{c\zeta}}{|V_{cr}|} \quad (\text{B.3})$$

Note that the relaxation lengths at free rolling are equal to each other ( $\sigma_{c\kappa 0} = \sigma_{c\zeta 0}$ ).

To prevent the longitudinal slip to approach plus or minus infinity at zero velocity conditions, the theoretical slip was limited in Section 6.2 to the value at which total sliding starts ( $\pm \zeta_{x,sl}$ ). The limitation was essential for the simulation of braking with wheel lock (Section 9.4) and braking to stand-still (Section 9.5).

If the Magic Formula is employed, the slip value at the peak in the characteristic ( $-\kappa_{sl1}$  and  $+\kappa_{sl2}$ ) cannot be used to limit the slip as the decreasing part of the characteristics beyond the peak may not be neglected. An approach similar to the method employed by Higuchi [40] may be adopted to overcome the problems that arise with a characteristic showing a decreasing part. However, a simpler but less accurate method is to limit the slip  $\kappa$  to  $\pm 1$ .



# R

## ferences

---

1. T. Akasaka, S. Kagami and S. Yamazaki, "Deformation analysis of a radial tire loaded on a crossbar", *Tire Science and Technology*, TSTCA, Vol. 21, Nr. 1, 1993, pp. 40-63.
2. R.W. Allen, R.E. Magdaleno, T.J. Rosenthal, D.H. Klyde and J.R. Hogue, "Tire modeling requirements for vehicle dynamics simulation", SAE paper 950312, 1995.
3. D.J. Allison and R.S. Sharp, "On the low frequency in-plane forced vibrations of pneumatic tyre / wheel / suspension assemblies". 2<sup>nd</sup> International Colloquium on Tyre Models for Vehicle Dynamic Analysis, Berlin, Germany, February 20-21, 1997, *Vehicle System Dynamics*, Vol. 27 supplement, 1996, pp. 151-162.
4. D. Ammon, J. Rauh, J. Wimmer and M. Gipser, "High performance system dynamics simulation on the entire system tire - suspension - steering - vehicle", Proceedings of *International Symposium on Advanced Vehicle Control (AVEC'96)*, Aachen, Germany, June 24-28, 1996, pp. 1125-1141.
5. J.M. Badalamenti and G.R. Doyle jr., "Radial-interradial spring tire models", *Journal of Vibration, Acoustic, Stress and Reliability in Design*, Vol. 110, Nr. 1, 1988, pp. 70-75.
6. E. Bakker, L. Nyborg and H.B. Pacejka, "Tyre modelling for use in vehicle dynamics studies", SAE paper 870421, 1987.

## References

---

7. E. Bakker, H.B. Pacejka and L. Lidner, "A new tire model with an application in vehicle dynamics studies", SAE paper 890087, 1989.
8. P. Bandel and C. Monguzzi, "Simulation model of the dynamic behavior of a tire running over an obstacle", *Tire Science and Technology*, TSTCA, Vol. 16, Nr. 2, 1988, pp. 62-77.
9. P. Bannwitz and Ch. Oertel, "Adaptive Reifenmodelle: Aufbau, Anwendung und Parameterbestimmung", *VDI Berichte*, Nr. 1224, 1995, pp. 207-220.
10. P. Bayle, J.F. Forissier and S. Lafon, "A new tyre model for vehicle dynamics simulations", *Proceedings of Automotive Technology International '93*, pp. 1993, pp. 193-198.
11. J.E. Bernard and C.L. Clover, "Tire modeling for low-speed and high-speed calculations", SAE paper 950311, 1995.
12. F. Böhm, "Mechanik des Gürtelreifens", *Ingenieur-Archiv*, Vol. 35, 1966, pp. 82-101.
13. F. Böhm, "Theorie schnell veränderlicher Rollzustände für Gürtelreifen", *Ingenieur-Archiv*, Vol. 55, 1985, pp. 30-44.
14. H.K. Brewer, "Measurement of steady state and transient aircraft tire forces", *Tire Science and Technology*, TSTCA, Vol. 3, Nr. 2, 1975, pp. 111-127.
15. S. Bruni, F. Cheli and F. Resta, "On the identification in time domain of the parameters of a tyre model for the study of in-plane dynamics". 2<sup>nd</sup> International Colloquium on Tyre Models for Vehicle Dynamic Analysis, Berlin, Germany, February 20-21, 1997, *Vehicle System Dynamics*, Vol. 27 supplement, 1996, pp. 136-150.
16. K.M. Captain, A.B. Boghani and D.N. Wormley, "Analytical tire models for dynamic vehicle simulation", *Vehicle System Dynamics*, Vol. 8, 1979, pp. 1-32.
17. A. Chiesa, L. Oberto and L. Tamburini, "Transmission of tyre vibrations", *Automobile Engineer*, Dec. 1964, pp. 520 - 530.
18. S.K. Clark, R.N. Dodge and G.H. Nybakken, "Dynamic properties of aircraft tires", *Journal of Aircraft*, Vol. 11, Nr. 3, 1974, pp. 166-172.
19. S.K. Clark, "A brief history of tire rolling resistance", *Proceedings of the Rubber Division Symposia*, Vol. 1, Tire Rolling Resistance, Chicago, U.S.A., October 5-7, 1982, pp. 1-23.
20. D.C. Davis, "A radial-spring terrain-enveloping tyre model", *Vehicle System Dynamics*, Vol. 3, 1974, pp. 55-69.

21. A.C. Deneuvy, "Modal analysis of a pneumatic tyre and dynamic simulation by a substructuring method", *Proceedings of 7<sup>th</sup> International Modal Analysis Conference*, Las Vegas, U.S.A, January 30 - February 2, 1989, pp.1427-1433.
22. J.C. Dixon, *Tyres, Suspension and Handling*, Cambridge University Press, Cambridge, U.K., 1991.
23. J.W. Dunn and O.A. Olatunbosun, "Linear and non-linear modelling of vehicle rolling tyre low frequency dynamic behaviour". 11<sup>th</sup> IAVSD Symposium, Kingston, Canada, August 21-25, 1989, *Vehicle System Dynamics*, Vol. 18 supplement, 1989, pp. 179-189.
24. M. Eichler, "Ride comfort calculations with adaptive tire models", *Proceedings of International Symposium on Advanced Vehicle Control (AVEC'96)*, Aachen, Germany, June 24-28, 1996, pp. 927-939.
25. M. Eichler, "A ride comfort tyre model for vibration analysis on full vehicle simulations", 2<sup>nd</sup> International Colloquium on Tyre Models for Vehicle Dynamic Analysis, Berlin, Germany, February 20-21, 1997, *Vehicle System Dynamics*, Vol. 27 supplement, 1996, pp. 109-122.
26. H. van Eldik Tieme, A.J. Dijks and S. Bobo, "Measurement of tire properties", Chapter 8 of *Mechanics of Pneumatic Tires*, editor S.K. Clark, U.S. Department of Transportation, DOT HS 805 952, Washington D.C., U.S.A., 1981, pp. 541-720.
27. I. Fejes and A.R. Savkoor, "Modelling and identification of pneumatic tires", 2<sup>nd</sup> International Conference on Motion and Vibration Control (MOVIC), Yokohama, Japan, August 30 - September 3, 1994, pp. 303-309.
28. G. Fritz, *Seitenkräfte und Rückstellmomente von Personnenwagenreifen bei Periodischer Änderung der Spurweite, des Sturz- und Schräglaufwinkel*. PhD Thesis, Technische Universität Karlsruhe, Germany, 1978.
29. W. Fritz, *Federhärte von Reifen und Frequenzgang der Reifenkräfte bei periodischer Vertikalbewegung der Felge*, PhD Thesis, Technische Universität Karlsruhe, Germany, 1977.
30. R. Gasch and H. Pfützner, *Rotordynamik - Eine Einführung*, Springer-Verlag, Berlin, Germany, 1975.
31. G. Gim and N. Kang, "Requirements of a tire model for practical cornering simulations of vehicles", SAE paper 960179, 1996.
32. S. Gong, *A Study of In-Plane Dynamics of Tires*, PhD Thesis, Delft University of Technology, The Netherlands, 1993.
33. S. Gong, A.R. Savkoor and H.B. Pacejka, "The influence of boundary conditions on the vibration transmission properties of tires", SAE paper 931280, 1993.

## References

---

34. V.E. Gough, "Tyres and air suspension", *Advances in Automobile Engineering*, editor G.H. Tidbury, Pergamon Press, Oxford, U.K., 1963, pp. 59-91.
35. R.R. Guntur, *Adaptive Brake Control Systems*, PhD Thesis, Delft University of Technology, The Netherlands, 1975.
36. K. Guo, "Tire roller contact model for simulation of vehicle vibration input", SAE paper 932008, 1993.
37. W. Halbmann and M. Hölscher, "Power Hop – Durch den Reifen angefachte Schwingung von Fahrwerk und Antriebsstrang", *Fortschritte der Kraftfahrzeugtechnik 1: Fahrzeug Dynamik*, Braunschweig, Germany, 1988, pp. 83-109.
38. K.-F. Hey, *Untersuchungen von Längskräften zwischen Reifen und Fahrbahn beim Überfahren von Hindernissen*, PhD Thesis, Technischen Hochschule Carolo-Wilhelmina zu Braunschweig, Germany, 1963.
39. A. Higuchi and H.B. Pacejka, "The relaxation length concept at large wheel slip and camber", 2<sup>nd</sup> International Colloquium on Tyre Models for Vehicle Dynamic Analysis, Berlin, Germany, February 20-21, 1996, *Vehicle System Dynamics*, Vol. 27 supplement, 1996, pp. 50-64.
40. A. Higuchi, *Transient Response of Tyres at Large Wheel Slip and Camber*, PhD Thesis, Delft University of Technology, The Netherlands, 1997.
41. M. Hoffmann, E. Fischer and B. Richter, "The incorporation of tire models into vehicle simulations", 1<sup>st</sup> International Colloquium on Tyre Models for Vehicle Dynamic Analysis, Delft, The Netherlands, October 21-22, 1991, *Vehicle System Dynamics*, Vol. 21 supplement, 1993, pp. 49-57.
42. S.-C. Huang and C.-K. Su, "In-plane dynamics of tires on the road based on an experimentally verified rolling ring model", *Vehicle System Dynamics*, Vol. 21, 1992, pp. 247-267.
43. S.-C. Huang, "The vibration of rolling tyres in ground contact", *International Journal of Vehicle Design*, Vol. 13, 1992, pp. 78-95.
44. P. van der Jagt, H.B. Pacejka and A.R. Savkoor, "Influence of tyre and suspension dynamics on the braking performance of an anti-lock system on uneven roads", *Proceedings of 2<sup>nd</sup> International EAEC Conference on New Developments in Powertrain and Chassis Engineering*, IMechE C382/047, Strasbourg, France, June 14-16, 1989, pp. 453-460.
45. S.T.H. Jansen, J.J.M. van Oosten, J.P. Pauwelussen and H.B. Pacejka, "Sensitivity of vehicle handling to combined slip tyre characteristics", *Proceedings of International Symposium on Advanced Vehicle Control (AVEC'96)*, Aachen, Germany, June 24-28, 1996, pp. 873-886.



46. A. Kamoulakos and B.G. Kao, "Transient response of a rotating tire under multiple impacts with a road bump using PAM-SHOCK", *Proceedings of International Conference on High Performance Computing in Automotive Design, Engineering and Manufacturing*, Enghien, France, October 7-10, 1996.
47. B.G. Kao, E.Y. Kuo, M.L. Adelberg, S.V. Sundaram, T.R. Richards and L.T. Charek, "A new tire model for vehicle NVH analysis", SAE paper 870424, 1987.
48. D. Karnopp and G. Heess, "Electronically controllable vehicle suspensions", *Vehicle System Dynamics*, Vol. 20, 1991, pp. 207-217.
49. J.R. Kilner, "Pneumatic tire model for aircraft simulation", *Journal of Aircraft*, Vol. 19, Nr. 10, 1982, pp. 851-857.
50. S.-J. Kim and A.R. Savkoor, "Modal and vibration properties of rolling tires", *3<sup>rd</sup> International Conference on Motion and Vibration Control (MOVIC)*, Chiba, Japan, September 1-6, 1996, Vol. 3, pp. 133-139.
51. S.-J. Kim and A.R. Savkoor, "The contact problem of in-plane rolling of tires on a flat road", *2<sup>nd</sup> International Colloquium on Tyre Models for Vehicle Dynamic Analysis*, Berlin, Germany, February 20-21, 1997, *Vehicle System Dynamics*, Vol. 27 supplement, 1996, pp. 189-206.
52. J. Kisilowski and Z. Lozia, "Modelling and simulating the braking process of automotive vehicle on uneven surface", *9<sup>th</sup> IAVSD Symposium*, Linköping, Sweden, June 24-28, 1985, *Vehicle System Dynamics*, Vol. 15 supplement, 1986, pp. 250-263.
53. Y. Kobiki, A. Kinoshita and H. Yamada, "Analysis of interior booming noise caused by tyre and powertrain-suspension system vibration", *International Journal of Vehicle Design*, Vol. 11, Nr. 3, 1990, pp. 303-313.
54. L.E. Kung, W. Soedel, T.Y. Yang and L.T. Charek, "Natural frequencies and mode shapes of an automotive tire with interpretation and classification using 3-D computer graphics", *Journal of Sound and Vibration*, Vol. 102, Nr. 3, 1985, pp. 329-346.
55. L.E. Kung, W. Soedel and T.Y. Yang, "On the dynamic response at the wheel axle of a pneumatic tire", *Journal of Sound and Vibration*, Vol. 107, Nr. 2, 1986, pp. 195-213.
56. F.J. Laermann, *Seitenführungsverhalten von Kraftfahrzeugreifen bei schnellen Radlaständerungen*. PhD Thesis, Universität Braunschweig, *VDI Fortschritt Berichte*, Reihe 12, Nr. 73, 1986.
57. C.-W. Lee, *Vibration Analysis of Rotors*, Kluwer Academic Publishers, Dordrecht, The Netherlands, 1993.

## References

---

58. S. Lee, J.P. Chrstos and D.A. Guenther, "Modeling of dynamic characteristics of tire lateral and longitudinal force responses to dynamic inputs", SAE paper 950314, 1995.
59. H. Leiber and A. Czinczel, "Der elektronische Bremsregler und seine Problematik", *Automobiltechnische Zeitschrift (ATZ)* Vol. 74, 1972, pp. 269-277.
60. H. Leiber and A. Czinczel, "Antiskid systems for passenger cars with a digital electronic control unit", SAE paper 790458, 1979.
61. S.A. Lippmann, W.A. Piccin and T.P. Baker, "Enveloping characteristics of truck tires - a laboratory evaluation", SAE paper 650184, 1965.
62. S.A. Lippmann and J.D. Nanny, "A quantitative analysis of the enveloping forces of passenger tires", SAE paper 670174, 1967.
63. J.S. Loeb, D.A. Guenther, H.-H. Chen and J.R. Ellis, "Lateral stiffness, cornering stiffness and relaxation length of the pneumatic tire", SAE paper 900129.
64. Z. Lozia, "A two-dimensional model of the interaction between a pneumatic tire and an even and uneven road surface", 10<sup>th</sup> IAVSD Symposium, Prague, Czechoslovakia, August 24-28, 1987, *Vehicle System Dynamics*, Vol. 17 supplement, 1988, pp. 227-238.
65. J.P. Maurice, PhD Thesis, Delft University of Technology, The Netherlands, to be published.
66. J.H. McLoughlin, "Limited slip braking", *Proceedings of Anti-Lock Braking Systems For Road Vehicles*, IMechE C177/85, London, U.K., 1985, pp. 23-34.
67. K.E. Meier-Dörnberg and B. Strackerjan, "Prüfstandsversuche und Berechnungen zur Querdynamik von Luftreifen". *Automobil-Industrie*, 1977, Nr. 4, pp. 15-24.
68. B. Mills and J.W. Dunn, "The mechanical mobility of rolling tyres", *Proceedings of Vibration and Noise in Motor Vehicles*, IMechE C104/71, London, U.K., July 6-7, 1971, pp. 90-101.
69. V. Misun, "Loads on lorries" driving systems due to road unevennesses", *Proceedings of 3<sup>rd</sup> International Symposium on Heavy Vehicle Weights and Dimensions*, Cambridge, U.K., June 28 - July 2, 1992, pp. 203-210.
70. V. Misun, "Road loads when a vehicle moves over an unevenness in a road", *Heavy Vehicle Systems*, Special Series, *International Journal of Vehicle Design*, Vol. 1, Nr. 4, 1994, pp. 417-432.
71. M. Mitschke, *Dynamik der Kraftfahrzeuge, Band A: Antrieb und Bremsung*, Springer-Verlag, Berlin, Germany, 1982.

72. M. Mitschke, "Fahrzeug-Ruckeln", *Automobiltechnische Zeitschrift (ATZ)*, Vol. 96, 1994, pp. 59-60.
73. C. de Molina and D.V. Singh, "Influence of the dynamical tyre properties on the motorcycle driving behaviour", SAE paper 871227, 1987.
74. C.W. Mousseau and S.K. Clark, "An analytical and experimental study of a tire rolling over a stepped obstacle at low velocity", *Tire Science and Technology*, TSTCA, Vol. 22, Nr. 3, 1994, pp. 162-181.
75. C.W. Mousseau, G.M. Hulbert and S.K. Clark, "On the modeling of tires for the prediction of automotive durability loads", 14<sup>th</sup> IAVSD symposium, Ann Arbor, U.S.A., August 21-25, 1995, *Vehicle System Dynamics*, Vol. 25 supplement, 1996, pp. 466-488.
76. E. Negrus, G. Anghelache and A. Stanescu, "Finite element analysis and experimental analysis of natural frequencies and mode shapes for a non-rotating tyre", 2<sup>nd</sup> International Colloquium on Tyre Models for Vehicle Dynamic Analysis, Berlin, Germany, February 20-21, 1997, *Vehicle System Dynamics*, Vol. 27 supplement, 1996, pp. 221-224.
77. Ch. Oertel, "Darstellung zweidimensionaler Reibschwingungen in komplexen Modellierungen des Reifens", *Fortschritte der Kraftfahrzeugtechnik 1*, Fahrzeug Dynamik, Referate der zweite Fahrzeugdynamik-Fachtagung, Braunschweig, Germany, 1988.
78. Ch. Oertel, "On modeling contact and friction – calculation of tyre response on uneven roads", 2<sup>nd</sup> International Colloquium on Tyre Models for Vehicle Dynamic Analysis, Berlin, Germany, February 20-21, 1997, *Vehicle System Dynamics*, Vol. 27 supplement, 1996, pp. 289-302.
79. H. Oldenettel and H.J. Köster, "Test procedure for the quantification of rolling tire belt vibrations", 2<sup>nd</sup> International Colloquium on Tyre Models for Vehicle Dynamic Analysis, Berlin, Germany, February 20-21, 1997, *Vehicle System Dynamics*, Vol. 27 supplement, 1996, pp. 37-49.
80. H.B. Pacejka, *The Wheel Shimmy Phenomenon*, PhD Thesis, Delft University of Technology, The Netherlands, 1966.
81. H.B. Pacejka, "Approximate dynamic shimmy response of pneumatic tires". *Vehicle System Dynamics*, Vol. 2, 1973, pp. 49-60.
82. H.B. Pacejka, J. v.d. Berg and P.J. Jillesma, "Front wheel vibrations". Proceedings of 5<sup>th</sup> VSD-2<sup>nd</sup> IUTAM Symposium, Vienna, Austria, September 19-23, 1977, pp. 1-20.
83. H.B. Pacejka, "Analysis of tire properties", Chapter 9 of *Mechanics of Pneumatic Tires*, editor S.K. Clark, U.S. Department of Transportation, DOT HS 805 952, Washington D.C., U.S.A., 1981, pp. 721-870.

## References

---

84. H.B. Pacejka and R.S. Sharp, "Shear force development by pneumatic tyres in steady state conditions: a review of modelling aspects", *Vehicle System Dynamics*, Vol. 20, 1991, pp. 121-176.
85. H.B. Pacejka and E. Bakker, "The Magic Formula tyre model", 1<sup>st</sup> International Colloquium on Tyre Models for Vehicle Dynamic Analysis, Delft, The Netherlands, October 21-22, 1991, *Vehicle System Dynamics*, Vol. 21 supplement, 1993, pp. 1-18.
86. H.B. Pacejka and T. Takahashi "Pure slip characteristics of tyres on flat and on undulated road surfaces", Proceedings of *International Symposium on Advanced Vehicle Control (AVEC'92)*, Yokohama, Japan, September 14-17, 1992, pp. 360-365.
87. H.B. Pacejka, "The tyre as a vehicle component", Proceedings of *XXVI Fisita Congress*, Prague, Czech Republic, June 16-23, 1996.
88. H.B. Pacejka and I.J.M. Besselink, "Magic formula tyre model with transient properties". 2<sup>nd</sup> International Colloquium on Tyre Models for Vehicle Dynamic Analysis, Berlin, Germany, February 20-21, 1997, *Vehicle System Dynamics*, Vol. 27 supplement, 1996, pp. 234-249.
89. G.R. Potts, "Application of holography to the study of tire vibration", *Tire Science and Technology*, TSTCA, Vol. 1, Nr. 3, 1973, pp. 255-266.
90. G.R. Potts and T.T. Csora, "Tire vibrations studies: the state of the art", *Tire Science and Technology*, TSTCA, Vol. 3, Nr. 3, 1975, pp. 196-210.
91. G.R. Potts, C.A. Bell, L.T. Charek and T.K. Roy, "Tire vibrations", *Tire Science and Technology*, TSTCA, Vol. 5, Nr. 4, 1977, pp. 202-225.
92. P. Ratti, "Tire model and vehicle handling", SAE paper 885009, 1988.
93. J. Reimpell and P. Sponagel, *Fahrwerktechnik: Reifen und Räder*, Vogel-Buchverlag, Würzburg, Germany, 1986.
94. R.A. Ridha and M. Theves, *Advances in Tyre Mechanics*, Report 77, Rapra Review Reports, Vol. 7, Nr. 5, 1994.
95. T.R. Richards, L.T. Charek and R.W. Scavuzzo, "The effects of spindle and patch boundary conditions on tire vibration modes", SAE paper 860243, 1986.
96. M. Satoh and S. Shiraishi, "Performance of antilock brakes with simplified control technique", SAE paper 830484, 1983.
97. R.W. Scavuzzo, T.R. Richards and L.T. Charek, "Tire vibration modes and effects on vehicle ride quality", *Tire Science and Technology*, TSTCA, Vol. 21, Nr. 1, 1993, pp. 23-39.
98. R. Schieschke and R. Heimenz, "The relevance of tire dynamics in vehicle simulations", SAE paper 905221, 1990.

99. R. Schieschke and R. Heimenz, "The decisive role the quality of tyre approximation plays in vehicle dynamics simulations", 1<sup>st</sup> International Colloquium on Tyre Models for Vehicle Dynamics Analysis, Delft, The Netherlands, October 21-22, 1991, *Vehicle System Dynamics*, Vol. 21 supplement, 1993, pp. 156-166.
100. D.J. Schuring, "Dynamic Responses of Tires", *Tire Science and Technology*, TSTCA, Vol. 4, Nr. 2, 1976, pp. 115-145.
101. C.G. Shapley, "The influence of tire modeling in commercial vehicle simulation", Proceedings of a *Symposium on Commercial Vehicle Braking and Handling*, UM-HSRI-PF-75-6, Ann Arbor, U.S.A., May 5-7, 1975.
102. R.S. Sharp, "The dynamics of single track vehicles", *Vehicle System Dynamics*, Vol. 5, 1975/1976, pp. 67-77.
103. W. Soedel and M.G. Prasad, "Calculation of natural frequencies and modes of tires in road contact by utilizing eigenvalues of the axisymmetric non-contacting tire", *Journal of Sound and Vibration*, Vol. 70, Nr. 4, 1980, pp. 573-584.
104. B. Strackerjan, "Die Querdynamik von Kraftfahrzeugreifen", *VDI-Schwingungstagung*, October 1976.
105. D.S. Stutts, C.M. Krousgrill and W. Soedel, "Parametric excitation of tire-wheel assemblies by a stiffness non-uniformity", *Journal of Sound and Vibration*, Vol. 179, Nr. 3, 1995, pp. 499-512.
106. T. Takahashi and H.B. Pacejka, "Cornering on uneven roads", 10<sup>th</sup> IAVSD Symposium, Prague, Czechoslovakia, August 24-28, 1987, *Vehicle System Dynamics*, Vol. 17 supplement, 187, pp. 469-480.
107. T. Takahashi and M. Hoshino, "The tyre cornering model on uneven roads for vehicle dynamics studies", Proceedings of *International Symposium on Advanced Vehicle Control (AVEC'96)*, Aachen, Germany, June 24-28, 1996.
108. C. Tanguy, "Antiskid systems and vehicle suspension", SAE paper 865134, 1986.
109. J.T. Tielking, "Plane vibration characteristics of a pneumatic tire model", SAE paper 650492, 1965.
110. D.R. Turpin and D.F. Evans, "High-fidelity road/tire interaction models for real time simulations", SAE paper 950170, 1995.
111. T. Ushijima and M. Takayama, "Modal analysis of tire and system simulation", SAE paper 880585, 1988.
112. E. Vinesse, "Tyre vibration testing from modal analysis to dispersion relations", Proceedings of *ISATA 88*, Vol. 1, paper 88048, 1988.

## References

---

113. E. Vinesse, "Three problems of tire vibration: a unifying approach", *Proceedings of International Symposium on Advanced Vehicle Control (AVEC'92)*, paper Nr. 923065, Yokohama, September 14-17, 1992.
114. Y.Q. Wang, *Ein Simulationsmodell zum dynamischen Schräglauferverhalten von Kraftfahrzeugreifen bei beliebigen Felgbewegungen*, PhD Thesis, Universität Karlsruhe, 1993, *VDI Fortschritt Berichte*, Reihe 12, Nr. 189.
115. Y.Q. Wang, R. Gnadler and R. Schieschke, "Einlaufverhalten und Relaxationslänge von Automobilreifen", *Automobiltechnische Zeitschrift (ATZ)*, Vol. 96, 1994, pp. 214-222.
116. M. Watanabe, N. Noguchi, "A new algorithm for ABS to compensate for road-disturbances", SAE paper 900205, 1990.
117. K.J. Whatmough, "Real-time wheel brake and tire lateral force models refined for low speeds", SAE paper 940178, 1994.
118. H.P. Willumeit and F. Böhm, "Wheel vibrations and transient tire forces", *Vehicle System Dynamics*, Vol. 24, 1995, pp. 525-550.
119. J.Y. Wong, *Theory of Ground Vehicles*, 2<sup>nd</sup> edition, John Wiley & Sons Inc., New York, U.S.A., 1993.
120. K. Yamagishi and J.T. Jenkins, "The circumferential contact problem for the belted radial tire", *Journal of Applied Mechanics*, Vol. 47, 1980, pp. 513-518.
121. A. van Zanten, W.D. Ruf and A. Lutz, "Measurement and simulation of transient tire forces", SAE paper 890640, 1989.
122. A. van Zanten, R. Erhardt and A. Lutz, "Measurement and simulation of transients in longitudinal and lateral tire forces", SAE paper 900210, 1990.
123. J.W. Zellner, "An analytical approach to antilock brake system design", SAE paper 840249, 1984.
124. T. Zhang, *Höherfrequente Übertragungseigenschaften der Kraftfahrzeug-Fahrwerkssysteme*, PhD Thesis, Technische Universität Berlin, Germany, 1991.

# S ummary

---

## **The dynamic response of tyres to brake torque variations and road unevennesses**

Peter W.A. Zegelaar

The pneumatic tyre is a vital component of the road vehicle as it interacts with the road in order to produce the forces necessary for the support and the movement of the vehicle. To analyse the dynamics of the vehicle it is important to understand the behaviour of tyres. For this purpose, different kinds of mathematical models of the behaviour of the pneumatic tyre are used in vehicle dynamic simulations.

In this thesis two models are developed and used to study the in-plane dynamics of the tyre. The in-plane dynamics of tyres deal with the forces and motions in the plane of rotation of the wheel. These motions are generally excited by brake torque variations, road unevennesses, longitudinal and vertical axle motions and tyre non-uniformities. The first model, the *flexible ring* model, is used to study the tyre behaviour in detail. The second model, the relatively compact *rigid ring* model, is developed to be used in vehicle simulations. Both tyre models are based on the typical construction of the radial tyre: a circular belt mounted on a relatively soft carcass.

The flexible ring model consists of a flexible circular beam supported on an elastic foundation. This model is well suited for the analysis of the higher frequency tyre dynamics. The *Modal Expansion Method* is used to transform the partial differential equations of the deformation of the beam into a set of ordinary differential equations representing the modal displacements. Comparison with the results of experimental modal analysis showed that the model based on the modes of the free tyre plus an adequate contact model can represent the modes of vibration of the tyre standing on the road as well.

The flexible ring model is also used to calculate the deformation of the tyre loaded on the road. When the non-linearity of the tyre sidewall stiffnesses is incorporated the model is able to show accurate load-deflection characteristics. The flexible ring model is used to calculate the response of the tyre rolling quasi-statically over short wavelength road unevennesses. Three responses may be identified for the tyre rolling at constant forward velocity and constant axle height over obstacles: a variation in the vertical force, a variation in the longitudinal force and a variation in the rotational velocity. The response of the flexible ring model is rather good in comparison with experimental results.

To simulate the dynamic response of the tyre rolling over short wavelength unevennesses, a tyre model which describes the deformation of the tyre in detail (e.g. the flexible ring model) should be used. Simple tyre models which do not describe the tyre deformation in detail cannot be used directly on short wavelength unevennesses. To obtain a similar excitation of the simple model the actual road surface is replaced by an effective road surface such that the quasi-static response of the simple tyre model on the effective road surface is similar to the response of the real tyre on the actual road surface.

The effective road surface consists of three effective inputs: the effective plane height, the effective plane angle and the effective rolling radius variation. These three effective inputs can be further decomposed into shifted basic functions. The shift of the basic functions is approximately 80% of the contact length (on an undisturbed road surface) and both the length and size of the basic functions are related to the shape of the obstacles. It is of interest that the shape of the basic functions and the motion response of a rigid wheel show remarkable similarities.

The second model used is the *rigid ring* model. The development of this model is the main goal of the research presented in this thesis. One of the requirements for the rigid ring model is that it is a compact tyre model as it has to be used in vehicle dynamic simulations. In the frequency range up to 80 Hz the free tyre belt remains almost rigid. Accordingly, the belt is modelled as a rigid ring suspended on the rim. The rigid ring has three degrees of freedom for the motion



in the wheel plane: the horizontal and the vertical motion of the ring and the rotation about the wheel axis. A radial spring (residual stiffness) is attached to the belt to accomplish a realistic normal compliance of the tyre model.

The analysis of a discrete multi tread element contact model showed that the transient response of the tyre to load variations and to slip variations may be represented by a first order differential equation with the 'relaxation length' as parameter. The responses of four of such pragmatic models have been studied. A contact model is chosen which can be simulated easily and which shows an adequate response to slip and load variations even at zero velocity. The relaxation length contact model provides the tyre model with a smooth transition between a slip stiffness at high velocity (force proportional to slip velocity) to a tangential stiffness at (almost) stand-still (force proportional to deflection).

The total relaxation length of the tyre is considered as a property of the rigid ring model rather than a parameter of this model. The total relaxation length of the model depends on all the longitudinal and rotational flexibilities of the model: the longitudinal and rotational sidewall stiffnesses and the relaxation length of the contact model. The expression of the longitudinal relaxation length of the total tyre (longitudinal slip stiffness divided by the longitudinal stiffness) is similar to the expression of the lateral relaxation length (lateral slip stiffness divided by the lateral stiffness).

Experimental modal analysis of the non-rotating tyre is used to validate the modes of the model. The free non-rotating tyre has three modes of vibration in the frequency range 0-80 Hz: a vertical motion of the ring, a longitudinal motion of the ring, and a rotation of the ring. The tyre standing on the road also has three modes of vibration: a vertical motion of the ring and two rotational modes where the rim and ring rotate either in-phase or in anti-phase with respect to each other. The relative damping of the in-phase rotational mode depends highly on the operating conditions (vertical load, average brake torque and velocity).

The dynamic experiments have been carried out on the rotating drum test stand. Two rigs can be mounted on this test stand: the *cleat and brake* rig for the study of the tyre responses to brake torque variations and road unevennesses in the frequency range 0-100 Hz, and the *tyre measurement tower* for the study of the tyre response to axle height variations during constant braking in the frequency range 0-20 Hz.

The parameters of the rigid ring model have been obtained from quasi-static experiments (contact patch dimensions, effective rolling radius, masses and moments of inertia), from stationary rolling experiments (stationary slip characteristics, rolling resistance coefficients, vertical tyre stiffness), and from dynamic

rolling experiments (sidewall stiffnesses and sidewall damping coefficients). The measured frequency response functions of the longitudinal force to brake torque variations appeared to be the most accurate method for identifying the dynamic parameters of the model. In addition to these brake experiments at least one cleat experiment was needed to identify the vertical mode of vibration.

The vertical load influences some parameters of the model: contact patch dimensions, stationary slip characteristics and vertical tyre stiffness. Furthermore, the following velocity dependencies were incorporated in the model: the tyre radii (free radius, effective rolling radius and loaded radius) which grow with the square of the rotational velocity due to the centrifugal forces acting on the tyre; the vertical tyre stiffness which shows an approximately linear increase with the rotational velocity; the tyre sidewall stiffnesses which decrease approximately with the square root of the rotational velocity.

The rigid ring model has been validated for a number of severe conditions: large variations of brake pressure and zero velocity conditions (wheel lock and braking to stand-still). The experiments and simulations of the tyre rolling over short wavelength obstacles showed that the effective excitation can be used also at higher velocities. However, the cleat impacts on the tyre are rather severe and the frequency spectrum of the responses showed that at higher velocity, the high frequency flexible modes of the tyre are strongly excited.

The most important suggestion for further research is that the rigid ring model should be validated with tests of a wheel operating in a vehicle on the actual road. So far validation experiments have been done only in the laboratory, even though the model has been particularly developed to be used in the study of the dynamics of vehicles on the road. Therefore, it is thought to be very important to compare simulations of a vehicle model including the rigid ring model with road measurement results. The model should also be tested for combined excitations: brake torque variations (*e.g.* ABS operation) on uneven roads in an actual vehicle (thus with the axle height not fixed).

The method of using effective road inputs (including effective rolling radius variations) has been validated for a number of short obstacles. It is obvious that the method will hold also for longer wavelength unevennesses. At large wavelengths the effective inputs approach the actual geometrical surface quantities (height and slope) and the actual effective rolling radius occurring on a flat surface. It is important to further develop the method for general application on a random road surface. For such an application the present method of finding the effective inputs is too cumbersome.

# S

## amenvatting

---

### **De dynamische responsie van autobanden op remmomentvariaties en wegdekoneffenheden**

Peter W.A. Zegelaar

De autoband vormt een essentieel onderdeel van wegvoertuigen vanwege de wisselwerking met de weg om de krachten te genereren welke nodig zijn voor de ondersteuning en de beweging van het voertuig. Het is belangrijk om het gedrag van autobanden te doorgronden om in staat te zijn het dynamisch gedrag van het voertuig te kunnen analyseren. Voor dit doel worden verschillende typen modellen die het gedrag van de autoband beschrijven toegepast voor simulaties van het dynamisch gedrag van wegvoertuigen.

In dit proefschrift worden twee modellen ontwikkeld en toegepast om het gedrag van de band in het wielvlak te bestuderen. Het gedrag in het wielvlak van het wiel wordt gekenmerkt door de krachten en de bewegingen in het vlak van rotatie van het wiel. Deze bewegingen worden in het algemeen aangestoten door remmomentvariaties, wegdekoneffenheden, langs- en verticale bewegingen van de as van het wiel en bandonrondheden. Het eerste model, het *flexibele-ring*-model, is gebruikt om het gedrag van de band in detail te kunnen bestuderen. Het tweede model, het relatief compacte *starre-ring*-model, is specifiek ontwikkeld om te kunnen worden toegepast in voertuigsimulaties.

Het flexibele-ring-model bestaat uit een vervormbare cirkelvormige balk afgesteund om een elastische ondergrond. Dit model is zeer geschikt om de hoog frequente banddynamica te onderzoeken. De modale decompositiemethode is toegepast om de partiële differentiaalvergelijking die de vervorming van de balk beschrijft te transformeren in een stelsel gewone differentiaalvergelijkingen welke de modale verplaatsingen beschrijven. De vergelijking met de resultaten van experimentele modale analyse laat zien dat een model gebaseerd op de trilvormen van een vrije band plus een geschikt contact model in staat is om de trilvormen van de band die op de weg staat te beschrijven.

Het flexibele-ring-model is ook toegepast om de vervorming te berekenen van een band die onder belasting op de weg staat. Het model kan nauwkeurige kracht-vervorming karakteristieken produceren als de niet-lineariteiten van de zijwangstijfheden ingevoerd worden in het model. Het flexibele-ring-model is gebruikt om de responsie van de band te bepalen wanneer deze onder quasi-statische condities over wegdekoneffenheden met korte golflengte rolt. Voor een band rollend over obstakels met constante snelheid en bij constante ashoogte kunnen drie responsies worden waargenomen: een variatie in de verticale kracht, een variatie in de horizontale kracht en een variatie in de rotatiesnelheid van het wiel. De responsies van het flexibele-ring-model komen goed overeen met de gemeten responsies.

Om de dynamische responsie van een band rollend over korte golflengte wegdekoneffenheden te kunnen simuleren moet een bandmodel gebruikt worden die de vervorming van de band gedetailleerd beschrijft (zoals het flexibele-ring-model). Eenvoudige bandmodellen, die de vervorming van de band niet in detail beschrijven, kunnen niet direct gebruikt worden voor deze korte golflengte wegdek oneffenheden. Om een gelijksoortig aanstoting van het eenvoudige model te verkrijgen wordt de geometrie van het wegdek vervangen door een effectief wegdek zodanig dat de quasi-statische responsie van het eenvoudige model op het effectieve wegdek overeenkomt met de responsie van een echte band op de echte weg.

Het effectieve wegdek geeft drie effectieve inputs: de effectieve wegdekhoogte, de effectieve wegdekhelling en de variatie van de effectieve rolstraal. Deze drie effectieve inputs kunnen nog verder worden ontbonden in verschoven basisfuncties. De verschuiving van deze basisfuncties is ongeveer gelijk aan 80% van de contactlengte op het onverstoorde wegdek. Zowel de lengte als de vorm van de basisfuncties zijn gerelateerd aan de vorm van de obstakels. De overeenkomsten tussen de vorm van de basisfuncties en de responsie van de beweging van een star wiel zijn opmerkelijk.

Het *starre-ring-model* is het tweede bandmodel dat toegepast is. De ontwikkeling van dit model is het belangrijkste doel van het onderzoek gepresenteerd in dit proefschrift. Een belangrijke eis gesteld aan dit model is dat het compact en relatief eenvoudig is omdat het toegepast moet kunnen worden in voertuigsimulaties. De vrije band blijft vrijwel star in het frequentiegebied tot 80 Hz. Daarom is de band gemodelleerd als een starre ring. Deze ring heeft drie graden van vrijheid voor bewegingen in het wielvlak: de horizontale en verticale beweging van de ring en de rotatie om de wielas.

De analyse met behulp van een discreet contact model laat zien dat het overgangsgedrag van de band op variaties in verticale belasting of in slip kan worden gerepresenteerd door middel van een eerste orde differentiaalvergelijking met de *relaxatielengte* als parameter. Er zijn vier van zulke pragmatische modellen bestudeerd. Uiteindelijk is een contactmodel gekozen dat eenvoudig gesimuleerd kan worden en dat een geschikte responsie geeft op slipvariaties en op verticale krachtvariaties zelfs bij snelheid nul. Het relaxatielengte contactmodel geeft het bandmodel een soepele overgang van een slipstijfheid bij hoge snelheid (kracht is evenredig met slipsnelheid) naar een langsstijfheid bij een vrijwel stilstaande band (kracht is evenredig met vervorming).

De totale relaxatielengte van de band wordt gezien als een eigenschap van het *starre-ring-model* en is geen parameter van dit model. De totale relaxatielengte van het model hangt af van alle langs- en rotatie-stijfheden in het model: de langs- en rotatie-stijfheid van de zijwangen en het contact model met zijn relaxatielengte. De uitdrukking voor de relaxatielengte voor het langsgedrag van de totale band (langsslipstijfheid gedeeld door totale langsstijfheid) is overeenkomstig aan uitdrukking voor de relaxatielengte voor het dwarsgedrag (dwarsslipstijfheid gedeeld door dwarsstijfheid).

Experimentele modale analyse van een niet-roterende band is gebruikt om de eigen-trilvormen van het model te valideren. De vrije niet-roterende band heeft drie eigen-trilvormen in het frequentiegebied 0-80 Hz: een verticale beweging van de ring, een langsbeweging van de ring en een rotatie beweging van de ring. Als de band op de weg staat zijn er ook drie eigen-trilvormen: één verticale beweging van de ring en twee rotatie-trilvormen waarbij de velg en de ring of in-fase of in anti-fase roteren ten opzichte van elkaar. De relatieve demping van de in-fase trilling hangt sterk af van de externe condities (verticale belasting, remmoment en snelheid).

De dynamische experimenten zijn uitgevoerd op de roterende trommeltest-bank. Twee testopstellingen kunnen gemonteerd worden: de *obstakel en rem* testopstelling om het bandgedrag op remmomentvariaties en wegdekoneffenheden in

het frequentiegebied 0-100 Hz te onderzoeken, en de bandenmeettoren om het bandgedrag op ashoogtevariatiës tijdens remmen in het frequentiegebied 0-20 Hz te onderzoeken.

De parameters van het starre-ring-model zijn verkregen door middel van quasi-statische experimenten (afmetingen van het contactvlak, effectieve rolstraal, massa's en massa-traagheidsmomenten), van stationaire rol-experimenten (stationaire slipkarakteristieken, rolweerstandscoefficiënt, verticale stijfheid van de band) en van dynamische experimenten (stijfheden en dempingscoefficiënten van de zijwangen). De gemeten frequentie-responsie-functies van de langskrachten op remmomentvariatiës bleek de meest accurate methode te zijn om de dynamische parameters van het model te identificeren. Naast deze rem-experimenten moet ten minste één obstakel-experiment gedaan worden om de verticale trilvorm te kunnen identificeren.

De verticale belasting beïnvloed een aantal parameters van het model: de afmetingen van het contactvlak, de stationaire slipkarakteristieken en de verticale stijfheid van de band. Tevens zijn een aantal snelheidsafhankelijke parameters in het model ingevoerd: de straal van de band (de vrije straal, de effectieve rolstraal en de belaste bandstraal) die toeneemt met het kwadraat van de snelheid ten gevolge van de centrifugale krachten in de band. De verticale stijfheid van de band neemt lineair met de snelheid toe. De afname van de zijwangstijfheden is evenredig met de wortel van de snelheid.

Het starre-ring-model is voor een aantal lastige condities gevalideerd: grote variatiës in remmoment en snelheid nul condities (een geblokkeerd wiel en het remmen tot stilstand). De experimenten en simulaties van de band rollend over korte wegdekoneffenheden laten zien dat de effectieve aanstotingen gebruikt kunnen worden. Maar de obstakelstoten zijn nogal zwaar en het frequentiespectrum van de gemeten responsie toont dat bij hoge snelheden de flexibele hoogfrequente modes van de band sterk aangestoten worden.

De belangrijkste aanbeveling voor verder onderzoek is dat het starre-ring-model gevalideerd moet worden met experimenten van een wiel aan een voertuig op de echte weg. Tot nu toe zijn de experimenten uitgevoerd in het laboratorium, ondanks het feit dat het model speciaal ontwikkeld is om te worden toegepast in voertuigsimulaties. Het is daarom uiterst belangrijk dat simulaties van een voertuig inclusief het starre-ring-model vergeleken worden met metingen. Het model zou ook getest moeten worden voor gecombineerde situaties: remmomentvariatiës (bijvoorbeeld met ABS) op een oneffen wegdek in een voertuig (dus met niet-constante ashoogte)

De methode van het gebruik maken van effectieve inputs (inclusief de variatie in effectieve rolstraal) is slechts gevalideerd voor een aantal korte obstakels. Natuurlijk zal de methode ook gelden voor obstakels met langere golflengten. Voor lange golflengten zullen drie effectieve inputs de geometrie (hoogte en helling) van de echte weg en de effectieve rolstraal op een vlakke weg benaderen. Voor de verdere ontwikkeling van deze methode is het belangrijk dat een algemene methode wordt ontwikkeld voor de toepassing van de effectieve inputs op een weg met willekeurige oneffenheden. Voor deze toepassing is de huidige methode voor het bepalen van de effectieve inputs te omslachtig.

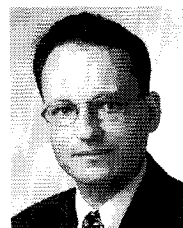




# C

## urriculum Vitae

---



Peter W.A. Zegelaar was born on the 22nd of April 1966 in Sliedrecht, the Netherlands. He graduated from the pre-university education (VWO) at the 'De Lage Waard' in Papendrecht in June 1985. In the summer of that year he participated both the Dutch Chemistry and Dutch Physics Olympiads. As a result he was able to participate the International Physics Olympiad in Yugoslavia.

Peter started studying Mechanical Engineering at the Delft University of Technology in September 1985. He graduated with credit in March 1991 on the modelling of elasto-kinematic elements and the control of the horizontal motion of a vehicle. The body of this vehicle was modelled as an elasto-kinematic element. He was awarded as best student Mechanical Engineering by the 'University Fund' of the Delft University of Technology. During his study he performed a practical trainee-ship at Volvo Car Company in Göteborg, Sweden, on the vertical vibrations using a quarter car vehicle model, and a trainee-ship at Bridgestone in Tokyo, Japan, on the objective and subjective rating of vehicle handling performance.

In March 1991 he became a PhD student at the Vehicle Research Laboratory of the Delft University of Technology where he performed the studies presented in this thesis. In August 1995 he was awarded the 'best paper award' for his presentation at the 14th IAVSD Symposium in Ann Arbor, U.S.A.



# **L**ist of publications

---

A.R. Savkoor, P.J.Th. Venhovens, P.W.A. Zegelaar, "Aspects of the application of modal analysis in vehicle dynamics", 16<sup>th</sup> International Seminar on Modal Analysis, Florence, Italy, September 9-12, 1991.

P.W.A. Zegelaar, S. Gong, H.B. Pacejka, "Tyre models for the study of in-plane dynamics", 13<sup>th</sup> IAVSD Symposium, Chengdu, P.R. of China, August 23-27, 1993, *Vehicle System Dynamics*, Vol. 23 supplement, 1994, pp. 578-590.

P.W.A. Zegelaar, H.B. Pacejka, "The in-plane dynamics of tires on uneven roads", 14<sup>th</sup> IAVSD Symposium, Ann Arbor, USA, August 21-25, 1995, *Vehicle System Dynamics*, Vol. 25 supplement, 1996, pp. 714-730.

P.W.A. Zegelaar and H.B. Pacejka, "Dynamic tyre responses to brake torque variations", 2<sup>nd</sup> International Colloquium on Tyre Models for vehicle Dynamic Analysis", Berlin, Germany, February 21-22, 1997, *Vehicle System Dynamics*, Vol. 27 supplement, 1996, pp. 65-79

P.W.A. Zegelaar, "Modal analysis of tyre in-plane vibrations", SAE paper 971101, SAE International Congress and Exposition, Detroit, USA, February 24-27, 1997.

J.P. Maurice, P.W.A. Zegelaar, H.B. Pacejka, "The influence of belt dynamics on the cornering and braking properties of tyres", 15<sup>th</sup> IAVSD Symposium, Budapest, Hungary, August 25-29, 1997, *Vehicle System Dynamics*, Vol. 29 supplement, 1998.

P.W.A. Zegelaar, "The tyre moving over short obstacles", Short Course on Tyre Models and Tydex Interface, Carl-Cranz-Gesellschaft, Oberpfaffenhoven, Germany, March 26-27, 1998.

